frontiers | Research Topics

The exploration of low-dimensional nanoparticles for disease diagnosis and therapy

Edited by
Hua Yue, Zhen Liu and Shaohua Wang

Published in
Frontiers in Bioengineering and Biotechnology

ISSN 1664-8714
ISBN 978-2-8325-3017-7
DOI 10.3389/978-2-8325-3017-7

About Frontiers

Frontiers is more than just an open access publisher of scholarly articles: it is a pioneering approach to the world of academia, radically improving the way scholarly research is managed. The grand vision of Frontiers is a world where all people have an equal opportunity to seek, share and generate knowledge. Frontiers provides immediate and permanent online open access to all its publications, but this alone is not enough to realize our grand goals.

Frontiers journal series

The Frontiers journal series is a multi-tier and interdisciplinary set of open-access, online journals, promising a paradigm shift from the current review, selection and dissemination processes in academic publishing. All Frontiers journals are driven by researchers for researchers; therefore, they constitute a service to the scholarly community. At the same time, the *Frontiers journal series* operates on a revolutionary invention, the tiered publishing system, initially addressing specific communities of scholars, and gradually climbing up to broader public understanding, thus serving the interests of the lay society, too.

Dedication to quality

Each Frontiers article is a landmark of the highest quality, thanks to genuinely collaborative interactions between authors and review editors, who include some of the world's best academicians. Research must be certified by peers before entering a stream of knowledge that may eventually reach the public - and shape society; therefore, Frontiers only applies the most rigorous and unbiased reviews. Frontiers revolutionizes research publishing by freely delivering the most outstanding research, evaluated with no bias from both the academic and social point of view. By applying the most advanced information technologies, Frontiers is catapulting scholarly publishing into a new generation.

What are Frontiers Research Topics?

Frontiers Research Topics are very popular trademarks of the *Frontiers journals series*: they are collections of at least ten articles, all centered on a particular subject. With their unique mix of varied contributions from Original Research to Review Articles, Frontiers Research Topics unify the most influential researchers, the latest key findings and historical advances in a hot research area.

Find out more on how to host your own Frontiers Research Topic or contribute to one as an author by contacting the Frontiers editorial office: frontiersin.org/about/contact

The exploration of low-dimensional nanoparticles for disease diagnosis and therapy

Topic editors

Hua Yue — Institute of Process Engineering, Chinese Academy of Sciences (CAS), China

Zhen Liu — Beijing University of Chemical Technology, China

Shaohua Wang — Ohio University, United States

Citation

Yue, H., Liu, Z., Wang, S., eds. (2023). *The exploration of low-dimensional nanoparticles for disease diagnosis and therapy*. Lausanne: Frontiers Media SA. doi: 10.3389/978-2-8325-3017-7

Table of contents

frontiers | Frontiers in Bioengineering and Biotechnology

TYPE Editorial
PUBLISHED 03 July 2023
DOI 10.3389/fbioe.2023.1227295

OPEN ACCESS

EDITED AND REVIEWED BY
Gianni Ciofani,
Italian Institute of Technology (IIT), Italy

*CORRESPONDENCE
Hua Yue,
hyue@ipe.ac.cn

RECEIVED 23 May 2023
ACCEPTED 23 June 2023
PUBLISHED 03 July 2023

CITATION
Yue H, Liu Z and Wang S (2023), Editorial: The exploration of low-dimensional nanoparticles for disease diagnosis and therapy.
Front. Bioeng. Biotechnol. 11:1227295.
doi: 10.3389/fbioe.2023.1227295

Editorial: The exploration of low-dimensional nanoparticles for disease diagnosis and therapy

Hua Yue[1]*, Zhen Liu[2] and Shaohua Wang[3,4]

[1]Institute of Process Engineering, Chinese Academy of Sciences (CAS), Beijing, China, [2]College of Life Science and Technology, Beijing University of Chemical Technology, Beijing, China, [3]Department of Biomedical Sciences, Ohio University Heritage College of Osteopathic Medicine, Athens, OH, United States, [4]Infectious and Tropical Disease Institute, Ohio University, Athens, OH, United States

KEYWORDS

low-dimensional nanoparticles, antioxidant platform, antibacterial implants/therapy, anticancer therapy, tumor DNA biosensors, cell imaging, 2D nanomaterials

Editorial on the Research Topic
The exploration of low-dimensional nanoparticles for disease diagnosis and therapy

In addition to 3D particles, low-dimensional nanoparticles (LDNs), such as 0D dots, 1D tubes, and 2D sheets, have garnered tremendous interest in the fields of nanotechnology and pharmacology. To bridge knowledge gaps for LDNs and inspire further developments in their bio-applications, we organized this Research Topic. So far, the Research Topic presents nine selected, peer-reviewed contributions, including six original researches, and three mini-reviews.

The contributions introduce fabrication strategies for LDNs-based vesicles from 0D nanocluster/quantum dot, 1D rod-shaped particles, and 2D MXenes, sourced from organic polymer or inorganic carbon/metal materials. Detailed research or reviews mainly focus on diagnosis and disease therapy, such as antioxidant platforms, antibacterial implants/therapy, anticancer therapy, tumor DNA biosensors, and cell imaging.

There are two contributions regarding LDNs-based biosensor/imaging. One contribution from Yu et al. focuses on the *in-situ* reduction of gold nanoparticles-decorated MXenes-based electrochemical sensing platform for gene detection. The biosensor has a linear detection range of 10 fM–10 nM and a detection limit of 0.38 fM. It also efficiently distinguishes single base mismatched DNA sequences. The biosensor has been successfully used for the sensitive detection of KRAS gene G12D, which has excellent potential for clinical analysis. The other contribution from Du et al. refers to Carbon dots (CDs), which are prepared from corn stalk powder and used as fluorescent sensors for the selective detection of $Fe3^{+}$ ions and biological cell imaging. The CDs have a low detection limit of 63 nM and high recognition for $Fe3^{+}$ ions, as well as low cytotoxicity and desirable biocompatibility. The study supports the potential of converting agricultural waste into carbon nanomaterials.

There are three contributions regarding LDNs-based antimicrobial therapy. The first article discusses the use of ultra-small molybdenum-based nanodots for the treatment of periodontal disease, a local inflammatory disease that results in the destruction of tissue due to inflammation. The study introduces ultra-small molybdenum-based nanodots (MoNDs) with strong reactive oxygen species (ROS) scavenging capabilities, which is an effective

strategy for oxidative stress-induced periodontal disease. Chen et al. demonstrate that MoNDs can alleviate periodontal inflammation by scavenging multiple ROS without any obvious side effects, thereby providing a candidate for the treatment of periodontal disease. The contribution from Hu et al. discusses the use of imidazole chloride ionic liquids for antibacterial activity. The authors comparatively evaluate the antimicrobial potency of imidazole chloride ILs (CnMIMCl) on *Staphylococcus aureus* (*S. aureus*). They discover that this nanozero material with long chain disrupted the bacteria membrane, causing the cytoplasm to flow out, and resulting in the fragmentation of the whole bacteria. The healing of skin abscesses was also accelerated within 12 days, demonstrating its potential as a candidate for the development of novel antibacterial agents. Another study in the Research Topic focuses on using gold nanoparticle decorated TiO_2 nanotubes for sonodynamic therapy against peri-implant infections. Sun et al. develop an antibacterial implant surface based on Au nanoparticle-modified TiO_2 nanotubes (AuNPs-TNTs). The study shows that the as-proposed AuNPs-TNTs exhibit significantly enhanced antibacterial activity under a simple ultrasound treatment, offering a way to design the surface of an artificial implant coating for resolving the bacterial infection-induced failure of dental implants.

The last original research is a study on the preparation strategy of one-dimensional poly (lactic-co-glycolic acid) particles for paclitaxel delivery. By using the emulsion solvent evaporation method with Na_2HPO^4 and sonication, the yield of nanorods in the optimal formula was 99%, and the aspect ratio was 5.35 ± 2.05. The size, shape, and aspect ratio of the nanoparticles could be controlled by manipulating process parameters, with surfactant PVA concentration being the most important factor. In addition, the anti-cancer drug paclitaxel could be successfully encapsulated in these nanorods. Although *in vitro* assessment has not been performed in detail, the present study provides an important avenue for fabricating non-spherical LDN using degradable materials, which endow the transform feasibility for further application in potential cancer therapy.

The Research Topic also includes three mini-reviews on LDNs as an emerging platform for cancer diagnosis and disease therapy. One review from Cui et al. summarizes the distinctive physicochemical capabilities of LDNs favored by biomedical applications. It emphasizes a multimodal nano-platform and relative applications in the imaging, diagnosis, and treatment of cancerous diseases. The review from Tang et al. highlights the advantages of 0-, 1-, and 2-dimensional carbon materials that help protect cells against oxidative stress. It also discusses their challenges and perspectives in biomedical fields and further clinical usages. Another review from Chen et al. focuses on the use of 2D nanomaterials (e.g., DNA origami, germanene, and MXene) for acute kidney injury (AKI) treatment. The review also highlights the challenges and future opportunities in the field, aiming to provide insights and theoretical support for the development of novel 2D nanomaterials for AKI treatment.

Overall, the Research Topic provides a comprehensive overview of recent research advances in nanomedicine and nanotechnology. The original work and reviews included in the Research Topic demonstrate the enormous potential of LDNs for a wide range of biomedical applications. The articles also provide insight into the current challenges and future opportunities associated with the development and application of these advanced materials. This Research Topic is expected to be of great interest to researchers and professionals working in the fields of bio-sensing, nanotechnology, and pharmacology.

Author contributions

HY collected the Research Topic information and wrote the editorial draft. ZL and SW reviewed and revised the manuscript. All authors contributed to the article and approved the submitted version.

Conflict of interest

The authors declare that the research was conducted in the absence of any commercial or financial relationships that could be construed as a potential conflict of interest.

Publisher's note

frontiers | Frontiers in Bioengineering and Biotechnology

TYPE Original Research
PUBLISHED 10 October 2022
DOI 10.3389/fbioe.2022.1042010

OPEN ACCESS

EDITED BY
Zhen Liu,
Beijing University of Chemical Technology, China

REVIEWED BY
Gao Fengxiang,
Changchun Institute of Applied Chemistry (CAS), China
Wensheng Chen,
Texas A&M University, United States

*CORRESPONDENCE
Qiong Huang,
qionghuang@csu.edu.cn

†These authors have contributed equally to this work

SPECIALTY SECTION
This article was submitted to Nanobiotechnology, a section of the journal Frontiers in Bioengineering and Biotechnology

RECEIVED 12 September 2022
ACCEPTED 20 September 2022
PUBLISHED 10 October 2022

CITATION
Chen L, Zhao T, Liu M, Chen Q, Yang Y, Zhang J, Wang S, Zhu X, Zhang H, Huang Q and Ai K (2022), Ultra-small molybdenum-based nanodots as an antioxidant platform for effective treatment of periodontal disease. *Front. Bioeng. Biotechnol.* 10:1042010. doi: 10.3389/fbioe.2022.1042010

Ultra-small molybdenum-based nanodots as an antioxidant platform for effective treatment of periodontal disease

Li Chen[1,2,3†], Tianjiao Zhao[1,2,3†], Min Liu[1,2], Qiaohui Chen[1,2], Yunrong Yang[3,4], Jinping Zhang[3,4], Shuya Wang[1,2], Xiaoyu Zhu[5], Huanan Zhang[5], Qiong Huang[1,4*] and Kelong Ai[2,3]

[1]Department of Pharmacy, Xiangya Hospital, Central South University, Changsha, China, [2]Hunan Provincial Key Laboratory of Cardiovascular Research, Xiangya School of Pharmaceutical Sciences, Central South University, Changsha, China, [3]Xiangya School of Pharmaceutical Sciences, Central South University, Changsha, China, [4]National Clinical Research Center for Geriatric Disorders, Xiangya Hospital, Central South University, Changsha, China, [5]Xiangya School of Stomatology, Central South University, Changsha, China

Periodontal disease (PD) is a local inflammatory disease with high morbidity, manifesting tissue destruction results from inflammation of the host immune response to bacterial antigens and irritants. The supportive function of connective tissue and skeletal tissue can be jeopardized without prompt and effective intervention, representing the major cause of tooth loss. However, traditional treatments exhibited great limitations, such as low efficacies, causing serious side effects and recurrent inflammatory episodes. As a major defense mechanism, reactive oxygen species (ROS) play important roles in the pathological progression of PD. Antioxidant therapy is widely believed to be an effective strategy for ROS-triggered diseases, including oxidative stress-induced PD. Most antioxidants can only scavenge one or a few limited kinds of ROS and cannot handle all kinds. In addition, current antioxidant nanomaterials present limitations associated with toxicity, low stability, and poor biocompatibility. To this end, we develop ultra-small molybdenum-based nanodots (MoNDs) with strong ROS in oxidative stress-induced PD. To the best of our knowledge, this is the first time that MoNDs have been used for PD. In the present study, MoNDs have shown extremely good therapeutic effects as ROS scavengers. Spectroscopic and *in vitro* experiments provided strong evidence for the roles of MoNDs in eliminating multiple ROS and inhibiting ROS-induced inflammatory responses. In addition, the mouse model of PD was established and demonstrated the feasibility of MoNDs as powerful antioxidants. It can alleviate periodontal inflammation by scavenging multiple ROS without obvious side effects and exhibit good biocompatibility. Thus, this newly developed nanomedicine is effective in scavenging ROS and inhibiting M1 phenotypic polarization, which provides promising candidates for the treatment of PD.

KEYWORDS

ROS, anti-inflammatory, gingival fibroblasts, periodontal disease, molybdenum-based nanodots

1 Introduction

As one of the most common oral diseases in the world, periodontal disease (PD) is recognized as the primary cause of tooth loss in adults (Kinane et al., 2017). This inflammatory disease damages the supporting structure of the teeth and finally results in tooth displacement and tooth loss, which poses a major threat to human health and life quality (Hajishengallis, 2015). Epidemiological reports indicate that PD is the sixth most common disease with an overall prevalence of 11.2%, affecting approximately 743 million people (Loesche and Grossman, 2001; Slots, 2017). Furthermore, it may cause local and systemic inflammatory responses when periodontal bacteria are transferred to the circulation through the bloodstream and the ulcerated epithelium of the periodontal pocket. Therefore, PD is also closely related to various systemic inflammatory diseases such as type 2 diabetes mellitus, atherosclerosis, rheumatoid arthritis, cancer, and inflammatory lung disease (Pihlstrom et al., 2005; Mealey, 2006; Krishna and De Stefano, 2016; Sczepanik et al., 2020; Hajishengallis and Chavakis, 2021; Zhu et al., 2022).

PD is caused by an imbalance between the bacterial flora of dental plaque and the host immune response (Cekici et al., 2014; Kinane et al., 2017; Fine et al., 2021). Specifically, the formation of dental plaque promotes the growth of pathogens and further accelerates the release of endotoxins (such as lipopolysaccharide (LPS)) during PD. Thereafter, immune cells are rapidly recruited to the damaged gingival tissue for initiating inflammation and host immune response to fight invading pathogens. If infection was not effectively blocked, a chronic inflammatory state may ensue with final progression to periodontal inflammation (redness, swelling, and bleeding) and periodontal injury (degradation of periodontal fibers and bones) (Liu et al., 2010; Hajishengallis, 2015; Bao et al., 2018). Traditional treatments for PD include mechanical plaque debridement, antibiotics, and anti-inflammatory drugs (Golub and Lee, 2020). However, these treatments are only effective in some patients because bacterial infection is only viewed as an initiating factor of PD. Uncontrollable inflammation and immune response eventually damage the periodontal tissue. Also, antibiotics and anti-inflammatory drugs often give rise to potential side effects and unwanted system immune responses. There is, therefore, an urgent need for effective and non-surgical therapeutics with minimal side effects.

During the initial stages of PD, i.e., the interval before the recruitment of immune cells to affected sites, the immediate protection provided by local resident cells in gingival tissues (e.g., gingival fibroblast and epithelial cells) is critical for limiting the amplification of infection (Buckley, 2011; Zhang et al., 2015; Wei et al., 2021). The gingival fibroblasts are the predominant cells within gingival connective tissue, and they play an important role in maintaining periodontal stability and regulating the host inflammatory immune response as key sentinel cells (Davidson et al., 2021). The expression of cell adhesion molecules on the surface of gingival fibroblasts is increased following the infection episode, which act as ligands and bind to receptors of immune cells. Then, these activated immune cells adhere and infiltrate into gingival tissue to induce a defense response against pathogens (Sui et al., 2020). However, adhesion molecules are further increased with continuing inflammatory factor stimulation, which exacerbate the local immune response. A large number of pro-inflammatory factors, reactive oxygen species (ROS), and matrix metalloproteinases are generated during the development of inflammation. ROS overproduction derived from activated immune cells overwhelms antioxidant systems insufficient for antioxidative defense and induces oxidative stress, which further interferes with cell cycle progression and promotes irreversible tissue injury (Liu et al., 2013; Sczepanik et al., 2020; Zhao et al., 2022). Massive apoptosis of gingival fibroblasts occurs under intensive oxidative stress, resulting in periodontal tissue destruction and even tooth loss. In addition, the phenotypic differentiation of macrophages is closely associated with the onset, progression, and resolution of acute inflammation during PD as the first line of host immune defense, which is affected by ROS overproduction (Holze et al., 2018; Garaicoa-Pazmino et al., 2019; Liu et al., 2022; Xiao et al., 2022). Specifically, macrophages are classified into two categories: the pro-inflammatory M1 phenotype and the anti-inflammatory M2 phenotype. M1 macrophages are involved in the pro-inflammatory response of PD by producing high levels of interleukin 6 (IL-6), tumor necrosis factor *a* (TNF-α), and IL-1β and causing periodontal tissue destruction with increased matrix-degrading protease production. In contrast, M2 macrophages exhibit significant anti-inflammatory and healing-promoting effects by secreting TGF-β, IL-10, and Arg-1, which play important roles in alleviating inflammation and repairing damaged tissues. ROS can promote macrophages to polarize into the M1 phenotype (Wang et al., 2021a; Chen et al., 2021). Therefore, inhibiting M1 macrophage polarization is also an important target for the treatment of PD.

In that case, we hypothesized that effective local ROS scavengers may effectively improve the periodontal microenvironment and alleviate the inflammatory condition. Currently, various antioxidative defense strategies based on natural enzymes, antioxidants, and nanozymes are being applied to treat PD (Bao et al., 2018). However, most conventional antioxidants are usually confined by the poor dispersity, low stability, and short duration of action. Meanwhile, natural enzymes and single-component nanozymes usually show a high specificity for a certain ROS and therefore, fail to scavenge various ROS generated during disease progression (Goyal et al., 2014; Yang et al., 2022a; Yang et al., 2022b; Xiao et al., 2022). Furthermore, the synthesis of the multienzyme-based antioxidant is often complicated, shows low stability, and is difficult to be repeated. More importantly, the potential side effects of various exogenous nanomaterials will be a

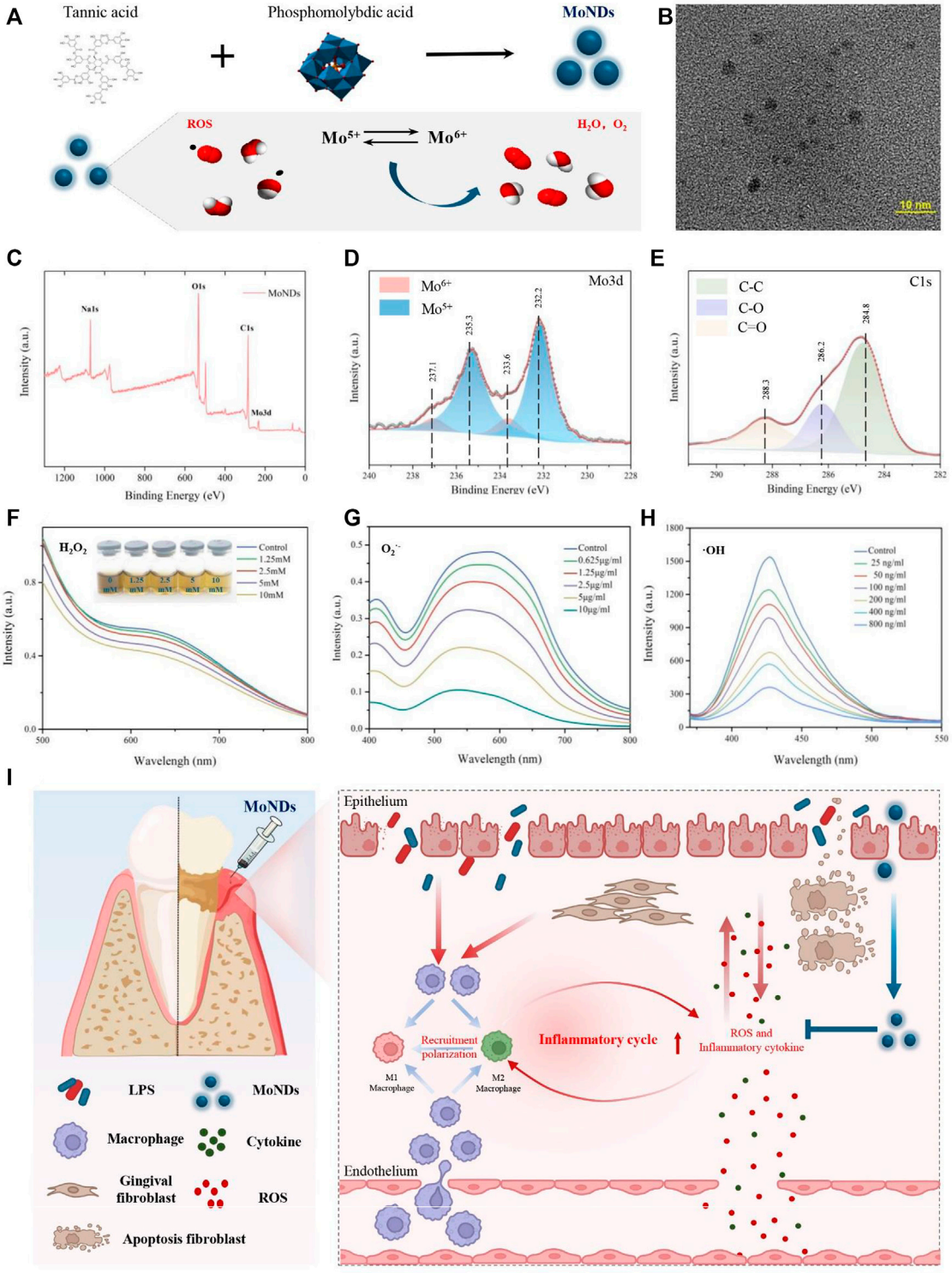

FIGURE 1
Preparation and characterization of MoNDs. **(A)** Schematic illustration of the preparation and ROS scavenging capacity of MoNDs. **(B)** TEM image of MoNDs in water, scale bar: 10 nm. **(C–E)** XPS spectrum of MoNDs. H_2O_2 **(F)**, $O_2^{\cdot-}$ **(G)**, and OH **(H)** scavenging ability of MoNDs. **(I)** Schematic illustration showing MoND treatment of mice with PD. After subgingival injections, MoNDs were effectively accumulated in gingival tissue through the damaged endothelium. As a ROS scavenger, MoNDs protected gingival fibroblasts from oxidative stress and alleviated ROS-induced apoptosis. In addition, MoNDs had the capacity to control inflammation *via* regulating macrophage polarization and recruitment.

tricky problem in practical use, limiting their clinical translation. Herein, we developed ultra-small molybdenum-based nanodots (MoNDs) with high redox activity to scavenge ROS in oxidative stress-induced PD, which also exerted potent anti-inflammatory effects. Polyoxometalate (POM) is an emerging anionic cluster material that has received extensive attention due to its unique physicochemical properties (Cherevan et al., 2020). Recently, many nanoparticles with low toxicity, high stability, and high activity have been synthesized by modifying and changing the structure, polarity, charge, and composition of POMs (Ni et al., 2017; Ni et al., 2018; Huang et al., 2023). Among them, Mo-based POM (Mo-POM) with advantages of small size, high physiological stability, high biocompatibility, and low toxicity is widely being used in biomedicine, including cancer treatment, and antibacterial and antiviral therapies (Ni et al., 2017; Zhao et al., 2020; Lu et al., 2021). More importantly, Mo-POM efficiently scavenges ROS through charge transfer between Mo(VI) and Mo(V) states (Zhao et al., 2020; Wang et al., 2021b). In our study, we extracted and cultured primary mouse gingival fibroblasts, which can better reflect the *in vivo* microenvironment and obtain data closer to the physiological functions. Overall, this nanomaterial is expected to overcome the shortcomings of traditional therapies that only target bacteria and pathogens and can effectively inhibit inflammation and oxidative stress at the same time, promoting the healing of the damaged gingival tissue (Figure 1I).

2 Results and discussion

2.1 Synthesis and characterization of MoNDs

MoNDs were synthesized by reducing phosphomolybdic acid with tannic acid under alkaline conditions (Figure 1A). The transmission electron microscopy (TEM) image indicated that MoNDs have uniformly dispersed nanodot structures with the diameter of about 2–5 nm (Figure 1B). The elemental composition and chemical properties were validated by the X-ray photoelectron spectroscopy (XPS) spectrum (Figures 1C–E; Supplementary Figure S1). The main valence states in MoNDs were Mo(V) and Mo(VI), and the content of Mo(V) was as high as 71.89%. The potential charge transfer between Mo(V) and Mo(VI) endows MoNDs strong abilities to eliminate multiple ROS. As expected, MoNDs efficiently scavenged hydrogen peroxide (H_2O_2), superoxide anion ($O_2^{\cdot-}$), and hydroxyl radical ($^{\cdot}OH$) (Figure 1A). MoNDs reacted with different concentrations of H_2O_2 (1.25–10 mM), resulting in noticeable color changes of MoNDs from a dark color to a lighter color and eventually yellow (Figure 1F).

Moreover, MoNDs had strong scavenging effects on $O_2^{\cdot-}$ and $^{\cdot}OH$ (Figures 1G,H). The SOD mimic activity of MoNDs was about 221U/mg, and 76% $^{\cdot}OH$ was quenched after incubation with 800 ng/ml MoNDs.

2.2 Therapeutic effects of MoNDs

To evaluate the therapeutic effects of MoNDs, an LPS-induced PD model was constructed by a subgingival injection of LPS for 5 days (Figure 2A). Subsequently, different doses of MoNDs were consecutively administered for 3 days. Representative pictures of the gums from the mice in each group were compared (Figure 2B). The symptoms of redness, swelling, and exudation were demonstrated in LPS-induced PD model mice, which were obviously alleviated by the treatment of MoNDs. Correspondingly, the food intake and body weight of the mice were reduced during the first 5 days of LPS injection, and they recovered gradually after stopping injection of LPS and starting MoND treatment (Figures 2C,D).

Moreover, MoNDs have been shown to have anti-inflammatory and anti-apoptotic activities in PD mice. During PD, a large number of inflammatory factors such as IL-6 and TNF-α were generated from activated inflammatory cells, while the high expression of cyclooxygenase-2 (COX-2) promotes the production of ROS (Hirose et al., 2001). In LPS-induced model mice, we detected obvious increased mRNA expression of COX-2, TNF-α, and IL-6 and high tissue levels of TNF-α and IL-6 (Figures 2E–I). MoNDs also significantly inhibited these inflammatory mediators. Further studies indicated the increased infiltration of inflammatory cells in the gingival tissues after LPS administration. Massive inflammatory cells and F4/80-positive macrophages were observed in the gingival tissues of the LPS group from the results of hematoxylin and eosin (HE) staining and F4/80 staining (Figures 2J,K, Figures 3A,D). Also, MoNDs alleviated the severe and destructive inflammatory status of the gingival tissues by reducing inflammatory cell aggregation. The cell apoptosis was further detected by terminal deoxynucleotidyl transferase dUTP nick end labeling (TUNEL). MoNDs substantially reduced the apoptosis of the gingival tissue in mice with PD (Figures 3B,E). More importantly, Ki-67 staining indicated that MoNDs effectively restored the proliferation capacity of gingival tissue (Figures 3C,F).

In periodontal tissue, gingival fibroblasts are the most ubiquitous residential cells. During the progression of chronic PD, activated immune cells infiltrate into the local periodontal tissue and then reside there (Hosokawa et al., 2005; Cheng et al., 2015; Chiquet et al., 2015). The excessive production of ROS by these immune cells can directly induce apoptosis of gingival fibroblasts, resulting in periodontal destruction (Zhu et al., 2021). Therefore, a timely and effective control of ROS generation can effectively hinder the progression in the early stage of inflammation. In this study, we extracted and cultured primary mice gingival fibroblasts by the tissue block culture method and then stimulated with H_2O_2 to recapitulate the oxidative stress state of PD (Figures 4A; Supplementary Figure S2). As shown in Figures 4B,C, gingival fibroblasts generated a

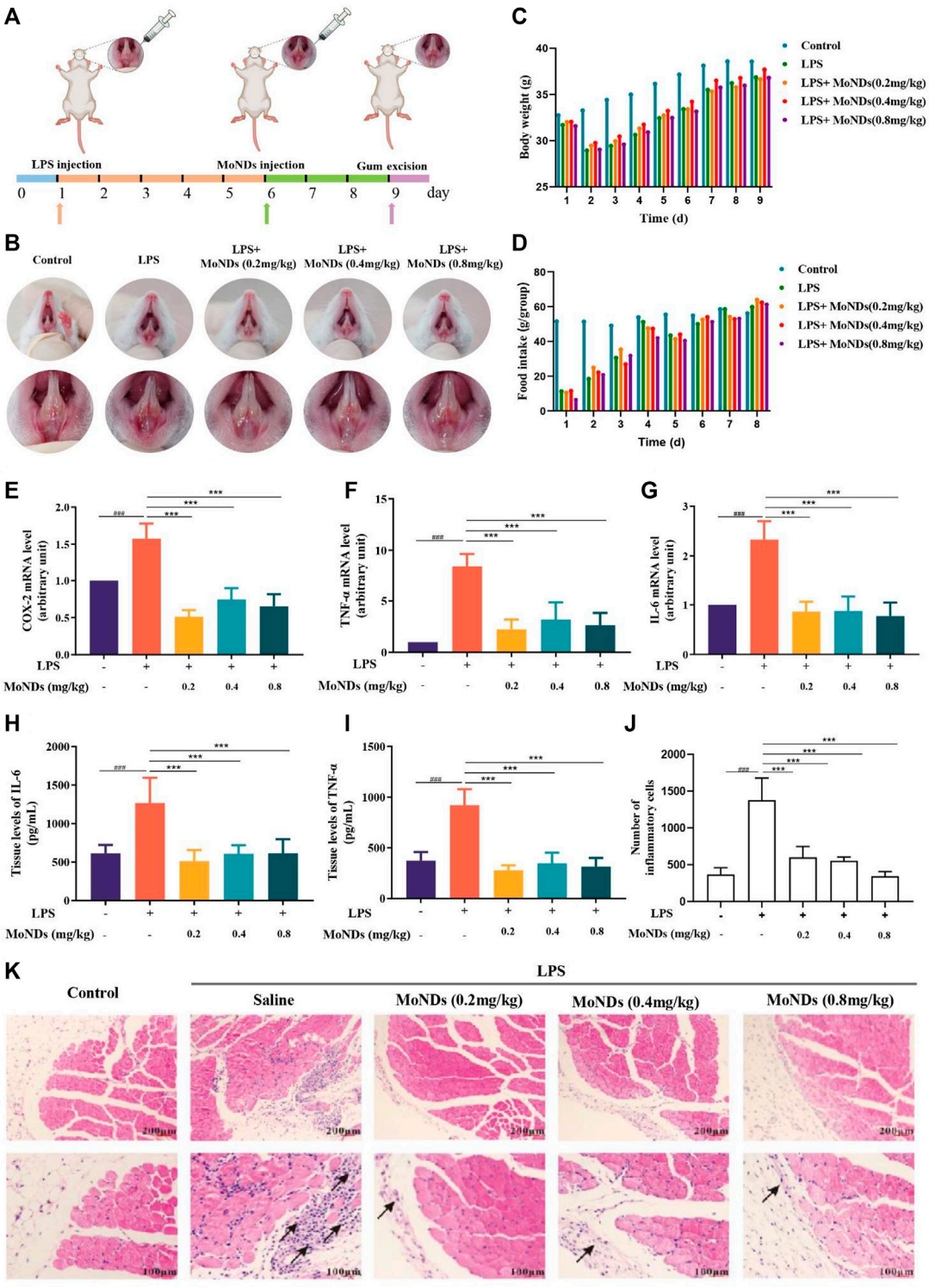

FIGURE 2
Therapeutic effects of MoNDs. **(A)** Schematic illustration of the establishment and treatment schedule of PD mice. **(B)** Photographic images of mice 3 days after various treatments. Changes in body weight **(C)** and food intake **(D)** of mice in different groups. **(E–G)** RT-qPCR analysis of the mRNA levels of the pro-inflammatory mediators (COX-2) **(E)**, TNF-α **(F)**, and IL-6 **(G)**). The IL-6 **(H)** and TNF-α **(I)** ELISA results of gingival tissue. **(J)** The quantitative statistical results of inflammatory cells in HE staining. **(K)** Representative images of HE staining after MoND treatment. Black arrows indicate the inflammatory infiltration. Scale bar: 100 μm and 200 μm.

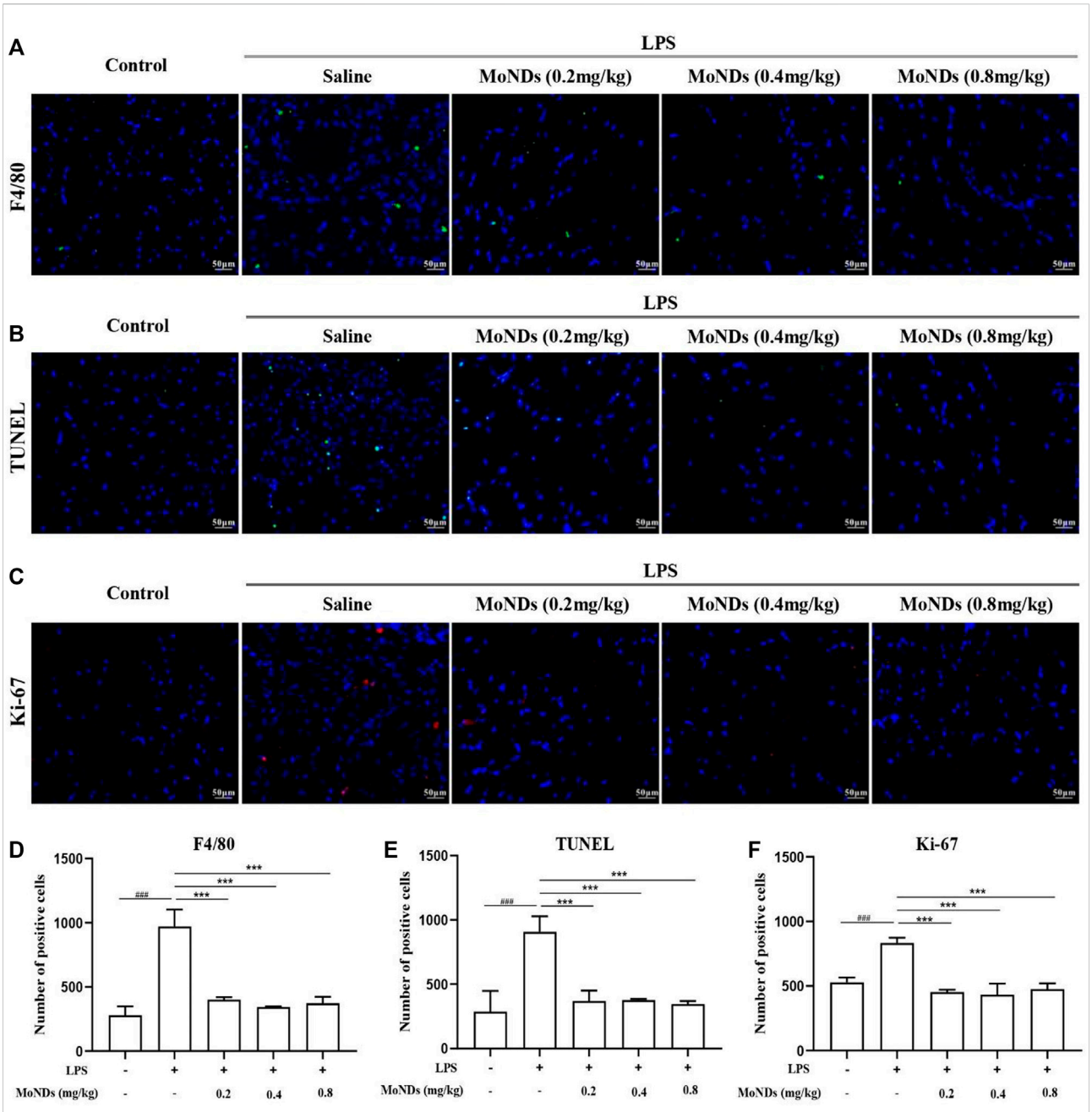

FIGURE 3
MoNDs alleviated inflammation and apoptosis in gingival tissue. Representative immunofluorescent images revealing F4/80-positive **(A)**, TUNEL-positive **(B)**, and Ki-67-positive **(C)** cells in gingival tissues. Quantitation of F4/80-positive cells **(D)**, TUNEL-positive cells **(E)**, and Ki-67-positive **(F)** cells in gingival tissues. MoNDs against H_2O_2-induced apoptosis and ROS production in primary gingival fibroblasts.

large amount of ROS with a high fluorescence signal under the stimulation of low concentration of H_2O_2. Importantly, MoND treatment effectively reduced the generation of intracellular ROS. Meanwhile, MoNDs can effectively reduce gingival fibroblast apoptosis by scavenging ROS. MoNDs reduced gingival fibroblast apoptosis through the caspase-3 pathway, as indicated by the expression levels of BAX, BCL-2, Cyt c, and caspase-3 (Figures 4D–H). The expression levels of BAX, Cyt c, and caspase-3 in the H_2O_2 group were much higher than those in the control group, and the anti-apoptotic factor BCL-2 was significantly decreased. Finally, MoND treatment significantly reduced gingival fibroblast apoptosis according to the Annexin V FITC results (Figures 4I,J).

10.3389/fbioe.2022.1042010

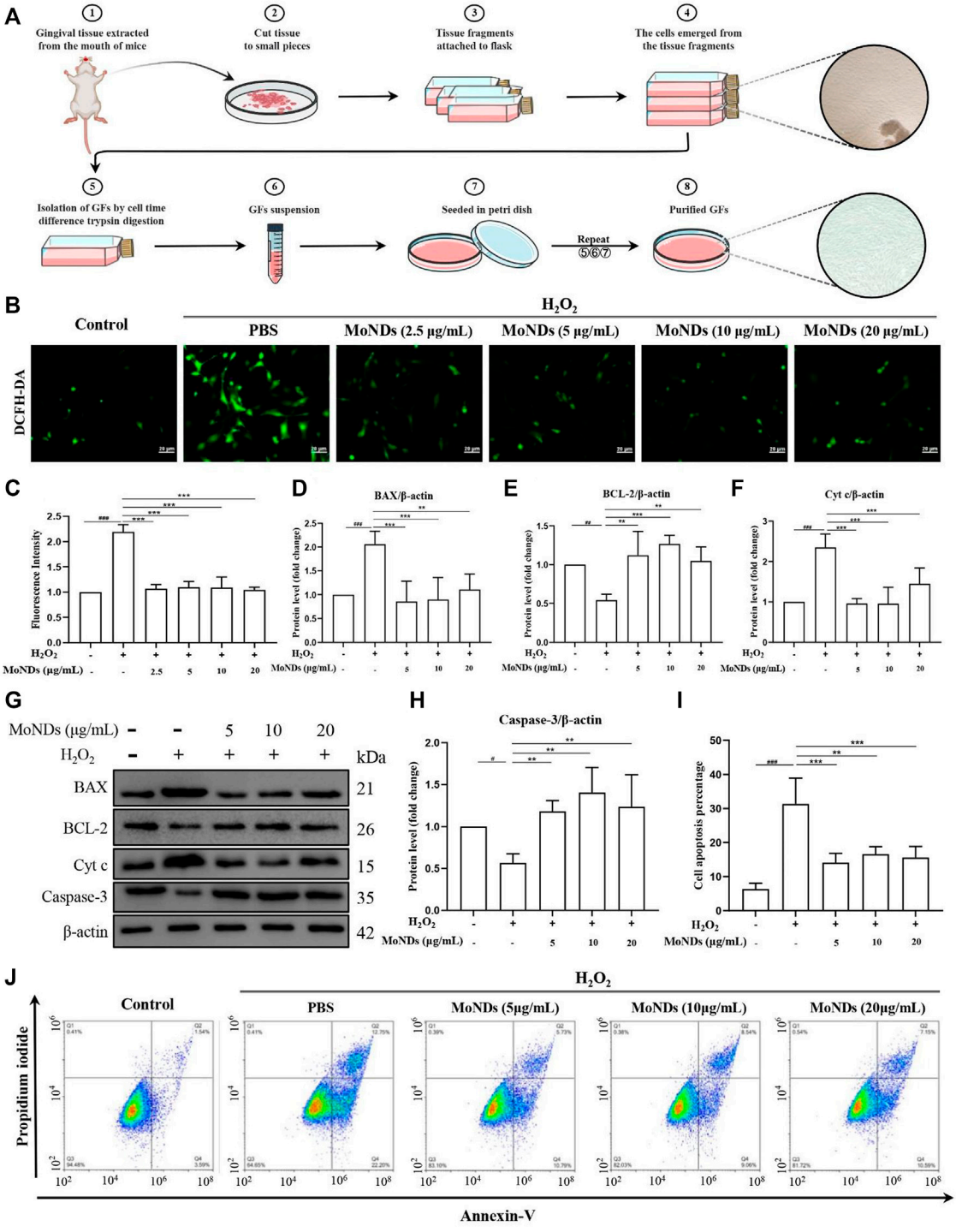

FIGURE 4
MoNDs alleviated oxidative stress in primary gingival fibroblasts. **(A)** Schematic illustration of the gingival fibroblast extraction process. **(B)** Measurement of ROS levels in gingiva fibroblasts from each group using a DCFH-DA probe (green). Scale bar: 20 μm. **(C)** Quantification of the fluorescence signal intensity of ROS. **(D–H)** Western blot analysis of apoptosis-related protein (BAX, BCL-2, Cyt c, and caspase-3) expression in primary gingival fibroblasts. All data are presented as the mean ± S.D. ($n = 3$). The quantitative statistical results of apoptotic cell ratios by Annexin V-FITC/PI flow cytometry **(I)** and the representative image **(J)**.

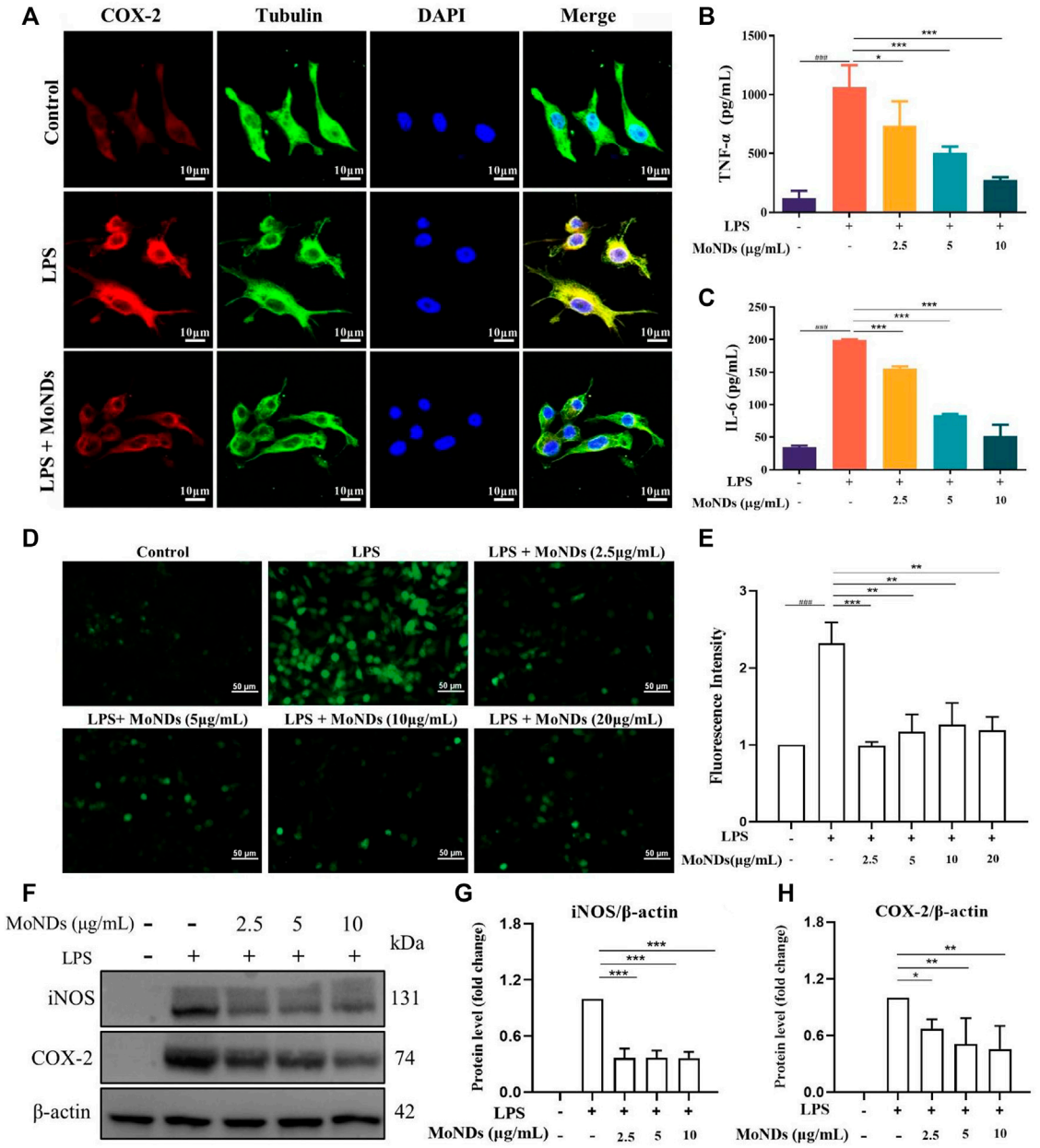

FIGURE 5
MoNDs alleviated inflammation and oxidative stress in macrophages. **(A)** Immunofluorescence staining of tubulin (green), COX-2 (red), DAPI (blue), and their merge images in RAW264.7 cells from each group. Scale bar: 10 μm. The TNF-α **(B)** and IL-6 **(C)** ELISA results of macrophages from each group. **(D)** Measurement of ROS levels in RAW264.7 cells from each group using a DCFH-DA probe (green). Scale bar: 50 μm. **(E)** Quantification of the fluorescence signal intensity of ROS. **(F–H)** Western blot analysis of iNOS and COX-2 expression in macrophages. All data are presented as the mean ± S.D. (n = 3).

2.2.1 MoNDs against LPS-induced inflammation and ROS production in macrophages

To investigate the immunoregulatory mechanism of MoNDs, the LPS-triggered inflammatory microenvironment was successfully constructed. Immune cells continuously migrate, infiltrate, and reside within the local gingival tissue in response to bacterial pathogens in the early stage of PD. Different kinds of immune cells including macrophages will be recruited to eliminate exogenous pathogens and undergo phenotype transition during the inflammatory process (Sima and Glogauer, 2013; Ni et al., 2019). M1 phenotype macrophages can be activated by the

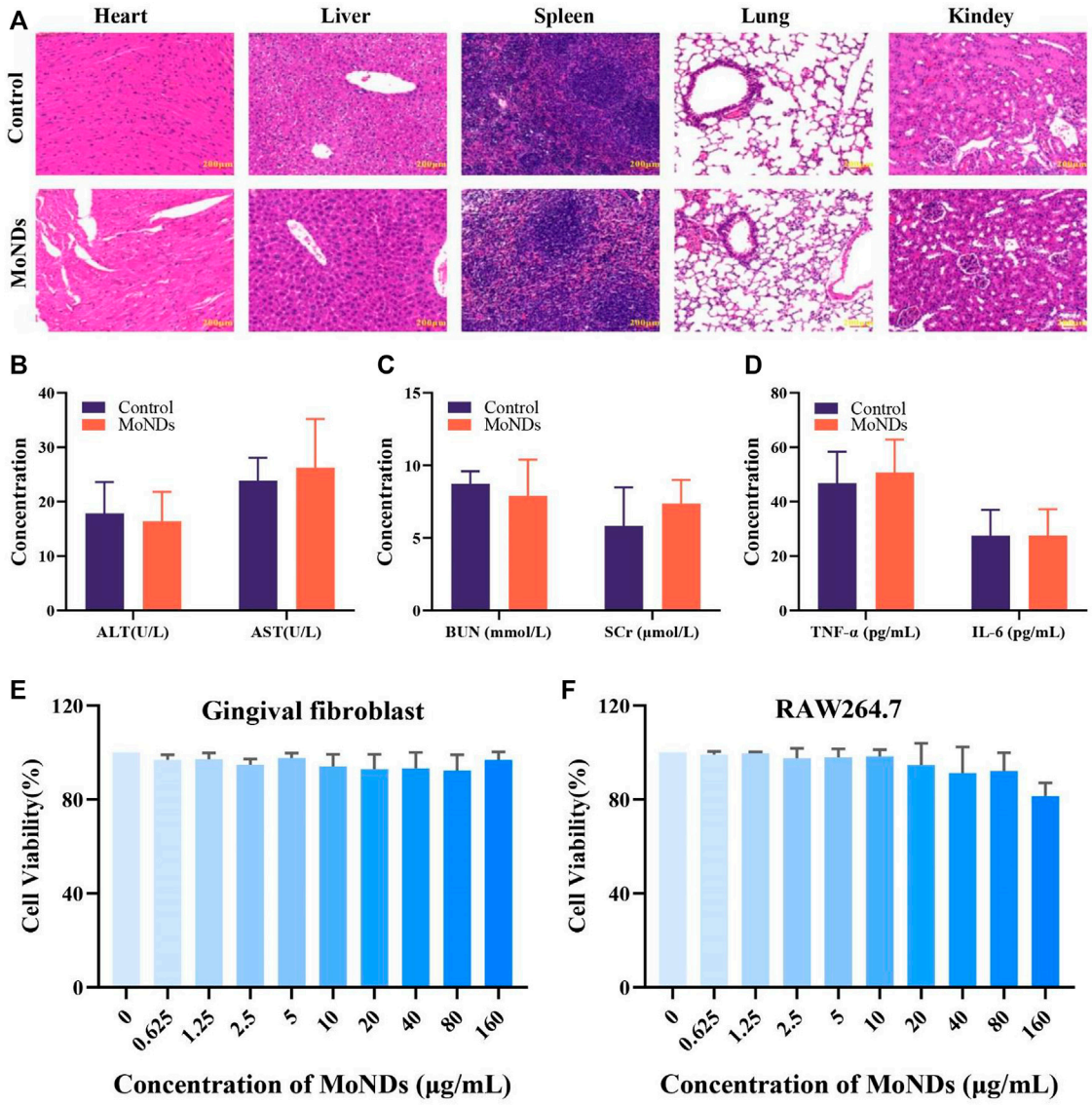

FIGURE 6
Biocompatibility of MoND therapy. HE staining of major organs on day 1 **(A)** after the administration. Mice were intravenously administered with injection of MoNDs (32 mg/kg) or PBS. **(B–D)** Serum levels of liver function indicators (ALT and AST), kidney function indicators (BUN and SCr), and inflammatory factors (TNF-α and IL-6). Viability of gingival fibroblasts **(E)** and macrophages **(F)** incubated with MoNDs.

stimulation of LPS, which can bind to toll-like receptor 4 (TLR4) on the surface of macrophages and activate NADPH oxidase (NOX2) to induce ROS overproduction. Surrounding normal gingival tissues will be damaged by the excessive inflammatory factors and ROS and further aggravate the pathological process of PD (Kanzaki et al., 2017). LPS can induce the secretion of many inflammatory factors and generate ROS through COX-2. Eventually, the vicious cycle between ROS and inflammation will further aggravate the periodontal tissue damage. As shown in Figures 5A,F,H, COX-2 stained with the red fluorescent dye was obvious in LPS-treated RAW264.7, and the protein expression of COX-2 was confirmed by the WB results. Increased secretion of TNF-α and IL-6 was also detected (Figures 5B,C). MoNDs obviously decreased the expression of COX-2 and reduced TNF-α and IL-6. Meanwhile, MoNDs effectively eliminated ROS (Figures 5D, E). Subsequently, we further investigated the effects of MoNDs on macrophage polarization. Inducible nitric oxide synthase (iNOS), a marker for the "M1" phenotype of macrophages, was greatly decreased by MoNDs (Figures 5F,G). Taken together, MoNDs can alleviate the inflammatory reaction of macrophages.

2.2.2 Biocompatibility of MoND therapy

Prior to the use of MoNDs as ROS scavengers in PD both *in vitro* and *in vivo*, the biocompatibility of nanomaterials was also investigated. HE staining and hematological markers can quantify the acute and chronic toxicity of MoNDs. First, MoNDs did not do any obvious damage to the heart, liver, spleen, lung, and kidney after 24 h (Figure 6A) and 1 month of treatment with MoNDs (Supplementary Figure S3). Moreover, MoNDs did not affect the serum levels of alanine aminotransferase (ALT), aspartate aminotransferase (AST), blood urea nitrogen (BUN), and serum creatinine (SCr), and these values were within the normal range (Figures 6B,C). In addition, MoNDs did not cause a serious inflammatory response in mice at 24 h post-injection, as indicated by the serum TNF-α and IL-6 levels within normal limits (Figure 6D).

Meanwhile, we also detected the effects of MoNDs on the viability of gingival fibroblasts and macrophages. After gingival fibroblasts and macrophages were treated with different concentrations of MoNDs for 24 h (Figures 6E,F), MoNDs were almost non-toxic to gingival fibroblasts, and 160 μg/ml had a slight anti-proliferation effect on macrophages. Overall, the safety of MoNDs was validated both *in vivo* and *in vitro*.

3 Discussion

In this study, we design and construct a MoND-based antioxidant defense platform to effectively scavenge ROS generated during PD. MoNDs with the ultra-small size can quench a variety of ROS (H_2O_2, $O_2^{\cdot-}$, and OH) and reduce their detrimental effects. *In vitro* findings confirmed that MoNDs can protect gingival fibroblasts from oxidative stress and alleviate ROS-induced apoptosis obviously. Moreover, MoNDs can also suppress the inflammatory state by scavenging ROS and inhibiting the M1 phenotype polarization of macrophages, presenting a significant role in inflammation control and tissue repair. Importantly, MoNDs showed good therapeutic effects on LPS-induced PD in the mouse, where only a very low dose significantly ameliorated gingival tissue damage and reduced local periodontal inflammation. In addition, *in vivo* and *in vitro* toxicity studies showed that MoNDs had high biocompatibility and low systemic toxicity, which will benefit the translation to the clinic. Taken together, our studies investigated the antioxidant and anti-inflammatory effects of MoNDs on PD and related mechanisms, which have a broad biomedical application value for the development of safe and effective anti-inflammatory and antioxidant defense platforms.

In this study, we only examined the ability of MoNDs to scavenge ROS. However, reactive nitrogen species (RNS) also play key roles in the regulation of the physiological and pathological processes within the damaged gingival tissue. With that in mind, we should further optimize and enhance the antioxidant activity of MoNDs so that it can scavenge multiple reactive oxygen and nitrogen species. With the continuous optimization of materials, this novel and safe antioxidant nanomedicine may be transformed into an effective therapy for the clinical treatment and solve the problems of recurrent episodes and high costs of PD. We believed that more breakthroughs in the treatment of PD will be made after full use of the advantages of nanomaterials and prominent ROS-scavenging ability.

4 Materials and methods

4.1 Materials

A CCK-8 assay kit was purchased from Dojindo Molecular Technologies (Kumamoto, Japan). AST, ALT, BUN, and SCr test kits were supported by the Nanjing Jiancheng Bioengineering Institute (Nanjing, China). TNF-α and IL-6 ELISA kits were purchased from Elabscience Biotechnology (Houston, Texas, United States). A TUNEL assay kit (C10617) was purchased from Thermo Fisher Scientific (Carlsbad, CA, United States). The ROS assay kit and Annexin V-FITC Apoptosis Detection Kit were purchased from Beyotime Biotechnology (Shanghai, China). COX-2 antibody (CST, 12282S) and F4/80 antibody (70076S) were purchased from Cell Signaling Technology (Danvers, MA, United States). BAX (ab32503) and iNOS (ab178945) were obtained from Abcam (Chicago, IL, United States). Bcl-2 antibody (BF9103) and beta-actin (AF7018) were obtained from Affinity Bioscience (Jiangsu, China). The Cyt c antibody (d10933-1-AP) was purchased from Proteintech (Rosemont, IL, United States). Goat anti-Rabbit IgG (H + L) Highly Cross-Adsorbed secondary antibody Alexa Fluor 488 (A11034) and Goat anti-Rabbit IgG (H + L) Highly Cross-Adsorbed secondary antibody Alexa Fluor 555 (A21428) were obtained from Thermo Fisher Scientific (Carlsbad, CA, United States).

4.2 Preparation of MoNDs

We added tannic acid (1.2 g) and phosphomolybdic acid (0.72 g) into ultra-pure water for full mixing and then added anhydrous sodium phosphate (3.75 g) to the mixed material to form an alkaline environment. Phosphomolybdic acid was reduced to a dark green solution after 12 h of reaction at room temperature (RT), and unreacted impurities were removed by dialysis and freeze-dried to obtain MoNDs.

4.3 O_2^- scavenging activity assay

The nitro-blue tetrazolium (NBT) method was used for detecting the scavenging efficiency of MoNDs to O_2^-. Different concentrations of **MoNDs** (0, 0.625, 1.25, 2.5, 5, and 10 μg/ml), methionine (20 μM), riboflavin (0.01 M), NBT

(0.01 M), PBS (0.01M, pH7.4), and ultra-pure water were added to the cuvette and mixed, respectively. Then, the cuvette was placed under UV light for 5 min, and the absorbance of blue methylhydrazone was measured at a wavelength of 560 nm. The O_2^- scavenging efficiency was calculated by the intensity of MoND-inhibited NBT photochemical reduction.

4.4 Free radical scavenging activity assay

The OH scavenging ability of MoNDs was detected by fluorescence spectrophotometry. We fabricated a reaction system by mixing terephthalic acid (0.1 mM), ferrous sulfate (0.05 mM), H_2O_2 (1 mM), and PBS (0.01 M, PH7.4) and then added different concentrations of MoNDs (0, 25, 50, 100, 200, 400, and 800 ng/ml) to the system. After resting for 6 min, the solution was transferred to a cuvette, and the corresponding fluorescence intensity was scanned at a wavelength of 320 nm.

The H_2O_2 scavenging capacity of MoNDs was detected by UV/Vis spectrophotometry. MoNDs were mixed (0.6 mg/ml) with different concentrations of H_2O_2 (1.25, 2.5, 5, and 10 mM), and the system was incubated in dark for 12 h. Finally, the ultraviolet absorption at 425 nm was detected to determine the clearance rate of H_2O_2.

4.4.1 X-ray photoelectron spectroscopy measurement

XPS was used to analyze the elemental/chemical state of MoNDs.

4.4.2 LPS-induced PD model and the experimental design euthanization of the mice

Kunming mice (male, 6–8 weeks old, 20–25 g) were purchased from Hunan STA Laboratory Animal CO., LTD. (Changsha, China). For the LPS-induced PD model, LPS (0.8 mg/kg) was administered *via* a subgingival injection every day. After administering LPS injection for 5 days, mice were used as PD models for subsequent study (Bao et al., 2018). Starting on the sixth day, different treatments were performed on LPS-induced PD mice: group 1 included healthy mice treated with 1x PBS; group 2 included PD mice treated with 1x PBS; group 3, 4, and 5 included PD mice treated with MoNDs (0.2, 0.4, and 0.8 mg/kg) ($n = 6$ in each group). PBS and MoNDs were injected *in situ* once a day for 3 days. The body weight of each mouse and the food intake of each group were weighed at a fixed time every day. At the end of the experiment, mice were anaesthetized by inhalation of 2% isoflurane gas. Mice were euthanized by carbon dioxide overdose followed by cervical dislocation.

4.4.3 *In vivo* toxicity assessment

Kunming mice, after the subgingival injection of MoNDs (6 mg/kg), were defined as the MoND group, and mice with PBS were denoted as the control group. On days 1 and 30 of the treatment, the heart, liver, spleen, lung, kidney, and blood were collected. Main organs were stained with HE. Blood was collected for AST, ALT, SCr, BUN, TNF-α and IL-6 assays.

4.4.4 Gingival fibroblast extraction

Mouse gingival fibroblasts were obtained from the male Kunming mouse (6–8 weeks old) gum tissue. The gingival tissue was cut into pieces and cultured in Dulbecco's modified Eagle's medium with 10% FBS and 100 IU/ml penicillin G and 100 mg/ml streptomycin at 37°C with 5% CO_2. Cells between passages 3 and 6 were used. The vimentin antibody was used to detect the purity of mouse gingival fibroblasts.

4.4.5 Cell culture

RAW264.7 macrophage cells were purchased from the National Collection of Authenticated Cell Cultures of China. RAW264.7 macrophage cells were cultured in Dulbecco's modified Eagle's medium with 10% newborn calf serum and maintained at 37°C in 5% CO_2.

4.4.6 Measurement of cell viability

A CCK8 assay was used to measure the proliferation of gingival fibroblast and macrophage cells. After being cultured overnight in a 96-well plate (7,500 cells/well, 100 μl of medium/well), the cells were treated with PBS or MoNDs with different concentrations for 24 h. Then, the CCK-8 reagent was added and incubated at 37°C for 4 h. Finally, the absorbance of each well was measured at 450 nm using a microplate reader (BioTek, United States).

4.4.7 Free radical scavenging activity assay on cells

The gingival fibroblast and macrophage cells were seeded into 24-well plates at the 3 × 10 (Slots, 2017)/well and incubated for 24 h. For gingival fibroblasts, MoNDs were dispersed in culture media at different concentrations (2.5, 5, 10, and 20 μg/ml, respectively), followed by H_2O_2 (250 μmol/L). After 4 h incubation under 5% CO_2 at 37°C, intracellular ROS levels were detected by using the DCFH-DA ROS probe. The cells were stained with 10 μM DCFH-DA at 37°C for 20 min, gently washed three times, and photographed by using a fluorescence microscope. For macrophage cells, MoNDs were dispersed in culture media at different concentrations (1.25, 2.5, 5, and 10 μg/ml, respectively), followed by LPS (1 μg/ml). After 24 h incubation under 5% CO_2 at 37°C, the DCFH-DA ROS probe was used to detect intracellular ROS levels.

4.4.8 RNA extraction and real-time PCR

Total RNA was extracted by using TRIzol reagent. RNA quantity and integrity were assessed on a NanoDrop 2000 instrument (Thermo Fisher Scientific, United States). The RNA was reverse transcribed into cDNA using an RT reagent kit from TaKaRa (Japan). qPCR was performed in a

Gene	Primer sequence
β-actin	Forward: ACATCCGTAAAGACCTCTATGCC
	Reverse: TACTCCTGCTTGCTGATCCAC
COX-2	Forward: AATACTGGAAGCCCGAGCACCT
	Reverse: ACACCCCTTCACATTATTGCAGA
IL-6	Forward: TCCTACCCCAATTTCCAATGCT
	Reverse: AACGCACTAGGTTTGCCGAG
TNF-α	Forward: AGCACAGAAAGCATGATCCG
	Reverse: CACCCCGAAGTTCAGTAGACA

total reaction volume of 20 μl containing 10 μl of SYBR Premix Ex Taq, 6.8 μl of ddH_2O, 0.4 μl of each primer (10 μM), 0.4 μl of ROX reference DyeII (50x), and 2 μl of cDNA template. The reaction was performed at 95°C for 30 s, followed by 40 cycles of 5 s at 95°C and 34 s at 65°C, 95°C for 15 s, 1 min at 60°C, and 15 s at 95°C. The relative changes in gene expression were estimated and normalized to GAPDH by using the $2^{-\Delta\Delta CT}$ method.

4.4.9 Immunofluorescence staining

Immunofluorescence staining was used to detect COX-2 and tubulin in RAW264.7 cells. The anti-COX-2 antibody (CST, dilution 1:200) was incubated overnight at 4°C and exposed to Alexa Fluor-555-conjugated goat-anti-rabbit (Invitrogen, dilution 1:500) antibody for 1 h at RT. After that, the anti-tubulin antibody (Abcam, dilution 1:200) was also incubated overnight at 4°C and exposed to Alexa Fluor-488-conjugated goat-anti-rabbit (Invitrogen, dilution 1:500) antibody. In addition, immunofluorescence staining was also used to detect Ki-67 and F4/80 in the gum tissue. The anti-Ki-67 antibody (Invitrogen, dilution 1:100) and the anti-F4/80 antibody (Abcam, dilution 1:50) were used as primary antibodies. After the removal of first antibodies, they were exposed to goat anti-mouse IgG H&L (Alexa Fluor® 594, Abcam, United States, dilution 1:500) and Alexa Fluor-488-conjugated goat-anti-rabbit (Invitrogen, dilution 1:500). Nuclei were counterstained with DAPI solution. Images were analyzed using a fluorescence confocal microscope.

4.5 Apoptosis analysis

The gingival fibroblast was collected for Annexin V FITC. A measure of 5 μl of Annexin V FITC and propidium iodide were mixed with 100 μl of single cell suspension and incubated for 15 min at RT in the dark. Then, the cells were analyzed using a NovoCyte 3130 flow cytometer after the 1× binding buffer was added. In addition, gum tissue apoptosis was detected by TUNEL staining, according to the instructions.

4.5.1 Western blotting

Mouse gingival fibroblasts and macrophages were lysed for 30 min with RIPA buffer (Beyotime, China) supplemented with protease and phosphatase inhibitors (Beyotime, China) on ice. The lysate was centrifuged at 12,000 rpm for 15 min at 4°C, and the protein concentrations of the supernatant were analyzed with a BCA kit (Beyotime, China). Each sample (20 μg of protein) was separated by SDS–PAGE gels and transferred to PVDF membranes. The membranes were immersed in 5% milk in the TBST buffer for 1 h at room temperature, followed by incubation with primary antibodies against *ß*-actin, BAX, BCL-2, caspase-3, cytochrome c, COX-2, iNOS, and vimentin overnight at 4°C. Then, the membranes were washed three times with TBST, followed by incubation with secondary antibodies for 1 h at room temperature. The bands were visualized using a gel documentation system (Bio-Rad, United States) and quantified by ImageJ software.

4.5.2 HE staining

Gingival, heart, liver, lung, spleen, and kidney specimens were fixed with formalin for 24 h, dehydrated by gradient ethanol, and vitrified with xylene. The specimens were embedded in paraffin and sliced into 5-μm sections. After being baked at 65°C for 1 h, the sections were routinely dewaxed and hydrated. Staining was performed as follows: hematoxylin staining for 5 min, incubation in hydrochloric acid alcohol solution for 2–3 s, incubation in blue-return solution for 3 s, eosin staining for 1–3 min, and rinsing with water. After being dehydrated, the sections were sealed with neutral resin. Finally, the sections were observed and photographed under a microscope.

4.5.3 Statistical analysis

The data were presented as means ± SD. Statistical analyses were performed with SPSS 22.0 software. One-way analyses of variance (ANOVA) were performed to detect the significant effects of the variables. Differences were accepted as significant at $p < 0.05$.

Data availability statement

The original contributions presented in the study are included in the article/Supplementary Material; further inquiries can be directed to the corresponding authors.

Ethics statement

All experimental procedures were approved by the Institutional Animal Care and Use Committee (IACUC), Xiangya Hospital, Central South University, China.

Author contributions

QH and KA contributed to the conception and design of the study. LC, TZ and YY performed the experiments and wrote the manuscript.

ML, XZ, and HZ revised the manuscript. QC, JZ, and SW contributed significantly to data analyses and picture arrangement. All authors reviewed and approved the final version of the manuscript.

Funding

This work was supported by the National Natural Science Foundation of China (Nos. 21974134 and 81974508), the Hunan Provincial Natural Science Foundation of China (No. 2021JJ31066), the Hunan Science Fund for Distinguished Young Scholar of China (No. 2021JJ10067), the InnovationDriven Project of Central South University (No. 202045005), and the Key Research Project of Ningxia Hui Autonomous Region in 2021 of China (Major Project) (No. 2021BEG01001).

Conflict of interest

The authors declare that the research was conducted in the absence of any commercial or financial relationships that could be construed as a potential conflict of interest.

Publisher's note

Supplementary material

The Supplementary Material for this article can be found online at: https://www.frontiersin.org/articles/10.3389/fbioe.2022.1042010/full#supplementary-material

SUPPLEMENTARY FIGURE 1
XPS O 1s spectrum of MoNDs.

SUPPLEMENTARY FIGURE 2
Western bolt analysis of Vimentin proteins in gingival fibroblast.

SUPPLEMENTARY FIGURE 3
HE staining of major organs on day 30 after the administration of MoNDs (32mg/kg) or normal saline.

References

Bao, X., Zhao, J., Sun, J., Hu, M., and Yang, X. (2018). Polydopamine nanoparticles as efficient scavengers for reactive oxygen species in periodontal disease. *ACS Nano* 12, 8882–8892. doi:10.1021/acsnano.8b04022

Buckley, C. D. (2011). Why does chronic inflammation persist: An unexpected role for fibroblasts. *Immunol. Lett.* 138, 12–14. doi:10.1016/j.imlet.2011.02.010

Cekici, A., Kantarci, A., Hasturk, H., and Van Dyke, T. E. (2014). Inflammatory and immune pathways in the pathogenesis of periodontal disease. *Periodontol.* 64, 57–80. doi:10.1111/prd.12002

Chen, L., Huang, Q., Zhao, T., Sui, L., Wang, S., Xiao, Z., et al. (2021). Nanotherapies for sepsis by regulating inflammatory signals and reactive oxygen and nitrogen species: New insight for treating COVID-19. *Redox Biol.* 45, 102046. doi:10.1016/j.redox.2021.102046

Cheng, R., Choudhury, D., Liu, C., Billet, S., Hu, T., and Bhowmick, N. (2015). Gingival fibroblasts resist apoptosis in response to oxidative stress in a model of periodontal diseases. *Cell Death Discov.* 1, 15046. doi:10.1038/cddiscovery.2015.46

Cherevan, A. S., Nandan, S. P., Roger, I., Liu, R., Streb, C., and Eder, D. (2020). Polyoxometalates on functional substrates: Concepts, synergies, and future perspectives. *Adv. Sci. (Weinh).* 7, 1903511. doi:10.1002/advs.201903511

Chiquet, M., Katsaros, C., and Kletsas, D. (2015). Multiple functions of gingival and mucoperiosteal fibroblasts in oral wound healing and repair. *Periodontol.* 68, 21–40. doi:10.1111/prd.12076

Davidson, S., Coles, M., Thomas, T., Kollias, G., Ludewig, B., Turley, S., et al. (2021). Fibroblasts as immune regulators in infection, inflammation and cancer. *Nat. Rev. Immunol.* 21, 704–717. doi:10.1038/s41577-021-00540-z

Fine, N., Chadwick, J., Sun, C., Parbhakar, K., Khoury, N., Barbour, A., et al. (2021). Periodontal inflammation primes the systemic innate immune response. *J. Dent. Res.* 100, 318–325. doi:10.1177/0022034520963710

Garaicoa-Pazmino, C., Fretwurst, T., Squarize, C. H., Berglundh, T., Giannobile, W. V., Larsson, L., et al. (2019). Characterization of macrophage polarization in periodontal disease. *J. Clin. Periodontol.* 46, 830–839. doi:10.1111/jcpe.13156

Golub, L. M., and Lee, H. M. (2020). Periodontal therapeutics: Current host-modulation agents and future directions. *Periodontol. 2000* 82, 186–204. doi:10.1111/prd.12315

Goyal, G., Garg, T., Rath, G., and Goyal, A. K. (2014). Current nanotechnological strategies for an effective delivery of drugs in treatment of periodontal disease. *Crit. Rev. Ther. Drug Carr. Syst.* 31, 89–119. doi:10.1615/critrevtherdrugcarriersyst.2014008117

Hajishengallis, G., and Chavakis, T. (2021). Local and systemic mechanisms linking periodontal disease and inflammatory comorbidities. *Nat. Rev. Immunol.* 21, 426–440. doi:10.1038/s41577-020-00488-6

Hajishengallis, G. (2015). Periodontitis: From microbial immune subversion to systemic inflammation. *Nat. Rev. Immunol.* 15, 30–44. doi:10.1038/nri3785

Hirose, M., Ishihara, K., Saito, A., Nakagawa, T., Yamada, S., and Okuda, K. (2001). Expression of cytokines and inducible nitric oxide synthase in inflamed gingival tissue. *J. Periodontol.* 72, 590–597. doi:10.1902/jop.2001.72.5.590

Holze, C., Michaudel, C., Mackowiak, C., Haas, D. A., Benda, C., Hubel, P., et al. (2018). Oxeiptosis, a ROS-induced caspase-independent apoptosis-like cell-death pathway. *Nat. Immunol.* 19, 130–140. doi:10.1038/s41590-017-0013-y

Hosokawa, Y., Hosokawa, I., Ozaki, K., Nakae, H., Murakami, K., Miyake, Y., et al. (2005). CXCL12 and CXCR4 expression by human gingival fibroblasts in periodontal disease. *Clin. Exp. Immunol.* 141, 467–474. doi:10.1111/j.1365-2249.2005.02852.x

Huang, Q., Yang, Y., Zhao, T., Chen, Q., Liu, M., Ji, S., et al. (2023). Passively-targeted mitochondrial tungsten-based nanodots for efficient acute kidney injury treatment. *Bioact. Mater.* 21, 381–393. doi:10.1016/j.bioactmat.2022.08.022

Kanzaki, H., Wada, S., Narimiya, T., Yamaguchi, Y., Katsumata, Y., Itohiya, K., et al. (2017). Pathways that regulate ROS scavenging enzymes, and their role in defense against tissue destruction in periodontitis. *Front. Physiol.* 8, 351. doi:10.3389/fphys.2017.00351

Kinane, D. F., Stathopoulou, P. G., and Papapanou, P. N. (2017). Periodontal diseases. *Nat. Rev. Dis. Prim.* 3, 17038. doi:10.1038/nrdp.2017.38

Krishna, R., and De Stefano, J. A. (2016). Ultrasonic vs. hand instrumentation in periodontal therapy: Clinical outcomes. *Periodontol. 2000* 71, 113–127. doi:10.1111/prd.12119

Liu, M., Huang, Q., Zhu, Y., Chen, L., Li, Y., Gong, Z., et al. (2022). Harnessing reactive oxygen/nitrogen species and inflammation: Nanodrugs for liver injury. *Mat. Today Bio* 13, 100215. doi:10.1016/j.mtbio.2022.100215

Liu, Y., Ai, K., Liu, J., Deng, M., He, Y., and Lu, L. (2013). Dopamine-melanin colloidal nanospheres: An efficient near-infrared photothermal therapeutic agent for *in vivo* cancer therapy. *Adv. Mat.* 25, 1353–1359. doi:10.1002/adma.201204683

Liu, Y. C., Lerner, U. H., and Teng, Y. T. (2010). Cytokine responses against periodontal infection: Protective and destructive roles. *Periodontol. 2000* 52, 163–206. doi:10.1111/j.1600-0757.2009.00321.x

Loesche, W. J., and Grossman, N. S. (2001). Periodontal disease as a specific, albeit chronic, infection: Diagnosis and treatment. *Clin. Microbiol. Rev.* 14, 727–752. doi:10.1128/CMR.14.4.727-752.2001

Lu, F., Wang, M., Li, N., and Tang, B. (2021). Polyoxometalate-based nanomaterials toward efficient cancer diagnosis and therapy. *Chem. Eur. J.* 27, 6422–6434. doi:10.1002/chem.202004500

Mealey, B. L. (2006). Periodontal disease and diabetes. *J Am Dent Assoc.* 137, 26S–31S. doi:10.14219/jada.archive.2006.0404

Ni, C., Zhou, J., Kong, N., Bian, T., Zhang, Y., Huang, X., et al. (2019). Gold nanoparticles modulate the crosstalk between macrophages and periodontal ligament cells for periodontitis treatment. *Biomaterials* 206, 115–132. doi:10.1016/j.biomaterials.2019.03.039

Ni, D., Jiang, D., Kutyreff, C. J., Lai, J., Yan, Y., Barnhart, T. E., et al. (2018). Molybdenum-based nanoclusters act as antioxidants and ameliorate acute kidney injury in mice. *Nat. Commun.* 9, 5421. doi:10.1038/s41467-018-07890-8

Ni, D., Jiang, D., Valdovinos, H. F., Ehlerding, E. B., Yu, B., Barnhart, T. E., et al. (2017). Bioresponsive polyoxometalate cluster for redox-activated photoacoustic imaging-guided photothermal cancer therapy. *Nano Lett.* 17, 3282–3289. doi:10.1021/acs.nanolett.7b00995

Pihlstrom, B. L., Michalowicz, B. S., and Johnson, N. W. (2005). Periodontal diseases. *Lancet* 366, 1809–1820. doi:10.1016/S0140-6736(05)67728-8

Sczepanik, F. S. C., Grossi, M. L., Casati, M., Goldberg, M., Glogauer, M., Fine, N., et al. (2020). Periodontitis is an inflammatory disease of oxidative stress: We should treat it that way. *Periodontol* 84, 45–68. doi:10.1111/prd.12342

Sima, C., and Glogauer, M. (2013). Macrophage subsets and osteoimmunology: Tuning of the immunological recognition and effector systems that maintain alveolar bone. *Periodontol. 2000* 63, 80–101. doi:10.1111/prd.12032

Slots, J. (2017). Periodontitis: Facts, fallacies and the future. *Periodontol. 2000* 75, 7–23. doi:10.1111/prd.12221

Sui, L., Wang, J., Xiao, Z., Yang, Y., Yang, Z., and Ai, K. (2020). ROS-scavenging nanomaterials to treat periodontitis. *Front. Chem.* 8, 595530. doi:10.3389/fchem.2020.595530

Wang, J., Sui, L., Huang, J., Miao, L., Nie, Y., Wang, K., et al. (2021). MoS2-based nanocomposites for cancer diagnosis and therapy. *Bioact. Mat.* 6, 4209–4242. doi:10.1016/j.bioactmat.2021.04.021

Wang, Y., Li, C., Wan, Y., Qi, M., Chen, Q., Sun, Y., et al. (2021). Quercetin-loaded ceria nanocomposite potentiate dual-directional immunoregulation via macrophage polarization against periodontal inflammation. *Small* 17, e2101505. doi:10.1002/smll.202101505

Wei, K., Nguyen, H. N., and Brenner, M. B. (2021). Fibroblast pathology in inflammatory diseases. *J. Clin. Invest.* 131, e149538. doi:10.1172/JCI149538

Xiao, Z., Huang, Q., Yang, Y., Liu, M., Chen, Q., Huang, J., et al. (2022). Emerging early diagnostic methods for acute kidney injury. *Theranostics* 12, 2963–2986. doi:10.7150/thno.71064

Yang, Y., Huang, Q., Xiao, Z., Liu, M., Zhu, Y., Chen, Q., et al. (2022). Nanomaterial-based biosensor developing as a route toward *in vitro* diagnosis of early ovarian cancer. *Mat. Today Bio* 13, 100218. doi:10.1016/j.mtbio.2022.100218

Yang, Y., Zhao, T., Chen, Q., Li, Y., Xiao, Z., Xiang, Y., et al. (2022). Nanomedicine strategies for heating "cold" ovarian cancer (OC): Next evolution in immunotherapy of OC. *Adv. Sci.*, e2202797. doi:10.1002/advs.202202797

Zhang, L. J., Guerrero-Juarez, C. F., Hata, T., Bapat, S. P., Ramos, R., Plikus, M. V., et al. (2015). Dermal adipocytes protect against invasive *Staphylococcus aureus* skin infection. *Science* 347, 67–71. doi:10.1126/science.1260972

Zhao, T., Wu, W., Sui, L., Huang, Q., Nan, Y., Liu, J., et al. (2022). Reactive oxygen species-based nanomaterials for the treatment of myocardial ischemia reperfusion injuries. *Bioact. Mat.* 7, 47–72. doi:10.1016/j.bioactmat.2021.06.006

Zhao, W., Wang, J., Wang, H., Lu, S., Song, Y., Chen, H., et al. (2020). Combinatorial discovery of Mo-based polyoxometalate clusters for tumor photothermal therapy and normal cell protection. *Biomater. Sci.* 8, 6017–6024. doi:10.1039/d0bm01015d

Zhu, L., Xie, H., Liu, Q., Ma, F., and Wu, H. (2021). Klotho inhibits H_2 O_2 -induced oxidative stress and apoptosis in periodontal ligament stem cells by regulating UCP2 expression. *Clin. Exp. Pharmacol. Physiol.* 48, 1412–1420. doi:10.1111/1440-1681.13547

Zhu, Y., Zhao, T., Liu, M., Wang, S., Liu, S., Yang, Y., et al. (2022). Rheumatoid arthritis microenvironment insights into treatment effect of nanomaterials. *Nano Today* 42, 101358. doi:10.1016/j.nantod.2021.101358

frontiers | Frontiers in Bioengineering and Biotechnology

TYPE Original Research
PUBLISHED 17 November 2022
DOI 10.3389/fbioe.2022.1074083

OPEN ACCESS

EDITED BY
Hua Yue,
Institute of Process Engineering (CAS), China

REVIEWED BY
Bin Chen,
Nanjing University, China
Yan-Yan Song,
Northeastern University, China

*CORRESPONDENCE
Lan A,
hialan1983_2001@jlu.edu.cn

†These authors have contributed equally to this work

SPECIALTY SECTION
This article was submitted to Nanobiotechnology, a section of the journal Frontiers in Bioengineering and Biotechnology

RECEIVED 19 October 2022
ACCEPTED 07 November 2022
PUBLISHED 17 November 2022

CITATION
Sun Y, Xu W, Jiang C, Zhou T, Wang Q and A L (2022), Gold nanoparticle decoration potentiate the antibacterial enhancement of TiO_2 nanotubes *via* sonodynamic therapy against peri-implant infections.
Front. Bioeng. Biotechnol. 10:1074083.
doi: 10.3389/fbioe.2022.1074083

Gold nanoparticle decoration potentiate the antibacterial enhancement of TiO_2 nanotubes *via* sonodynamic therapy against peri-implant infections

Yue Sun[1,2†], Wenzhou Xu[3†], Cong Jiang[1], Tianyu Zhou[1], Qiqi Wang[3] and Lan A[1,2*]

[1]Department of Oral Implantology, School and Hospital of Stomatology, Jilin University, Changchun, China, [2]Jilin Provincial Key Laboratory of Sciences and Technology for Stomatology Nanoengineering, Changchun, China, [3]Department of Periodontology, School and Hospital of Stomatology, Jilin University, Changchun, China

Inflammatory damage from bacterial biofilms usually causes the failure of tooth implantation. A promising solution for this challenge is to use an implant surface with a long-term, in-depth and efficient antibacterial feature. In this study, we developed an ultrasound-enhanced antibacterial implant surface based on Au nanoparticle modified TiO_2 nanotubes (AuNPs-TNTs). As an artificial tooth surface, films based on AuNPs-TNTs showed excellent biocompatibility. Importantly, compared to bare titania surface, a larger amount of reactive oxygen radicals was generated on AuNPs-TNTs under an ultrasound treatment. For a proof-of-concept application, *Porphyromonas gingivalis (P. gingivalis)* was used as the model bacteria; the as-proposed AuNPs-TNTs exhibited significantly enhanced antibacterial activity under a simple ultrasound treatment. This antibacterial film offers a new way to design the surface of an artificial implant coating for resolving the bacterial infection induced failure of dental implants.

KEYWORDS

sonodynamic therapy, titania nanotube, antibacterial, dental implant, ROS

1 Introduction

Safe, effective, and convenient therapeutic treatments are goals for nanomedicine development. For oral implantology, a titanium (Ti) dental implant is the most commonly used teeth substitution in the dental implant surgery owing to excellent biocompatibility. Unfortunately, it has still some shortcomings. The weak antibacterial activity of the titanium implant leads to patients suffering from complications and severely affects the success rate of implant treatment. Peri-implantitis, an inflammatory disease caused by bacterial biofilm, is the most common postoperative complication that leads to the failure of dental implant (Li et al., 2019). A conventional implant surface does not exhibit antibacterial activity, in contrast it accumulates bacteria and in turn facilitates the

attachment loss and a rapid progress in peri-implantitis (Vargas-Reus et al., 2012). In spite of strict sterilizing procedures, bacterial contamination is difficult to avoid in an oral environment. As soon as the microbes arrive at the surface of implant, the extracellular viscous polysaccharide secreted by the aggregates of bacteria forms a biological film, which cause a high resistance to antibacterial agents and host defense. Ultimately, it leads to obstinate infections (Chung and Khanum, 2017; Skariyachan et al., 2018). To overcome the infection, endowing the surface of implants with a long-term and efficient antibacterial capability would be an effective measure, which can inhibit the bacterial colonization and succeeding formation of the biological film (Gao et al., 2014; Raphel et al., 2016; Zheng et al., 2020).

For decades, plenty of strategies have been used to enhance the antibacterial capability of titanium surfaces by modification with antibacterial agents such as antimicrobial peptides (Ma et al., 2012), metals ions (Zielińska-Jurek et al., 2015), polymers (Kubacka et al., 2007), and antibiotics (Kutuzova et al., 2021). In recent years, for minimal invasiveness and well-established clinical effect, reactive oxygen species (ROS)-associated antibacterial therapy has attracted much attention, such as photodynamic therapy (PDT) (Xu et al., 2019). PDT utilizes light of a specific wavelength to generate ROS *via* activating photosensitizers. ROS can cause cell membrane damage and subsequent death (Wang Z. et al., 2018) while stimulate the host immune system combat disease. Although PDT has been regarded as a hopeful substitutive strategy to traditional immunotherapy and chemotherapy, the low penetration (0.5–2.0 mm) of light radiation in biological tissue limits the application of PDT for deep tumors or infections in clinic (Wan et al., 2016). Therefore, sonodynamic therapy (SDT) has attracted much more attention, using therapeutic ultrasound instead of light to generate ROS, causing the apoptosis, necrosis, and autophagy of bacteria, together with mechanical death and necrosis caused by the implosion of cavitating bubbles (Zhu et al., 2021). On account of the low tissue attenuation and radiation-less nature, ultrasound can penetrate much thicker tissues without degradation of energy compared to light (Xu T. et al., 2020). Additionally, it passes through multi-layer of tissue without harming anything and stimulates the sensitizer only at its focus with a high spatial accuracy, whereas near-infrared light may excite all the sensitizers that appear during its propagation. Thus, all the advantages mentioned above confirm the safety of SDT when dealing with deep-seated diseases (Deepagan et al., 2016). Nevertheless, some challenges still limit the development and clinical application of SDT. For example, the quantum yield and biological safety should be the bran-new perspective to enhance the performance of the sonosensitizer, thus increasing the SDT efficiency.

Unlike organic sensitizers, an inorganic TiO_2 nanostructure, a stable SDT agent of tolerance to oxidative degradation, could resist more ultrasound exposure time (Wei et al., 2013; Deepagan et al., 2016). Moreover, TiO_2 nanostructures will not trigger the immune response as it is inert materials (El-Fray et al., 2009). When irradiated with energy from an external source, nano-TiO_2 could generate ROS, containing superoxide radical ($\bullet O_2^-$), hydroxyl radical ($\bullet OH$), and singlet oxygen ($^1O_2$) (Wang et al., 2011; Ma et al., 2012; Wang et al., 2013). Nevertheless, there is a problem: The performance of pure TiO_2 as a sensitizer is limited by the low yield of ROS, causing a fast electron-hole recombination (Jie et al., 2009). To improve ROS generation, noble metals, such as Ag and Au, have been considered to modify the TiO_2 nanostructures. Recently, Park et al. verified hydrophilized TiO_2 nanostructures could be a long-circulating SDT agent for treating both deep and superficial tumors (You et al., 2016). It has been well demonstrated that noble metals/TiO_2 heterostructures not only exhibit an increased absorption activity in the visible-light region *via* local surface plasmon resonance (LSPR), but also prevent electron-hole recombination by trapping the photoexcited electrons (Ola and Maroto-Valer, 2015; Qu et al., 2022). Although, Ag nanoparticle modified TiO_2 nanotubes (TNTs) display excellent antibacterial activity (Chen et al., 2017), the antibacterial performance would decrease with the solubilization of Ag in an aqueous environment. Owing to their excellent biocompatibility and chemical stability, Au nanoparticles (AuNPs) are extensively used in biosensors, photocatalysis, cancer therapeutics, and tumor imaging (Zhang S. et al., 2019; Xu J. et al., 2020; Zhao et al., 2022). Specially, AuNPs are ideal metal nanostructures because of tunable optical properties related to their geometrical structure (Wang et al., 2020a). In our previous study, the absorption of TNTs shifted from the UV region to the visible-light region by decorating with AuNPs (Zheng et al., 2020). Although Au/TiO_2 interfaces have exhibited good performance in antibacterial PDT, the tissue penetration depth is still limited, endowing failure in inhibition and killing activities against pathogenic biofilms. Till now, less attention has been paid to the utilization of AuNPs-TNTs as an antibacterial platform in SDT, especially for the treatment of peri-implantitis.

In this study, we established an efficient, strongly penetrating, and safe nano-therapy platform and systematically evaluated the effect of AuNP loading on the antibacterial properties of TNTs under ultrasonic irradiation. On one side, the Au in AuNPs- TNTs could increase the generation of ROS by preventing the fast recombination of triggered electron-hole. For another, the ultrasound increased the depth of treatment. In addition, the nanoplatform exhibited a high security. In the evaluation of antibacterial activity, the major pathogen in oral environment (*P. gingivalis*), which is responsible for the failure and infections of implant, were chosen as the model bacteria. The antibacterial ability of the AuNPs- TNTs synthetic materials was found to rely on the Au loading amount. Based on all the above-mentioned results, AuNPs- TNTs were found to be a biocompatible platform with excellent

ROS generating characteristics for an efficient antibacterial treatment. This study provides a new route to treat the inflammatory damage from bacterial biofilm on artificial dental implants.

2 Experimental and methods

2.1 Synthesis of TNTs arrays

The TNTs layer was fabricated using a two-electrode-setup anodic oxidation process following a previous study. In brief, Ti sheets were precleaned ultrasonically in acetone and ethanol for 20 min, rinsed three times with distilled water and dried in a N_2 stream. Then, the working electrode and flakes were prepared by adding 0.27 M of NH_4F in an electrolyte mixture of water/glycerol (50:50) and treated at 30 V for 4 h. A platinum foil was functioned as counter electrode. Eventually, the as-fabricated amorphous structured TNTs were crystallized into an anatase structure by annealing samples at 450°C in ambient air for 1 h (Wang G. et al., 2018).

2.2 Preparation of AuNPs-TNTs

All samples applied to AuNP decoration had anatase crystalline phases. For AuNPs-TNTs, all the samples were firstly immersed in the $HAuCl_4$ solution (10 mg/ml) with pH of 9–10 for 16 h followed by rinsing with DI water carefully. Then, the samples were beamed with UV light (500 W) using a medium-pressure Hg lamp (maximum emission center around 360 nm); 8 cm for 30 min was the fixed distance between the lamps and samples (Gao et al., 2012). The above procedures were repeated three times in order to embellish a higher amount of AuNPs. Four groups of antibacterial surfaces were prepared as follows: 1) bare TNTs group (denoted as "TNTs"), 2) a low mount of AuNP-loaded TNTs which was prepared by one cycle of Au coating procedure (denoted as L-AuNPs-TNTs), 3) a medium mount of AuNP-loaded TNTs, which was prepared by two cycles of Au coating procedure (denoted as M-AuNPs-TNTs), 4) a high mount of AuNP-loaded TNTs, which was prepared by three cycles of Au coating procedure (denoted as H-AuNPs-TNTs).

2.3 Sample characterization

With the aid of field-emission scanning electron microscopy (FE-SEM, S-4800; Hitachi, Japan), the sample morphology was characterized. The structure of the samples was identified by use of an X-ray diffractometer (XRD, Rigaku, Tokyo, Japan) with Cu Kα radiation. Utilizing X-ray photoelectron spectroscopy (XPS, ESCA Lab 250, Thermo Fisher Scientific, New York, United States), the elemental composition was determined. The absorption range was registered using a UV-vis spectrophotometer (Shimadzu Corporation, Tokyo, Japan).

2.4 ROS capture experiments

2,2′-Bis(anthracene-9,10-diylbis (methylene))-dimalonic acid (ABDA) was selected to be a specific probe to detect the generation of $^1O_2$. Typically, 5 μl of ABDA [10 μM in dimethyl sulfoxide (DMSO)] was put into AuNPs-TNTs solutions (200 μg/ml). Subsequently, the UV-vis absorbance range was registered using a Shimadzu UV-2550 spectrophotometer for the duration of ultrasound exposure (1.0 MHz, 1.5 W/cm^2). The peak of appearance for ABDA at 378 nm indicates the generation of ROS (Liu et al., 2019).

2.5 Bacteria culture

P. gingivalis (ATCC33277, Manassas, VA, United States) was applied to produce a single-species biofilm. The bacteria were authorized by the Institutional Review Board of Jilin University, School of Dentistry and anaerobically cultured at 37°C in tryptic soy broth (TSB) added menadione (1 mg/L), L-cysteine hydrochloride (0.5 g/L), hemin (5 mg/L), and yeast extract (5 g/L) with 80% N2, 10% CO_2 and10% H_2 (Park et al., 2016). The inoculum was altered to 108 colony-forming unit counts (CFU/ml) for biofilm formation according to the standard curve of OD_{600nm} vs CFU/mL. The sheets were diverted to the 24-well plate, and every single well was inoculated in an anaerobic environment at 37°C. At every 24 h, the medium was changed to a fresh medium. Culturing for 4-day in total was adequate for the formation of a mature *P. gingivalis* biofilm (Cai et al., 2014).

2.6 *In vitro* antibacterial effect

An STYO9-PI assay was performed for the sterilization of *P. gingivalis* on the biofilm. After dealing with each group, SYTO9 (0.25 μM, Molecular Probes, Eugene, OR, United States)/propidium iodide (PI, 0.25 μM, Molecular Probes, Eugene, OR, United States) was added to the biofilm for staining live/dead bacteria, respectively. The red-stained bacteria represent the lifeless bacteria, and the bacteria colored by green represent the live bacteria. The images were obtained by using a confocal laser scanning microscope (CLSM, C2si, Nikon, Japan) (Zeng et al., 2017).

For CFU enumerating, the 4-day biofilm was diverted into vials with 1 ml media, scraping, sonicating, and vortexing

(Thermo Scientific Fisher) to obtain the biofilms. In the wake of a serial attenuation, the bacterial suspension was dispersed onto the TSB culture medium and anaerobically incubated at the temperature of 37°C for 72 h. The number of colonies was counted utilizing a colony counter and CFU was calculated utilizing a dilution factor. In order to evaluate the activity of metabolization of *P. gingivalis* bio-membranes, an MTT method was performed. Handle the Ti sheets with biofilms by MTT dye and culture at the temperature of 37°C for 1 h, followed by treating equivalently with DMSO, shaken in horizontal direction for 30 min in the darkness. Pipet the solution into a new 96-well plate, and then measure the absorbance at OD_{540nm}. Calculate the metabolic activity of the biofilm by the higher absorbance (Li et al., 2015). All of the samples were assayed in 3 replicates.

2.7 Cell culture

The human gingival fibroblasts (HGFs) were cultivated in the cell culture media, containing 89% Dulbecco's modified Eagle's medium (DMEM), 10% (v/v) fetal bovine serum (FBS), and 1% antibiotics (penicillin and streptomycin) at 37°C in a damp atmosphere with 5% CO_2 (Tsugeno et al., 2014).

The biosecurity was evaluated with cytological staining. The nucleus of HGFs was stained using 4,6-diamidino-2-phenylindole (DAPI), while the cytoplasm was dyed using fluorescein isothiocyanate (FITC). Then, the CLSM images were recorded. To study the cytotoxicity of those slices with different samples, HGFs inoculated in 24-well plates at a density of 2.5×10^5 per well were incubated with TNTs, L-AuNPs-TNTs, M-AuNPs-TNTs, and H-AuNPs-TNTs for 24 h. Relative cyto-activity was estimated in virtue of a cell counting kit-8 (CCK8) assay (Wang et al., 2016).

Fresh rabbit blood was detached from plasma by means of centrifuging at 1500 rpm for 15 min at 4°C. The separated RBCs were first washed with PBS to make the supernatant translucent, and then suspended again in PBS. Then, TNTs slices with different treatments were added to the RBC turbid liquid. As long as putting in an incubator at the temperature of 37°C for 2 h, the suspension was separated at the speed of 1500 rpm. The supernatant obtained from every single centrifugal cuvette was applied to assay the hemoglobin release utilizing a microplate reader at $OD_{576\ nm}$ (Mazare et al., 2016). Comparison groups were detected under the identical condition; PBS was added as the negative control. In contrast, Triton X-100 at 0.5% was added to be the positive comparison group. Each group used six samples. Use the following formula to calculate the percentage of hemolysis:

$$\text{Hemolysis} = \frac{\left(OD_{sample} - OD_{negative\ control}\right)}{\left(OD_{Positive\ control} - OD_{negative\ control}\right)^{*}100\%}. \quad (1)$$

2.8 Statistical analysis

The data were represented as the means ± standard error of the mean. The significant differences between sample groups were performed by a one-way analysis of variance with a Tukey's post hoc test using the GraphPad Prism 7.0. A value of $p < 0.05$ was considered to indicate statistical significance.

3 Results and discussion

3.1 Material design and morphology characterization

As the schematic image shown in Figure 1A, TNTs with AuNPs decoration were designed and fabricated for potential application in dental implants. The functional surface modification of implant was achieved by ultrasound irradiation and subsequent release of ROS to induce the lipid peroxidation of bacteria membrane. The bacteria were dissolved, broken, and killed owing to the excellent antibacterial activity of highly activated ROS.

Figure 1(B1–E1) show the SEM images of TNTs and AuNPs-TNTs. TNTs exhibited a self-standing nanotubular structure with a diameter in the range of 150 ± 10 nm (Figure 1B1) and around 1.3 μm in length (Figure 1B2). Before the AuNP embellishment, in order to transfer the amorphous TiO_2 to the anatase phase, the TNTs were annealed at 450°C in air and lasted for 1 h. In the time of exposing $AuCl_4^-$-TNTs to UV light, the photo-induced electrons were triggered to the conduction band of TiO_2. Subsequently, these electrons drive to the surface of TNTs and then reduces the combination between the adsorbed $AuCl_4^-$ and Au (0) by the internal field. In addition, from dental materials' perspective, such an engineered cover with TNTs ranging from 55 to 110 nm would not impact the mechanical properties when used as dental implant base, demonstrating its beneficial fracture load-bearing capabilities under external masticatory pressure conditions. Consequently, this engineered design did not have mechanical compromise and it is a promising dental implant surface.

Furthermore, three categories of AuNPs-TNTs had uniform tube diameters, which indicated that Au decoration would not compromise the structure of TNTs (Figure 1C1–E1). AuNPs with good morphology were observed on the tube surface with a shape of 20 nm in contrast with the bare TNTs.

As shown in Figure 1(B2–D2), the images of intersecting surface show that the tube lengths of all samples were similar, and AuNPs were grafted on the tube wall. According to an increase in the reaction cycles, the AuNPs were located deeper into the tubular structure, which revealed that SPR-Au improved the potential of photocatalytic. Predictably, it led to an increase in nanoparticle density when the number of

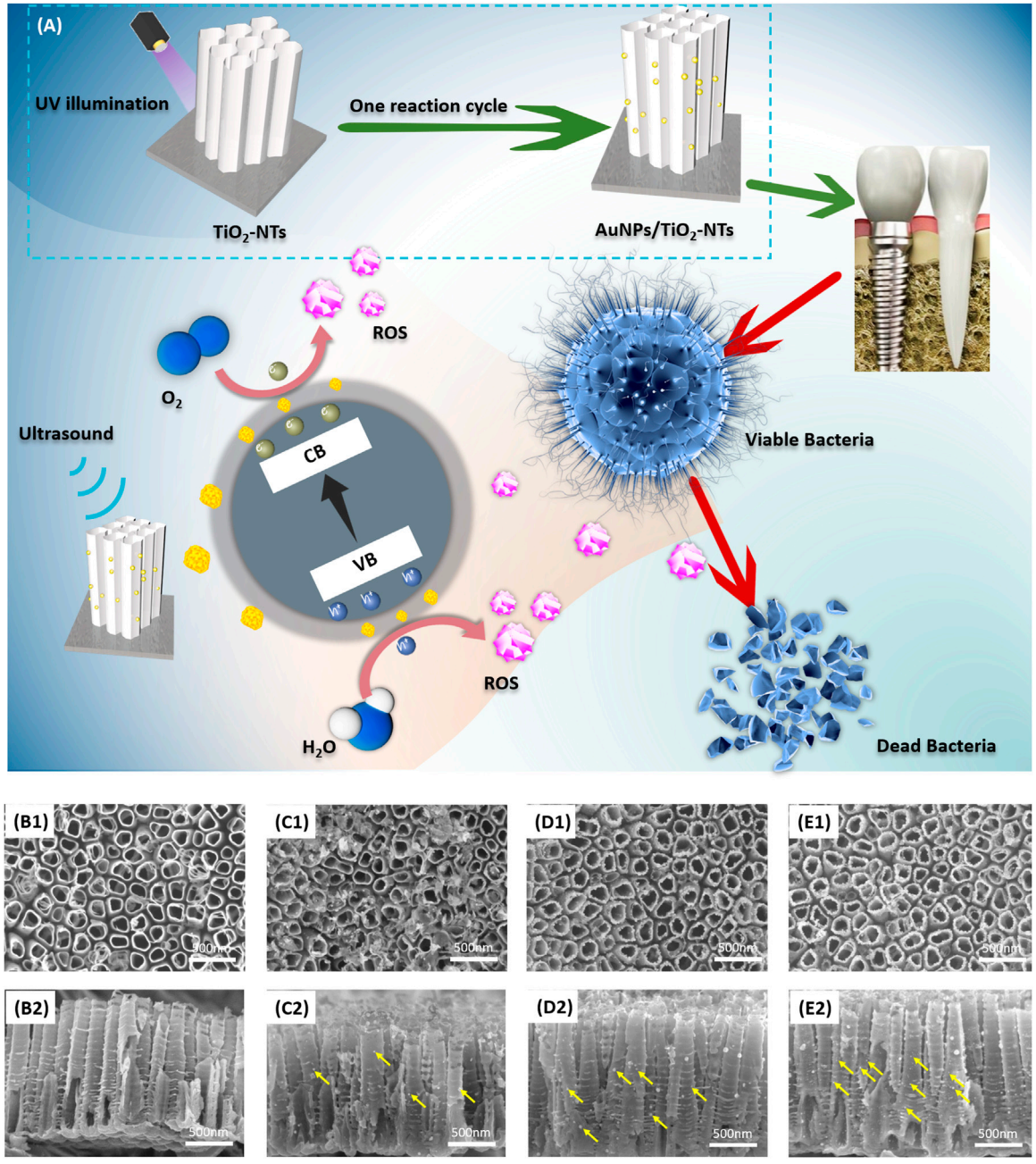

FIGURE 1
(A) Schematic image of TNTs surface with AuNP decoration. This designed surface exhibited antibacterial activity after ultrasound irradiation. The vertical view **(B1–E1)** and cross-sectional view **(B2–E2)** of **(B)** TNTs, **(C)** L-AuNPs-TNTs, **(D)** M-AuNPs-TNTs, and **(E)** H-AuNPs-TNTs. Yellow arrows show AuNPs loaded on the tube wall.

modification cycles was in the high level (Figure 1C1–E1, C2-E2). These AuNPs are equally distributed on the inner and outer surfaces of nanotubes. Notably, the increase of decoration cycles did not instigate a segregation phenomenon. The size of these nanoparticles was similar to the size obtained in the first cycle.

3.2 Physical and chemical characterization of AuNPs loaded on TNTs

We carried out XPS analysis as a means to further validate the chemical composition of the as-prepared TNTs and AuNPs-TNTs surface. The survey and high-resolution XPS spectra of

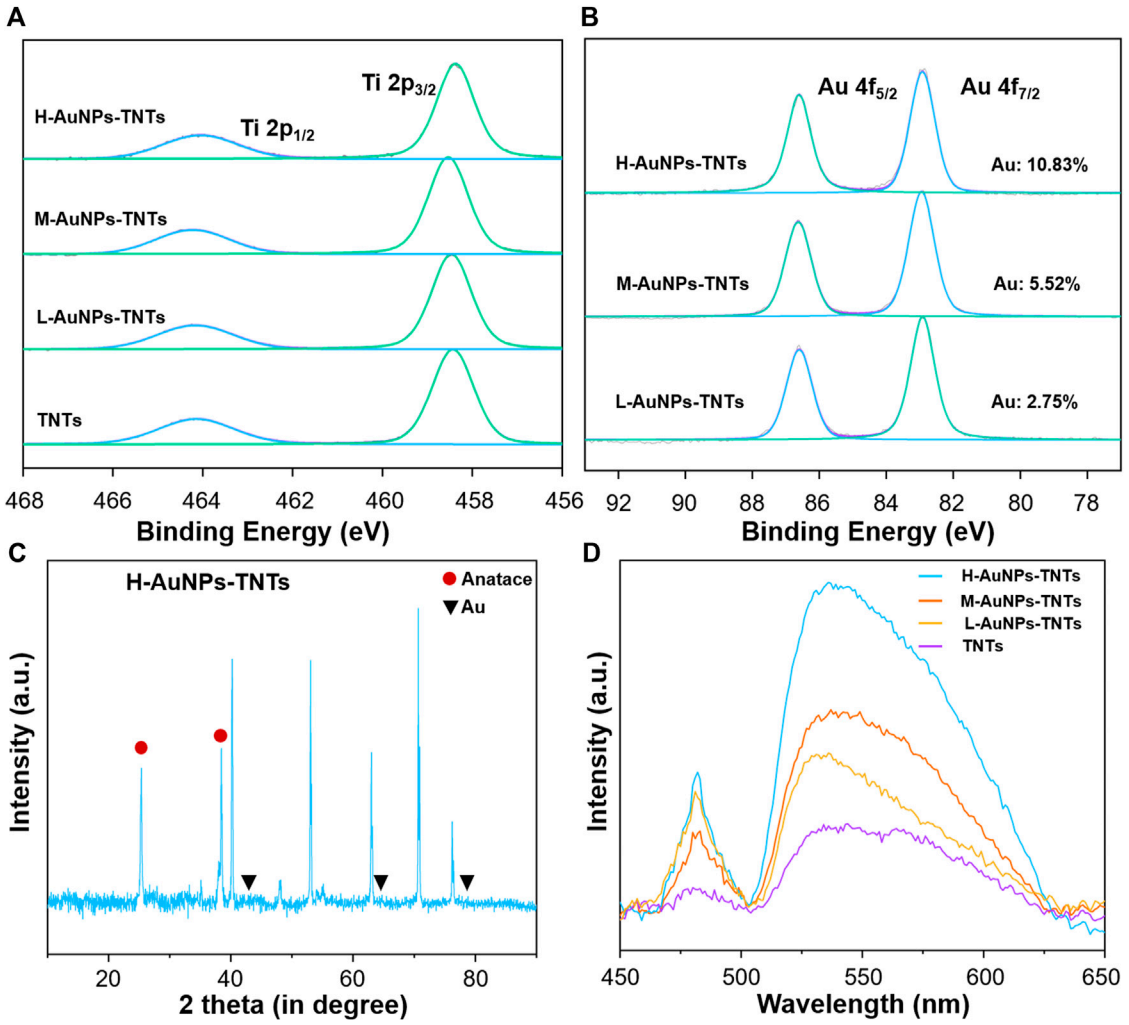

FIGURE 2
(A) XPS measurement of TNTs and AuNPs-TNTs substrate. **(B)** XPS measurement of Au 4f spectra for AuNPs-TNTs. **(C)** XRD patterns of H-AuNPs-TNTs. **(D)** UV-vis spectra of pure TNTs and AuNPs-TNTs with different cycles.

AuNPs- TNTs are shown in Figure 2A,B and Supplementary Figure S1. After UV-induced photoreduction, the emergence of Au 4f signals was observed. The intense peaks at 83.0 and 86.8 eV could be observed in the Au 4f spectrum in Figure 2B, which indicated a normal state of Au 2p and the metallic Au generation in AuNPs-TNTs. In addition, the results of XPS analysis indicate that the Au contents Au in different AuNPs-TNTs varied. Draw a distinction between L-AuNPs-TNTs and M-AuNPs-TNTs, H-AuNPs-TNTs had the highest amount of Au, and the surface loading mount is up to 10.83%. For comparison, the Au content in the L-AuNPs-TNTs group is 5.52% and in M-AuNPs-TNTs group is 2.75%. An X-ray diffraction (XRD) analysis was also conducted to designate the TNTs before and after decoration with AuNPs by photo-catalytically induced reduction (Figure 2C and Supplementary Figure S2). Beside the typical peaks obtained from the anatase crystalline state of TiO_2, the diffraction peaks at $\theta = 45$, 64, and 77° are correlated to the monoclinic Au phase, and detected on the obtained sample (JCPDS No: 01–1174). The increasing quantity of AuNP incorporation was verified from the UV-vis spectra. As shown Figure 2D, an absorption peak representing the Au appeared in the 500–700 nm range, and it showed a growing trend with the Au-loading amount, especially on the H-AuNPs-TNTs sample.

As surface wettability is an important required property for biomedical artificial implants, the contact angle (CA) of TNTs and AuNPs-TNTs samples was measured by a contact angle system (3 μl, room temperature, Dataphysics-OCA20, Germany) (Supplementary Figure S3). Owing to the presence of abundant Ti-OH groups on the surface, the as-formed TNTs are

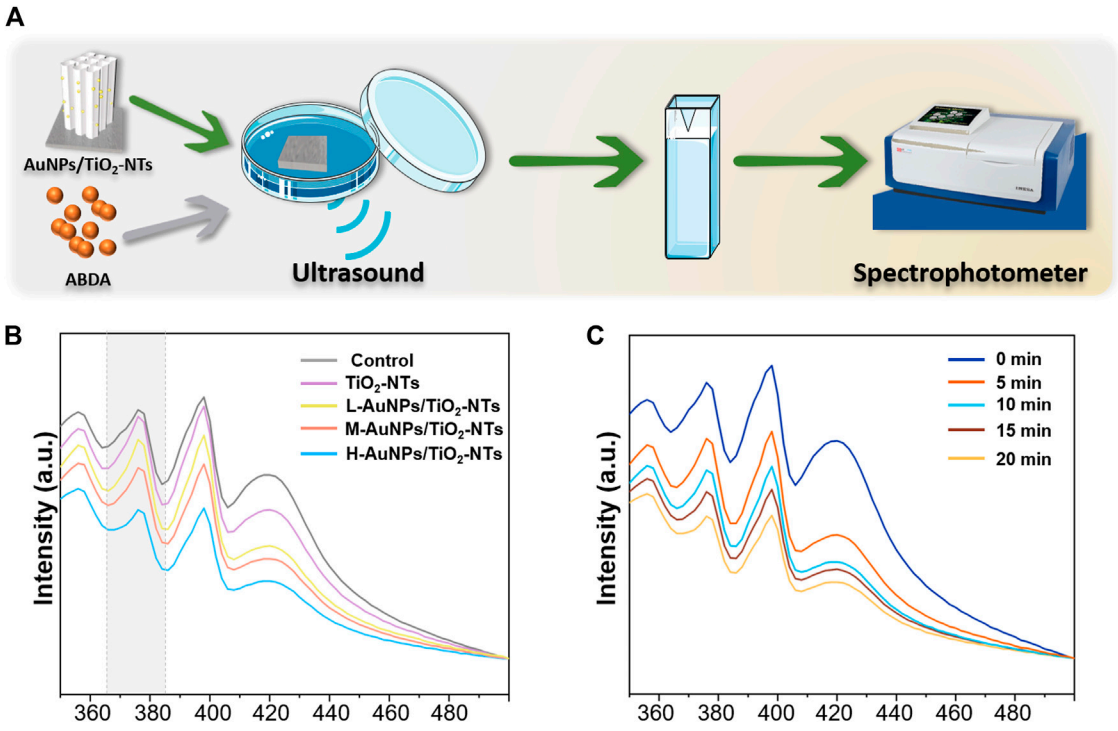

FIGURE 3
(A) Schematic images of $^1O_2$ generation with time. **(B)** ROS generation testified by the absorbance of ABDA under ultrasound irradiation for 10 min. **(C)** The amount of ROS generation changed in the H-AuNPs-TNTs group under ultrasound treatment in 20 min.

hydrophilic (CA = 11.8). Although the contact angles slightly increased with AuNP coating amount, the surface still maintains hydrophilicity even at a high AuNPs loading, i.e., the contact angles of L-AuNPs-TNTs, M-AuNPs-TNTs, and H-AuNPs-TNTs were determined as 26.5, 26.9, and 28.2, respectively.

3.3 ROS generation under ultrasound

To achieve a satisfactory antibacterial outcome, a high-caliber of ROS is preferred. The ROS can induce MDA, resulting in membrane lipid solubilization, which further kills the bacteria (Yang et al., 2019). Therefore, a dynamic ROS generation/production yield is crucial for achieving a high antibacterial efficiency. In general, $^1O_2$ has been previously reported as the main ROS species generated during ultrasound treatment (Zhang et al., 2021). To gain insight on the antibacterial possibility, the $^1O_2$ generation kinetics on the different AuNPs-TNTs groups was evaluated using ABDA as the trapping agent, and the results were obtained using a UV-vis spectrophotometer (Figure 3A).

ABDA is widely used as a trap for $^1O_2$ in the biomedical realm, and also it could be easily monitored by UV-vis. The underlying operational principle involves the disappearance of its main absorption centered at 375 nm after reaction with $^1O_2$, which could be recorded to generate ROS (Cao et al., 2019).

As shown in Figure 3B, the ROS production on L-AuNPs-TNTs and M-AuNPs-TNTs was higher than that of TNTs. Obviously, the absorbance of ABDA at 378 nm showed the most significant decreasing tendency due to the consumption of ROS, indicating that H-AuNPs-TNTs generated the maximum $^1O_2$ dose. This performance indicates that the quantity of ROS for AuNPs-TNTs was positively correlated with Au content decoration. This is probably because the band gap of AuNPs-TNTs (2.90 eV) was narrower than absolute TiO_2 (3.20 eV) (Chen et al., 2011), preventing the rapid recombination between excited electrons and holes, and leading to a higher quantum yield of ROS production (Felip-León et al., 2019). it could also speed up the rate constant and thus increase the productivity of ROS when combined Au with TiO_2 (Chen et al., 2011). To evaluate the ROS production kinetics, the time-dependent ABDA consumption in the presence of H-AuNPs-TNTs under ultrasound treatment in each 5 min time interval was plotted in Figure 3C. The change in ABDA absorption indicates the continuous and controllable $^1O_2$ generation under sonodynamic stimulation. These results show that ultrasound activation is an effective route to release negligible ROS on TiO_2-based nanomaterials instead of applying the

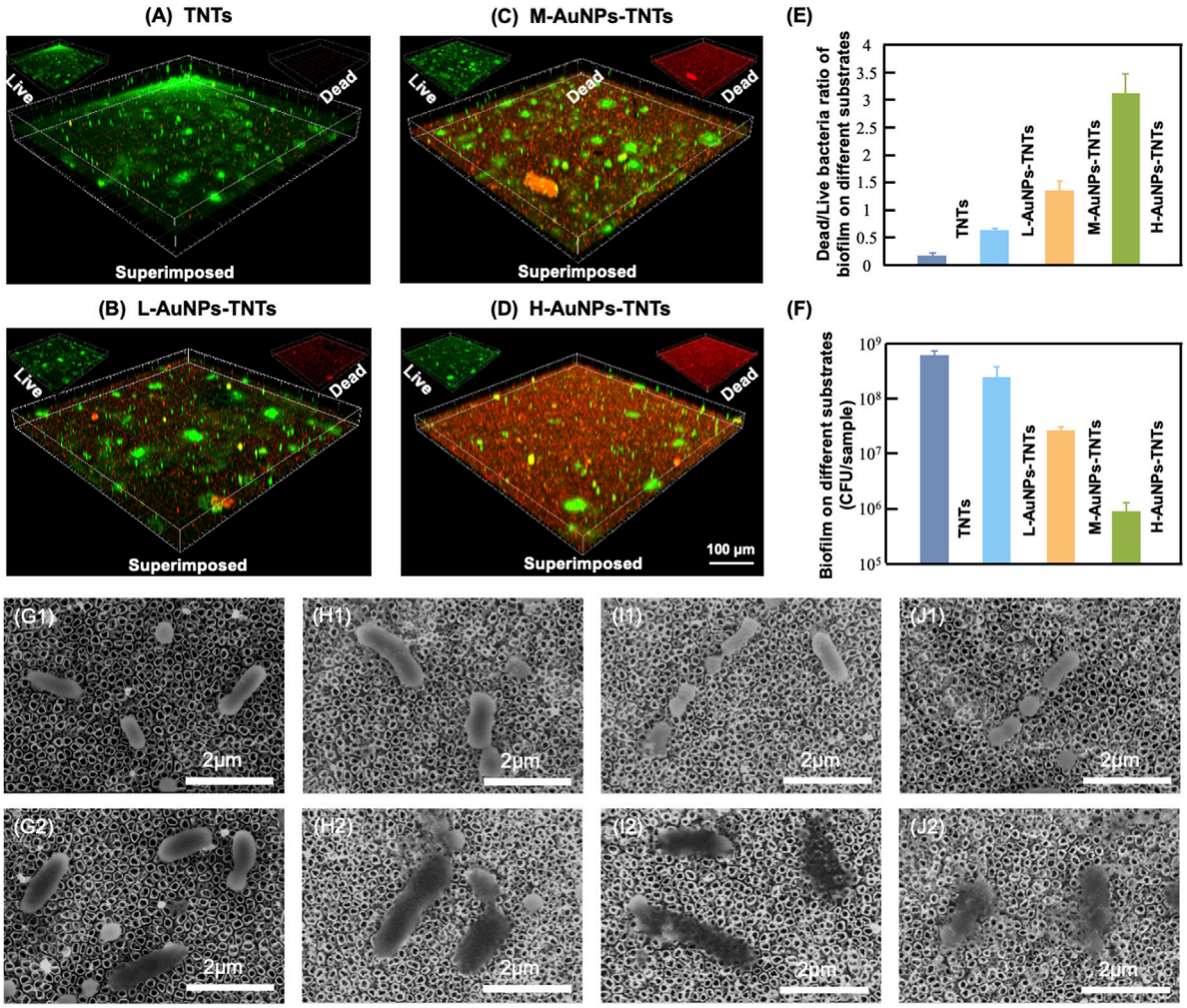

FIGURE 4
Antibacterial effect. **(A–D)** Confocal fluorescence microscopy images of *P. gingivalis* incubated with AuNPs-TNTs at ultrasound power densities 1.5 W/cm^2 and stained with STYO9-PI (green: live bacteria, red: dead bacteria). **(E)** Colony formation units of *P. gingivalis* in different agar plates. **(F)** Statistical bar chart of dead/live bacteria. SEM images show the morphology of *P. gingivalis* adhered on **(G)** TNTs, **(H)** L-AuNPs-TNTs, **(I)** M-AuNPs-TNTs, and **(J)** M-AuNPs-TNTs samples before **(G1–J1)** and after **(G2–J2)** ultrasound-induced antibacterial process.

photocatalysis. Based on $^1O_2$ generation, it can be hypothesized that AuNPs-TNTs would be a promising material to kill the pathogen by ultrasound activation. The time-sequential and rational function of H-AuNPs-TNTs may enhance the antibacterial application of TNTs in infectious disease. The morphologies of H-AuNPs-TNTs before and after the ultrasound irradiation were evaluated (Supplementary Figure S4). The sample maintained its initial structure with intact nanotubes and the well-decorated AuNPs in ultrasound, verifying the excellent mechanical stability of AuNPs-TNTs. Plenty of ROS generation and good stability of AuNPs-TNTs by ultrasound treatment indicate good potential of the as-proposed AuNPs-TNTs as an STD agent in antibacterial application.

3.4 Antibacterial properties of AuNPs-TNTs samples

The antibacterial properties were then studied to elucidate the peri-implantitis therapeutic mechanism of the AuNPs-TNTs samples. In this study, *P. gingivalis*, one of the major pathogenic bacteria that may occur in the peri-implantitis to form a biofilm *in vivo*, was selected as the representative pathogen. Figure 4(A–D) show the antibiofilm efficacy of different nanostructure *via* typical dead/live bacterial images. PI was used to stain dead bacteria and exhibited as red color bacteria by pseudo-color processing, styo6 was used to stain live bacteria and exhibited as green color bacteria by pseudo-color processing. Figure 4E shows the ultrasound inactivation results of *P.*

gingivalis using the traditional colony counting method and agar plates. Compared with the TNTs group, the CFU values for M-AuNPs-TNTs group, L-AuNPs-TNTs group, and H-AuNPs-TNTs group exhibited a reduction of approximately 1, 2, and 3 orders of magnitude for periodontal biofilm, respectively. The difference in bactericidal abilities is associated with different ROS yields on these samples during the ultrasound treatment. In this case, ROS, a strong oxidant, had the characteristic of high reactivity, causing various ROS-related reactions, such as oxidation, reduction, or dissolution. These reactions further cause bacterial lipid oxidation and membrane lipid destruction, leading to bacterial death. Remarkably, H-AuNPs-TNTs act as a ROS-generation warfare agent, exhibiting superior antibacterial properties among the tested groups. A statistical bar chart of dead/live bacteria is shown in Figure 4F, consistent with the fluorescent graphs in Figure 4(A–D).

The SEM images show the morphology of intact bacteria (Figure 4G1–J1) and the bacteria undergoing ultrasound treatment (Figure 4G2–J2) on different sample groups. *P. gingivalis* exhibited a smooth and unbroken cell body. In addition, no difference was observed for the bacteria morphology on these different samples before ultrasound induced antibacterial inactivation. The intracellular substance was released into the extracellular microenvironment following the perforation of cell membrane which can be confirmed by the bacterial fragments found nearby. However, the morphology of *P. gingivalis* adhered on AuNPs-TNTs samples showed remarkable changes after ultrasonication irradiation. The bacteria were deformed and collapsed. However, the bacteria loaded on TNTs still maintained most of their original structure even under the same ultrasound experiment. In this study, AuNP decoration facilitated the triggering of TNTs under ultrasound owing to the surface plasmon resonance (SPR) influence of precious metals. At the same time, the power density of an ultrasound source is 1.5 W/cm^2, which could be easily attained from a conventional clinical device. This would overcome the limitation of light penetration. TNTs decorated with a great quantity of AuNPs had perfect inhibitory effect on the main pathogenic bio-membrane, which implied favorably antibacterial potential in terms of clinical applications. This nano-engineered structure showed parallel antibacterial efficiency with porphyrin sensitizer-DVDMS added TNTs and superior to TNTs only (Wang et al., 2020b).

3.5 *In vitro* cellular compatibility

In addition, ultrasound, a mechanical wave with better ability of tissue penetration and limited energy attenuation, is considered safer than the visible light in PDT (Zhang S. et al., 2019). Large amounts of ROS would be produced when activated by external ultrasound energy, resulting in an intense restriction and killing activities against plaque biofilm (Wang Z. et al., 2018). Nevertheless, with regard to the treatments of infectious diseases, excessive production of ROS could worsen the internal inflammation. Generally, the diffusion distance of ROS is just about 100 nm and the half-time is shorter than 0.04 μs (Misba et al., 2018), thereby, the distance that ROS diffuse into the cells is important for the SDT activity (Zhang T. et al., 2019). According to a contact killing mechanism, the modification of the surface AuNPs-TNTs in this research provided beneficial antibacterial activity. It is interesting that peri-implantitis is caused by a dental biofilm attached to implants. The ROS produced by ultrasound-photocatalytic process would cause the inactivation of the attached bacteria, thereby preventing and impeding the development and progress of peri-implantitis. Furthermore, in a typical ultrasound process, collapse cavitation can bring about temperatures in excess of 5000 K and over 50 MPa pressures on a nanosecond time scale (Merouani et al., 2014). These generate a high liquid shear force, impact waves, localized heating, and appearance of free substrate, contributing to the antibacterial activity of sonosensitizer *via* several mechanisms.

The biocompatibility of nanomaterials is a key indicator for biological applications. The initial interaction and reaction between cells and the surfaces of biomaterials decide the life span of an implants (Bowles and Setton, 2017). Insufficient cell adhesion hinders tissue repair and regeneration, resulting in implant instability, usually leading to the failure of dental implant and even inducing severe septicemia. To evaluate the feasibility of AuNPs-TNTs used as an antibacterial platform, cellular cytotoxicity of AuNPs-TNTs platform towards HGFs was investigated. The cytotoxicity of AuNPs-TNTs was evaluated based on the apoptosis and morphological changes of HGFs. As shown in Figure 5A, HGFs were separately incubated with TNTs, L-AuNPs-TNTs, M-AuNPs-TNTs, and H-AuNPs-TNTs, and then stained with DAPI and FITC. The nuclei which were labeled by DAPI in each group show blue fluorescence, homogeneous distribution, and intact structure. The FITC-labeled cytoplasm in each group emits green fluorescence, fusiform, and consecutive. These results indicate an ignorable cytotoxic effect from AuNPs-TNTs surface. To quantify the cytotoxicity of AuNPs-TNTs platform toward HGFs, we carried out a standard trial CCK-8 cell viability. After incubation with the three types of AuNPs-TNTs and TNTs samples for 24 h, the cell viability of HGFs was measured using the method of CCK-8. As shown in Figure 5B, the cell viability of the HGFs on these samples is still higher than 85%, indicating that the as-proposed AuNPs-TNTs antibacterial materials have low cytotoxicity and satisfactory biocompatibility. By further increasing the incubation time to 48 and 72 h, the HGFs still maintained good state on H-AuNPs-TNTs with ignorable apoptosis and morphologic changes (Supplementary Figure S5). Moreover, we also examined the influence of the test materials on the wholeness of RBC membrane that might lead to the fracture of RBC, and thus calculated the hemolytic index. The hemolysis of RBCs in the

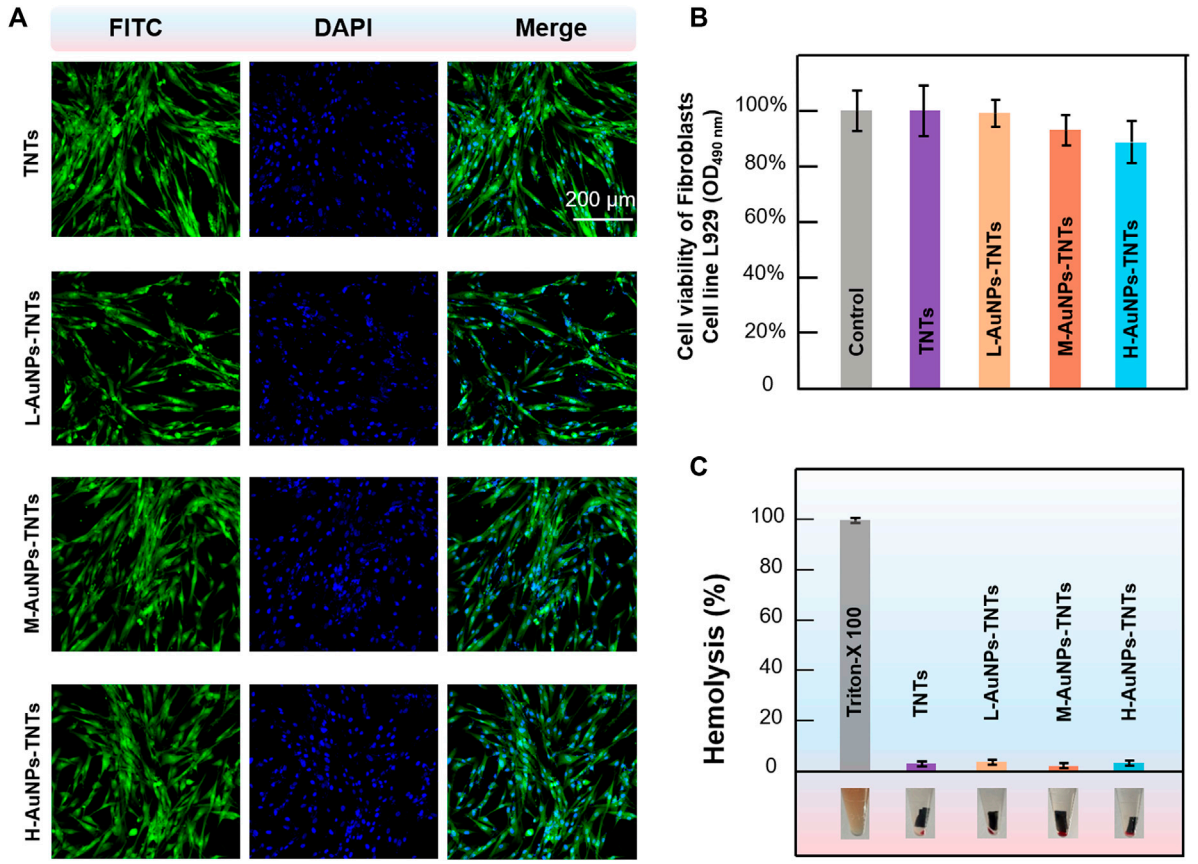

FIGURE 5
Confocal fluorescence microscopy images of HGFs (incubated with AuNPs-TNTs stained with DAPI and FITC, scale bar: 200 μm. **(B)** Viability of HGFs incubated with AuNPs-TNTs. **(C)** Hemolysis of RBCs coincubated with AuNPs-TNTs.

presence of TNTs, L-AuNPs-TNTs, M-AuNPs-TNTs, and H-AuNPs-TNTs was lower than 5%, indicating excellent hemocompatibility (Figure 5C).

These results indicate that the presence of AuNPs-TNTs had less negative impact on the proliferation and state of cell. These phenomena can be ascribed to the large surface area of nanotubular TiO_2-based materials, which provide plenty of sites, with the features of better hydrophilicity and protein adsorption capacity. Due to these advantages, cell attachment and proliferation are improved, thereby promoting osseointegration (Su et al., 2018). Moreover, the negatively charged TNTs and AuNPs-TNTs surface can attract positively charged proteins, which would also improve cell attachment (Kabaso et al., 2011). As the result of high surface charge density, there is a strong bonding between the AuNPs-TNTs and cells (Su et al., 2018). In addition, noble-metal nanoparticles would also improve cell proliferation *via* enhancing the gene expression (Balu et al., 2020).

Furthermore, *in vivo* animal study was conducted to confirm the wound tissue healing around different surfaces. As shown in Supplementary Figure S6, substantial inflammatory cells infiltrated around the four groups, indicating local inflammatory reaction was induced by LPS. While, both H&E staining images and the histomorphometric analysis demonstrated that the total number of inflammatory cells in three groups of AuNPs/TNTs were reduced significantly than TNTs group. The thick collagen fibers (Masson staining) of the three groups of AuNPs/TNTs were significantly increased compared with TNTs group, fibroblasts tend to be mature. Whereas, the TNTs group exhibited blood clots and large amount of big and round fibroblasts, demonstrating that they were still at the early stage of wound healing.

4 Conclusion

In conclusion, we designed a TNTs substrate decorated by AuNPs for application prospect in the antibacterial effect of dental implant surfaces. AuNPs decoration on TNTs surface would induce a large amount of ROS generation just by

applying a simple ultrasound treatment. The generated ROS has been demonstrated to be effective to inactivate the bacteria attached on the sample surface. Importantly, the results of cytotoxicity tests show that AuNPs-TNTs have excellent biocompatibility for promising implant applications. Considering securer and superior tissue penetration accompanied by limited energy attenuation than photo-catalytically triggered bacteria inactivation, the AuNPs-TNTs provide a promising surface for achieving excellent antibacterial properties against the main pathogenic biofilm by SDT. Our study thus proposes a strategy to develop a nanoplatform for effective anti-bacteria combining ultrasound with TiO_2 doping metal ions, which may extend the applications of TiO_2-based nanomaterials in treating the inflammatory damage from bacterial biofilm on artificial dental implants Park et al., 2016, Xu et al., 2020.

Data availability statement

The original contributions presented in the study are included in the article/Supplementary Material, further inquiries can be directed to the corresponding author.

Author contributions

YS and WX contributed equally to this work. YS and WX conceived and designed the experiments. ML, CJ and TZ conducted the sample preparation. YS, WX, QW and LA conducted the data and bioinformatics analyses. YS, WX and LA wrote the manuscripts. LA oversaw the completion of this study and edited the manuscript.

Funding

This work was supported by Bethune Project of Jilin University (2020B44), National Natural Science Foundation of China (82201102), General program of Natural Science of Jilin Province(YDZJ202201ZYTS017), Science and Technology Project of Jilin Province Financial Department (JCSZ2021893-2i), Science and Technology Project of Jilin Province (20220201121GX), EducationScience and Technology Research Project of Jilin Province Department (JJKH20221098KJ).

Conflict of interest

The authors declare that the research was conducted in the absence of any commercial or financial relationships that could be construed as a potential conflict of interest.

Publisher's note

All claims expressed in this article are solely those of the authors and do not necessarily represent those of their affiliated organizations, or those of the publisher, the editors and the reviewers. Any product that may be evaluated in this article, or claim that may be made by its manufacturer, is not guaranteed or endorsed by the publisher.

Supplementary material

The Supplementary Material for this article can be found online at: https://www.frontiersin.org/articles/10.3389/fbioe.2022.1074083/full#supplementary-material

References

Balu, S., Andra, S., Kannan, S., Vidyavathy S, M., and Muthalagu, M. (2020). Facile synthesis of silver nanoparticles with medicinal grass and its biological assessment. *Mat. Lett.* 259 (15), 126900. doi:10.1016/j.matlet.2019.126900

Bowles, R. D., and Setton, L. A. (2017). Biomaterials for intervertebral disc regeneration and repair. *Biomaterials* 129, 54–67. doi:10.1016/j.biomaterials.2017.03.013

Cai, Y., Strømme, M., and Welch, K. (2014). Bacteria viability assessment after photocatalytic treatment. *3 Biotech.* 4 (2), 149–157. doi:10.1007/s13205-013-0137-1

Cao, Y., Wu, T., Dai, W., Dong, H., and Zhang, X. (2019). TiO_2 nanosheets with the Au nanocrystal-decorated edge for mitochondria-targeting enhanced sonodynamic therapy. *Chem. Mat.* 31 (21), 9105–9114. doi:10.1021/acs.chemmater.9b03430

Chen, M., Yang, L., Zhang, L., Han, Y., Lu, Z., Qin, G., et al. (2017). Effect of nano/micro-Ag compound particles on the bio-corrosion, antibacterial properties and cell biocompatibility of Ti-Ag alloys. *Mater. Sci. Eng. C* 75 (1), 906–917. doi:10.1016/j.msec.2017.02.142

Chen, X., Liu, L., Yu, P. Y., and Mao, S. S. (2011). Increasing solar absorption for photocatalysis with black hydrogenated titanium dioxide nanocrystals. *Science* 331, 746–750. doi:10.1126/science.1200448

Chung, P. Y., and Khanum, R. (2017). Antimicrobial peptides as potential anti-biofilm agents against multidrug-resistant bacteria. *J. Microbiol. Immunol. Infect.* 50 (4), 405–410. doi:10.1016/j.jmii.2016.12.005

Deepagan, V. G., You, D. G., Um, W., Ko, H., Kwon, S., Choi, K. Y., et al. (2016). Long-circulating Au-TiO_2 nanocomposite as a sonosensitizer for ROS-mediated eradication of cancer. *Nano Lett.* 16 (10), 6257–6264. doi:10.1021/acs.nanolett.6b02547

El-Fray, M., Piegat, A., and Prowans, P. (2009). Influence of TiO_2 nanoparticles incorporated into elastomeric polyesters on their biocompatibility *in vitro* and *in vivo*. *Adv. Eng. Mat.* 11 (11), B200–B203. doi:10.1002/adem.200900104

Felip-León, C., Puche, M., Miravet, J. F., Galindo, F., and Feliz, M. (2019). A spectroscopic study to assess the photogeneration of singlet oxygen by graphene oxide. *Mat. Lett.* 251, 45–51. doi:10.1016/j.matlet.2019.05.001

Gao, A., Hang, R., Huang, X., Zhao, L., Zhang, X., Wang, L., et al. (2014). The effects of titania nanotubes with embedded silver oxide nanoparticles on bacteria and osteoblasts. *Biomaterials* 35 (13), 4223–4235. doi:10.1016/j.biomaterials.2014.01.058

Gao, Z. D., Liu, H. F., Li, C. Y., and Song, Y. Y. (2012). Biotemplated synthesis of Au nanoparticles-TiO_2 nanotube junctions for enhanced direct electrochemistry of heme proteins. *Chem. Commun.* 49 (8), 774–776. doi:10.1039/c2cc38183d

Jie, H., Park, H., Chae, K.-H., Anpo, M., and Park, J.-K. (2009). Suppressed recombination of electrons and holes and its role on the improvement of

photoreactivity of flame-synthesized TiO_2 nanopowders. *Chem. Phys. Lett.* 470 (4), 269–274. doi:10.1016/j.cplett.2009.01.065

Kabaso, D., Gongadze, E., Perutková, Š., Matschegewski, C., Kralj-Iglič, V., Beck, U., et al. (2011). Mechanics and electrostatics of the interactions between osteoblasts and titanium surface. *Comput. Methods Biomech. Biomed. Engin.* 14 (5), 469–482. doi:10.1080/10255842.2010.534986

Kubacka, A., Serrano, C., Ferrer, M., Lünsdorf, H., Bielecki, P., Cerrada, M. L., et al. (2007). High-performance dual-action Polymer–TiO_2 nanocomposite films via melting processing. *Nano Lett.* 7 (8), 2529–2534. doi:10.1021/nl0709569

Kutuzova, A., Dontsova, T., and Kwapinski, W. (2021). Application of TiO_2-based photocatalysts to antibiotics degradation: Cases of sulfamethoxazole, trimethoprim and ciprofloxacin. *Catalysts* 11 (6), 728. doi:10.3390/catal11060728

Li, J. Y., Wang, X. J., Wang, L. N., Ying, X. X., Ren, X., Liu, H. Y., et al. (2015). High *in vitro* antibacterial activity of pac-525 against Porphyromonas gingivalis biofilms cultured on titanium. *Biomed. Res. Int.* 2015, 1–8. doi:10.1155/2015/909870

Li, X., Qi, M., Sun, X., Weir, M. D., Tay, F. R., Oates, T. W., et al. (2019). Surface treatments on titanium implants via nanostructured ceria for antibacterial and anti-inflammatory capabilities. *Acta Biomater.* 94, 627–643. doi:10.1016/j.actbio.2019.06.023

Liu, H., Carter, P. J. H., Laan, A. C., Eelkema, R., and Denkova, A. G. (2019). Singlet oxygen sensor green is not a suitable probe for $^1O_2$ in the presence of ionizing radiation. *Sci. Rep.* 9 (1), 8393. doi:10.1038/s41598-019-44880-2

Ma, H., Brennan, A., and Diamond, S. A. (2012). Photocatalytic reactive oxygen species production and phototoxicity of titanium dioxide nanoparticles are dependent on the solar ultraviolet radiation spectrum. *Environ. Toxicol. Chem.* 31 (9), 2099–2107. doi:10.1002/etc.1916

Mazare, A., Totea, G., Burnei, C., Schmuki, P., Demetrescu, I., and Ionita, D. (2016). Corrosion, antibacterial activity and haemocompatibility of TiO_2 nanotubes as a function of their annealing temperature. *Corros. Sci.* 103, 215–222. doi:10.1016/j.corsci.2015.11.021

Merouani, S., Hamdaoui, O., Rezgui, Y., and Guemini, M. (2014). Theoretical estimation of the temperature and pressure within collapsing acoustical bubbles. *Ultrason. Sonochem.* 21 (1), 53–59. doi:10.1016/j.ultsonch.2013.05.008

Misba, L., Zaidi, S., and Khan, A. U. (2018). Efficacy of photodynamic therapy against Streptococcus mutans biofilm: Role of singlet oxygen. *J. Photochem. Photobiol. B Biol.* 183, 16–21. doi:10.1016/j.jphotobiol.2018.04.024

Ola, O., and Maroto-Valer, M. M. (2015). Review of material design and reactor engineering on TiO_2 photocatalysis for CO_2 reduction. *J. Photochem. Photobiol. C Photochem. Rev.* 24, 16–42. doi:10.1016/j.jphotochemrev.2015.06.001

Park, J., Shokeen, B., Haake, S. K., and Lux, R. (2016). Characterization of Fusobacterium nucleatum ATCC 23726 adhesins involved in strain-specific attachment to Porphyromonas gingivalis. *Int. J. Oral Sci.* 8 (3), 138–144. doi:10.1038/ijos.2016.27

Qu, K., Xu, J., Xue, Y., Guo, J., Gao, Z., Song, Y., et al. (2022). Near infrared light-driven photothermal effect on homochiral Au/TiO2 nanotube Arrays for enantioselective desorption. *Anal. Chem.* 94 (2), 588–592. doi:10.1021/acs.analchem.1c04981

Raphel, J., Holodniy, M., Goodman, S. B., and Heilshorn, S. C. (2016). Multifunctional coatings to simultaneously promote osseointegration and prevent infection of orthopaedic implants. *Biomaterials* 84, 301–314. doi:10.1016/j.biomaterials.2016.01.016

Skariyachan, S., Sridhar, V. S., Packirisamy, S., Kumargowda, S. T., and Challapilli, S. B. (2018). Recent perspectives on the molecular basis of biofilm formation by *Pseudomonas aeruginosa* and approaches for treatment and biofilm dispersal. *Folia Microbiol. (Praha).* 63 (4), 413–432. doi:10.1007/s12223-018-0585-4

Su, E., Justin, D., Pratt, C., Sarin, V., Nguyen, V., Oh, S., et al. (2018). Effects of titanium nanotubes on the osseointegration, cell differentiation, mineralisation and antibacterial properties of orthopaedic implant surfaces. *Bone Jt. J.* 100-B (1), 9–16. doi:10.1302/0301-620X.100B1.BJJ-2017-0551.R1

Tsugeno, Y., Sato, F., Muragaki, Y., and Kato, Y. (2014). Cell culture of human gingival fibroblasts, oral cancer cells and mesothelioma cells with serum-free media, STK1 and STK2. *Biomed. Rep.* 2 (5), 644–648. doi:10.3892/br.2014.306

Vargas-Reus, M. A., Memarzadeh, K., Huang, J., Ren, G. G., and Allaker, R. P. (2012). Antimicrobial activity of nanoparticulate metal oxides against peri-implantitis pathogens. *Int. J. Antimicrob. Agents* 40 (2), 135–139. doi:10.1016/j.ijantimicag.2012.04.012

Wan, G. Y., Liu, Y., Chen, B.-W., Liu, Y.-Y., Wang, Y.-S., Zhang, N., et al. (2016). Recent advances of sonodynamic therapy in cancer treatment. *Cancer Biol. Med.* 13 (3), 325–338. doi:10.20892/j.issn.2095-3941.2016.0068

Wang, G., Feng, H., Hu, L., Jin, W., Hao, Q., Gao, A., et al. (2018a). An antibacterial platform based on capacitive carbon-doped TiO_2 nanotubes after direct or alternating current charging. *Nat. Commun.* 9 (1), 2055. doi:10.1038/s41467-018-04317-2

Wang, J., Guo, Y., Liu, B., Jin, X., Liu, L., Xu, R., et al. (2011). Detection and analysis of reactive oxygen species (ROS) generated by nano-sized TiO_2 powder under ultrasonic irradiation and application in sonocatalytic degradation of organic dyes. *Ultrason. Sonochem.* 18 (1), 177–183. doi:10.1016/j.ultsonch.2010.05.002

Wang, L., Wang, P., Liu, Y., Nie, W., Lv, X., Wei, Y., et al. (2013). Near-infrared indocyanine materials for bioanalysis and nano-TiO_2 photoanodes of solar cell. *J. Nanomater.* 2013, 1–5. doi:10.1155/2013/695107

Wang, X., Lu, T., Wen, J., Xu, L., Zeng, D., Wu, Q., et al. (2016). Selective responses of human gingival fibroblasts and bacteria on carbon fiber reinforced polyetheretherketone with multilevel nanostructured TiO_2. *Biomaterials* 83, 207–218. doi:10.1016/j.biomaterials.2016.01.001

Wang, L., Hasanzadeh, M., and Meunier, M. (2020a). Optical properties and applications of plasmonic-metal nanoparticles. *Adv. Funct. Mater.* 30, 2005400. doi:10.1002/adfm.202005400

Wang, Y., Sun, Y., Liu, S., Zhi, L., and Wang, X. (2020b). Preparation of sonoactivated TiO_2-DVDMS nanocomposite for enhanced antibacterial activity. *Ultrason. Sonochem.* 63, 104968. doi:10.1016/j.ultsonch.2020.104968

Wang, Z., Liu, C., Zhao, Y., Hu, M., Ma, D., Zhang, P., et al. (2018b). Photomagnetic nanoparticles in dual-modality imaging and photo-sonodynamic activity against bacteria. *Chem. Eng. J.* 356, 811–818. doi:10.1016/j.cej.2018.09.077

Wei, B.-X., Zhao, L., Wang, T.-J., Gao, H., Wu, H.-X., and Jin, Y. (2013). Photo-stability of TiO_2 particles coated with several transition metal oxides and its measurement by rhodamine-B degradation. *Adv. Powder Technol.* 24 (3), 708–713. doi:10.1016/j.apt.2012.12.009

Xu, D., Zhou, C., Zhan, C., Wang, Y., You, Y., Pan, X., et al. (2019). Enzymatic micromotors as a mobile photosensitizer platform for highly efficient on-chip targeted antibacteria photodynamic therapy. *Adv. Funct. Mat.* 29 (17), 1807727. doi:10.1002/adfm.201807727

Xu, J., Liu, N., Wu, D., Gao, Z., Song, Y., and Schmuki, P. (2020b). Upconversion nanoparticle-assisted payload delivery from TiO2 under near-infrared light irradiation for bacterial inactivation. *ACS Nano* 14 (1), 337–346. doi:10.1021/acsnano.9b05386

Xu, T., Zhao, S., Lin, C., Zheng, X., and Lan, M. (2020a). Recent advances in nanomaterials for sonodynamic therapy. *Nano Res.* 13 (11), 2898–2908. doi:10.1007/s12274-020-2992-5

Yang, B., Chen, Y., and Shi, J. (2019). Reactive oxygen species (ROS)-Based nanomedicine. *Chem. Rev.* 119 (8), 4881–4985. doi:10.1021/acs.chemrev.8b00626

You, D. G., Deepagan, V. G., Um, W., Jeon, S., Son, S., Chang, H., et al. (2016). ROS-generating TiO_2 nanoparticles for non-invasive sonodynamic therapy of cancer. *Sci. Rep.* 6 (1), 23200. doi:10.1038/srep23200

Zeng, H., Liu, J., and Ling, J. (2017). Efflux inhibitor suppresses Streptococcus mutans virulence properties. *FEMS Microbiol. Lett.* 364 (7), fnx033. doi:10.1093/femsle/fnx033

Zhang, S., Gao, F., He, G., Yin, H., Chen, J., Liu, Y., et al. (2019a). Titania coated 2D gold nanoplates as nanoagents for synergistic photothermal/sonodynamic therapy in the second near-infrared window. *Nanoscale* 11 (5), 2374–2384. doi:10.1039/C8NR07188H

Zhang, T., Ying, D., Qi, M., Li, X., Fu, L., Sun, X., et al. (2019b). Anti-Biofilm Property of Bioactive Upconversion Nanocomposites Containing Chlorin e6 against Periodontal Pathogens. *Molecules* 24 (15), 2692. doi:10.3390/molecules24152692

Zhang, Y., Zhang, X., Yang, H., Yu, L., Xu, Y., Sharma, A., et al. (2021). Advanced biotechnology-assisted precise sonodynamic therapy. *Chem. Soc. Rev.* 50 (20), 11227–11248. doi:10.1039/D1CS00403D

Zhao, C., Jian, X., Gao, Z., and Song, Y. (2022). Plasmon-mediated peroxidase-like activity on an asymmetric nanotube Architecture for rapid visual detection of bacteria. *Anal. Chem.* 13 (40), 14038–14046. doi:10.1021/acs.analchem.2c03471

Zheng, X., Sun, J., Li, W., Dong, B., Song, Y., Xu, W., et al. (2020). Engineering nanotubular titania with gold nanoparticles for antibiofilm enhancement and soft tissue healing promotion. *J. Electroanal. Chem. (Lausanne).* 871, 114362. doi:10.1016/j.jelechem.2020.114362

Zhu, W., Chen, Q., Jin, Q., Chao, Y., Sun, L., Han, X., et al. (2021). Sonodynamic therapy with immune modulatable two-dimensional coordination nanosheets for enhanced anti-tumor immunotherapy. *Nano Res.* 14 (1), 212–221. doi:10.1007/s12274-020-3070-8

Zielińska-Jurek, A., Wei, Z., Wysocka, I., Szweda, P., and Kowalska, E. (2015). The effect of nanoparticles size on photocatalytic and antimicrobial properties of Ag-Pt/TiO_2 photocatalysts. *Appl. Surf. Sci.* 353, 317–325. doi:10.1016/j.apsusc.2015.06.065

frontiers | Frontiers in Bioengineering and Biotechnology

TYPE Original Research
PUBLISHED 16 December 2022
DOI 10.3389/fbioe.2022.1103990

OPEN ACCESS

EDITED BY
Shaohua Wang,
Ohio University, United States

REVIEWED BY
Enping Lai,
Guangxi University of Science and Technology, China
Feng Qi,
University of Missouri, United States

*CORRESPONDENCE
Shurong Wang,
wangshurong011@swmu.edu.cn
Qingze Fan,
qingzefan017@swmu.edu.cn

†These authors have contributed equally to this work

SPECIALTY SECTION
This article was submitted to Nanobiotechnology, a section of the journal Frontiers in Bioengineering and Biotechnology

RECEIVED 21 November 2022
ACCEPTED 05 December 2022
PUBLISHED 16 December 2022

CITATION
Xu M, Liao Z, Liu Y, Guo S, Hu H, Chen T, Wu Y, Wan S, Zhou M, Lu M, Jiluo S, Yao L, Pu X, Wang S and Fan Q (2022), Preparation and optimization of poly (lactic-co-glycolic acid) rod-shaped particles in nano size range for paclitaxel delivery.
Front. Bioeng. Biotechnol. 10:1103990.
doi: 10.3389/fbioe.2022.1103990

Preparation and optimization of poly (lactic-co-glycolic acid) rod-shaped particles in nano size range for paclitaxel delivery

Mengyao Xu[1,2†], Zuyue Liao[1,2†], Yang Liu[1,2†], Shiwei Guo[1,2], Haiyang Hu[1,2], Tao Chen[1,2], Yuesong Wu[1,2], Shengli Wan[1,2], Meiling Zhou[1,2], Muhe Lu[2], Shiluo Jiluo[2], Lan Yao[1], Xiaofeng Pu[1], Shurong Wang[1,2*] and Qingze Fan[1,2*]

[1]Department of Pharmacy, The Affiliated Hospital of Southwest Medical University, Luzhou, Sichuan, China, [2]Department of Clinical Pharmacy, School of Pharmacy, Southwest Medical University, Luzhou, Sichuan, China

Nanoparticle shape has been acknowledged as an important design parameter due to its influence on nanoparticle interaction with biological systems. However, there is lacking of simple and scalable preparation technique for drug loaded non-spherical polymeric nanoparticles for a long time, thus hindering the potential applications. Although our previous research has modified the traditional emulsion solvent evaporation technique by adding guest molecules to prepare non-spherical poly (lactic-co-glycolic acid) (PLGA) particles, it is difficult to obtain nano-sized rods with minor axis less than 200 nm, which may have great potential in cancer therapy. Herein, in present research, the two-step ESE method was used and optimized to prepare poly (lactic-co-glycolic acid) nanorods for paclitaxel delivery. Firstly, the single-factor experiment was used to screen the influence of multi-factors including type of guest molecules, concentration of guest molecules, emulsification method, surfactant concentration, oil volume, poly (lactic-co-glycolic acid) concentration on the size and shape to determine the range of variables; based on the above range, a multi-factor and multi-level orthogonal experiment was designed. The formula is evaluated by the rod fabrication yield and the aspect ratio of major axis to minor axis. The results showed that the yield of nanorods in the optimal formula was 99% and the aspect ratio was 5.35 ± 2.05 with the minor axis of 135.49 ± 72.66 nm, and major axis of 657.77 ± 307.63 nm. In addition, the anti-cancer drug paclitaxel was successfully encapsulated in PLGA nanorods by the same technique. Our results not only enrich the ESE technique for preparing small sized poly (lactic-co-glycolic acid) nanorods, but also envision the potential application of nanorods for targeted cancer therapy with the delivery of paclitaxel.

KEYWORDS

non-spherical polymeric nanoparticle, rod shape, poly (lactic-co-glycolic) acid, emulsion solvent evaporation method, orthogonal experiment

1 Introduction

Over the past few decades, biodegradable polymeric particulate systems such as nano/micro spheres have been widely recommended for various drug delivery due to ease of fabrication, stability during storage and delivery, controlled drug release, improved therapeutic effects and fewer side effects (Birk et al., 2021; Jana et al., 2021). It is widely acknowledged that the physiochemical properties such as size, surface chemistry and material composition have important influences on their interaction with biological systems, eventually affecting their therapeutic effects (Yoo et al., 2011; Albanese et al., 2012) However, the effect of shape is usually ignored. Recently, researchers have found that the use of non-spherical drug delivery carriers can be an effective way to overcome certain limitations associated with spherical systems (Lomelí-Rosales et al., 2019). Drug carriers with different shapes can offer different properties in cellular interactions, vascular transport, biodistribution, and immune response (Champion et al., 2007b; Gratton et al., 2008; Barua et al., 2013; Thompson et al., 2013; Gong et al., 2014; Namdee et al., 2014; Safari et al., 2020; Kapate et al., 2021). Champion and Mitragotri (2006) have found that cells can determine whether or not phagocytose a nanoparticle through recognizing the surface shape of the nanoparticle at the initial contact. Meanwhile, non-spherical particles have increased margination (localization and adhesion) to the blood vessel wall in flow (Thompson et al., 2013; Lomelí-Rosales et al., 2019). Similarly, studies suggest that non-spherical particles such as nanorods (Zhou et al., 2013), nanoworms (Wang G. et al., 2014), and nanodisks (Muro et al., 2008) also exhibit longer blood-circulation time and improved tumor accumulation in comparison with their spherical counterpart. Collectively, shape of nanoparticles is increasingly considered as an important parameter in the design of drug delivery carriers due to its significant influence on biological process.

Seeing the aforementioned unique properties of non-spherical shapes, several different shape-engineering techniques have been developed for polymeric nanoparticles which include non-wetting templates, photolithography, microfluidic systems, template assemblies, and film stretching (Gratton et al., 2008; Wang W. et al., 2014; Mathaes et al., 2015; Kapate et al., 2021). Collectively, these methods have produced particles of several distinct shapes. Some of these methods provide advantages such as precise control over particle shape and complex shape preparation. However, they also suffer from drawbacks including complex process of preparation, requirement of special equipment, high cost, and difficult to scale up (Xu et al., 2005; Perry et al., 2011; Wang W. et al., 2014; Cao et al., 2019). Accordingly, lack of simple, versatile, inexpensive, and high-throughput methods for fabricating non-spherical polymeric particles remains a bottleneck in the fields of drug delivery system (Champion et al., 2007a). On the other hand, emulsion solvent evaporation (ESE) method has been considered as a simple, versatile, inexpensive and easy to scale up method to prepare polymeric particles (Heslinga et al., 2009; Rahman et al., 2010). But nanoparticles prepared by the emulsion solvent evaporation method are usually spherical shape due to the spontaneous minimization of interfacial energy for emulsion droplets. Fabrication of non-spherical polymeric nanoparticles by the ESE method remains to be a great challenge. Recently, some researchers have found that, by adding some small guest molecules such as sodium tripolyphosphate (STP), tris base or glycerol, the oil droplets of polymer can be deformed to non-spherical shape in ESE (Heslinga et al., 2009; Li et al., 2010). For example, Omolola Eniola-Adefeso's group has fabricated rod shaped poly (lactic-co-glycolic acid) (PLGA) microparticles by ESE method with the addition of guest molecule of tris base (Heslinga et al., 2009). Through modifying the fabrication method with two-step ESE method, rod-shaped PLGA submicron particles with minor axis down to 700 nm are successfully obtained (Safari et al., 2018). However, this size of nanoparticle is still too large when applied in tumor targeted therapy.

Previously, we also fabricated the non-spherical PLGA particles by the ESE method (Fan et al., 2016). A more commonly used inorganic salt, phosphate buffer saline (PBS) was adopted by us as the guest molecules. However, the rod-shaped particles were still in micro size range and the guest molecule PBS was mixed compounds, which made our system more complicated to optimize and hard to elucidate the underlying mechanism. Moreover, several formulation and process variables have great effects on the shape and size of the prepared particles. Researchers can identify the influence of parameters on particle deformation by changing one variable at a time, also defined as a single parameter optimizing method to obtain the optimal formula for rod-shaped nanoparticles. However, when associated with multiple variables, this single parameter method usually consumes a lot of time, money and effort and even fails. Meanwhile, the multi-factor and multi-level orthogonal experiment design is widely used to analyze the influence of multiple variables at the same time with decreased number of experiments (Mensah et al., 2019; Rafiei and Haddadi, 2019). Each variable can be assessed independently of all other variables so that it is more effective and economic than conventional experimental methods (Du et al., 2020).

Herein, we show that with the addition of the single guest molecule disodium hydrogen phosphate (Na_2HPO_4), the deformed PLGA particles can be obtained by ESE technique. By combining the ultrasonication method with two-step ESE technique, smaller PLGA nanorods with the minor axis down to 200 nm can be successfully prepared. Moreover, the influence of process parameters including ultrasonic power, Na_2HPO_4 concentration, surfactant concentrations, oil volume and PLGA concentration on the fabrication yield and aspect ratio of nanoparticles was comprehensively investigated by the orthogonal experiment method and the optimal combination

of factor levels was achieved (Mensah et al., 2019; Rafiei and Haddadi, 2019; Du et al., 2020). Finally, the anti-cancer drug paclitaxel was successfully encapsulated in PLGA nanorods by the same technique.

2 Materials and methods

2.1 Materials

PLGA copolymers with lactic: glycolic acid ratios of 75:25 (Molecular weight (MW): 17–20 kDa) were purchased Daigang Biological Engineering Co., Ltd., (Shandong, China). Paclitaxel (PTX, degree of purity ≥99%, BR) was procured from Dalian Meilun Biotechnology Co., Ltd., China. Dichloromethane was procured from Sichuan Fairbest Technology Co., Ltd., China. PBS was purchased from Solarbio Biological Technology Co., Ltd., China. Sodium Chloride (NaCl), Sodium Dihydrogen Phosphate Anhydrous (NaH_2PO_4) and Acetone were analytical reagent (AR) and purchased from Chengdu Kelong Chemical Co., Ltd., China. Acetonitrile (chromatographic grade) was purchased from Chengdu Kelong Chemical Co., Ltd., China. Disodium hydrogen phosphate (Na_2HPO_4) (AR) was purchased from Tianjin Zhiyuan Chemical Reagent Co., Ltd., China. Polyvinyl alcohol (PVA, PVA-217, degree of polymerization 1700) was purchased from Shanghai Yingjia Industrial Development Co., Ltd., China.

2.2 Methods

2.2.1 One-step preparation of PLGA micro-rods

Firstly, the conventional one-step emulsion solvent evaporation technique was used to develop PLGA non-spherical nanoparticles and the flow chart of one-step method is shown in Supplementary Figure S1A. Briefly, PLGA was dissolved into dichloromethane as the oil phase. Subsequently, the oil phase was added to the water phase which was consisted of a certain amount of PVA and guest molecules (PBS and other inorganic salts) under stirring. And the formed oil-in-water emulsion was stirred at 500 rpm for at least 4 h on a magnetic stirrer (RT 10, IKA, Germany) for particle solidification. Finally, the formed nanoparticles were observed under an inverted light microscope.

2.2.2 Two-step preparation of PLGA nanorods

In this experiment, the fabrication of biodegradable PLGA non-spherical nanoparticles was completed by a two-step method The flow chart of two-step method is shown in Supplementary Figure S1B. First of all, the PLGA oil phase was poured into PVA 1. Then, an O/W emulsion was made on an ultrasonic homogenizer (SONOPULS HD4100, BANDELIN, Germany) in an ice bath for 2 min (the first step for emulsion formation). Subsequently, the O/W emulsion was poured into PVA 2 which contained the guest molecules of Na_2HPO_4 for droplets stretching and deforming (the second step for emulsion deformation). The concentration of PVA 1 was lower than the concentration of PVA 2. And the emulsion was solidified with magnetic stirring at 500 rpm for at least 4 h at room temperature to allow for sufficient evaporation of the organic solvent. The resultant nanoparticles were collected and washed with distilled water for six times in a high-speed centrifuge (40,000 g, 10 min) (LYNX6000, Thermo Scientific, America) and subsequently stored at −20°C until further use. Scanning electron microscopy (SEM) (JEM -6700F, JEOL, Japan) was used to observe the size and morphology of PLGA nanorods. Specifically, fabricated nanoparticles were suspended in deionized water and naturally dried on a clean silver paper. Then, dried particles were sprayed with gold before SEM imaging.

2.3 Experimental design

2.3.1 The single-factor experiment

At the beginning of optimizing the two-step ESE process for nanorods, the single-factor experiment design was used to explore the influence of multi-factors including emulsification method, ultrasonic power, guest molecule concentration of causing particles deformation, PVA concentrations oil volume and PLGA concentration on the size and shape to determine the range of variables. The factors were selected based on the previous researches (Fan et al., 2016; Safari et al., 2018). Supplementary Table S1 lists the experimental scheme. The deformation of PLGA nanoparticles was observed by SEM.

2.3.2 The multi-factors and multi-levels orthogonal experiment

Based on the range of the single-factor experiment, a multi-factor multi-level orthogonal experiment was designed (Table 1). Six factors including ultrasonic power, Na_2HPO_4 concentration, PVA 1 concentration in the first aqueous phase, PVA 2 concentration in the second aqueous phase, oil volume and PLGA concentration were evaluated at three levels. When each of the six parameters was studied at three levels, the number of experiments required for full factorial design could reach 729 ($=3^6$), which was too large to be fulfilled in a limited time and at acceptable test expenses. In the multi-factor multi-level orthogonal experiment, however, the number for the six-factor three-level case could be significantly reduced to 18 according to an L_{18} (3^6) orthogonal table, which obviously alleviates the workload compared to 729 in the full factorial design schemes. Supplementary Table S2 lists 18 different combinations of factor levels based on the orthogonal arrangement principle with the help of the software "IBM SPSS Statistics." The formula was evaluated by the rod fabrication yield and the aspect ratio of major axis to minor axis. Major axis and minor axis of PLGA nanorods were

TABLE 1 Variables (factors) along with their corresponding levels in the orthogonal experiment design for fabrication of PLGA nanorods by two-step ESE method.

Parameters	Factors	Units	Levels		
			Low	Medium	High
A	Na_2HPO_4 conc[a]	mM	10	75	150
B	Ultrasonic power	W	40	80	120
C	Oil volume	ml	.5	1.0	1.5
D	PLGA conc[a]	mg/ml	10	20	40
E	PVA 1 conc[a]	wt%	.1	.5	1.0
F	PVA 2 conc[a]	wt%	1.0	2.0	3.0

[a]Conc, concentration.

measured by the software ImageJ (ImageJ, National Institutes of Health) under the images of SEM, and the number of nanorods measured was more than 50. Nanorods were defined as nanoparticles that had the aspect ratio greater than 2. So, the rod fabrication yield was defined as the percentage of nanoparticles with the aspect ratio greater than 2 in an individual experiment.

The effect of each factor on the aspect ratio and rod fabrication yield PLGA nanorods was evaluated based on K values and range analysis of *R* values, which were the reference standard values and equations for K and R of the orthogonal test were described as follows (Du et al., 2020):

$$K_i = S_i/S\,(i = 1,\ 2,\ 3) \tag{1}$$

$$R = \mathrm{Max}\{K_1, K_2, K_3\} - \mathrm{Min}\{K_1, K_2, K_3\} \tag{2}$$

where S_i indicated the sum of the test results corresponding to the *i*th level number (i = 1, 2, 3 in the six-factor three-level case) and S was the number of occurrences of each level in the orthogonal test (S = 6 according to Supplementary Table S2); The R value represented the difference between the maximum and minimum K value of the specific factor, reflecting the significance of the studied factor on the fabricated PLGA nanoparticles. Based on the K and *R* values, the effect and significance of each influential parameter on the aspect ratio and rod fabrication yield of PLGA nanoparticles could be obtained, and thereby the reasonable combinations of factor and level could be proposed to achieve the optimal nanorods with large aspect ratio and high yield.

2.4 Preparation and characterization of paclitaxel loaded PLGA nanorods

2.4.1 Preparation

Based on the optimized combination, paclitaxel was added into the oil phase to prepare paclitaxel loaded PLGA nanorods. The preparation methods were the same as Section 2.2.2.

2.4.2 Characterization

The size and morphology of the paclitaxel loaded PLGA nanoparticles were detected by SEM and the major axis, minor axis and the aspect ratio were detected and calculated from SEM images with ImageJ software. The drug loading efficiency (LE) and encapsulation efficiency (EE) of the paclitaxel in PLGA nanorods were evaluated through high-performance liquid chromatography (HPLC) detection (Le Broc-Ryckewaert et al., 2013). Briefly, 2 mg of the freeze-dried drug-loaded nanorods were dissolved in 1 ml of acetonitrile. The mixture was vortexed for 1 min, sonicated for 30 min, and filtered by organic filter head. The concentration of the paclitaxel was then quantified HPLC (Agilent, USA) with the following conditions: column: Kromasil 100-5-C18 (5 μm × 4.6 mm × 150 mm) chromatographic column; mobile phase: the ultrapure water and acetonitrile (40:60, V/V); flow rate: 1 ml/min; detection wavelength: 227 nm; column temperature: 30°C ± 1°C and injection volume: 20 μl.

Then, the drug loading efficiency and encapsulation efficiency of the preparation were calculated as follows:

$$\mathrm{LE}\,\% = \frac{\text{weight of PTX in particles}}{\text{weight of particles}} \times 100\% \tag{3}$$

$$\mathrm{EE}\,\% = \frac{\text{weight of PTX in particles}}{\text{initial weight of PTX added}} \times 100\% \tag{4}$$

3 Results and discussion

3.1 Screening of guest molecules

Our previous research had proved that PBS could be used as the guest molecule (also described as the deformation inducer) to induce the deformation of emulsion droplets and acquire rod-shaped microparticles (Fan et al., 2016). However, PBS was a mixed salt, containing NaH_2PO_4, Na_2HPO_4 and NaCl and there

was no systematic study on the main compound that cause deformation. Therefore, the amounts of Na_2HPO_4, NaH_2PO4 and NaCl contained in 5 mM PBS were added to the aqueous phase respectively to assess their capacity to induce deformation. As shown in Supplementary Figure S2, both PBS and Na_2HPO_4 could induce particle deformation, while the other components did not change the spherical morphology of particles. Therefore, it could be concluded that the Na_2HPO_4 was the main component in PBS that caused microparticle deformation. Compared with the previously used deformation inducer PBS which was a mixed compound, the inorganic compound Na_2HPO_4 was simple and pure and its concentration could be accurately adjusted, thereby benefited for optimizing the effect of its concentration on deformation and clarifying the mechanism. Therefore, in our present system, the formulation of non-spherical PLGA nanoparticles would be carefully and comprehensively optimized with Na_2HPO_4 as the guest molecule/deformation inducer.

3.2 Preparation and optimization of PLGA nanorods by single parameter method

Although rod-shaped PLGA particles could be prepared by one-step ESE method with the deformation inducer Na_2HPO_4, the size of deformed particles prepared was still large in the micron range. Microrods were not conducive to be used as the drug carriers for intravenous administration and might cause serious problems such as vascular embolism. On the other hand, a large number of studies had shown that nanoparticles with a size of <200 nm could be passively targeted to tumor tissue through the enhanced permeation and retention (EPR) effect (Duan and Li, 2013; Hoshyar et al., 2016). Therefore, further optimizing the formulation to obtain nanorods with a short diameter of about 200 nm was the key to solve the problems existing in intravenous injection and tumor targeted therapy.

Previously, the capillary number (Ca) and the viscosity ratio of the dispersed phase to continuous phase (M) were used in our research to explain the possibility and ease of deformation of the emulsion droplets in one-step ESE with the deformation inducer PBS (Fan et al., 2016). Capillary number, also known as interfacial tension number, was a dimensionless concept, which represented the ratio of fluid viscosity force to fluid interfacial tension and could be calculated as follows:

$$Ca = \gamma \eta_s \alpha / \Gamma \quad (5)$$

$$M = \eta_d / \eta_s \quad (6)$$

where γ was the shear rate, α was the initial droplet size, and Γ was the interfacial tension between the dispersed phase and continuous phase, η_d and η_s were the viscosity of the dispersed phase and continuous phase, respectively. In general, a high Ca value (high viscous forces or low interfacial tension) and/or a low M value result in emulsion conditions that favored droplet deformation. Intermediate values of the viscosity ratio ($M \approx 1$) at a fixed capillary number led to severe droplet breakup and high values of M result in no droplet deformation or breakup (Heslinga et al., 2009; Murphy et al., 2020). In order to obtain smaller rods, the size of the initial droplets needed to be very small, which meant a low α value. However, decreasing α would reduce the Ca value, which then made the deformation process difficult to occur. Therefore, in one-step ESE method, there was contradiction between the formation of smaller droplets and the deformation of droplets. Indeed, the rod-shaped particles fabricated in our previous research by the one-step ESE method were limited to a micron size range (Fan et al., 2016).

Surprising, the research group of Omolola Eniola-Adefeso modified the ESE and found that the contradiction between initial droplet size and droplet tensile deformation could be balanced by changing from one-step method to two-step method (Safari et al., 2018). In other words, by using two different PVA concentrations in the droplet formation step (PVA 1 concentration used) and stretching step (PVA 2 concentration used), a lower α and higher Ca/lower M could be simultaneously acquired because the deformation step was temporarily separated from the droplet formation step. After optimization, rod-shaped PLGA particles with the submicron size range were successfully prepared. However, because the emulsion was prepared with the overhead mixer like homogenization, the size of the rods was still large for tumor targeted therapy.

Based on the above analysis, the two-step ESE was adopted with Na_2HPO_4 as the deformation inducer to prepare smaller nanorods. A single-factor experimental design was used to investigate the effects of parameters including emulsification method, ultrasonic power, concentration of deformation inducer Na_2HPO_4, oil volume, PLGA concentration, and PVA concentration (PVA 1 concentration and PVA 2 concentration) on deformation for further orthogonal experimental optimization.

3.2.1 Effect of emulsification method

In the ESE, the non-spherical droplets were deformed from the spherical droplets. Therefore, the initial size of the droplet plays a decisive role in the size of the final rods. The smaller the initial particle size, the smaller the rods after stretching theoretically. At the same time, the initial droplet diameter also affected the Ca value. So, it was a key step to explore an appropriate emulsification method so that the droplets were in nano size range and could also effectively deformed. Therefore, we first investigated the influence of three emulsification methods, namely magnetic stirring method, homogenization method and ultrasonic method, on the size and shape of nanoparticles. As shown in Figure 1, the size of the non-spherical particles prepared by magnetic stirring method,

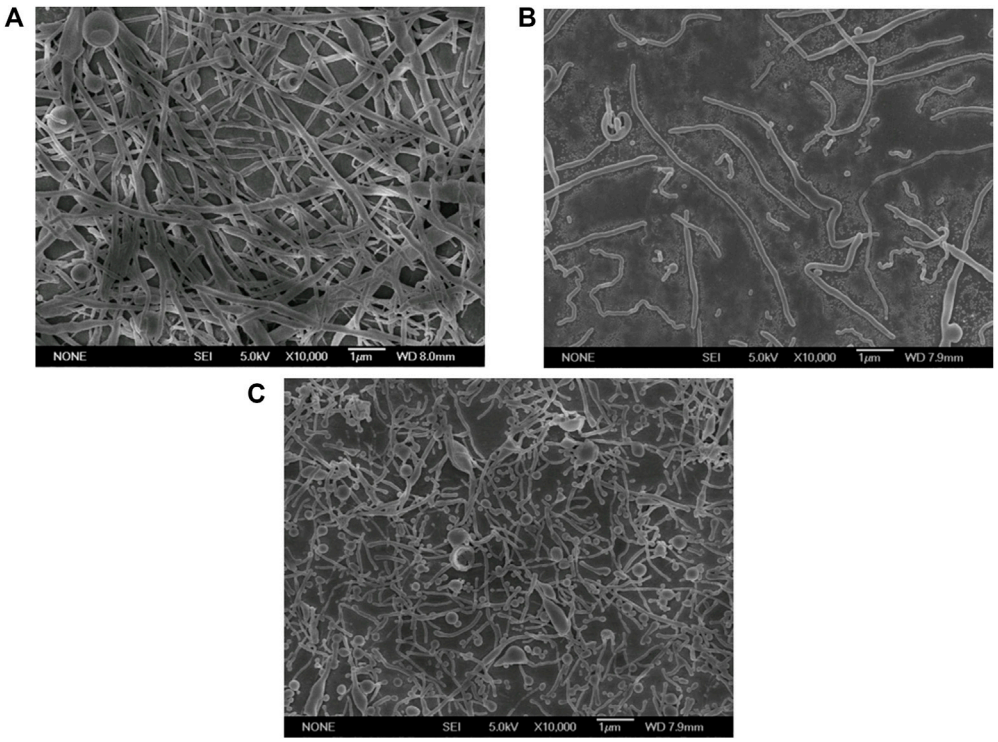

FIGURE 1
Electron micrographs of PLGA nanoparticles prepared by different emulsification methods (Scale bar: 1 μm). **(A)** Magnetic stirring; **(B)** Homogenization; **(C)** Ultrasonication.

homogenization method and ultrasonic method gradually decreased, which could be attributed to the reduced size of the initial emulsion fabricated by ultrasonic method (Supplementary Figure S3).

Therefore, further optimization by ultrasonic technique was expected to obtain ultra-small nanorods.

3.2.2 Effect of ultrasonic power

In this experiment, four ultrasonic powers were respectively set as 40, 80, 120, and 160 W. As shown in Figure 2, when the ultrasonic power was 40 and 80 W, many of the nanoparticles were deformed to short and small rods; Subsequently, when the ultrasonic power increased to 120 W, the nanoparticles deformed almost completely but were not uniform, with some long rods and short rods. However, when the ultrasonic power was further increased to 160 W, the nanoparticles prepared were irregular bulk particles. Theoretically, the initial droplet size decreased with ultrasound power increasing. Our results showed that, within a certain ultrasonic power range, the deformability and the size of the nanorods had no obvious difference; When the ultrasonic power increased to a certain value (160 W), larger bulk nanoparticles appeared after stretching and solidifying. This phenomenon could be explained by the capillary number. When the ultrasonic power was too large, the initial droplets were too small, so the capillary number decreased and the deformed nanoparticles also decreased. Besides that, nanoparticles prepared by high sonication power were not uniform and the droplets collided with each other during the stretching phase, so the small droplets converged into large droplets to form the irregular bulk particles.

3.2.3 Effect of Na_2HPO_4 concentration

As indicated in the one-step ESE results, disodium hydrogen phosphate is the key substance causing the deformation of nanoparticles. As a consequence, four concentrations of Na_2HPO_4, 50, 100, 150, and 200 mM, were experimentally examined for their effect on nanoparticle deformation. As shown in Figure 3, different concentrations of disodium hydrogen phosphate could cause different degrees of deformation of nanoparticles. In detail, when Na_2HPO_4 was 50 mM, there were many undeformed spherical nanoparticles in the SEM images. When the concentration of Na_2HPO_4 increased to 100 mM, most of the nanoparticles were deformed. The deformed nanoparticles were maximum in the concentration of 150 and 200 mM. So, it could be deduced that the deformation degree of the nanoparticles increased as the concentration of deformation inducer increased.

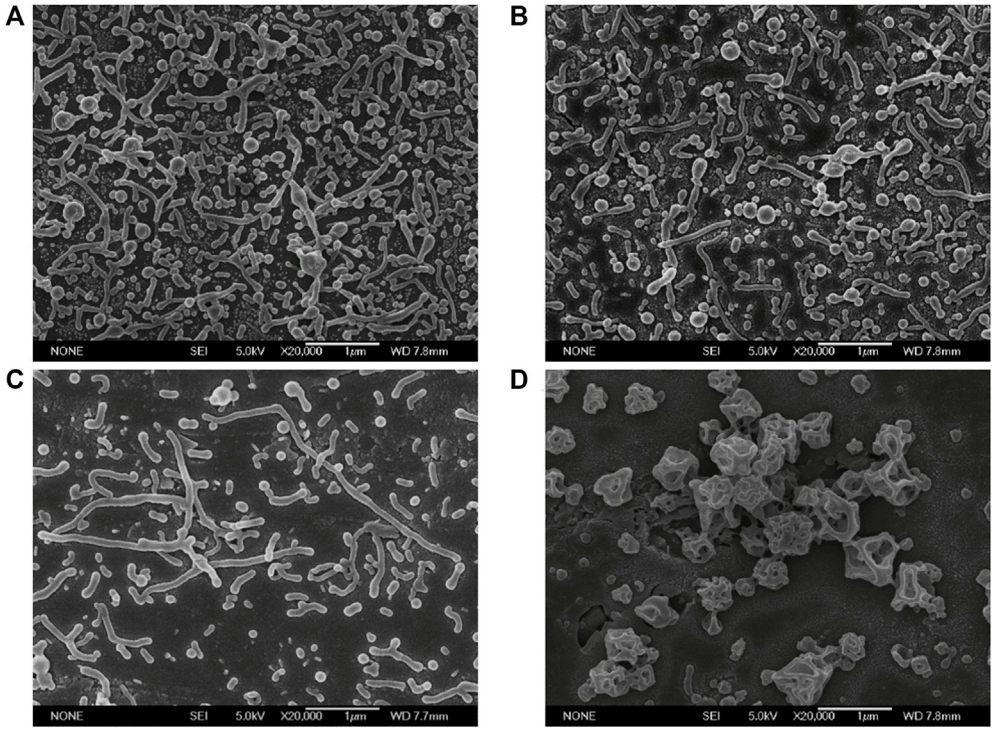

FIGURE 2
Electron micrographs of PLGA nanoparticles fabricated at different ultrasonic powers (Scale bar: 1 μm). **(A)** 40 W; **(B)** 80 W; **(C)** 120 W; **(D)** 160 W.

3.2.4 Effect of PLGA concentration

Three PLGA concentrations, namely 10, 20, and 40 mg/ml, were experimentally set up to explore the effect on PLGA nanoparticles. As shown in Figure 4, when the PLGA concentration was lower than 20 mg/ml, the nanoparticles were uniform with rod shape. When the PLGA concentration increased to 40 mg/ml, many nanoparticles were still in the similar thin and rod shape, but a few large nanorods occured. The PLGA concentration could affect the viscosity of the oil phase. The three concentration investigated were relatively lower than the normal concentration used for preparing nanospheres by ESE (Baghaei et al., 2015; Mensah et al., 2019), so the M value was relatively low and the droplets were all deformed into nanorods. However, under the same sonication power, higher viscosity of the oil phase would be harmful to the uniformity of the droplets, thereby some large nanorods were fabricated with 40 mg/ml. Comprehensively consider the relationship between PLGA concentration, particle size and amount of nanorods, PLGA concentration was chosen as 20 mg/ml for the subsequent investigation.

3.2.5 Effect of oil volume

The experiment investigated different oil phase volumes at the PLGA concentration of 20 mg/ml, which were .5, 1.0, and 1.5 ml, respectively. As shown in Figure 5, it seemed that the oil volume had no obvious effect on the particle size and deformation. Only a few near spherical particles occurred when the higher oil volume (1.0 and 1.5 ml) was used. The uniformity of initial droplet size was a key factor to determine the uniformity of nanorods. When the emulsification conditions (ultrasonic power) were the same, the initial droplets obtained with small volume of oil phase volume were relatively uniform. When the volume of the oil phase increased, the insufficient ultrasonic emulsification might lead to uneven initial droplets, and finally, the nanorods also deformed unevenly.

3.2.6 Effect of PVA concentration

As mentioned above in the beginning of Section 3.2, the contradiction between initial droplet size and droplet deformation can be balanced by changing from one-step method to two-step method. Therefore, there was two PVA concentrations in the two-step ESE method, which was thePVA 1 concentration for particle formation and the PVA 2 concentrationfor deforming and stretching.

First of all, The influence of three different levels (.1 wt%, .5 wt%, and 1.0 wt%) of the PVA 1concentration was explored on the deformation and yields of nanoparticles. As shown in Figure 6, there was no significant difference in the

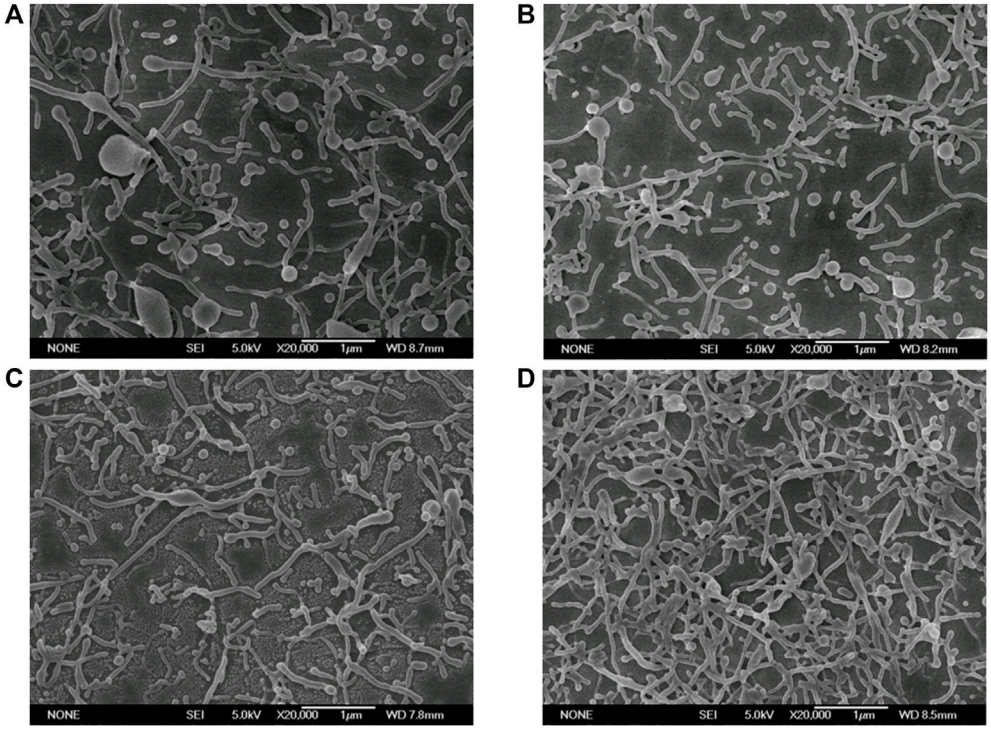

FIGURE 3
Electron micrographs of PLGA nanoparticles prepared with different concentrations of Na_2HPO_4. (Scale bar: 1 μm). **(A)** 50 mM; **(B)** 100 mM; **(C)** 150 mM; **(D)** 200 mM.

morphology among the nanoparticles fabricated by different concentration of the PVA 1. While, nanorods with the lowest PVA 1 concentration showed a little bit thinner minor axis than other groups. But many ultrasmall nanospheres could be found in this group. This phenomenon was probably due to the unstable droplets formed at this very low concentration of PVA 1 concentration. Some droplets could be broken up again during the emulsification and solidification. In consideration of the stability problem, the intermediate concentration of .5 wt% was used as the PVA 1 concentration in subsequent experiment.

Furthermore, the three different PVA 2 concentrations (1.0 wt%, 2.0 wt%, and 3.0 wt%) in the second step were investigated. As shown in Figure 7, nanoparticles prepared by different concentrations of PVA 2 showed little difference in the deformation ability. However, with the increase of the concentration of PVA, the size of minor axis was decreased, which could be attributed to the high Ca and low M values at high concentration of PVA 2 in the second step.

Overall, through the two-step ESE method and combined with Na_2HPO_4 as the deformation inducer and sonication as the emulsification technique, rod-shaped nanoparticles with the size in the nano range could be obtained. By using the single parameter optimization method, both the aspect ratio and the rod fabrication yield were increased. However, there were still some problems: 1) At the end of single factor optimization, there were still a few nanospheres fabricated with nanorods (Figure 7C), which could be due to that the single factor optimization could miss some important parameter and level combinations; 2) The significance of the studied parameters on the nanorods cannot be obtained through this single factor method. We cannot tell which parameter had the most powerful effect on the nanodroplets deformation; 3) It could be difficult to find the difference in size and shape between different levels through visual observation of the SEM images, thereby calling for the quantitative description. In order to solve these problem, the orthogonal experiment design combined with the quantitative measurement of the size and yield was adopted in following section to optimize the formulation of nanorods.

3.3 Optimization and preparation of PLGA nanorods by orthogonal test

Figure 8 displays the electron micrographs of PLGA nanoparticles prepared with 18 orthogonally arranged tests for the six-factor three-level case and Supplementary Tables S3, S4 demonstrate the important particle characteristics obtained from

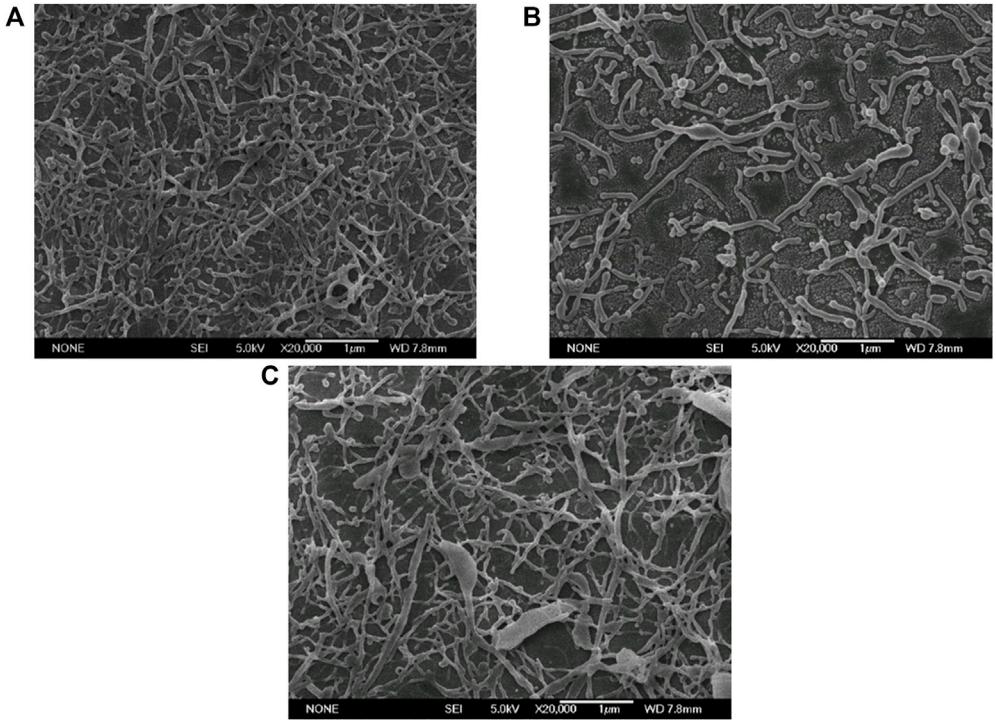

FIGURE 4
Electron micrographs of PLGA nanoparticles fabricated with different PLGA concentrations (Scale bar: 1 μm). **(A)** 10 mg/ml; **(B)** 20 mg/ml; **(C)** 40 mg/ml.

each run including the aspect ratio and the rod fabrication yield. Nanoparticles prepared at 18 different combinations of factors/levels demonstrated the aspect ratio between 1.14 ± .09 and 6.01 ± 2.29 (Supplementary Table S3) and the rod fabrication yield between 0% and 100% (Supplementary Table S4). And nanoparticle preparations resulted in a range of length between 67.8 ± 36.2 nm and 810.38 ± 321.88 nm (Supplementary Table S5), and width between 20.38 ± 9.64 nm and 286.50 ± 95.87 nm (Supplementary Table S6). The outcome of statistical analysis performed on each characteristic individually was also provided below.

The main effect plots for the aspect ratio versus different factor/level in Supplementary Table S3 shows that how aspect ratio was affected by factors at different levels. The difference between the maximum and minimum aspect ratio (*R* value) was highest in case of PVA 2 concentration (2.25), followed by PVA 1 concentration (1.66), Na_2HPO_4 concentration (1.50), PLGA concentration (1.27), oil volume (.19) and ultrasonic power (.06), which meant the PVA 2 concentration had the largest effect on aspect ratio, followed by PVA 1 concentration, Na_2HPO_4 concentration, PLGA concentration, oil volume and ultrasonic power.

Supplementary Table S4 demonstrates how the rod fabrication yield is changed with various factors/levels. PVA 2 concentration had the highest *R* value (40.00%) followed by Na_2HPO_4 concentration (32.33%), PVA 1 concentration (32.00%), PLGA concentration (29.67%), oil volume (15.67%), and ultrasonic power (11.33%). Accordingly, The three most important parameters affecting the rod fabrication yield were PVA 2 concentration, Na_2HPO_4 concentration and PVA 1 concentration, followed by oil volume, PLGA concentration and ultrasonic power. To gain insight into each factor's effect and thereby to propose an optimal parameter combination, more detailed analysis had been carried out in the following sections. Figure 9 demonstrates the main effect plot for the aspect ratio and the rod fabrication yield versus factor/levels.

3.3.1 Na_2HPO_4 concentration

As shown in Table 1, three levels of Na_2HPO_4 concentrations of 10, 75, and 150 mM were employed in the study. Figure 9A displays the K values of the aspect ratio and the rod fabrication yield on the left and right sidebar, respectively, corresponding to the three different levels of Na_2HPO_4 concentration. As can be clearly seen from the Figure 9A, with the increase of Na_2HPO_4 concentration, the aspect ratio and the rod fabrication yield increased; When the concentration exceeded 75 mM, they shown a slight downward trend. Thus, the Na_2HPO_4 concentration with 75 mM produced the best aspect ratio results, showing the best rod fabrication yield.

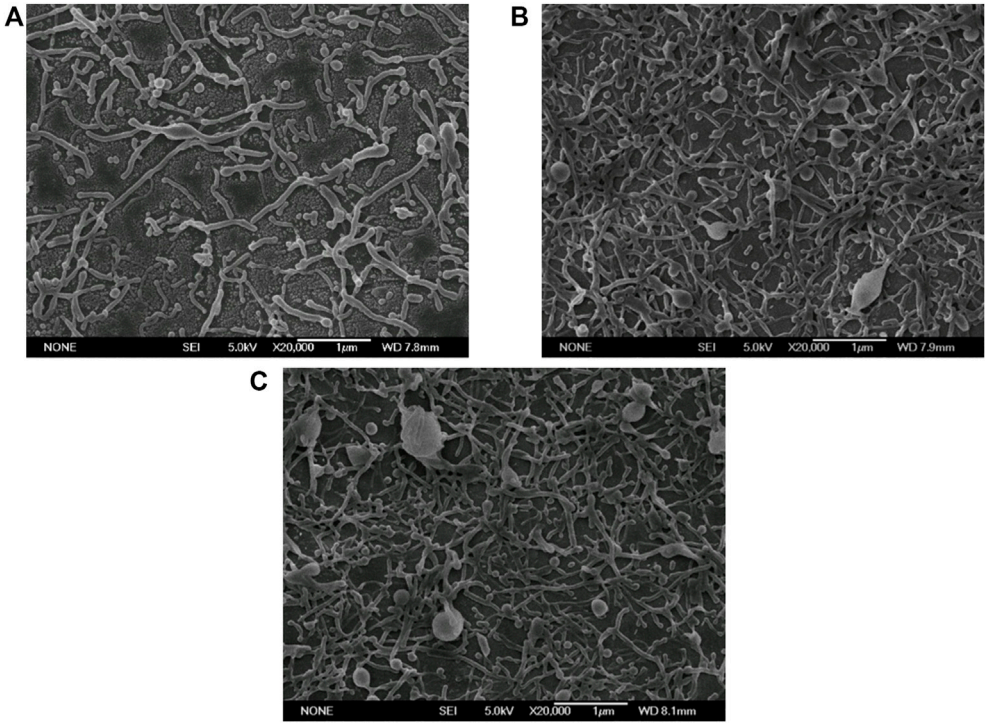

FIGURE 5
Electron micrographs of PLGA nanoparticles prepared at different oil phase volumes (Scale bar: 1 μm). **(A)** .5 ml; **(B)** 1.0 ml; **(C)** 1.5 ml.

It was speculated that the Na_2HPO_4 molecule was in favor of forming hydrogen bonds with the carboxyl groups of PLGA, which induced the deformation of emulsion and resulted in the fabrication of non-spherical polymeric nano/micro-architectures. Similar results could be found in Ruifeng Li's research team, who considered that the special chemical structure of STP might be in favor of inducing the formation of non-spherical polymeric micro-architectures and indicated that the hydrogen bonds formed between hydroxyl groups in PLGA and oxygen atoms in STP (Li et al., 2010). With the increase of Na_2HPO_4, the hydrogen bond interaction became strong so that the deformation was severe. Nevertheless, when the Na_2HPO_4 concentration exceeded 75 mM, the hydrogen bond interaction became saturation and then the competitive inhibition between molecules led to the decrease in the aspect ratio and nanorod fabrication yield.

3.3.2 Ultrasonic power

The effects of the ultrasonic power on the aspect ratio and the rod fabrication yield are displayed in Figure 9B. The K value of the aspect ratio was between 3.25 and 3.31 in all of the studied ultrasonic power range, indicating that the ultrasonic power had little effect on the aspect ratio. Similarly, the K value of rod fabrication yield was between 52.33% and 63.67%, demonstrating that the ultrasonic power also had little effect on the deformability capacity of nanoparticles.

As is well-known, the ultrasonic power could affect the size of the initial emulsion droplets. In general, the initial droplet size decreased with increasing ultrasound power, which could lead to a low Ca and then hinder deformation. However, there was no obvious difference between the results of the aspect ratio and the rod fabrication yield on the three levels, which was probably due to that the ultrasonic power of the three levels had little effect on the initial size of the droplets.

3.3.3 Oil voulme

Three levels of oil volume of .5, 1.0, and 1.5 ml had been employed in the tests, and their effects on the aspect ratio and rod fabrication yield were plotted in Figure 9C. It was observed that an oil volume of 1.0 ml produced the rod fabrication yield of 47.00%. The low and high oil volume produced the slightly higher yield of 62.67% and 62.33%, respectively. While, the aspect ratio was stable between 3.16 and 3.35 in the oil volume range of .5–1.5 ml.

This phenomenon could be explained by the balance between the interfacial tension and the initial droplet size. Due to the more hydrophobic nature of lactic acid (extra methyl side group) of PLGA, a higher interfacial tension often exist between the oil

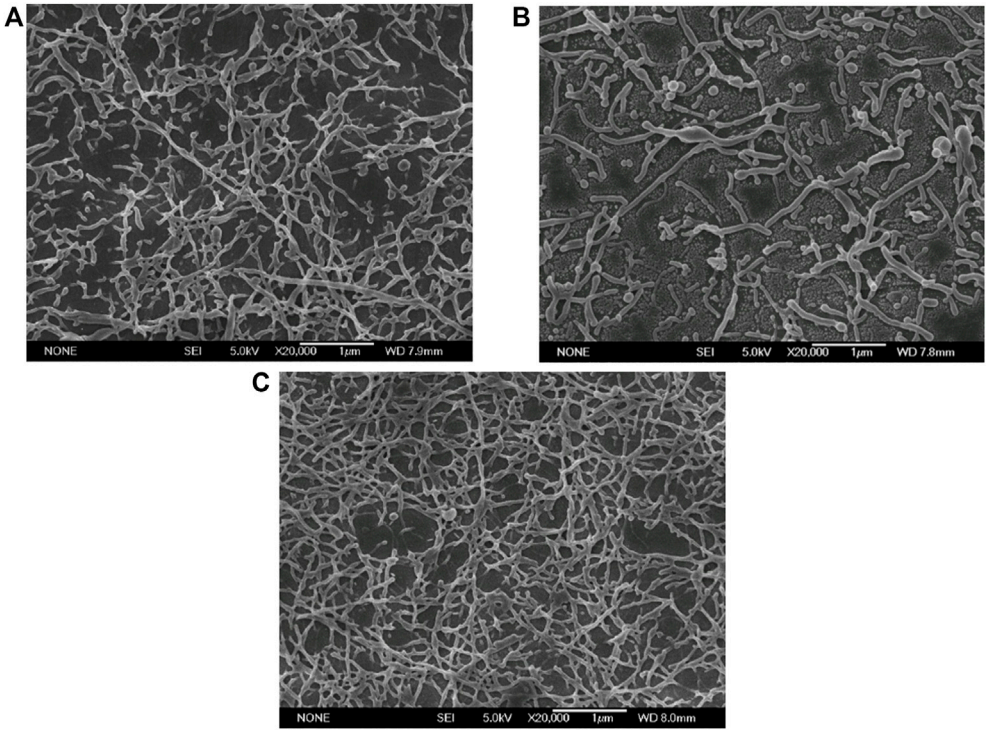

FIGURE 6
Electron micrographs of PLGA nanoparticles prepared with different PVA 1 concentrations (Scale bar: 1 μm).**(A)** .1 wt%; **(B)** .5 wt%; **(C)** 1.0 wt%.

droplet and the continuous phase (Panyam et al., 2004). Therefore, when the concentration of PLGA in oil phase was constant, the amount of PLGA would increase with the volume of the oil. Thus, the interfacial tension between the oil droplet and the continuous phase also increased and the Ca value decreased, which could hinder the deformation and made the rod yield decreased. However, further increasing the oil volume to 1.5 ml could result in large initial droplets due to insufficient shearing, which could overcome the higher interfacial tension produced by PLGA organic phase and increase the Ca value. Thus, rod fabrication yield decreased first and then increased with the increase of the oil volume.

3.3.4 PLGA concentration

Figure 9D displays obviously the effect of PLGA concentration on deformation. Increasing PLGA concentration corresponded to increase in the oil phase viscosity. The percentage of nanorods in the fabricated particles was 43%, 72.67%, and 56.33% for an oil phase with PLGA concentration of 10, 20, and 40 mg/ml, respectively. The corresponding average aspect ratios were 2.71, 3.98, and 3.15.

At a low PLGA concentration, droplets were easily broken up into small droplets, leading to a low α value and thereby decrease the Ca value to weaken deformation. So increasing the PLGA concentration could stabilize the droplets into a suitable size to increase Ca value and promote deformation. Nevertheless, further increasing the PLGA concentration to 40 mg/ml decreased the aspect ratio and rods yield, which could be explained by the increase in the viscosity ratio M to hinder the deformation.

3.3.5 PVA concentration

The two-step method was set up with two different PVA concentrations of aqueous phase. Small-sized droplets are formed at PVA 1 concentration in the first step, followed by a second step of increasing the viscosity of continuous phase to enable the stretching of small droplets into rod particles.

As is shown in Figure 9E, the effect of PVA concentration on aspect ratio and yield was studied for PVA 1 concentration of .1 wt%, .5 wt%, and 1.0 wt% in the first step and PVA 2 concentration of 1.0 wt%, 2.0 wt%, and 3.0 wt% in the second step. In the results of the PVA 1 concentration (first step), the aspect ratio of nanoparticles had a tendency to decrease first and then increase when PVA concentration was increased from .1 wt% to 1.0 wt%, which were respecctively 2.06, 3.47, and 4.31. And the rod fabrication yield had same trend as the aspect ratio, which were respectively 76.33%, 44.33%, and 51.33%.

According to the above results, the PVA 1 concentration in the first step was more favorable for the deformation. This was because the PVA 1 concentration could help produce large

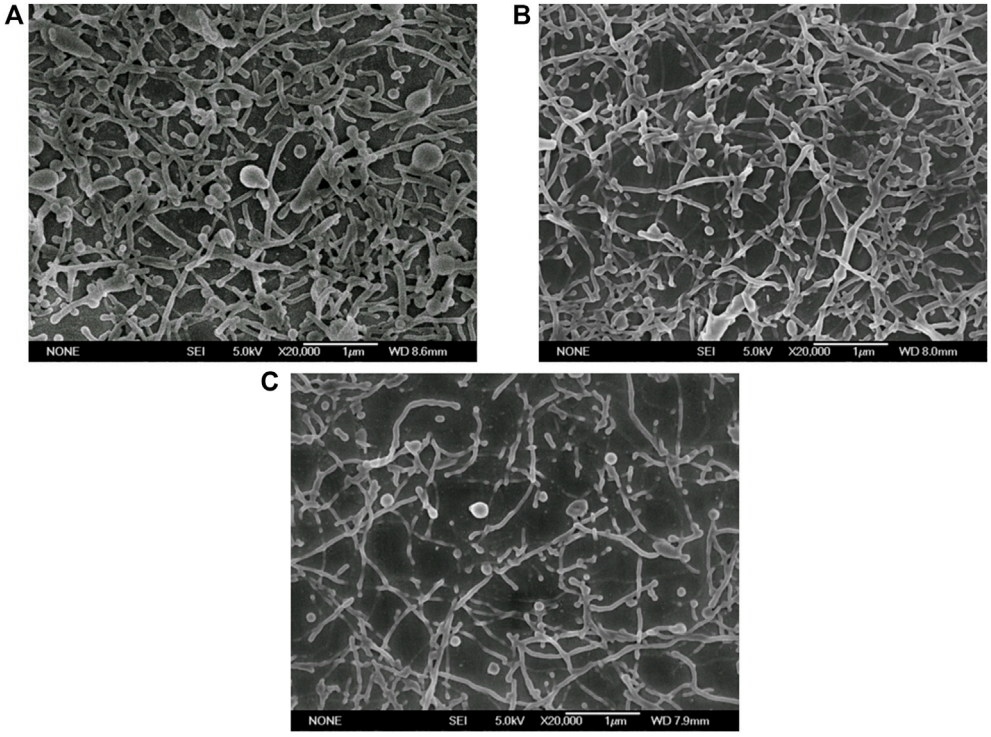

FIGURE 7
Electron micrographs of PLGA nanoparticles prepared with different high PVA concentrations (Scale bar: 1 μm) **(A)** 1.0 wt%; **(B)** 2.0 wt%; **(C)** 3.0 wt%.

droplets (high α value), which was beneficial to the high Ca and then the deformation. When the PVA concentration was from .5 wt% to 1.0 wt%, there was very slight increase in the aspect ratio and rods yield because the initial droplets size was reduced to its limit under sonication but the viscosity of the final continuous phase might increase modestly with the help of the increased PVA amount in the first step.

Furthermore, the more significant impact of PVA 2 concentration (second step) on the aspect ratio and the rod fabrication yieldcan be observed from Figure 9F, in which the K values of increased with the increase of PVA concentration. An increase in PVA concentration from 1.0 wt% to 3.0 wt% made the K values of the aspect ratio increase from 2.06 to 4.31, and the K values of the rod fabrication yield increased from 35.67% to 75.67%. It was not difficult to clarify the mechanism behind it. When the PVA 2 concentration in the second step was increased, the viscosity of aqueous phase increased, which produced a low M value and the particles were easily stretched into rod-shaped nanoparticles.

3.3.6 Optimal parameters based on the results of orthogonally designed experiments

Taken collectively the results above, we could propose the optimal combination of parameters to preparate nanorods with high aspect ratio and rods fabrication yield. Overall, fabrication conditions for an optimized PLGA nanorods formulation were determined in our system as:

Na_2HPO_4 concentration: 75 mM (Level 2)
Ultrasonic Power: 80 W (Level 2)
Oli Volume: .5 ml (Level 1)
PLGA Concentration: 20 ml (Level 2)
PVA 1 Concentration in the first step: .1 wt% (Level 1)/1.0 wt % (level 3)
PVA 2 Concentration in the second step: 3.0 wt% (Level 3)

The blank PLGA nanorods based on the above prescriptions were prepared. Morphologies and characteristics of nanoparticles are shown in Figures 10, 11. The optimized fabrication method prepared PLGA nanorods with major axis of 808.01 ± 442.11/657.77 ± 307.63 nm, minor axis of 151.72 ± 88.44/135.49 ± 72.66 nm, and aspect ratio of 5.93 ± 2.39/5.35 ± 2.05. The minor axis was down to 150 nm, which was significantly lower than the research of Omolola Safari et al. (2018), who had prepared the PLGA nanorods with the minor axis down to 700 nm. To the best of our knowledge, this was the first time to successfully prepare the PLGA nanorods in nano size range by the ESE method. Compared

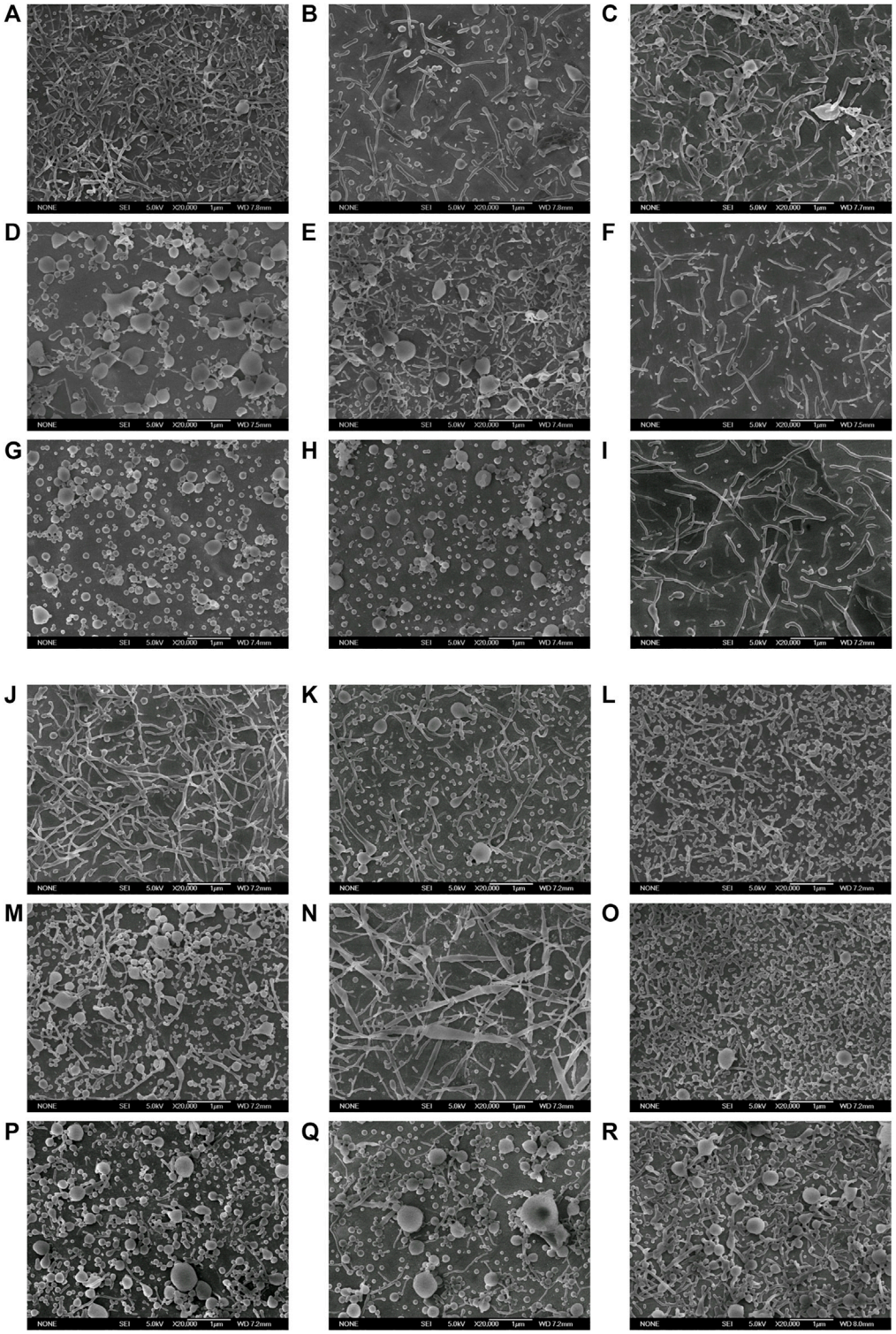

FIGURE 8
Electron micrographs of PLGA nanoparticles prepared with 18 orthogonally arranged tests for the six-factor three-level case (Scale bar: 1 μm). (A–R) represented prescriptions 1–18 in Supplementary Table S2 respectively.

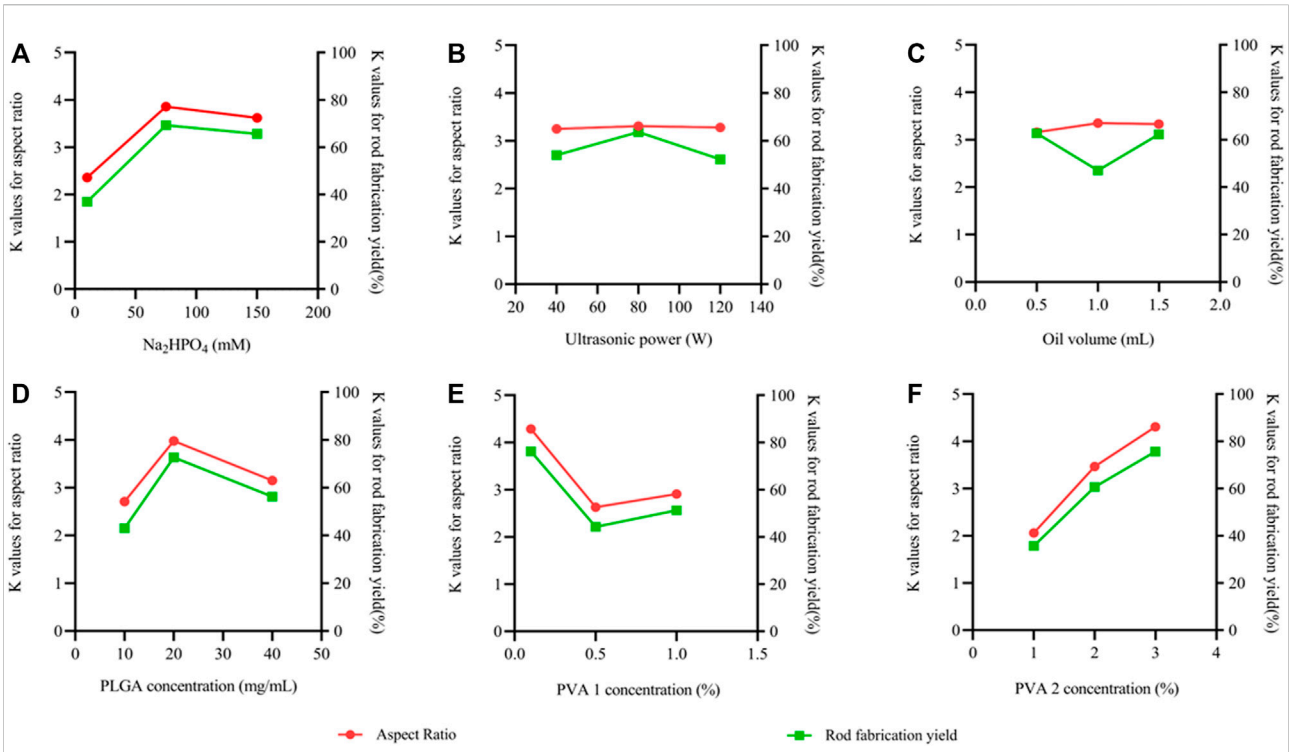

FIGURE 9
Main effect plots for the effects of the 6 parameters on the mean aspect ratio and the mean rod fabrication yield for the L18 orthogonally arranged design. The left vertical axis shows the mean aspect ratio, the right vertical axis shows the mean rod fabrication yield and the horizontal axis shows three levels (low, medium and high) of the parameters. **(A)** Na_2HPO_4 concentration, **(B)** Ultrasonic power, **(C)** Oil volume, **(D)** PLGA concentration, **(E)** PVA 1 concentration, **(F)** PVA 2 concentration.

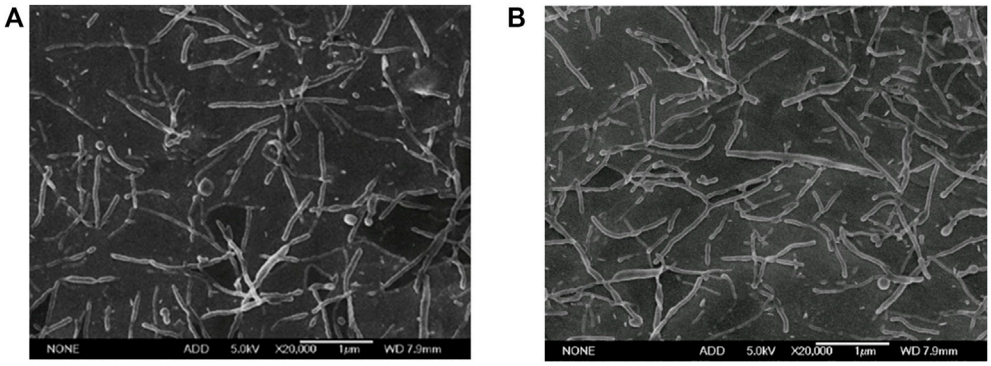

FIGURE 10
Electron micrographs of PLGA nanorods prepared with optimized formulation (Scale bar: 1 μm). **(A)** The PVA 1 concentration of .1 wt%; **(B)** the PVA 1 concentration of 1.0 wt%.

with other method for constructing polymeric nanorods such as the film stretching technique (Kapate et al., 2021), our modified ESE method was simple, cheap, easy to scale up and did not need special instruments and harsh conditions. Moreover, the ESE method had been widely used to encapsulate hydrophilic and hydrophobic drugs. So, the nanorods prepared by the modified ESE method might also have great potential in application in drug delivery system.

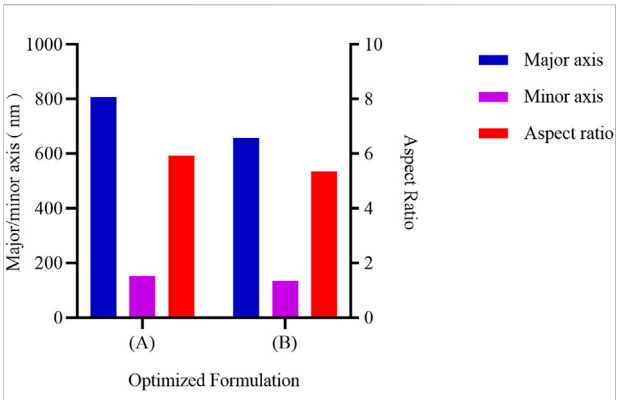

FIGURE 11
The size and aspect ratio of PLGA nanorods prepared with optimized formulation. The left vertical axis shows the mean major/minor axis, the right vertical axis shows the mean aspect ratio. **(A)** The PVA 1 concentration of .1 wt%; **(B)** The PVA 1 concentration of 1.0 wt%.

3.4 Preparation and characterization of the paclitaxel loaded PLGA nanorods

The anti-cancer drug paclitaxel was added in the oil phase as the model drug to investigate the feasibility of our method for preparing drug loaded nanorods. Three paclitaxel concentrations of 4%, 5%, and 6% (percentage of the weight of paclitaxel in the PLGA particles) were used respectively and the results are represented in Figure 12 and Table 2.

The results showed that the optimized fabrication method produced paclitaxel loaded PLGA nanorods with major axis of 809.74 ± 325.02, 993.48 ± 434.48, and 913.70 ± 279.66, with minor axis of 178.62 ± 56.57, 182.11 ± 65.94, and 204.26 ± 63.73 nm, and with aspect ratio of 4.75 ± 1.90, 5.60 ± 1.84, and 4.69 ± 1.39 at the PTX concentration of 4%, 5%, 6% (Table 2). The drug loading rate and encapsulation efficiency of paclitaxel loaded PLGA nanorods also showed an upward trend with the increase of the PTX concentration. The highest LE and EE investigated in the present study can achieve 4.26% and 71.03% (Table 2), demonstrating that our method could effectively encapsulte drugs without changing the size and shape of the nanorods. The minor axis of the paclitaxel loaded PLGA rods was down to 180 nm, which is smaller than 200 nm, indicating the potential application of nanorods for targeted cancer therapy. In our future research, the anti-cancer efficacy and the *in vivo* benefit of the prepared paclitaxel loaded nanorods will be thoroughly investigated.

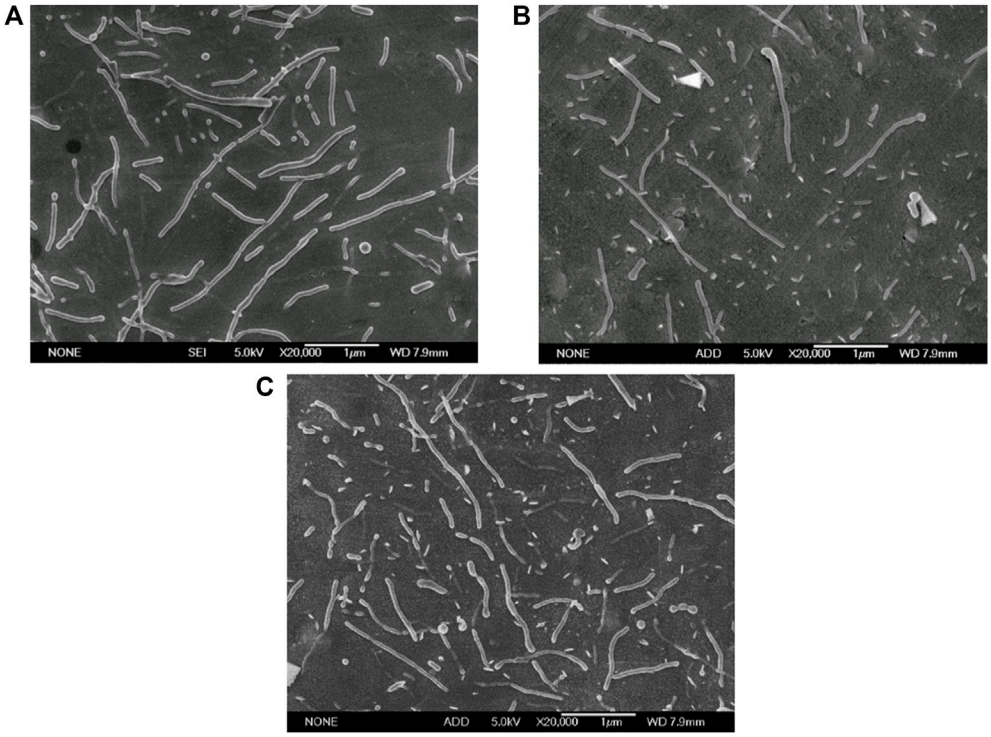

FIGURE 12
Electron micrographs of PTX loaded PLGA nanorods prepared with optimized formulation in different PTX concentrations (Scale bar: 1 μm). **(A)** 4% PTX; **(B)** 5% PTX; **(C)** 6% PTX.

TABLE 2 Characterization of the paclitaxel-loaded PLGA nanorods prepared with different PTX concentration.

PTX conc. (%)	Major axis		Minor axis		Aspect ratio		LE%	EE%
	Mean (nm)	SD	Mean (nm)	SD	Mean	SD		
4	809.74	325.02	178.62	56.57	4.75	1.90	1.78	44.43
5	993.48	434.48	182.11	65.94	5.60	1.84	2.55	51.04
6	913.70	279.66	204.26	63.73	4.69	1.39	4.26	71.03

[a]Conc, concentration.

4 Conclusion

Non-spherical geometries were increasingly considered as an important factor in the design of drug delivery carriers. Here, the rod-shaped PLGA particles in the nano size range were successfully prepared using the two-step emulsion-solvent evaporation (ESE) method combined with the guest molecule Na_2HPO_4 and sonication technique. It was shown that the size, shape and aspect ratio of these non-spherical nanoparticles could be controlled by careful manipulation of key process parameters. The orthogonal experimental design could help investigate the influence of parameters on the aspect ratio and rod fabrication yield and find the optimal formulation. The data showed that surfactant PVA concentration in the second step was the most important influential factor and the high concentration of PVA 2 was beneficial to the deformation. Detailed mechanism under the deformation was also discussed thoroughly. Finally, paclitaxel was successfully encapsulated into the nanorods. Overall, the modified ESE method for fabricating nanorods had advantages of simplicity in setup, small size in nano range, high nanorod yield and adaptability to different biodegradable polymers and therapeutics. In summary, our results not only enrich the ESE technique for preparing rod-shaped PLGA particles in nano size range, but also envision the potential application of nanorods for targeted cancer therapy with the delivery of paclitaxel.

Data availability statement

The original contributions presented in the study are included in the article/Supplementary Material, further inquiries can be directed to the corresponding authors.

Author contributions

MX, ZL, and YL contributed equally to this work. QF and SG conceived and designed the experiments. MX, ZL, and YL completed the experiment. HH, TC, and YW analyzed the data. MX and ZL wrote the original manuscripts. ML, SJ, XP, and LY revised the manuscript. QF, MZ, SW, and SW oversaw the completion of this study and edited the manuscript. QF provided resources and funding support. All authors reviewed and approved the final version of the manuscript.

Funding

This study was supported by The Science and Technology Planning Project of Sichuan Province, China (No. 2022NSFSC1429), The National Natural Science Foundation of China (No. 22208269), The Joint Project between Luzhou Municipal People's Government and Southwest Medical University (No. 2021LZXNYD-J17), Foundation of Southwest Medical University (No. 2021ZKZD012).

Conflict of interest

The authors declare that the research was conducted in the absence of any commercial or financial relationships that could be construed as a potential conflict of interest.

Publisher's note

Supplementary material

The Supplementary Material for this article can be found online at: https://www.frontiersin.org/articles/10.3389/fbioe.2022.1103990/full#supplementary-material

References

Albanese, A., Tang, P. S., and Chan, W. C. (2012). The effect of nanoparticle size, shape, and surface chemistry on biological systems. *Annu. Rev. Biomed. Eng.* 14, 1–16. doi:10.1146/annurev-bioeng-071811-150124

Baghaei, B., Jafari, S. H., Khonakdar, H. A., Saeb, M. R., Wagenknecht, U., and Heinrich, G. (2015). A multioptimization approach to assessment of drug delivery of PLGA nanoparticles: Simultaneous control of particle size and release behavior. *Int. J. Polym. Mater. Polym. Biomaterials* 64 (12), 641–652. doi:10.1080/00914037.2014.996714

Barua, S., Yoo, J. W., Kolhar, P., Wakankar, A., Gokarn, Y. R., and Mitragotri, S. (2013). Particle shape enhances specificity of antibody-displaying nanoparticles. *Proc. Natl. Acad. Sci. U. S. A.* 110 (9), 3270–3275. doi:10.1073/pnas.1216893110

Birk, S. E., Boisen, A., and Nielsen, L. H. (2021). Polymeric nano- and microparticulate drug delivery systems for treatment of biofilms. *Adv. Drug Deliv. Rev.* 174, 30–52. doi:10.1016/j.addr.2021.04.005

Cao, J., Choi, J. S., Oshi, M. A., Lee, J., Hasan, N., Kim, J., et al. (2019). Development of PLGA micro- and nanorods with high capacity of surface ligand conjugation for enhanced targeted delivery. *Asian J. Pharm. Sci.* 14 (1), 86–94. doi:10.1016/j.ajps.2018.08.008

Champion, J. A., and Mitragotri, S. (2006). Role of target geometry in phagocytosis. *Proc. Natl. Acad. Sci. U. S. A.* 103 (13), 4930–4934. doi:10.1073/pnas.0600997103

Champion, J. A., Katare, Y. K., and Mitragotri, S. (2007a). Making polymeric micro- and nanoparticles of complex shapes. *Proc. Natl. Acad. Sci. U. S. A.* 104 (29), 11901–11904. doi:10.1073/pnas.0705326104

Champion, J. A., Katare, Y. K., and Mitragotri, S. (2007b). Particle shape: A new design parameter for micro- and nanoscale drug delivery carriers. *J. Control. Release* 121 (1-2), 3–9. doi:10.1016/j.jconrel.2007.03.022

Du, D., Zhang, X., Yu, K., Song, X., Shen, Y., Li, Y., et al. (2020). Parameter screening study for optimizing the static properties of nanoparticle-stabilized CO(2) foam based on orthogonal experimental design. *ACS Omega* 5 (8), 4014–4023. doi:10.1021/acsomega.9b03543

Duan, X., and Li, Y. (2013). Physicochemical characteristics of nanoparticles affect circulation, biodistribution, cellular internalization, and trafficking. *Small* 9 (9-10), 1521–1532. doi:10.1002/smll.201201390

Fan, Q., Qi, F., Miao, C., Yue, H., Gong, F., Wu, J., et al. (2016). Direct and controllable preparation of uniform PLGA particles with various shapes and surface morphologies. *Colloids Surfaces A Physicochem. Eng. Aspects* 500, 177–185. doi:10.1016/j.colsurfa.2016.04.028

Gong, T., Zhao, K., Wang, W., Chen, H., Wang, L., and Zhou, S. (2014). Thermally activated reversible shape switch of polymer particles. *J. Mater. Chem. B* 2 (39), 6855–6866. doi:10.1039/c4tb01155d

Gratton, S. E., Ropp, P. A., Pohlhaus, P. D., Luft, J. C., Madden, V. J., Napier, M. E., et al. (2008). The effect of particle design on cellular internalization pathways. *Proc. Natl. Acad. Sci. U. S. A.* 105 (33), 11613–11618. doi:10.1073/pnas.0801763105

Heslinga, M. J., Mastria, E. M., and Eniola-Adefeso, O. (2009). Fabrication of biodegradable spheroidal microparticles for drug delivery applications. *J. Control. Release* 138 (3), 235–242. doi:10.1016/j.jconrel.2009.05.020

Hoshyar, N., Gray, S., Han, H., and Bao, G. (2016). The effect of nanoparticle size on *in vivo* pharmacokinetics and cellular interaction. *Nanomedicine (Lond)* 11 (6), 673–692. doi:10.2217/nnm.16.5

Jana, P., Shyam, M., Singh, S., Jayaprakash, V., and Dev, A. (2021). Biodegradable polymers in drug delivery and oral vaccination. *Eur. Polym. J.* 142, 110155. doi:10.1016/j.eurpolymj.2020.110155

Kapate, N., Clegg, J. R., and Mitragotri, S. (2021). Non-spherical micro- and nanoparticles for drug delivery: Progress over 15 years. *Adv. Drug Deliv. Rev.* 177, 113807. doi:10.1016/j.addr.2021.05.017

Le Broc-Ryckewaert, D., Carpentier, R., Lipka, E., Daher, S., Vaccher, C., Betbeder, D., et al. (2013). Development of innovative paclitaxel-loaded small PLGA nanoparticles: Study of their antiproliferative activity and their molecular interactions on prostatic cancer cells. *Int. J. Pharm. X.* 454 (2), 712–719. doi:10.1016/j.ijpharm.2013.05.018

Li, R., Li, X., Liu, L., Zhou, Z., Tang, H., and Zhang, Q. (2010). High-yield fabrication of PLGA non-spherical microarchitectures by emulsion solvent evaporation method. *Macromol. Rapid Commun.* 31 (22), 1981–1986. doi:10.1002/marc.201000332

Lomelí-Rosales, D. A., Zamudio-Ojeda, A., Cortes-Llamas, S. A., and Velázquez-Juárez, G. (2019). One-step synthesis of gold and silver non-spherical nanoparticles mediated by Eosin Methylene Blue agar. *Sci. Rep.* 9 (1), 19327. doi:10.1038/s41598-019-55744-0

Mathaes, R., Winter, G., Besheer, A., and Engert, J. (2015). Non-spherical micro- and nanoparticles: fabrication, characterization and drug delivery applications. *Expert Opin. Drug Deliv.* 12 (3), 481–492. doi:10.1517/17425247.2015.963055

Mensah, R. A., Kirton, S. B., Cook, M. T., Styliari, I. D., Hutter, V., and Chau, D. Y. S. (2019). Optimising poly(lactic-co-glycolic acid) microparticle fabrication using a Taguchi orthogonal array design-of-experiment approach. *PLoS One* 14 (9), e0222858. doi:10.1371/journal.pone.0222858

Muro, S., Garnacho, C., Champion, J. A., Leferovich, J., Gajewski, C., Schuchman, E. H., et al. (2008). Control of endothelial targeting and intracellular delivery of therapeutic enzymes by modulating the size and shape of ICAM-1-targeted carriers. *Mol. Ther.* 16 (8), 1450–1458. doi:10.1038/mt.2008.127

Murphy, R. P., Riedel, Z. W., Nakatani, M. A., Salipante, P. F., Weston, J. S., Hudson, S. D., et al. (2020). Capillary RheoSANS: measuring the rheology and nanostructure of complex fluids at high shear rates. *Soft Matter* 16 (27), 6285–6293. doi:10.1039/d0sm00941e

Namdee, K., Thompson, A. J., Golinski, A., Mocherla, S., Bouis, D., and Eniola-Adefeso, O. (2014). *In vivo* evaluation of vascular-targeted spheroidal microparticles for imaging and drug delivery application in atherosclerosis. *Atherosclerosis* 237 (1), 279–286. doi:10.1016/j.atherosclerosis.2014.09.025

Panyam, J., Williams, D., Dash, A., Leslie-Pelecky, D., and Labhasetwar, V. (2004). Solid-state solubility influences encapsulation and release of hydrophobic drugs from PLGA/PLA nanoparticles. *J. Pharm. Sci.* 93 (7), 1804–1814. doi:10.1002/jps.20094

Perry, J. L., Herlihy, K. P., Napier, M. E., and Desimone, J. M. (2011). PRINT: A novel platform toward shape and size specific nanoparticle theranostics. *Acc. Chem. Res.* 44 (10), 990–998. doi:10.1021/ar2000315

Rafiei, P., and Haddadi, A. (2019). A robust systematic design: Optimization and preparation of polymeric nanoparticles of PLGA for docetaxel intravenous delivery. *Mater. Sci. Eng. C* 104, 109950. doi:10.1016/j.msec.2019.109950

Rahman, Z., Zidan, A. S., Habib, M. J., and Khan, M. A. (2010). Understanding the quality of protein loaded PLGA nanoparticles variability by Plackett-Burman design. *Int. J. Pharm. X.* 389 (1-2), 186–194. doi:10.1016/j.ijpharm.2009.12.040

Safari, H., Adili, R., Holinstat, M., and Eniola-Adefeso, O. (2018). Modified two-step emulsion solvent evaporation technique for fabricating biodegradable rod-shaped particles in the submicron size range. *J. Colloid Interface Sci.* 518, 174–183. doi:10.1016/j.jcis.2018.02.030

Safari, H., Kelley, W. J., Saito, E., Kaczorowski, N., Carethers, L., Shea, L. D., et al. (2020). Neutrophils preferentially phagocytose elongated particles-An opportunity for selective targeting in acute inflammatory diseases. *Sci. Adv.* 6 (24), eaba1474. doi:10.1126/sciadv.aba1474

Thompson, A. J., Mastria, E. M., and Eniola-Adefeso, O. (2013). The margination propensity of ellipsoidal micro/nanoparticles to the endothelium in human blood flow. *Biomaterials* 34 (23), 5863–5871. doi:10.1016/j.biomaterials.2013.04.011

Wang, G., Inturi, S., Serkova, N. J., Merkulov, S., McCrae, K., Russek, S. E., et al. (2014a). High-relaxivity superparamagnetic iron oxide nanoworms with decreased immune recognition and long-circulating properties. *ACS Nano* 8 (12), 12437–12449. doi:10.1021/nn505126b

Wang, W., Zhang, M. J., and Chu, L. Y. (2014b). Functional polymeric microparticles engineered from controllable microfluidic emulsions. *Acc. Chem. Res.* 47 (2), 373–384. doi:10.1021/ar4001263

Xu, S., Nie, Z., Seo, M., Lewis, P., Kumacheva, E., Stone, H. A., et al. (2005). Generation of monodisperse particles by using microfluidics: control over size, shape, and composition. *Angew. Chem. Int. Ed.* 44 (5), 724–728. doi:10.1002/anie.200462226

Yoo, J. W., Irvine, D. J., Discher, D. E., and Mitragotri, S. (2011). Bio-inspired, bioengineered and biomimetic drug delivery carriers. *Nat. Rev. Drug Discov.* 10 (7), 521–535. doi:10.1038/nrd3499

Zhou, Z., Ma, X., Jin, E., Tang, J., Sui, M., and Shen, Y. (2013). Linear-dendritic drug conjugates forming long-circulating nanorods for cancer-drug delivery. *Biomaterials* 34, 5722–5735. doi:10.1016/j.biomaterials.2013.04.012

frontiers | Frontiers in Bioengineering and Biotechnology

TYPE Mini Review
PUBLISHED 19 January 2023
DOI 10.3389/fbioe.2023.1101673

OPEN ACCESS

EDITED BY
Zhen Liu,
Beijing University of Chemical Technology, China

REVIEWED BY
Chunxia Li,
Shandong University, China
Qiong Huang,
Xiangya Hospital, Central South University, China

*CORRESPONDENCE
Jianhua Liu,
jian_hua@jlu.edu.cn
Nannan Xu,
nnxu@jlu.edu.cn

SPECIALTY SECTION
This article was submitted to Nanobiotechnology, a section of the journal Frontiers in Bioengineering and Biotechnology

RECEIVED 18 November 2022
ACCEPTED 02 January 2023
PUBLISHED 19 January 2023

CITATION
Cui F, Liu J, Zhang T, Pang S, Yu H and Xu N (2023), Low-dimensional nanomaterials as an emerging platform for cancer diagnosis and therapy.
Front. Bioeng. Biotechnol. 11:1101673.
doi: 10.3389/fbioe.2023.1101673

Low-dimensional nanomaterials as an emerging platform for cancer diagnosis and therapy

Fengzhi Cui, Jianhua Liu*, Tianqi Zhang, Siwen Pang, Haijia Yu and Nannan Xu*

Department of Radiology, The Second Hospital of Jilin University, Changchun, China

The burden of cancer is increasing, being widely recognized as one of the main reasons for deaths among humans. Despite the tremendous efforts that have been made worldwide to stem the progression and metastasis of cancer, morbidity and mortality in malignant tumors have been clearly rising and threatening human health. In recent years, nanomedicine has come to occupy an increasingly important position in precision oncotherapy, which improves the diagnosis, treatment, and long-term prognosis of cancer. In particular, LDNs with distinctive physicochemical capabilities have provided great potential for advanced biomedical applications, attributed to their large surface area, abundant surface binding sites, and good cellular permeation properties. In addition, LDNs can integrate CT/MR/US/PAI and PTT/PDT/CDT/NDDS into a multimodal theranostic nanoplatform, enabling targeted therapy and efficacy assessments for cancer. This review attempts to concisely summarize the classification and major properties of LDNs. Simultaneously, we particularly emphasize their applications in the imaging, diagnosis, and treatment of cancerous diseases.

KEYWORDS

0D nanomaterials, 1D nanomaterials, 2D nanomaterials, imaging, cancer therapy

1 Introduction

Cancer has been having a significant impact on public health concerns and it is emerging globally, being widely recognized as one of the main reasons for deaths among humans. Approximately 1,918,030 new cancer cases and 609,360 deaths cases were reported according to cancer statistics in 2022 and, despite global efforts, the incidence and mortality rates have been universally estimated to be increasing in recent years (Mullard, 2020; Siegel et al., 2022). Traditional anti-cancer treatment approaches are in use for cancer therapy today, usually composed of four categories, namely, surgical resection (Akinoso-Imran et al., 2022), radiotherapy (Duemer, 2016), chemotherapy (Godishala et al., 2018), and immunotherapy (Bergman, 2019), which have achieved a certain degree of success in relation to inhibiting cancer cells' proliferation and lengthening patients' survival periods. Due to the complexity, diversity, and heterogeneity in tumor cells, combined with the long treatment cycle, obvious side effects, high recurrence rate, and multidrug resistance (MDR) in tumor treatment (Pe'er et al., 2021; Zhang et al., 2022), traditional therapeutic methods are not obviously effective, with high rates of recurrence and metastasis (Peitzsch et al., 2017) that do not lead to a relatively favorable survival prognosis. Therefore, finding effective anti-cancer approaches for accurate diagnosis and treatment has extremely important application prospects.

Alongside the rapid progress of advanced nanotechnology, there exist many works applying nanomaterials in a wide variety of industries, leading to great advantages in particular for biomedical applications. LDNs have gained intense interest and attention for a variety of

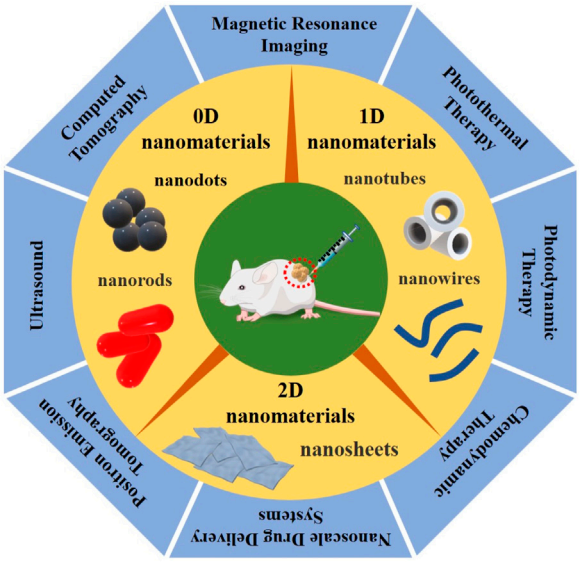

FIGURE 1
Graphical summarization of the three types of LDNs, according to dimensional and structure characteristics, divided into 0D nanomaterials (such as quantum dots and nanorods), 1D nanomaterials (such as nanowires and nanotubes), and 2D nanomaterials (such as nanosheets), combined with the novel therapeutic methods and imaging techniques, including PTT/PDT/CDT/NDDS and MRI/US/PAI/CT/PET, which have great promise for imaging-guided non-invasive cancer therapy.

biomedical applications owing to their unique physicochemical characteristics, such as the large surface area, abundant surface binding sites, and good cellular permeation properties. Compared to conventional 3D nanomaterials, LDNs can be easily realized for effective drug-loading, exclusive surface modification, and functionalization, as well as targeted drug delivery, which provides valuable advanced multi-diagnostic approaches for efficient and precise tumor-targeted therapy (Gao et al., 2017; Zhou et al., 2022).

LDNs combined with novel therapeutic methods, including PTT (photothermal therapy), PDT (photodynamic therapy), CDT (chemodynamic therapy), and NDDS (nanoscale drug delivery systems), have been shown to have great potential for non-invasive tumor therapy, which decreases the severity of surrounding normal histiocytic destruction. Tracking the biodistribution of nanoparticles in living tissues can be imaged with magnetic resonance (MR), ultrasound (US), photoacoustic (PA), computed tomography (CT), positron emission tomography (PET), and single-photon emission computed tomography (SPECT). Simultaneously, medical imaging modalities can also monitor the treatment procedure in real-time and detect the LDNs accumulating at the tumor site, achieving precise tumor localization and assessing the therapeutic effects, as seen in Figure 1. Thus, LDNs combined with novel therapeutic methods and imaging techniques have given birth to "nanomedicine." Nanomedicine, as an emerging and rapidly expanding field, has become the most important field of medical research, constantly promoting medical advances (Kim, 2019; Yang et al., 2019; Lammers and Ferrari, 2020). Compared with traditional treatment methods, nanomedicine has significantly reduced tumor recurrence and metastasis, showing many advantages and great prospects concerning the optimization of therapeutic efficiency.

In this review article, we present a brief account of the classification and major properties of LDNs. In addition, we particularly emphasize their applications in the diagnosis and treatment of cancerous diseases.

2 Novel therapeutic methods for cancer

Unfortunately, eradicating tumors *via* monotherapy has been limited by its inherent defect, which is the lack of feasibility. An increasing number of recent studies have discovered that combination therapy can significantly improve patients' symptoms and quality of life, which suggests a new therapeutic approach for cancer. In combination therapy, monotherapy can compensate for some disadvantages of other therapies. Therefore, the synergistic effect may not only improve the prognosis but also enhance the therapeutic effect of monotherapy. Currently, combined therapy is a clinical treatment recommended for its efficiency, and many potentially lucrative forms of combination therapy are being discovered.

2.1 Photothermal therapy for cancer

In addition to having limited side effects and being a high-efficiency cancer treatment, photothermal therapy (PTT) has the advantage of minimizing the risk of damage to normal tissues (Doughty et al., 2019). Photothermal agents (PTA) are the principal element in photothermal absorption, which plays an important role in PTT (Hwang and Jung, 2021). The basic principle of PTT is to use PTA to generate enough heat under the irradiation of near-infrared (NIR) and other external light sources to destroy and eliminate cancer cells, in which the strong light absorption and high photothermal conversion efficiency of PTA are the keys to the success of PTT (Nasseri et al., 2022). When the cancer tissue temperature reach to 42°C, this leads to local tissue irreversible damage, and with the increase of the reaction temperature, the following reactions will occur: protein denaturation; DNA synthesis weakening; oxygen-depletion; and pH levels dropping (Yu et al., 2020). Eventually, PTT effectively inhibits tumor recurrence and metastasis. In conclusion, compared with the traditional treatment of tumors, PTT has become one of the most promising and effective cancer treatments.

2.2 Photodynamic therapy for cancer

Photodynamic therapy (PDT) is a therapeutic modality for the local treatment of disease that requires the eradication of pathological cells based on the interaction of light, a photosensitizer (PS), and oxygen (Abrahamse et al., 2017). PDT treatment consists of three steps: first, the controlled PS forms selective endocytosis and retention in tumor cells; second, the PS is excited by light of the appropriate wavelength to release ROS, which includes singlet oxygen ($^1O_2$), peroxide (O_2^{2-}), superoxide (O^{2-}), and hydroxyl radical (•OH), leading to the apoptosis, necrosis, and autophagy in cancer cells; third, PDT motivates a number of immune responses to cause inflammatory cells (Wang et al., 2021a). The PDT process destroys tumors through a variety of mechanisms, including the apoptosis and

necrosis of neoplastic cells, the degeneration or shut-down of tumor blood supply, the stimulation of anti-tumor immune responses, and the induction of inflammation in the treated location. PDT has been regarded as an alternative therapy option, having remarkable therapeutic effects, leading to it being applied in cancers of various types and locations of therapy (Mansoori et al., 2019).

2.3 Chemodynamic therapy for cancer

Chemodynamic therapy (CDT) has emerged as a cutting-edge and effective cancer treatment method that can produce highly harmful hydroxyl radicals (•OH) from endogenous hydrogen peroxide (H_2O_2) under the presence of catalysts *via* a Fenton or Fenton-like reaction utilizing the unique feature of tumor microenvironments to eradicate cancer cells that can cause DNA necrosis, protein inactivation, lipid oxidation, and finally induce cell apoptosis or necrosis (Wang et al., 2020; Yang and Liu, 2020). In addition, Fenton and Fenton-like reactions can also produce O_2, which can relieve the hypoxia and antioxidant capability of the tumor (Li et al., 2021). Furthermore, with a huge influx of "All-in-One" theranostic nano-agents, it is usually combined with chemotherapy, radiotherapy, phototherapy, sonodynamic therapy, and immunotherapy, which can not only improve the comprehensive synergistic therapeutic effect of cancer, but also enhance the anti-cancer therapeutic effect. In short, CDT presents a new route of treatment for highly efficient cancer theranostics.

2.4 Nanoscale drug delivery systems for cancer

One of the most important and significant potential opportunities in targeted drug delivery treatment modalities and diagnostic agents is nanoscale drug delivery systems (NDDS). In recent years, numerous chemotherapeutic drugs, inhibitors, vaccinations, proteins, and contrast agents have all been introduced. NDDS may be categorized into pH-sensitive delivery systems, enzyme-sensitive delivery systems, thermo-sensitive delivery systems, redox-sensitive delivery systems, and light-sensitive delivery systems, based on the unique features of the diseased microenvironment (Dheer et al., 2019; Li et al., 2019; Mirhadi et al., 2020). In addition, a variety of NDDS formulations, such as liposomes, nanoparticles, micelles, etc., have been designed as innovative cancer therapies. Especially in the area of tumor-targeted therapy, NDDS can not only resolve MDR and the recurrence of malignant tumors but also modify the immune response to improve the treatment of MDR cancer, providing more inspiration and thoughts for the precise treatment of tumors in the next stage (Wei et al., 2016).

3 Applications of LDNs

In accordance with their dimensional and structure characteristics, nanomaterials can be divided into 0D nanomaterials (such as quantum dots and nanorods) (Li Volsi et al., 2018), 1D nanomaterials (such as nanowires and nanotubes) (Cha et al., 2016), 2D nanomaterials (such as nanosheets) (Wang et al., 2021b), and 3D nanomaterials (such as nanocubes), in which the first three are collectively known as low-dimensional nanomaterials (LDNs) (Koh, 2010; Chai et al., 2021).

3.1 0D nanomaterials imaging diagnosis and treatment

Nanodots, ranging in size from 2 to 20 nm, are among the most representative LDNs, due to the characteristics of their chemical or physical properties, such as the low cost of synthesis, small size, low toxicity, excellent biocompatibility, chemical stability, and some attractive newly emerging properties, leading to them being at the forefront of cancer diagnostic imaging (Zou et al., 2017; Jia et al., 2018).

Lei et al. (2017) successfully synthesized ultrasmall poly-protected bismuth nanodots *via* an ultrafine strategy (Table 1). Due to their significant near-infrared absorption, nanodots exhibit outstanding photothermal conversion efficiency and can be used as a nano theranostic agent for PTT. Additionally, PVP-Bi nanodots demonstrate photothermal imaging and computed tomography (CT) imaging characteristics, which might successfully promote the PTT process. Additionally, PVP-Bi nanodots have high biocompatibility and low cytotoxicity in *in vitro* and *in vivo* experiments, indicating their excellent reliability for cancer imaging and treatment (Lei et al., 2017). In this direction, Li et al. (2017a) investigated ultrasmall PEG–Bi_2S_3 nanodots prepared according to a "hot injection" method (Table 1). Due to the presence of the Bi element with a larger X-ray attenuation coefficient, PEG–Bi_2S_3 nanodots possess the capacity for CT imaging. Additionally, Bi_2S_3 is a semiconductor with a low energy gap that exhibits significant NIR absorption. As a result, Bi_2S_3 might perform as a highly productive CT/PTT dual-functional agent by itself for imaging-guided photothermal therapy for effective and reliable cancer treatment (Li et al., 2017a). In their study, Xu et al. (2018) suggested that monodisperse Gd/Ru@BSA nanodots could be successfully synthesized through a simple protocol with high photothermal conversion efficiency, which achieved a significant efficacy for anti-cancer therapy under PTT both *in vitro* and *in vivo* (Table 1). Meanwhile, Gd/Ru@BSA nanodots exhibit superior T1-weighted magnetic resonance (MR) imaging ability to evaluate the treatment effect (Xu et al., 2018). Furthermore, Xu et al. (2019) found that phthalocyanine-based nanodots (ZnPc-NDs) have dual synergistic photodynamic/photothermal effects to realize the diagnostic function, demonstrated by HeLa tumor both *in vitro* and *in vivo* (Table 1). Gd(III) on the surface of nanodots provided magnetic resonance performances, having achieved magnetic resonance imaging-guided tumor phototherapy. The as-prepared nanodots, regarded as powerful and safe nano theranostic agents, have great clinical promise for cancer nano-imaging-guided theranostic nanoplatforms (Xu et al., 2019).

3.2 1D nanomaterials imaging diagnosis and treatment

One-dimensional (1D) nanostructures with characteristic surface-to-volume and aspect ratios, such as nanowires (NWs), nanobelts (NBs), nanoneedles (NNs), nanorods (NRs), nanotubes (NTs) (Contreras-Torres et al., 2022), and nanofibers (NFs), which might adsorb or conjugate to various therapeutic compounds, have a

TABLE 1 Illustrative examples of LDNs and their biomedical applications.

LDNs	Type	Imaging	Therapy	Application	Reference
Poly-protected bismuth nanodots	0D nanomaterials	CT imaging	PTT therapy	Tumor tissue	Lei et al. (2017)
PEG–Bi_2S_3 nanodots	0D nanomaterials	CT imaging	PTT therapy	Tumor tissue	Li et al. (2017a)
Gd/Ru@BSA nanodots	0D nanomaterials	T1-weighted MRI	PTT therapy	Tumor tissue	Xu et al. (2018)
Phthalocyanine-based nanodots (ZnPc-NDs)	0D nanomaterials	T1-weighted MRI	PTT/PDT therapy	Tumor tissue	Xu et al. (2019)
Ag/$BaGdF_5$: Yb^{3+}, Er^{3+} nanocomposites	1D nanomaterials	CT/MR imaging	PTT therapy	Tumor tissue	Chen et al. (2019)
Si–Au	1D nanomaterials	PA imaging	PTT therapy	Tumor tissue	Sun et al. (2019)
Synthesized silicon nanowires (SiNWs)	1D nanomaterials		NDDS therapy	Tumor tissue	Peng et al. (2014)
Pd@Au, Pd@Ag nanoplates, and mesocrystalline Pd nanocorolla	2D nanomaterials	PA/CT imaging	PTT/chemotherapy; PTT/PDT therapy	Tumor tissue	Chen et al. (2017)
Nanosheets (MnO_2 NSs)	2D nanomaterials	T1/T2-weighted MRI		Tumor tissue	Zhao et al. (2014)
TiNSs-PEG nanosheets	2D nanomaterials	PA and CT imaging	PTT therapy	Tumor tissue	Xie et al. (2019)
MnO_2 nanosheets (M-NSs)	2D nanomaterials	PA and PET imaging	PTT therapy	Tumor tissue	Tang et al. (2019)
MUCNPs@BPNs-Ce6	2D nanomaterials	T1/T2-weighted MR and US imaging	PTT/PDT therapy	Tumor tissue	Zhang et al. (2020)

significant benefit in terms of disease diagnostics, monitoring, and efficacy evaluation (Roehlecke and Schmidt, 2020).

Chen et al. (2019) discovered that Ag/$BaGdF_5$: Yb^{3+}, Er^{3+} nanocomposites, synthesized by Ag nanowires and PVP-modified $BaGdF_5$: Yb^{3+}, Er^{3+} spherical nanoparticles *via* convenient solvothermal and hydrothermal procedure, exhibit remarkable performance on photothermal conversion and CT/MR imaging efficiency (Table 1). Further evidence of the PTT effect was validated by Hela cells under a 808 nm laser. Meanwhile, CT/MR was used for the assessment of cancer therapeutic effects. Experimental results showed that the obtained nanoparticles not only possess an extraordinary photothermal conversion effect but also an excellent imaging capability for CT/MR (Chen et al., 2019). In this direction, Sun et al. (2019) investigated silicon nanowires decorated with gold nanoparticles (Si–Au) that were synthesized *via* a simple and convenient method (Table 1). Si–Au showed a good photothermal effect under NIR-I in *in vitro* and *in vivo* experiments, and it also demonstrated highly efficient PA imaging under NIR-II in 4T1 to guide photothermal cancer therapy (Sun et al., 2019). Due to the abundant surface binding sites in 1D nanomaterials, they can conjugate to various therapeutic molecules. In this direction, Peng et al. (2014) synthesized silicon nanowires (SiNWs) of large-area porous structures with high drug-loading capacity through a facile route and loaded doxorubicin (DOX) to remove drug-resistant cancer cells (Table 1). *In vitro* experiments showed that nanoparticles with a low RF value are extremely effective for reversing drug resistance. SiNWs-DOX solves the question of cancer resistance to the drugs and prevents blindly using the medicine (Peng et al., 2014). Additionally, as observed in some research, 1D nanomaterials have characteristic surface-to-volume and aspect ratios, making them potential carriers of biomolecules and chemotherapeutic medications for various cancer-related treatments (García-Hevia et al., 2016).

3.3 2D nanomaterials imaging diagnosis and treatment

Among nanomaterials, 2D nanomaterials (2D-NMs) have gained considerable interest from researchers due to their physical and chemical properties, including their planar structure, ultra-thin thickness, and ease of functionalization (Mohammadpour and Majidzadeh, 2020). Furthermore, 2D-NMs are capable of adsorbing or conjugating various contrast agents, enabling rapid multimodal imaging with a quick turnaround time, as well as the detection of tumors and metastases (Ashfaq et al., 2022).

Chen et al. (2017) summarized Pd@Au, Pd@Ag nanoplates, and mesocrystalline Pd nanocorolla applications in cancer diagnosis and therapy (Table 1). The different forms of 2D Pd nanosheets were used to carry out extensive research because of their many benefits. The main advantages are a large surface area, strong absorption in the NIR region, high photothermal conversion efficiency, high photothermal stability, and excellent PA or CT imaging capability. Experimental results indicated that the combination of PTT/chemotherapy and PTT/PDT therapy achieved high synergistic therapeutic effects, realizing PA and CT imaging-guided PTT for cancer treatment (Chen et al., 2017). Another successful implementation of manganese dioxide nanosheets (MnO_2 NSs) is presented in the work of Zhao et al. (2014), where MnO_2 NSs

were employed for MRI bimodal tumor cell imaging (Table 1). Moreover, Xie et al. (2019) discovered that Ti nanosheets (NSs) exfoliated through simple methods (Table 1). The experiment confirmed that TiNSs-PEG possesses excellent light absorbance, preeminent photothermal performance, and stability. Therefore, TiNSs-PEG combined with PTT can achieve high tumor cell-killing efficiency. The effectiveness of treatment can be assessed using dual-modal contrast-enhanced PA and CT imaging (Xie et al., 2019). Tang et al. (2019) synthesized MnO_2 nanosheets (M-NSs) for a tumor-targeted multimodal diagnostic imaging probe *via* a one-step wet-chemical method. Through the surface functionalization of the M-NSs, 64Cu radionuclides were successfully chelated onto nanoparticles to achieve PET imaging. In addition, the obtained nanomaterials not only possessed a good photothermal therapeutic effect but also realized effective photoacoustic-imaging-guided synergistic starvation-enhanced photothermal therapy (Tang et al., 2019). Zhang et al. (2020) designed MUCNPs@BPNs-Ce6 nanocomposites for tumor phototherapy guided by multimodal imaging. BPNs and Ce6, as a component of nanomaterials with high photothermal conversion efficiency, were employed to promote PTT and PDT under a single irradiation light of 808 nm. In addition, Fe_3O_4 and MnO_2 nanoparticles realized T1/T2-weighted magnetic resonance imaging, and Ce6 has the capability of fluorescence imaging. It was proved by experiments that the bubbles produced by H_2O_2 decomposition in the tumor microenvironment could be used for ultrasound imaging. Further, MnO_2 can transform excess H_2O_2 in the tumor microenvironment into O_2 to enhance PDT. The obtained MUCNPs@BPNs-Ce6 not only enhances the therapeutic effect of PDT/PTT but also enables multimodal imaging to evaluate the therapeutic effect of cancer in real-time (Zhang et al., 2020). The development of effective diagnostic and cancer therapies relies on the development of 2D nanomaterials, which are constantly expanding. Therefore, the development of 2D-NMs will improve clinical decision-making and advance precision medicine (Li et al., 2017b; Wang et al., 2017; Zhao et al., 2022; Zhao et al., 2023).

4 Outlooks

In recent years, LDNs have emerged and attracted intense attention due to their exclusive physical and chemical properties, such as their small size, high durability, chemical stability, biocompatibility, non-toxicity, environmental friendliness, and the ease of chemical functionalization and surface modification. LDN-based nano-imaging-guided theranostic nanoplatforms have opened new frontiers in cancer precision medicine, integrated imaging and therapy into multimodal theranostic nanoplatforms to achieve individualized diagnostic accuracy and therapy for patients (Aminolroayaei et al., 2021; Huang et al., 2023). However, transforming academic research into clinical practice is still a challenging and currently unresolved problem in anti-cancer clinical practice therapies. In the context of the clinical effectiveness and safety of drugs, LDNs are expected to realize clinical application by continually improving nanomaterials' performance in the future. In conclusion, theranostic nanoplatforms based on LDNs have the tremendous potential to be employed as cancer therapies and diagnostic tools, providing more powerful and useful means for biologists and clinicians (Cheng and Zhang, 2018; Li et al., 2022).

Author contributions

JL conceived the presented research. JL and FC designed the structure of the paper. FC drafted the manuscript. NX provided critical revision of this article. JL, NX, TZ, SP, and HY supervised the findings of the work and approved the manuscript for submission. All authors agreed with the final version of this manuscript.

Funding

This work was supported by the National Natural Science Foundation of China (Nos 82071981 and 21635007), the Health Special Project of Jilin Province Department of Finance (Nos 3D518V283429 and 201817301863), and the Fundamental Research Funds for the Central Universities (No. 419070600032).

Conflict of interest

The authors declare that the research was conducted in the absence of any commercial or financial relationships that could be construed as a potential conflict of interest.

Publisher's note

All claims expressed in this article are solely those of the authors and do not necessarily represent those of their affiliated organizations, or those of the publisher, the editors and the reviewers. Any product that may be evaluated in this article, or claim that may be made by its manufacturer, is not guaranteed or endorsed by the publisher.

References

Abrahamse, H., Kruger, C. A., Kadanyo, S., and Mishra, A. (2017). Nanoparticles for advanced photodynamic therapy of cancer. *Photomed. Laser Surg.* 35 (11), 581–588. doi:10.1089/pho.2017.4308

Akinoso-Imran, A. Q., O'Rorke, M., Kee, F., Jordao, H., Walls, G., and Bannon, F. J. (2022). Surgical under-treatment of older adult patients with cancer: A systematic review and meta-analysis. *J. Geriatric Oncol.* 13 (4), 398–409. doi:10.1016/j.jgo.2021.11.004

Aminolroayaei, F., Shahbazi-Gahrouei, D., Shahbazi-Gahrouei, S., and Rasouli, N. (2021). Recent nanotheranostics applications for cancer therapy and diagnosis: A review. *IET Nanobiotechnology* 15 (3), 247–256. doi:10.1049/nbt2.12021

Ashfaq, M., Talreja, N., Chauhan, D., Afreen, S., Sultana, A., and Sriturayanich, W. (2022). Two-dimensional (2D) hybrid nanomaterials for diagnosis and treatment of cancer. *J. Drug Deliv. Sci. Technol.* 70, 103268. doi:10.1016/j.jddst.2022.103268

Bergman, P. J. (2019). Cancer immunotherapies. *Veterinary Clin. N. Am. Small Animal Pract.* 49 (5), 881–902. doi:10.1016/j.cvsm.2019.04.010

Cha, J., Jin, S., Shim, J. H., Park, C. S., Ryu, H. J., and Hong, S. H. (2016). Functionalization of carbon nanotubes for fabrication of CNT/epoxy nanocomposites. *Mater. Des.* 95, 1–8. doi:10.1016/j.matdes.2016.01.077

Chai, L., Fan, X., Zuo, Y., Zhang, B., Nie, G. h., Xie, N., et al. (2021). Low-dimensional nanomaterials enabled autoimmune disease treatments: Recent advances, strategies, and future challenges. *Coord. Chem. Rev.* 432, 213697. doi:10.1016/j.ccr.2020.213697

Chen, X., Shi, S., Wei, J., Chen, M., and Zheng, N. (2017). Two-dimensional Pd-based nanomaterials for bioapplications. *Sci. Bull.* 62 (8), 579–588. doi:10.1016/j.scib.2017.02.012

Chen, Z., Liu, G., Zhang, X., Sui, J., Dong, X., Yu, W., et al. (2019). Synthesis of multifunctional rare-earth fluoride/Ag nanowire nanocomposite for efficient therapy of cancer. *Mater. Sci. Eng. C* 104, 109940. doi:10.1016/j.msec.2019.109940

Cheng, Y., and Zhang, H. (2018). Novel bismuth-based nanomaterials used for cancer diagnosis and therapy. *Chem. – A Eur. J.* 24 (66), 17405–17418. doi:10.1002/chem.201801588

Contreras-Torres, F. F., Salas-Treviño, D., Soto-Domínguez, A., and De Jesus Garcia-Rivas, G. (2022). Carbon nanotubes in tumor-targeted chemotherapeutic formulations: A review of opportunities and challenges. *ACS Appl. Nano Mater.* 5 (7), 8649–8679. doi:10.1021/acsanm.2c01118

Dheer, D., Nicolas, J., and Shankar, R. (2019). Cathepsin-sensitive nanoscale drug delivery systems for cancer therapy and other diseases. *Adv. Drug Deliv. Rev.* 151-152, 130–151. doi:10.1016/j.addr.2019.01.010

Doughty, A. C. V., Hoover, A. R., Layton, E., Murray, C., Howard, E., and Chen, W. (2019). Nanomaterial applications in photothermal therapy for cancer. *Materials* 12 (5), 779. doi:10.3390/ma12050779

Duemer, J. (2016). Radiation therapy. *Chest* 150 (6), 1405. doi:10.1016/j.chest.2016.07.046

Gao, W., Qiu, C., and He, X. (2017). Low-dimensional nanomaterials and their functional architectures: Synthesis, properties, and applications. *J. Nanomater.* 2017, e7350491–e7350492. doi:10.1155/2017/7350491

García-Hevia, L., Villegas, J. C., Fernández, F., Casafont, I., Gonzalez, J., Valiente, R., et al. (2016). Multiwalled carbon nanotubes inhibit tumor progression in a mouse model. *Adv. Healthc. Mater.* 5 (9), 1080–1087. doi:10.1002/adhm.201500753

Godishala, A., Yang, S., and Asnani, A. (2018). Cardioprotection in the modern era of cancer chemotherapy. *Cardiol. Rev.* 26 (3), 113–121. doi:10.1097/crd.0000000000000194

Huang, Q., Yang, Y., Zhao, T., Chen, Q., Liu, M., Ji, S., et al. (2023). Passively-targeted mitochondrial tungsten-based nanodots for efficient acute kidney injury treatment. *Bioact. Mater.* 21, 381–393. doi:10.1016/j.bioactmat.2022.08.022

Hwang, E., and Jung, H. S. (2021). Organelle-targeted photothermal agents for cancer therapy. *Chem. Commun.* 57 (63), 7731–7742. doi:10.1039/d1cc02168k

Jia, Y., Li, J., Chen, J., Jiang, L., Chen, X., et al. (2018). Smart photosensitizer: Tumor-triggered oncotherapy by self-assembly photodynamic nanodots. *ACS Appl. Mater. Interfaces* 10 (18), 15369–15380. doi:10.1021/acsami.7b19058

Kim, E. E. (2019). Radionanomedicine: Combined nuclear and nanomedicine. *J. Nucl. Med.* 60 (6), 873. doi:10.2967/jnumed.119.229211

Koh, S. J. (2010). Low-dimensional nanomaterials: Synthesis and application of zero-and one-dimensional nanomaterials. *JOM* 62 (4), 34. doi:10.1007/s11837-010-0056-0

Lammers, T., and Ferrari, M. (2020). The success of nanomedicine. *Nano Today* 31, 100853. doi:10.1016/j.nantod.2020.100853

Lei, P., An, R., Zhang, P., Yao, S., Song, S., Dong, L., et al. (2017). Ultrafast synthesis of ultrasmall poly(vinylpyrrolidone)-protected bismuth nanodots as a multifunctional theranostic agent for *in vivo* dual-modal CT/Photothermal-Imaging-Guided photothermal therapy. *Adv. Funct. Mater.* 27 (35), 1702018. doi:10.1002/adfm.201702018

Li, J., Gong, S., Li, S., Li, X., Lan, S., Sun, M., et al. (2022). Tumor-penetrating iron oxide nanoclusters for T_1/T_2 dual mode MR imaging-guided combination therapy[J]. *Biomaterials Sci.* 10 (18), 5254–5264. doi:10.1039/d2bm00667g

Li, L., Yang, W-W., and Xu, D-G. (2019). Stimuli-responsive nanoscale drug delivery systems for cancer therapy. *J. Drug Target.* 27 (4), 423–433. doi:10.1080/1061186x.2018.1519029

Li, S-L., Jiang, P., Jiang, F-L., and Liu, Y. (2021). Recent advances in nanomaterial-based nanoplatforms for chemodynamic cancer therapy. *Adv. Funct. Mater.* 31 (22), 2100243. doi:10.1002/adfm.202100243

Li Volsi, A., Fiorica, C., D'Amico, M., Scialabba, C., Palumbo, F. S., Giammona, G., et al. (2018). Hybrid Gold/Silica/Quantum-Dots supramolecular-nanostructures encapsulated in polymeric micelles as potential theranostic tool for targeted cancer therapy. *Eur. Polym. J.* 105, 38–47. doi:10.1016/j.eurpolymj.2018.05.013

Li, X., Shan, J., Zhang, W., Su, S., Yuwen, L., and Wang, L. (2017). Recent advances in synthesis and biomedical applications of two-dimensional transition metal dichalcogenide nanosheets. *Small* 13 (5), 1602660. doi:10.1002/smll.201602660

Li, Z., Ai, K., Yang, Z., Zhang, T., Liu, J., and Cui, X. (2017). Untrasmall Bi_2S_3 nanodots for *in vivo* X-ray CT imaging-guided photothermal therapy of cancer. *RSC Adv.* 7 (47), 29672–29678. doi:10.1039/c7ra04132b

Mansoori, B., Mohammadi, A., Amin Doustvandi, M., Mohammadnejad, F., Kamari, F., Gjerstorff, M. F., et al. (2019). Photodynamic therapy for cancer: Role of natural products. *Photodiagnosis Photodyn. Ther.* 26, 395–404. doi:10.1016/j.pdpdt.2019.04.033

Mirhadi, E., Mashreghi, M., Faal Maleki, M., Alavizadeh, S. H., Arabi, L., Badiee, A., et al. (2020). Redox-sensitive nanoscale drug delivery systems for cancer treatment. *Int. J. Pharm.* 589, 119882. doi:10.1016/j.ijpharm.2020.119882

Mohammadpour, Z., and Majidzadeh, -A. K. (2020). Applications of two-dimensional nanomaterials in breast cancer theranostics. *ACS Biomaterials Sci. Eng.* 6 (4), 1852–1873. doi:10.1021/acsbiomaterials.9b01894

Mullard, A. (2020). Addressing cancer's grand challenges. *Nat. Rev. Drug Discov.* 19 (12), 825–826. doi:10.1038/d41573-020-00202-0

Nasseri, B., Alizadeh, E., Bani, F., Akbarzadeh, A., Rabiee, N., et al. (2022). Nanomaterials for photothermal and photodynamic cancer therapy. *Appl. Phys. Rev.* 9 (1), 011317. doi:10.1063/5.0047672

Pe'er, D., Ogawa, S., Elhanani, O., Keren, L., Oliver, T. G., and Wedge, D. (2021). Tumor heterogeneity. *Cancer Cell* 39 (8), 1015–1017. doi:10.1016/j.ccell.2021.07.009

Peitzsch, C., Tyutyunnykova, A., Pantel, K., and Dubrovska, A. (2017). Cancer stem cells: The root of tumor recurrence and metastases. *Seminars Cancer Biol.* 44, 10–24. doi:10.1016/j.semcancer.2017.02.011

Peng, F., Su, Y., Ji, X., Zhong, Y., Wei, X., and He, Y. (2014). Doxorubicin-loaded silicon nanowires for the treatment of drug-resistant cancer cells. *Biomaterials* 35 (19), 5188–5195. doi:10.1016/j.biomaterials.2014.03.032

Roehlecke, C., and Schmidt, M. H. H. (2020). Tunneling nanotubes and tumor microtubes in cancer. *Cancers* 12 (4), 857. doi:10.3390/cancers12040857

Siegel, R. L., Miller, K. D., Fuchs, H. E., and Jemal, A. (2022). Cancer statistics, 2022. *A Cancer J. Clin.* 72 (1), 7–33. doi:10.3322/caac.21708

Sun, L., Chen, Y., Gong, F., Dang, Q., Xiang, G., Cheng, L., et al. (2019). Silicon nanowires decorated with gold nanoparticles *via in situ* reduction for photoacoustic imaging-guided photothermal cancer therapy. *J. Mater. Chem. B* 7 (28), 4393–4401. doi:10.1039/c9tb00147f

Tang, W., Fan, W., Zhang, W., Yang, Z., Li, L., Wang, Z., et al. (2019). Wet/sono-chemical synthesis of enzymatic two-dimensional MnO_2 nanosheets for synergistic catalysis-enhanced phototheranostics. *Adv. Mater.* 31 (19), 1900401. doi:10.1002/adma.201900401

Wang, J., Liu, Y-X., Li, X-L., Chen, H. Y., and Xu, J. J. (2021). Core–shell plasmonic nanomaterials toward: Dual-mode imaging analysis of glutathione and enhanced chemodynamic therapy. *Anal. Chem.* 93 (29), 10317–10325. doi:10.1021/acs.analchem.1c01858

Wang, L., Xiong, Q., Xiao, F., and Duan, H. (2017). 2D nanomaterials based electrochemical biosensors for cancer diagnosis. *Biosens. Bioelectron.* 89, 136–151. doi:10.1016/j.bios.2016.06.011

Wang, W., Jin, Y., Xu, Z., Liu, X., Bajwa, S. Z., Khan, W. S., et al. (2020). Stimuli-activatable nanomedicines for chemodynamic therapy of cancer. *WIREs Nanomedicine Nanobiotechnology* 12 (4), e1614. doi:10.1002/wnan.1614

Wang, X., Luo, D., and Basilion, J. P. (2021). Photodynamic therapy: Targeting cancer biomarkers for the treatment of cancers. *Cancers* 13 (12), 2992. doi:10.3390/cancers13122992

Wei, X., Luo, Q., Sun, L., 等Zhu, H., Guan, P., et al. (2016). Enzyme- and pH-sensitive branched polymer–doxorubicin conjugate-based nanoscale drug delivery system for cancer therapy. *ACS Appl. Mater. Interfaces* 8 (18), 11765–11778. doi:10.1021/acsami.6b02006

Xie, Z., Chen, S., Duo, Y., Zhu, Y., Fan, T., Zou, Q., et al. (2019). Biocompatible two-dimensional titanium nanosheets for multimodal imaging-guided cancer theranostics. *ACS Appl. Mater. Interfaces* 11 (25), 22129–22140. doi:10.1021/acsami.9b04628

Xu, G., Bao, X., Chen, J., Zhang, B., Li, D., Zhou, D., et al. (2019). *In vivo* tumor photoacoustic imaging and photothermal therapy based on supra-(carbon nanodots). *Adv. Healthc. Mater.* 8 (2), 1800995. doi:10.1002/adhm.201800995

Xu, P., Wu, H., Wang, D., Zhao, G., Li, F., Qiu, B., et al. (2018). Ultra-small albumin templated Gd/Ru composite nanodots for *in vivo* dual modal MR/thermal imaging guided photothermal therapy. *Adv. Healthc. Mater.* 7 (19), 1800322. doi:10.1002/adhm.201800322

Yang, B., Chen, Y., and Shi, J. (2019). Nanocatalytic medicine. *Nanocatalytic Med. Adv. Mater.* 31 (39), 1901778. doi:10.1002/adma.201901778

Yang, Y., and Liu, Z. (2020). Chemiluminescent nanosystems for imaging cancer chemodynamic therapy. *J. Chem.* 6 (9), 2127–2129. doi:10.1016/j.chempr.2020.08.013

Yu, C., Xu, L., Zhang, Y., Huang, Y., and Liang, X. J. (2020). Polymer-based nanomaterials for noninvasive cancer photothermal therapy. *ACS Appl. Polym. Mater.* 2 (10), 4289–4305. doi:10.1021/acsapm.0c00704

Zhang, Q., Wang, W., Zhang, M., Wu, F., Zheng, T., Sheng, B., et al. (2020). A theranostic nanocomposite with integrated black phosphorus nanosheet, Fe3O4@ MnO2-doped upconversion nanoparticles and chlorin for simultaneous multimodal imaging, highly efficient photodynamic and photothermal therapy. *Chem. Eng. J.* 391, 123525. doi:10.1016/j.cej.2019.123525

Zhang, W., Ke, Y., Liu, X., Jin, M., and Huang, G. (2022). Drug resistance in NSCLC is associated with tumor micro-environment. *Reprod. Biol.* 22 (3), 100680. doi:10.1016/j.repbio.2022.100680

Zhao, H., Huang, J., Huang, L., Yang, Y., Xiao, Z., Chen, Q., et al. (2023). Surface control approach for growth of cerium oxide on flower-like molybdenum disulfide nanosheets enables superior removal of uremic toxins. *J. Colloid Interface Sci.* 630, 855–865. doi:10.1016/j.jcis.2022.10.142

Zhao, H., Huang, J., Miao, L., Yang, Y., Xiao, Z., Chen, Q., et al. (2022). Toward Urease-free wearable artificial kidney: Widened interlayer spacing MoS2 nanosheets with highly effective adsorption for uremic toxins. *Chem. Eng. J.* 438, 135583. doi:10.1016/j.cej.2022.135583

Zhao, Z., Fan, H., Zhou, G., Bai, H., Liang, H., Wang, R., et al. (2014). Activatable fluorescence/MRI bimodal platform for tumor cell imaging via MnO_2 nanosheet–aptamer nanoprobe[J]. *J. Am. Chem. Soc.* 136 (32), 11220–11223. doi:10.1021/ja5029364

Zhou, L., Zhu, Q., Feng, Y., and Wang, R. (2022). Preparation and characterization of iron oxide low-dimensional nanomaterials. *Integr. Ferroelectr.* 225 (1), 240–254. doi:10.1080/10584587.2021.1911259

Zou, Q., Abbas, M., Zhao, L., Shen, G., and Yan, X. (2017). Biological photothermal nanodots based on self-assembly of peptide–porphyrin conjugates for antitumor therapy. *J. Am. Chem. Soc.* 139 (5), 1921–1927. doi:10.1021/jacs.6b11382

frontiers | Frontiers in Bioengineering and Biotechnology

TYPE Mini Review
PUBLISHED 20 January 2023
DOI 10.3389/fbioe.2023.1121477

OPEN ACCESS

EDITED BY
Shaohua Wang,
Ohio University, United States

REVIEWED BY
Yan Yan Huang,
Nanjing Forestry University, China
Yue Huang,
China Agricultural University, China

*CORRESPONDENCE
Xingfu Bao,
baoxf@jlu.edu.cn

SPECIALTY SECTION
This article was submitted to Nanobiotechnology, a section of the journal Frontiers in Bioengineering and Biotechnology

RECEIVED 11 December 2022
ACCEPTED 09 January 2023
PUBLISHED 20 January 2023

CITATION
Tang N, Ding Z, Zhang J, Cai Y and Bao X (2023), Recent advances of antioxidant low-dimensional carbon materials for biomedical applications.
Front. Bioeng. Biotechnol. 11:1121477.
doi: 10.3389/fbioe.2023.1121477

Recent advances of antioxidant low-dimensional carbon materials for biomedical applications

Nan Tang[1,2], Zhen Ding[1,2], Jin Zhang[2], Yanting Cai[1] and Xingfu Bao[1]*

[1]Department of Orthodontics, Jilin Provincial Key Laboratory of Tooth Development and Bone Remodeling, School and Hospital of Stomatology, Jilin University, Changchun, China, [2]Beijing Advanced Innovation Center for Soft Matter Science and Engineering, College of Life Science and Technology, Beijing University of Chemical Technology, Beijing, China

As the primary cause of many tissue damage and diseases, reactive oxygen species (ROS) and reactive nitrogen species (RNS) are well known to be extremely harmful to a variety of biological components in cells including lipids, proteins and DNA. Numerous antioxidative nanomaterials have been artificially designed and rationally synthesized to protect cells from the oxidative damage caused by reactive oxygen species/reactive nitrogen species. Recent studies demonstrate that low dimensional carbon antioxidative nanomaterials have received a lot of attention owing to their tiny nanoscales and unique physicochemical property. As a result, a brief overview of recent advancements in antioxidant low-dimensional carbon materials is provided. Typically, carbon nanomaterials are classified according to their nanostructure dimensions, which are zero-dimension, one-dimension, and two-dimension. Last but not least, the challenges and perspectives of these high-performance low-dimensional materials in biomedical fields and further clinical usages are discussed as well.

KEYWORDS

low-dimensional materials, carbon, nanotheranostics, biomedical applications, nanomaterials

Introduction

The discovery of reactive oxygen species (ROS) originated from the study of oxidative damage. Oxygen is partially reduced to oxidizing free radicals through respiratory chain reactions, which are named "reactive oxygen species." Typical ROS contains hydroxyl radical (·OH), superoxide radical anion ($O_2^{\bullet-}$), singlet oxygen ($^1O_2$), and hydrogen peroxide (H_2O_2). Represented by nitric oxide (NO), reactive nitrogen species (RNS) is another oxide that plays an important role in the metabolism of living organisms. Typical RNS including NO radical (NO·), nitroso ion (NO^+), peroxynitrite ($ONOO^-$), S-nitrosomercaptan (SNOs), and nitrogen oxides (NO_x) can be derived from the interaction between NO and various ROS. Moreover, ROS could convert into RNS in the presence of enzyme in cells (Liu and Shi, 2019). ROS and RNS act as essential roles in the body, participating in normal cell metabolism and responding to external stimuli by mediating signal transduction. The electrons carried by ROS and RNS grant them sensitive reactivity and can oxidize a variety of molecules including DNA, lipid, and proteins. As a double-edged sword, oxidation facilitates the defense system of living things to fight against invaders like bacteria, but ROS and RNS will cause damage to the body if they are out of control. Normally, the generation and removal of ROS and RNS are in a delicate dynamic balance. The cellular antioxidant system is responsible for removing excessive ROS and RNS. Once the balance is broken, whether excessive ROS and RNS are produced in the cell or the antioxidant system of the cell fails, oxidative stress occurs, marked by the oxidation of a variety of molecules

and the following inflammatory reactions. Numerous studies have confirmed the causal relationship between oxidative stress and various diseases, such as inflammation, cardiovascular disease, autoimmune disorders, and neurodegenerative diseases. Therefore, antioxidant therapy is expected to prevent and treat oxidative stress-related diseases.

As a class of substances that can scavenge free radicals, antioxidants are usually formed within the body or outside the body. The endogenous antioxidants are mainly various natural enzymes or small molecules. Superoxide dismutase (SOD) and catalase (CAT) can catalyze the conversion of $O_2^{\cdot-}$ into water and molecular O_2, whereas glutathione peroxidase (GPx) can convert H_2O_2 and fatty acid hydroperoxides. But the substrate specificity and pH sensitivity of enzymes limit their ability to eliminate ROS and RNS in practical application. As a supplement, endogenous macromolecules (bilirubin, albumin) and other small biomolecules (vitamins, cysteine) have been applied to prevent oxidative damage. The disadvantage of these molecules is that they are less safe and may cause a series of clinical symptoms, including but not limited to bleeding, hemorrhagic stroke, and cancer incidence. The shortcomings of endogenous antioxidants prompted researchers to develop exogenous antioxidants. Recently, nanomaterials have drawn the attention of scientists due to their various advantages. On the one hand, nanomaterials can change the pharmacokinetics of natural antioxidant molecules when they act as carriers. Moreover, nanomaterials with the activities of antioxidative enzymes usually exhibit higher stability and a stronger tolerance to harsh microenvironments. In view of further clinical translation, these antioxidative nanomaterials seem much more feasible and attract great attention.

Several kinds of antioxidative nanomaterials have been well identified including metal-based nanomaterials, bioinspired polymer-based nanomaterials, and carbon-based nanomaterials. As typical bioinspired polymer-based nanomaterials, polydopamine (PDA) nanoparticles with excellent antioxidative activity could act as efficient scavengers for ROS and RNS in the treatments of periodontal disease and ischemic stroke (Liu et al., 2016; Bao et al., 2018). Moreover, various novel metal-based nanomaterials, such as Mn_3O_4 and Pt-modified PCN222-Mn MOFs, exhibited admirable ROS/RNS removal efficacy *in vivo*, which could protect live mice from both ear-inflammation and inflammatory bowel disease (Yao et al., 2018; Liu et al., 2020). Significantly, low-dimensional carbon-based nanomaterials have been proved to hold multiple radical scavenging abilities and exceptional antioxidative stability (Sun et al., 2018; Liu and Shi, 2019). Furthermore, advantages like low cost and ease of operation make these nanomaterials more attractive in further applications. In this review, we summarize the antioxidant properties of low-dimensional carbon materials based on their fascinating structures. We also highlight the potential antioxidant mechanism and recent biomedical usages of these low-dimensional carbon nanomaterials. Finally, we discuss the challenges and opportunities presented by low-dimensional carbon materials from the viewpoint of further clinical translation.

Application of antioxidant low-dimensional carbon materials in biomedical fields

A wide range of carbon-based nanomaterials with antioxidative properties have been well explored including carbon particles, carbon sheet structure, carbon nanotubes, carbon clusters, and carbon dots. Here, we classified the carbon-based nanomaterials according to their structure as zero-dimension, one-dimension, two-dimension, and three-dimension. Moreover, we discuss the practical usage of low-dimensional carbon materials against numbers of ROS in biomedical fields because of their special structural properties and relatively high antioxidant activity.

Zero-dimension carbon nanomaterials

Since the first report of fullerene as an antioxidant, various fullerenes has been well investigated for its unique cage structure and scavenging activities towards OH and $O_2^{\cdot-}$. The conjugated double bonds and the low-lying lowest unoccupied molecular orbital can account for their excellent antioxidative ability. Though they bears the name of "Radical Sponge," their practical biomedical usages are often limited by the hydrophobic nature of original fullerenes. Derivatives including fullerenols, carboxyl-modified fullerenes, metal-modified fullerenes, and ethylenediamine-modified fullerenes usually exhibit better water solubility. Recent studies indicate that fullerenols can well eliminate free radicals both *in vivo* and *in vitro*. Better biocompatibility of fullerenol than native fullerene can be explained by its excretion in urine. So the fullerenol can be used to protect tissues or organs against oxidative injury induced by doxorubicin, Co. γ-rays and reduplicative chemotherapy (Figure 1A) (Zhou et al., 2017). The cage size, in particular, will affect the radical scavenging capability indicated by C_{70} fullerenols' superior protection over C_{60}-fullerenols. The reason for the difference can be attributed to the fact that C_{70}-fullerenols hold more intrinsically coupled double bonds, is closer to electrons, and is more polarizable.

Carboxyl modification is another strategy for hydrophilic alternation. As a high-performance neuroprotective antioxidant, $C_{60}(C(COOH)_2)_3$ has been shown to effectively prevent dopaminergic neuron apoptosis *in vitro* and protect cerebellar granule cells from apoptosis. Then, $C_{60}(C(COOH)_2)_2$ dots with similar structure were well synthesized and tested for their ability to protect the blood-brain barrier. As expected, $C_{60}(C(COOH)_2)_2$ dots can enter oxidized cerebral microvessel endothelial cells (CMECs) rather than normal cells and maintain CMEC integrity by inhibiting H_2O_2-induced F-actin depolymerization. It is of interest that carboxyl and cage size have an influence on the level of oxidative stress relaxation. To answer this question, different origins of acid including dimalonic acid, trimalonic acid, and quadrimalonic acid are selected and used to react with C_{60} and C_{70}, respectively. These results suggest dimalonic acid-modified C_{70} fullerenes and trimalonic acid-modified C_{70} fullerenes exhibit an obviously more protective effect than others. The authors consider that the extended system and lower symmetric structure of the C_{70} fullerene cage, which possess higher activated electron-deficient areas on the cage surface, can extremely quench various free radicals (Liu et al., 2013).

The typical representative of the metallofullerene family is Gd@C_{82}, while gadolinium endohedral metallofullerenol comprises a functionalized C_{82} fullerene cage with metal trapped inside (Yin et al., 2009). It has been reported that the chemical and physical properties of gadolinium endohedral metallofullerenols are determined by the number and position of the hydroxyl groups on the fullerene cage. These metallofullerenols hold excellent scavenging activity against reactive oxygen species and exhibit great cell

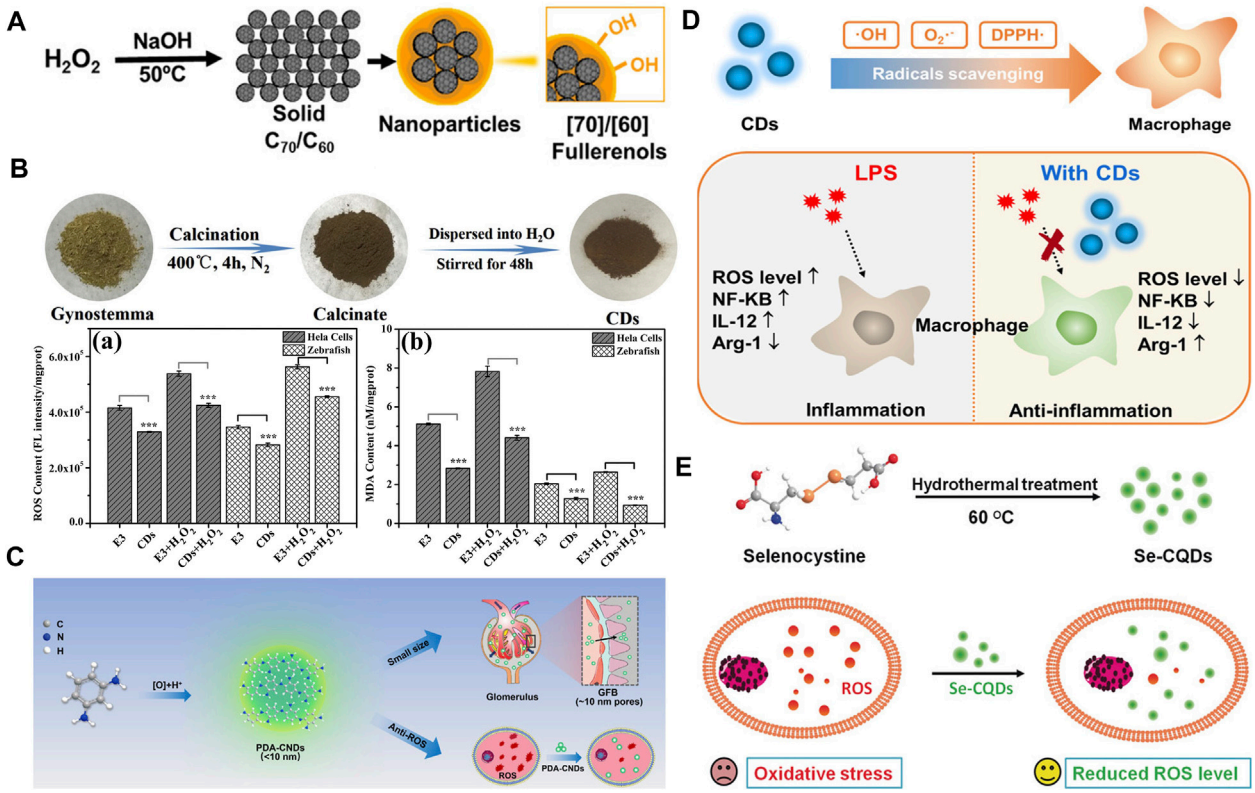

FIGURE 1
(A) Preparation of C_{70}-OH and C_{60}-OH nanoparticles against oxidative injury (Zhou et al., 2017). **(B)** Carbon dots derived from gynostemma as antioxidant against H_2O_2-induced oxidative in both Hela cells and zebrafish (Wei et al., 2019). **(C)** Phenylenediamine-based carbon nanodots were used to eliminate ROS in acute kidney injury (Gao et al., 2020). **(D)** Carbon dots made of citric acid and glutathione serve as a highly efficient intracellular ROS scavenger in macrophage (Wang et al., 2020a). **(E)** Selenium-doped carbon quantum dots protecting biosystems from oxidative stress (Li F. et al., 2017).

protection effect. Amino acid modification is also used to change the hydrophilic properties; Zhou et al. find that L-lysine modified C_{70} fullerenes reveal higher scavenging activity than L-alanine modified C_{70} fullerene (Zhou et al., 2018). The difference is because of the different integrity of fullerene cage. Recently, C_{60}-PDA-GSH are rationally designed and synthesized, and their relative cytoprotective effects against oxidative stress provide a candidate for the treatment of ROS-related diseases (Zhang et al., 2019). During the typical synthesis, C_{60} is modified by the self-polymerization of dopamine into C_{60}-PDA hybrids. Subsequently, glutathione (GSH) is covalently immobilized onto the surface of C_{60}-PDA hybrids *via* Michael addition reaction. Inspired by above successful preparation of various derivatives and relative modifications, Chen and her colleagues compare the discrepancy of three fullerene derivatives on free radical scavenging efficiency (Yin et al., 2009). $C_{60}[C(COOH)_2]_2$ are found to be significantly less active than carboxyl-free fullerenes $C_{60}(OH)_{22}$ and $Gd@C_{82}(OH)_{22}$. Of particular importance, these fullerene derivatives can neutralize all physiologically relevant ROS and RNS, promising great potential in biomedical applications.

Generally, carbon dots (CDs) usually have an average particle size of 2–8 nm, and they have been widely used in biomedical fields due to their good photochemical properties, biocompatibility, as well as stability. Besides the bioimaging applications based on the fascinating fluorescence performance, some CDs have also been employed to treat oxidative stress-related diseases because of their great ROS scavenging ability. For instance, CDs prepared by using gynostemma and garlic as carbon source have been successfully synthesized (Figure 1B) (Wei et al., 2019). These CDs can efficiently eliminate excess ROS in both Hela cells and zebrafish. In another study, phenylenediamine-based CDs have been well designed and constructed for the treatment of acute kidney injury. The ultra-small size can facilitate the CDs to penetrate the glomerular filtration barrier and present the antioxidant properties at the kidney target (Figure 1C) (Gao et al., 2020). Since the various origins of carbon have been reported, it has provided an excellent demonstration for the "bottom-to-top" strategy. However, the mechanism of the antioxidant effect is rarely elucidated. Besides the precursor selection method mentioned above, some agents are used to enhance the antioxidant ability. A kind of CDs made from glutathione and citric acid *via* hydrothermal method has been designed with the ability to eliminate various free radicals including DPPH· (1,1-diphenyl-2-trinitro phenylhydrazine free radicals, a kind of experimental RNS), ·OH, and $O_2^{\cdot-}$ (Figure 1D) (Wang et al., 2020a). In addition, metallic heteroatom selenium has been doped into the CDs to fulfill the need for OH scavenging and imaging at the same time (Figure 1E) (Li F. et al., 2017).

As a typical representative of CDs, graphene quantum dots (GQDs) are well researched because of their low toxicity and unique structure. Researchers have created GQDs with antioxidant

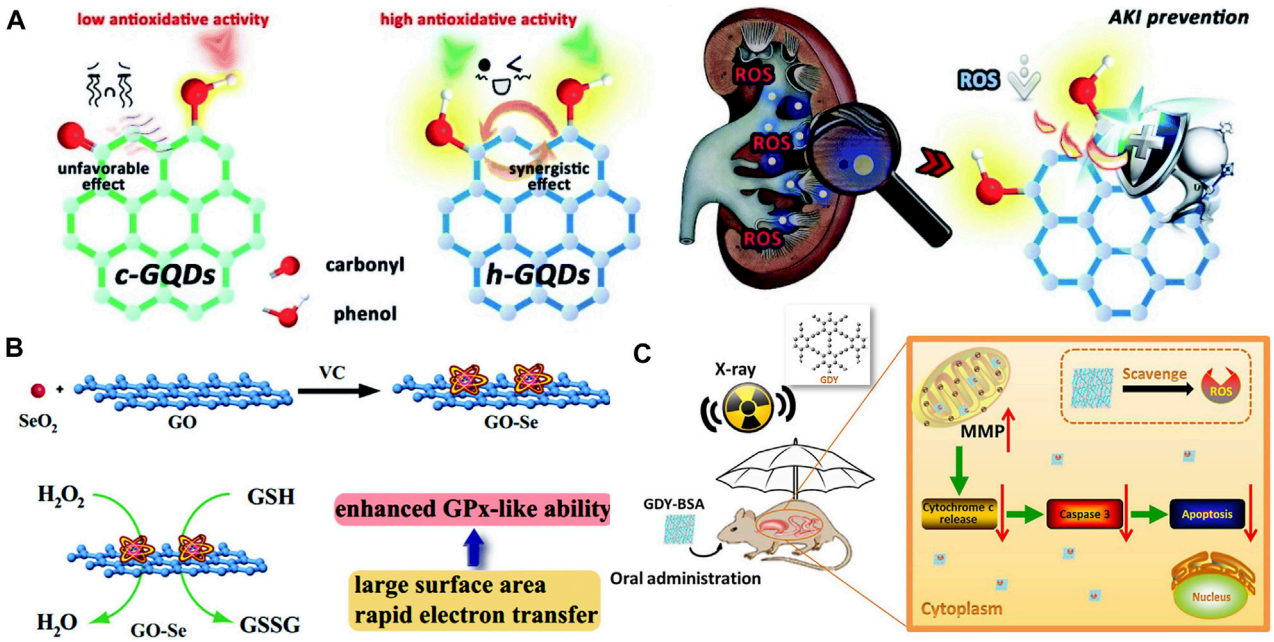

FIGURE 2
(A) Usage of phenol-like group functionalized graphene quantum dots (h-GQDs) for the treatment of acute kidney injury (Wang et al., 2020b). **(B)** GO-Se nanocomposites with great GPx-like properties to alleviate cellular oxidative stress (Huang et al., 2017). **(C)** Oral administration of BSA-modified GDYs for gastrointestinal radioprotection (Xie et al., 2020).

characteristics, which can efficiently scavenge free radicals and protect cells from oxidative damage. They say ROS was eliminated *via* surface imperfections and unpaired electrons. Furthermore, the π-conjugated nature facilitated electron transformation and storage (Chong et al., 2016). Based on this theory, phenol-like group functionalized GQDs were rationally designed and well proved to be a better antioxidant in the acute kidney injury model (Figure 2A) (Wang et al., 2020b). Other attempts to improve scavenging results have been made, such as the use of phosphorus-doped GQDs in the efficient elimination of DPPH and ·OH (Li Y. et al., 2017).

One-dimension carbon nanotubes

Carbon nanotubes (CNTs) are seamless cylinders of rolled-up graphene sheets with distinct intrinsic characteristics, which can be divided into single-wall and multiwall carbon nanotubes, with diameters ranging from 0.4 to 2.5 nm and a few nanometers to 100 nm, respectively. CNTs are believed to be a radical scavenger due to their exceptional electron donation and acceptability abilities acquired from conjugated carbon double bonds. Researchers demonstrate that pristine single-walled CNTs and phenolic-functionalized CNTs are powerful antioxidants (Lucente-Schultz et al., 2009). According to another study, two types of carbon nanotubes with varying thicknesses and lengths exhibit comparable free radical scavenging efficacy. CNTs with smaller diameters and shorter lengths have been shown to be more poisonous and capable of causing inflammation. In another study, the effects of carbon nanotube length, diameter, and chirality on their ability to scavenge free radicals are calculated theoretically (Galano, 2009). According to previous studies, the length and chirality of CNTs usually reveal no effect on antioxidant efficacy. The antioxidant activity of armchair nanotubes can be more affected by changes in tube diameter. Aside from physical properties, both amine modification and polydopamine modification can improve the antioxidant activities of CNTs, as demonstrated in stroke and skin models (Lee et al., 2011; Liang et al., 2019). The location of defects in the material also influences their ability to scavenge free radicals. Methods like ball milling, benzoyl peroxide, and acid treatment can consecutively create defect sites, increasing free radical scavenging ability, whereas microwave treatment repair flaws. Significantly, extended microwave time can extremely reduce fault locations and free radical capabilities (Shieh and Wang, 2014).

Two-dimension carbon graphene and graphdiyne

Since the first discovery of graphene (G) in 2004, a number of its derivatives, from graphene oxide (GO) to reduced graphene oxide (RGO), have been well investigated in various fields. The obvious difference between G and GO is the addition of oxygen atoms bound to the carbon scaffold. As a result, G is hydrophobic in nature, whereas GO is hydrophilic, which is more applicable *in vivo*. RGO is reported to react with DPPH·, $O_2^{\cdot-}$, and OH. The ability to clear OH has been ranked as high as few-layer graphene, GO, and RGO. These results indicate that the primary active sites are highly associated with the pristine graphenic network rather than oxygen-containing functional groups (Qiu et al., 2014; Suresh et al., 2015). In addition, the oxidation resistance of G is also solved through its use as a template to enhance the oxidation activity of molecules of clusters. Huang et al. have reported that GO-Se nanocomposites with excellent GPx-like

properties can efficiently protect cells against oxidative stress *in vitro* (Figure 2B) (Huang et al., 2017).

As a new 2D form of carbon, graphdiyne (GDY) is only one atom thick. Owing to the presence of its good sp- and sp^2-hybridized carbon atoms, evenly spaced pores, high conjugation, and unique electronic, physical, and chemical properties, a lot of work has been done to find ways to use it. It is a 2D periodic structure whose fundamental structural unit is a big triangular ring containing 18 carbon atoms. Due to the unique structure of GDY, it has been proved that GDY usually exhibits better performance and higher stability than other carbon-based materials in various practical applications including the fields of energy and biomedicine. For the scavenging free radicals usages, bovine serum albumin (BSA)-modified GDYs have been used as a high-performance radioprotector (Figure 2C) (Xie et al., 2020). These BSA-modified GDYs hold a strong free radical scavenging ability including $O_2^{\cdot-}$ and OH. By eliminating intracellular ROS, BSA-modified GDYs can extremely reduce DNA damage and protect major organs from radiation-induced damage *in vivo*. In addition, GDYs can be doped into sodium hyaluronate hydrogel to form nano-graphdiyne hydrogels (Xie et al., 2022). These well-prepared graphdiyne-contained hydrogels not only exhibit great broad-spectrum free radical scavenging activity, but also process admirable physically shielding function against low-energy X-ray, which can be used for the external skin radioprotection. Compared to G and its derivatives, GDYs and their derivatives seem to hold better free radical scavenging activity in biomedical fields, which can be researched more in the future.

Conclusion and perspective

In this review, we summarize the rational design and synthesis of 0-, 1-, and 2-dimensional carbon materials and their applicability as antioxidants in biomedical fields. As expected, low-dimensional carbon materials can offer the benefits of a high ratio of surface area to volume, ease of modification, and high-efficiency electron transmission, as well as promising anti-oxidation regulation and application potential. Prior to further clinical translation, numbers of concerns must be further researched and resolved. First, as dual-active materials, carbon-based nanomaterials can not only scavenge ROS/RNS, but also demonstrate a promotion effect on ROS/RNS formation in some settings; however, the mechanism underlying this action remains unknown. Accordingly, the impact of this dual activity on biological use must be taken into account in order to determine the optimal therapeutic dose and typical application environment. Second, the ultra-small size and strong reactivity of low-dimensional carbon materials necessitate the additional research into their biosafety and systemic toxicity. Future studies must focus on the long-term toxicity and multiple organ toxicity after proper administration, given that the vast majority of clinical application situations require materials to reach the bloodstream. How to evaluate the relationship between the structure and oxidation resistance of low-dimensional carbon materials and how to realize their relative anti-oxidative properties by selecting appropriate preparation strategy, surface modification, element doping, as well as other factors must be the final and most fundamental issue.

Author contributions

All authors contributed to the conception, design, writing, and final approval of this mini review.

Funding

Financial support was provided by National Natural Science Foundation of China (22075011, 22178140, 81901036, 21908005), Jilin Province Science and Technology Development Plan Project (20200201358JC), Fundamental Research Funds for the Central Universities (BUCT-PT-2021-05), Bethune Plan of Jilin University (2022B30), and Chinese Stomatological Association Youth Clinical Research Foundation for Orthodontics (COS-B2021-06).

Conflict of interest

The authors declare that the research was conducted in the absence of any commercial or financial relationships that could be construed as a potential conflict of interest.

Publisher's note

References

Bao, X., Zhao, J., Sun, J., Hu, M., and Yang, X. (2018). Polydopamine nanoparticles as efficient scavengers for reactive oxygen species in periodontal disease. *ACS Nano* 12, 8882–8892. doi:10.1021/acsnano.8b04022

Chong, Y., Ge, C., Fang, G., Tian, X., Ma, X., Wen, T., et al. (2016). Crossover between anti- and pro-oxidant activities of graphene quantum dots in the absence or presence of light. *ACS Nano* 10, 8690–8699. doi:10.1021/acsnano.6b04061

Galano, A. (2009). Influence of diameter, length, and chirality of single-walled carbon nanotubes on their free radical scavenging capability. *J. Phys. Chem. C* 113, 18487–18491. doi:10.1021/jp904646q

Gao, J., Liu, Y., Jiang, B., Cao, W., Kan, Y., Chen, W., et al. (2020). Phenylenediamine-based carbon nanodots alleviate acute kidney injury via preferential renal accumulation and antioxidant capacity. *Acs. Appl. Mat. Interfaces* 12, 31745–31756. doi:10.1021/acsami.0c05041

Huang, Y., Liu, C., Pu, F., Liu, Z., Ren, J., and Qu, X. (2017). A GO-Se nanocomposite as an antioxidant nanozyme for cytoprotection. *Chem. Commun.* 53, 3082–3085. doi:10.1039/c7cc00045f

Lee, H., Park, J., Yoon, O., Kim, H., Lee, D., Kim, D., et al. (2011). Amine-modified single-walled carbon nanotubes protect neurons from injury in a rat stroke model. *Nat. Nanotechnol.* 6, 121–125. doi:10.1038/nnano.2010.281

Li, F., Li, T., Sun, C., Xia, J., Jiao, Y., and Xu, H. (2017a). Selenium-doped carbon quantum dots for free-radical scavenging. *Angew. Chem. Int. Ed.* 56, 9910–9914. doi:10.1002/anie.201705989

Li, Y., Li, S., Wang, Y., Wang, J., Liu, H., Liu, X., et al. (2017b). Electrochemical synthesis of phosphorus-doped graphene quantum dots for free radical scavenging. *Phys. Chem. Chem. Phys.* 19, 11631–11638. doi:10.1039/c6cp06377b

Liang, Y., Zhao, X., Hu, T., Han, Y., and Guo, B. (2019). Mussel-inspired, antibacterial, conductive, antioxidant, injectable composite hydrogel wound dressing to promote the

regeneration of infected skin. *J. Colloid. Interface. Sci.* 556, 514–528. doi:10.1016/j.jcis.2019.08.083

Liu, Q., Zhang, X., Zhang, X., Zhang, G., Zheng, J., Guan, M., et al. (2013). C_{70}-carboxyfullerenes as efficient antioxidants to protect cells against oxidative-induced stress. *Acs. Appl. Mater Interfaces* 5, 11101–11107. doi:10.1021/am4033372

Liu, Y., Ai, K., Ji, X., Askhatova, D., Du, R., Lu, L., et al. (2016). Comprehensive insights into the multi-antioxidative mechanisms of melanin nanoparticles and their application to protect brain from injury in ischemic stroke. *J. Am. Chem. Soc.* 139, 856–862. doi:10.1021/jacs.6b11013

Liu, Y., Cheng, Y., Zhang, H., Zhou, M., Yu, Y., Lin, S., et al. (2020). Integrated cascade nanozyme catalyzes *in vivo* ROS scavenging for anti-inflammatory therapy. *Sci. Adv.* 6, eabb2695. doi:10.1126/sciadv.abb2695

Liu, Y., and Shi, J. (2019). Antioxidative nanomaterials and biomedical applications. *Nano Today* 27, 146–177. doi:10.1016/j.nantod.2019.05.008

Lucente-Schultz, R., Moore, V., Leonard, A., Price, B., Kosynkin, D., Lu, M., et al. (2009). Antioxidant single-walled carbon nanotubes. *J. Am. Chem. Soc.* 131, 3934–3941. doi:10.1021/ja805721p

Qiu, Y., Wang, Z., Owens, A., Kulaots, I., Chen, Y., Kane, A., et al. (2014). Antioxidant chemistry of graphene-based materials and its role in oxidation protection technology. *Nanoscale* 6, 11744–11755. doi:10.1039/c4nr03275f

Shieh, Y., and Wang, W. (2014). Radical scavenging efficiencies of modified and microwave-treated multiwalled carbon nanotubes. *Carbon* 79, 354–362. doi:10.1016/j.carbon.2014.07.077

Sun, H., Zhou, Y., Ren, J., and Qu, X. (2018). Carbon nanozymes: Enzymatic properties, catalytic mechanism, and applications. *Angew. Chem. Int. Ed.* 57, 9224–9237. doi:10.1002/anie.201712469

Suresh, D., UdayabhanuPavan Kumar, M., Nagabhushana, H., and Sharma, S. (2015). Cinnamon supported facile green reduction of graphene oxide, its dye elimination and antioxidant activities. *Mater. Lett.* 151, 93–95. doi:10.1016/j.matlet.2015.03.035

Wang, H., Yu, D., Fang, J., Zhou, Y., Li, D., Liu, Z., et al. (2020b). Phenol-like group functionalized graphene quantum dots structurally mimicking natural antioxidants for highly efficient acute kidney injury treatment. *Chem. Sci.* 11, 12721–12730. doi:10.1039/d0sc03246h

Wang, H., Zhang, M., Ma, Y., Wang, B., Huang, H., Liu, Y., et al. (2020a). Carbon dots derived from citric acid and glutathione as a highly efficient intracellular reactive oxygen species scavenger for alleviating the lipopolysaccharide-induced inflammation in macrophages. *Acs. Appl. Mat. Interfaces* 12, 41088–41095. doi:10.1021/acsami.0c11735

Wei, X., Li, L., Liu, J., Yu, L., Li, H., Cheng, F., et al. (2019). Green synthesis of fluorescent carbon dots from gynostemma for bioimaging and antioxidant in zebrafish. *Acs. Appl. Mat. Interfaces* 11, 9832–9840. doi:10.1021/acsami.9b00074

Xie, J., Wang, C., Wang, N., Zhu, S., Mei, L., Zhang, X., et al. (2020). Graphdiyne nanoradioprotector with efficient free radical scavenging ability for mitigating radiation-induced gastrointestinal tract damage. *Biomaterials* 244, 119940. doi:10.1016/j.biomaterials.2020.119940

Xie, J., Zhao, M., Wang, C., Zhu, S., Niu, W., Yong, Y., et al. (2022). External use of Nano-graphdiyne hydrogel for skin radioprotection via both physically shielding of low-energy X-ray and chemically scavenging of broad-spectrum free radicals. *Chem. Eng. J.* 430, 132866. doi:10.1016/j.cej.2021.132866

Yao, J., Cheng, Y., Zhou, M., Zhao, S., Lin, S., Wang, X., et al. (2018). ROS scavenging Mn_3O_4 nanozymes for *in vivo* anti-inflammation. *Chem. Sci.* 9, 2927–2933. doi:10.1039/c7sc05476a

Yin, J., Lao, F., Fu, P., Wamer, W., Zhao, Y., Wang, P., et al. (2009). The scavenging of reactive oxygen species and the potential for cell protection by functionalized fullerene materials. *Biomaterials* 30, 611–621. doi:10.1016/j.biomaterials.2008.09.061

Zhang, X., Ma, Y., Fu, S., and Zhang, A. (2019). Facile synthesis of water-soluble fullerene (C_{60}) nanoparticles via mussel-inspired chemistry as efficient antioxidants. *Nanomaterials* 9, 1647. doi:10.3390/nano9121647

Zhou, Y., Li, J., Ma, H., Zhen, M., Guo, J., Wang, L., et al. (2017). Biocompatible [60]/[70] fullerenols: Potent defense against oxidative injury induced by reduplicative chemotherapy. *Acs. Appl. Mat. Interfaces* 9, 35539–35547. doi:10.1021/acsami.7b08348

Zhou, Y., Zhen, M., Guan, M., Yu, T., Ma, L., Li, W., et al. (2018). Amino acid modified [70] fullerene derivatives with high radical scavenging activity as promising bodyguards for chemotherapy protection. *Sci. Rep.* 8, 16573. doi:10.1038/s41598-018-34967-7

frontiers | Frontiers in Microbiology

TYPE Original Research
PUBLISHED 06 February 2023
DOI 10.3389/fmicb.2023.1109972

OPEN ACCESS

EDITED BY
Zhen Liu,
Beijing University of Chemical Technology, China

REVIEWED BY
Xiaomin Liu,
Qingdao University, China
Baocun Zhu,
University of Jinan, China

*CORRESPONDENCE
Gongying Wang
✉ wanggongying1102@126.com
Yanyan Diao
✉ yydiao@ipe.ac.cn

SPECIALTY SECTION
This article was submitted to Antimicrobials, Resistance and Chemotherapy, a section of the journal Frontiers in Microbiology

RECEIVED 06 December 2022
ACCEPTED 09 January 2023
PUBLISHED 06 February 2023

CITATION
Hu Y, Xing Y, Ye P, Yu H, Meng X, Song Y, Wang G and Diao Y (2023) The antibacterial activity and mechanism of imidazole chloride ionic liquids on *Staphylococcus aureus*. *Front. Microbiol.* 14:1109972. doi: 10.3389/fmicb.2023.1109972

The antibacterial activity and mechanism of imidazole chloride ionic liquids on *Staphylococcus aureus*

Yanhui Hu[1,2,3,4], Yuyuan Xing[2,3,4], Peng Ye[5], Haikuan Yu[6], Xianglei Meng[2,3], Yuting Song[2,3], Gongying Wang[1,3]* and Yanyan Diao[2,3,4]*

[1]Chengdu Institute of Organic Chemistry, Chinese Academy of Sciences, Chengdu, China, [2]Beijing Key Laboratory of Ionic Liquids Clean Process, CAS Key Laboratory of Green Process and Engineering, State Key Laboratory of Multiphase Complex Systems, Institute of Process Engineering, Chinese Academy of Sciences, Beijing, China, [3]University of Chinese Academy of Sciences, Beijing, China, [4]Innovation Academy for Green Manufacture, Chinese Academy of Sciences, Beijing, China, [5]Beijing Key Laboratory of Lignocellulosic Chemistry, Beijing Forestry University, Beijing, China, [6]Senior Department of Orthopedics, Chinese PLA Medical School, Beijing, China

Ionic liquids (ILs) have garnered increasing attention in the biomedical field due to their unique properties. Although significant research has been conducted in recent years, there is still a lack of understanding of the potential applications of ILs in the biomedical field and the underlying principles. To identify the antibacterial activity and mechanism of ILs on bacteria, we evaluated the antimicrobial potency of imidazole chloride ILs (C_nMIMCl) on *Staphylococcus aureus* (*S. aureus*). The toxicity of ILs was positively correlated to the length of the imidazolidinyl side chain. We selected C_{12}MIMCl to study the mechanism of *S. aureus*. Through the simultaneous change in the internal and external parts of *S. aureus*, C_{12}MIMCl caused the death of the bacteria. The production of large amounts of reactive oxygen species (ROS) within the internal parts stimulated oxidative stress, inhibited bacterial metabolism, and led to bacterial death. The external cell membrane could be destroyed, causing the cytoplasm to flow out and the whole cell to be fragmented. The antibacterial effect of C_{12}MIMCl on skin abscesses was further verified *in vivo* in mice.

KEYWORDS

ionic liquids, *Staphylococcus aureus*, antibacterial activity, mechanism, skin abscess

1. Introduction

In recent years, diseases caused by bacteria have plagued human beings. Although antibiotics have alleviated this problem, excessive use also causes problems such as bacterial resistance. Considering the overuse of antibiotics and the increasing resistance to antibacterial agents, there is an urgent need to develop tunable antibacterial compounds and drug delivery systems to treat high-mortality diseases. Moreover, the COVID-19 pandemic has garnered more attention than ever regarding the need for more effective medical methods to diagnose and cure the disease. New, high-performing antimicrobial and antiviral materials have to be developed. As a combination of salt and organics, ionic liquids (ILs) have been endowed with abundant and diverse properties (Zhang et al., 2014), including low volatility, a wide electrochemical window, a highly tunable structure, and thermal stability, which have been widely used as solvents (Liang et al., 2019; Shamshina and Berton, 2020), extractants (Gao et al., 2020; Wang et al., 2022), catalysts (Li et al., 2021; Sadjadi, 2021; Yuan et al., 2023), electrolytes (Fu et al., 2022), and so on. ILs could be self-assembled into low-dimensional nanoparticles due to their strong interactions between the cations and anions, H-bond direction, and large molecular volume (Dupont, 2011; Chen et al., 2014). Their unique properties have attracted increasing attention in the biomedical field, such as the extraction and conservation of proteins (Schröder, 2017; Veríssimo et al., 2021; Xue et al., 2022) and nuclear

acids (Dinis et al., 2020), drug transport enhancers (Md Moshikur et al., 2020; Zhang et al., 2020), drug carriers (Lu et al., 2020; Moshikur et al., 2021), drug additives (Tang et al., 2016), and disease diagnosis (Zhu et al., 2020) and therapy (Albadawi et al., 2021; Gao et al., 2021). The nanoparticle structure of ILs provides a variety of possibilities for biomedical applications. *Staphylococcus aureus* is a common foodborne pathogenic gram-positive bacterium which can cause a variety of serious infections (e.g., pneumonia, enteritis, pericarditis, and sepsis) in humans and animals through the skin and food (Shangguan et al., 2015; Nithya and Sundrarajan, 2020). In the treatment process, *S. aureus* has strong resistance and low susceptibility to drugs; thus, it is urgent to develop new ingredients to counteract the problem of drug resistance (Hess et al., 2005). In this study, *S. aureus* was selected to study the toxicity and mechanism of ILs on the bacterium.

Although ILs have been extensively studied in various directions for biomedical applications (Egorova et al., 2017), they currently remain in the preliminary stage due to a lack of systematic research and theoretical basis. In addition, there is little relevant research on ILs as an agent *in vivo*. An exciting avenue for research is to determine whether ILs can be used in developing antibacterial drugs due to their wide variety, adjustable structure, excellent properties, and the mechanism by which they interact with bacteria. Florio et al. (2019) compared and evaluated the antimicrobial efficacy of 15 ILs, including 1-methyl-3-dodecylimidazolium bromide, 1-dodecyl-1-methylpyrrolidinium bromide, and 1-dodecyl-1-methylpiperidinium bromide, which had strong inhibitory effects on the biofilm formation of *S. aureus* or *Pseudomonas aeruginosa* (*P. aeruginosa*) (Florio et al., 2019). Brunel et al. (2016) found that triphenylamine phosphonium ILs could self-assemble into nanoparticles, which have a good antibacterial effect on *S. aureus*. The IL nanoparticles were likely to strongly affect bacterial metabolism (Brunel et al., 2016). Although some researchers have speculated on the mechanism by which ILs interact with *S. aureus*, it remains unknown how ILs affect bacterial membranes and influence bacterial metabolism. Further studies are needed to better understand the mechanisms involved in antibacterial activity.

Because imidazole chloride ILs are widely available and studied in a variety of fields, a series of C_nMIMCl were chosen to investigate toxicity mechanisms on bacteria and gain additional insight into the effects of IL structure on antibacterial properties. This study explored the toxicity and mechanism of ILs in gram-positive bacteria (*S. aureus*) and designed and developed ILs for infection prevention and control. A skin abscess model was established to demonstrate the antimicrobial efficacy of ILs *in vivo*.

2. Materials and methods

2.1. Strains, culture conditions, and ILs

The *S. aureus* BNCC 186335 and USA300-sfgfp strains were purchased from Forhigh Biotech. The *S. aureus* strain was cultivated in LB medium (18 g/L Nutrient Broth (NB), Solarbio) for 24 h at 37°C and 180 r/min in a shaker incubator. A microplate reader (Tecan, Infinite M2000) was used to measure OD_{600}. ILs (C_2MIMCl, C_3MIMCl, C_4MIMCl, C_6MIMCl, C_8MIMCl, C_{12}MIMCl, C_{16}MIMCl, ≥99%) were prepared by Shanghai Cheng Jie Chemical Co., Ltd. Then, the ILs were diluted in sterile, distilled water. Cy5 NHS Ester (Cy5, SE) was purchased from Beijing Fanbo Biochemicals Co., Ltd. Then, 4% of the paraformaldehyde fix solution was purchased from Solarbio.

2.2. Antibacterial assay

Iconic liquids were diluted in sterile, distilled water following the corresponding concentration gradient. Then, 50 μL of bacteria solutions and different ILs were added to 5 ml of LB medium. Afterward, mixed solutions were hatched at 37°C and 180 r/min in a shaker incubator for 24 h. Before measuring OD_{600}, the solution was fully shaken to distribute *S. aureus* and ensure the accuracy of the measurement. Finally, 100 μL of solutions were removed from each sample and placed into 96-well plates to measure OD_{600}. To avoid human or machine error, every OD_{600} value was repeated at least three times. EC50s were determined from OD_{600} by GraphPad Prism8. The activity of *S. aureus* cultured with ILs was observed by a confocal microscope, and the fluorescence was quantified.

Then, 200 μL of IL was added to 10 mL of solid LB medium (18 g/L NB, 1L water, and 15 g agarose), which was melted to liquid in advance and put in 10-cm plates. Then, 100 μL of bacterial suspension ($OD_{600=}$ 0.15) with further dilution was spread on solid LB plates and cultured at 37°C for 48 h. The CFUs were counted after being cultured, and the cultures were photographed with a camera.

2.3. Oxidative stress in *S. aureus*

C_3MIMCl or C_{12}MIMCl was added to *S. aureus* (OD_{600} = 0.15) and mixed with the ROS Assay Kit (DCFH-DA), and the mixed solution was placed in a 96-well plate for 30 min at 37°C. Then, the ROS value was detected with the microplate reader at the excitation wavelength of 488 nm and the emission wavelength of 525 nm. Following the above experimental procedure, 200 μL of the mixture was added to a confocal dish, and fluorescence was photographed using confocal laser scanning microscopy (Nikon Corporation, A1, CLSM) at the excitation wavelength of 488 nm with green as the pseudo color.

2.4. Surface morphology characterization and status observation of *S. aureus*

Staphylococcus aureus (OD_{600} = 0.15) was cultured in a liquid LB medium with ILs within 3 h at 37°C. Then, the bacteria were washed with PBS three times and fixed in 4% of the paraformaldehyde fix solution at 4°C overnight. The next day, bacteria were washed with PBS three times and treated with ethanol gradient dehydration at different concentrations (30, 40, 50, 60, 70, 80, 90, 95, and 100%). Bacteria were successfully mixed with different ethanol solution concentrations, were left to stand, were dehydrated for 15 min, and were collected by centrifugation. Finally, the bacteria dehydrated with 100% ethanol onto the tin foil was dropped and dried at 37°C for 2 h. The morphological changes of *S. aureus* treated with ILs were characterized by scanning electron microscopy (SEM, HITACHI, SU8020).

S. aureus was cultured with ILs, centrifuged (8000 r/min, 8 min), washed with water (3 times), and fixed with glutaraldehyde solution (PH = 7.4) overnight. They were taken in cross-sections and stained for further transmission electron microscopy (TEM, HITACHI, H-7650B) observation.

2.5. Measurement of *S. aureus* surface zeta potential

S. aureus (OD_{600} = 0.25) was treated with C_3MIMCl and C_{12}MIMCl (the final concentrations: 0.01 mM, 0.04 mM, and 0.16 mM) in liquid LB medium at 37°C for 3 h with gentle shaking. Then, *S. aureus* was washed with PBS three times and sterilized with water one time a day. The obtained bacteria were dispersed in 1 mL of water. The uniform suspension was measured for zeta potential using a Zetasizer Nano ZS (Malvern Instruments Ltd., Zetasizer Nano ZS90). As a control group, the bacteria were treated with an LB medium containing corresponding volumes of water at the same conditions. At the same time, we used Cy5, SE labeled C_{12}MIMCl to interact with *S. aureus* and CLSM to observe the interaction between IL and bacteria.

2.6. Mice

BALB/c mice (6–8 weeks old, female) were obtained from Vital River Laboratories (Beijing, China). The Institutional Animal Care and Use Committees approved the animal protocol of the Institute of Process Engineering, Chinese Academy of Sciences (approval ID: IPEAECA 2022103). This study was performed in strict accordance with the Regulations for the Care and Use of Laboratory Animals and the Guideline for the Ethical Review of Animals.

2.7. Skin abscess model and antibacterial activity of ionic liquid *in vivo*

For the skin abscess model, mice were divided into three groups (controls, infected group, and ILs). Mice were anesthetized with pentobarbital sodium (1%) and inoculated with 100 μl of PBS containing 10^{13} cfu/L *S. aureus* or sterile PBS in the right flank by subcutaneous injection. After abscess formation, 50 μl of C_{12}MIMCl (2 mM) was injected daily at the abscess site for 3–4 days. We observed the abscess healing continuously. Skin biopsy samples collected on day 11 were fixed and prepared for histopathological evaluation. The tissues were stained with hematoxylin and eosin (H&E) and 4′,6-diamidino-2-phenylindole (DAPI) and visualized by the scanner (3DHISTECH, P250 FLASH).

3. Results and discussion

3.1. Antibacterial activities of C_nMIMCl against *S. aureus*

The antibacterial activities of a series of imidazole chloride ILs against *S. aureus* were determined. To evaluate different ILs' antimicrobial activity against *S. aureus*, different concentrations of six ILs were used to measure EC50 (Figure 1A). The EC50 values in the LB medium of C_2MIMCl, C_3MIMCl, C_4MIMCl, C_6MIMCl, C_8MIMCl, C_{12}MIMCl, C_{16}MIMCl were 76.7, 28.7, 18.2, 3.5, 0.3, 1.9 x 10^{-3}, and 0.5 x 10^{-3} mM for *S. aureus*, respectively. Imidazolium chloride ILs with substituents of 12 and 16 carbon lengths had strong antibacterial effects on *S. aureus*. The toxicity of *S. aureus* increased with the length of the cation side chain. It may be due to the increased hydrophobicity. With an increase in C_nMIMCl concentration, the inhibition rate of *S. aureus* increased. For example, when the concentration of C_{12}MIMCl was 0.0015, 0.0020, 0.0025, and 0.0030 mM, the inhibition rates of *S. aureus* were 23.2, 60.5, 83.1, and 87.7%, respectively (Figure 1B). It showed that the toxicity of C_nMIMCl varied for each concentration. *S. aureus* transfected with a green fluorescent protein (GFP) was incubated with C_3MIMCl or C_{12}MIMCl and observed by CLSM. There was no difference in GFP fluorescence intensity between the C_3MIMCl group and the control group, while *S. aureus* GFP fluorescence intensity in the C_{12}MIMCl group was significantly reduced (Figures 1C, D).

To further verify the toxicity of C_nMIMCl, the less toxic C_3MIMCl and the more toxic C_{12}MIMCl were selected for plate coating experiments (Figure 2). Compared with the control group, there was no bacterial inhibition when the concentration of C_3MIMCl was 0.0040 mM. The inhibition rates were 65.8 ± 0.8%, 89.1 ± 5.1%, and 94.6 ± 4.7% when the C_3MIMCl concentration was 26 mM, 32 mM, and 40 mM, respectively. C_{12}MIMCl showed a significant inhibitory effect on *S. aureus* compared with C_3MIMCl. When the concentrations of C_{12}MIMCl were 0.0026 mM, 0.0032 mM, and 0.0040 mM, the inhibition rates were 9.7 ± 3.9%, 23.0 ± 5.1%, and 98.4 ± 0.8%, respectively. With ∼95% inhibition of *S. aureus*, the concentration used for C_3MIMCl is about 10^4 times higher than that used for C_{12}MIMCl.

The toxicity of C_nMIMCl to *S. aureus* was proportional to the length of the imidazolidinyl side chain. At the same time, the longer the alkyl side chain length of the imidazole, the greater the hydrophobicity of C_nMIMCl. Therefore, the toxicity of C_nMIMCl to *S. aureus* increased with the enhancement of hydrophobicity. It is well known that phospholipid is one of the main components of the cell membrane, and the outer surface of the cell membrane is electronegative. The ILs were easily adsorbed to the bacterial surface due to the positive charge of the cationic part, and then, the ILs interacted with the phospholipid bilayer due to hydrophobicity. Therefore, C_3MIMCl with a short carbon chain and C_{12}MIMCl with a long carbon chain were selected for the subsequent research.

3.2. Oxidative stress of *S. aureus* by C_{12}MIMCl

To further investigate the mechanisms leading to the inhibitory and destructive effects of C_{12}MIMCl on *S. aureus,* as well as the significant reduction of the viability of the exposed bacteria induced by ILs, the release of reactive oxygen species (ROS) within *S. aureus* was explored. ROS is a general term for a class of molecules with oxidative activity produced by cells during energy metabolism under aerobic conditions. In bacteria, excess ROS can damage nucleic acids, proteins, and lipids (Brynildsen et al., 2013). Moreover, it can also lead to bacterial oxidative stress and inhibit bacterial metabolism (Ning et al., 2019; Zhao et al., 2022). Bacterial death occurs when

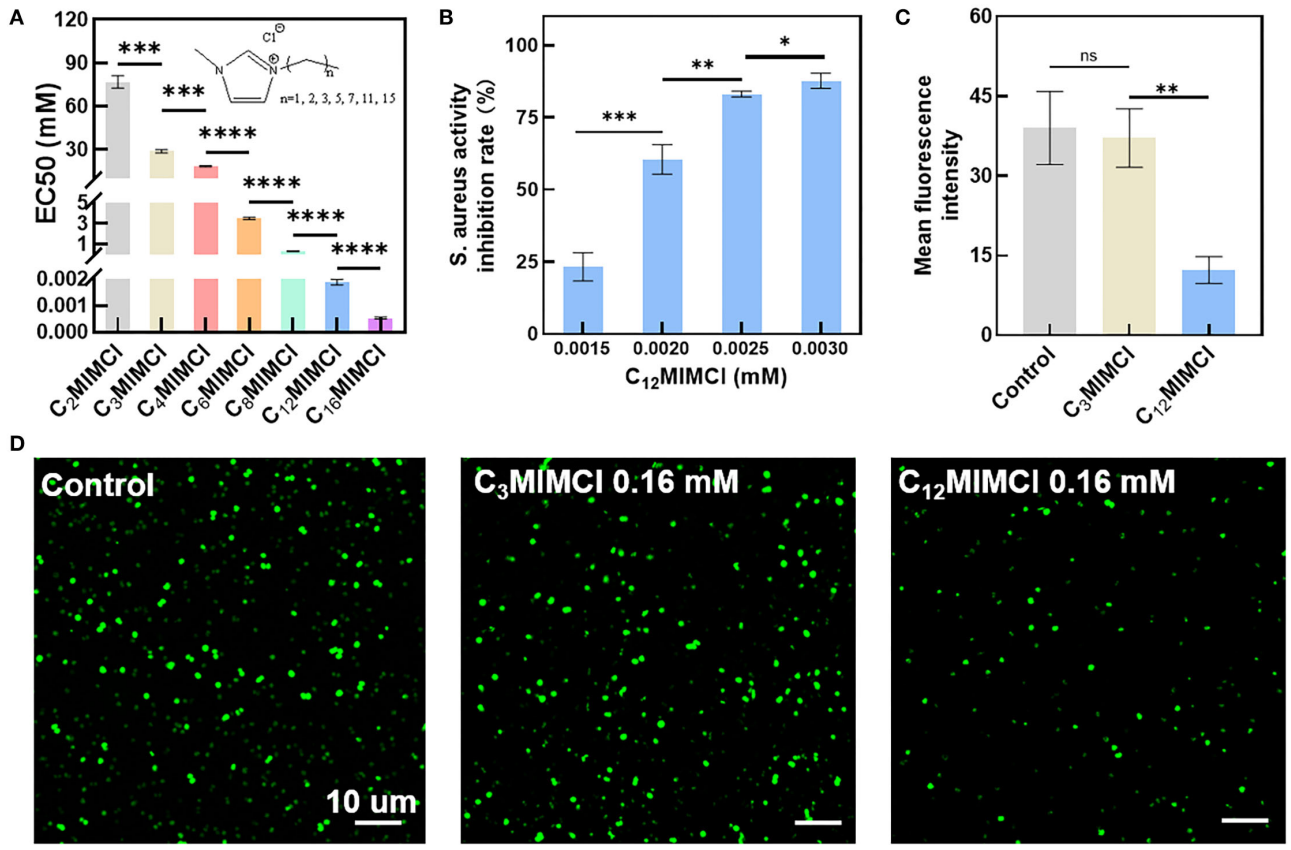

FIGURE 1
Toxicity test of C_nMIMCl against *Staphylococcus aureus*. **(A)** EC50 values of *Staphylococcus aureus* incubated with C_nMIMCl for 24 h. **(B)** Effects of $C_{12}MIMCl$ on *Staphylococcus aureus* at different concentrations. **(C)** Quantitative analysis of bacterial activity. **(D)** CLSM images of bacterial activity. Data in **(A–C)** represent the mean ± s.d. Statistical significance was calculated *via* two-tailed unpaired Student's *t*-test **(A–C)**. Ns means no significant difference, $^{*}P<0.05$, $^{**}P < 0.01$, $^{***}P < 0.001$, $^{****}P < 0.0001$.

intracellular ROS exceeds the cell's ability to detoxify and repair. Therefore, it is necessary to determine the amount of ROS in bacteria to reveal the mechanism of IL acting on bacteria. Figure 3 shows CLSM images of ROS (green). No significant changes in ROS fluorescence values were observed with 0.16 mM C_3MIMCl compared with the control group. It was found that $C_{12}MIMCl$ could significantly increase ROS in bacteria compared with C_3MIMCl at the same concentration, and the ROS gradually increased with an increase in $C_{12}MIMCl$ concentration. Therefore, $C_{12}MIMCl$ could induce ROS release intracellularly.

3.3. Damage to the *S. aureus* membrane by $C_{12}MIMCl$

3.3.1. Surface morphology observation of *S. aureus*

SEM images were utilized to observe the morphological changes of *S. aureus* after incubation with ILs for 3 h. It could be seen that the normal form of *S. aureus* strains displayed regular and clear edges, smooth surfaces with rounded projections, and complete cell walls. To further investigate the antibacterial activities of short and long cation side chains, the damage of C_3MIMCl and $C_{12}MIMCl$ on the bacterial membrane of *S. aureus* was evaluated (Figure 4). Furthermore, similar to their control counterparts, the morphologies of the bacteria treated with 0.16 mM C_3MIMCl for 3 h remained intact and smooth. However, the morphology of *S. aureus* treated with $C_{12}MIMCl$ was collapsed by depression or wrinkling on the surface, indicating that partial or complete membrane lysis might occur. As the concentration of $C_{12}MIMCl$ increased, a greater effect on the surface morphology of *S. aureus* could be observed. This result indicated that $C_{12}MIMCl$ could damage the membranes of *S. aureus*.

3.3.2. Changes on the *S. aureus* surface

Bacterial membrane potential is the proton motive force of bacterial metabolism and respiration. Antibacterial activity strongly correlates with the dissipation of the membrane potential in bacteria (Schilling et al., 2019). When studying the antibacterial mechanisms, the integrity of bacterial membranes is a non-negligible factor. In our study, when the concentration of $C_{12}MIMCl$ was 0.16 mM, $C_{12}MIMCl$ increased the bacterial membrane potential to 16.3%, and the change in membrane potential increased with an increase in ILs concentration. Compared with C_3MIMCl, *S. aureus* showed an increase in zeta potentials after co-culturing with $C_{12}MIMCl$ (0.16 mM) (Figure 5A), indicating that the positively charged $C_{12}MIMCl$ underwent electrostatic interactions with the negatively charged components of the *S. aureus* membrane. With an increase in $C_{12}MIMCl$ concentration, the change in *S. aureus*

10.3389/fmicb.2023.1109972

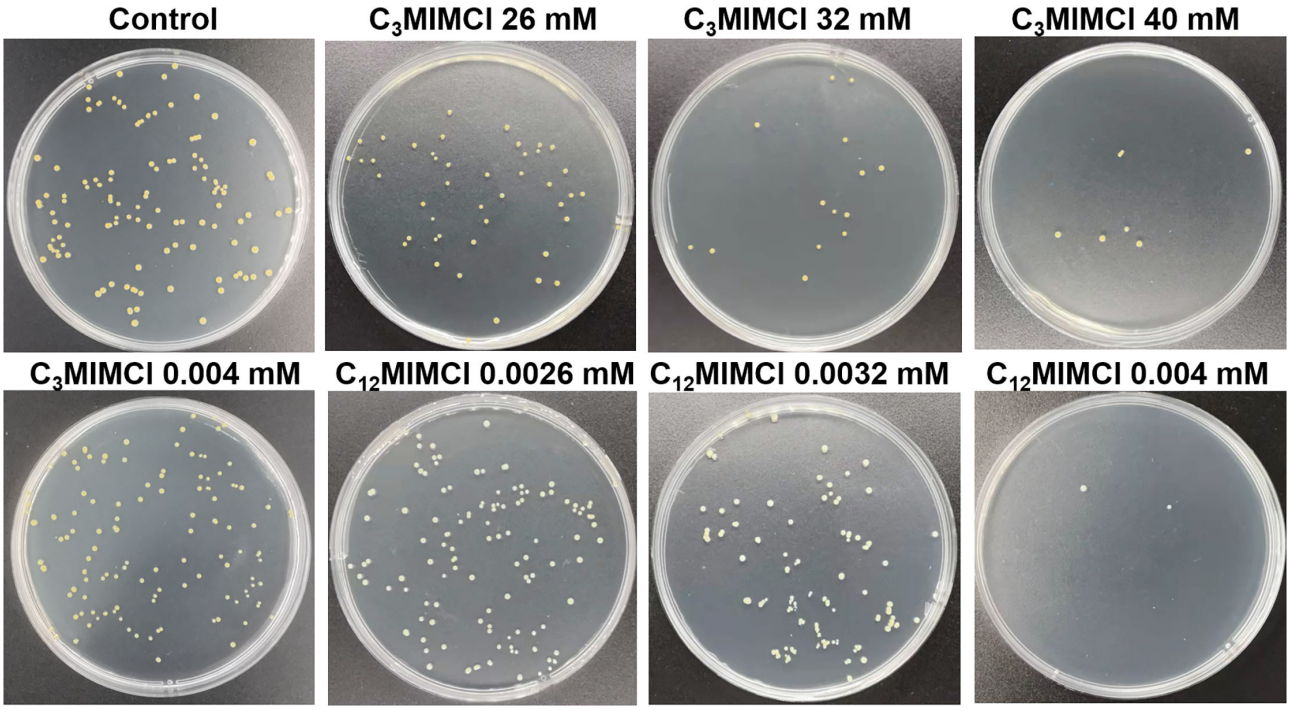

FIGURE 2
Bacterial colony photos of *Staphylococcus aureus* incubated with various concentrations of C_3MIMCl and C_{12}MIMCl for 48 h.

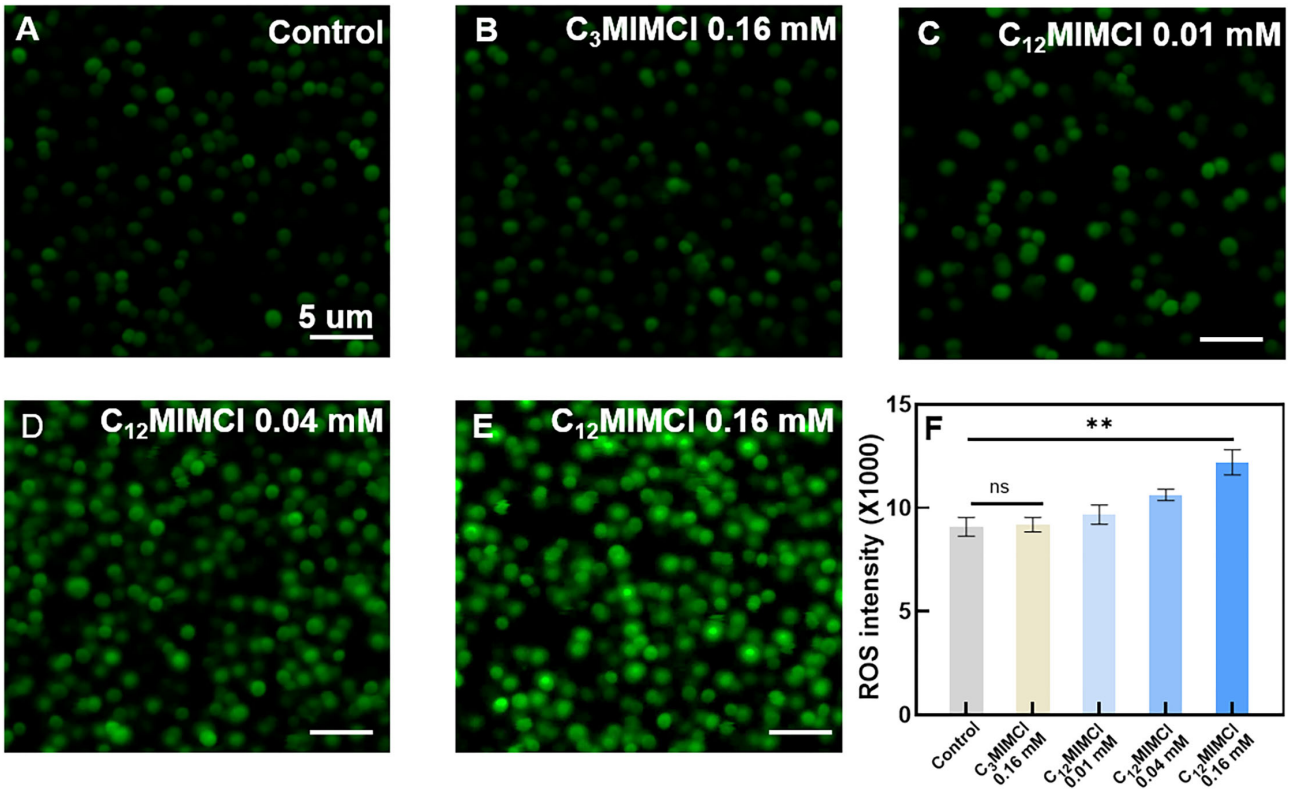

FIGURE 3
Oxidative stress of *Staphylococcus aureus*. **(A)** CLSM images of ROS release from bacteria in control. **(B–E)** CLSM images of ROS release from bacteria in the presence of 0.16 mM C_3MIMCl **(B)**, 0.01 mM C_{12}MIMCl **(C)**, 0.04 mM C_{12}MIMCl **(D)**, 0.16 mM C_{12}MIMCl **(E)**. **(F)** Quantitative analysis of ROS release by a microplate reader. Data in **(F)** represent the mean ± s.d. Statistical significance of **(F)** was calculated *via* two-tailed unpaired Student's *t*-test. Ns means no significant difference, $^{**}P < 0.01$.

10.3389/fmicb.2023.1109972

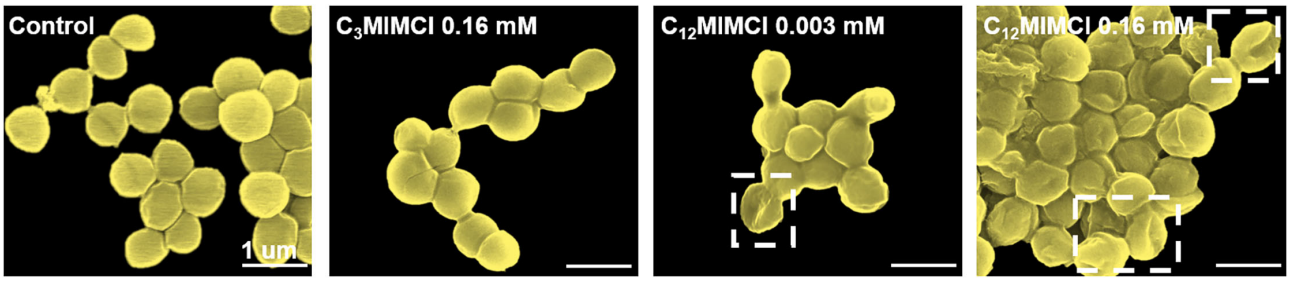

FIGURE 4
SEM characterization of *Staphylococcus aureus* morphologies and membrane integrities after 3h co-culture with water (control group), 0.16 mM C_3MIMCl or different concentrations of C_{12}MIMCl (0.003 mM and 0.16 mM).

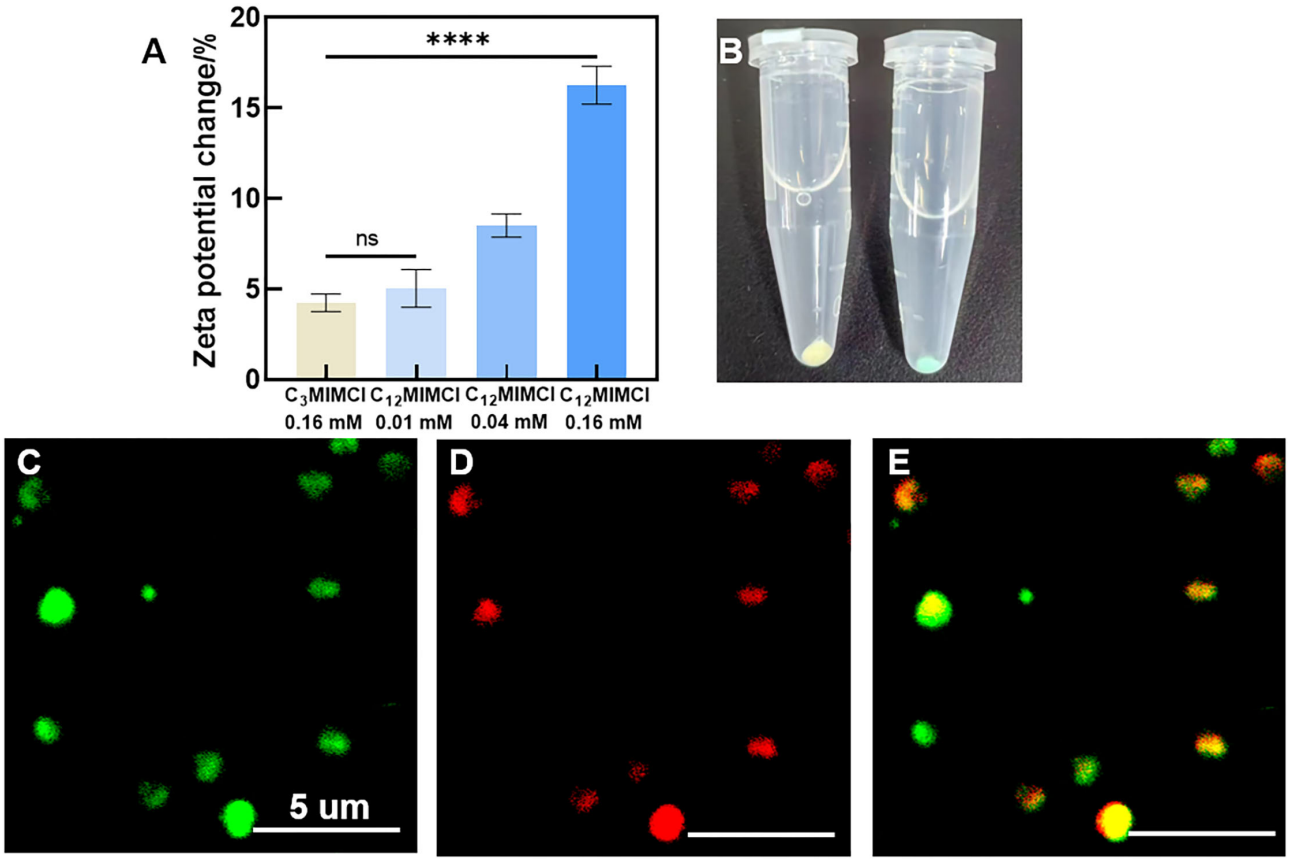

FIGURE 5
The changes of *Staphylococcus aureus* surface. **(A)** Zeta potentials of *Staphylococcus aureus* co-cultured with C_3MIMCl or C_{12}MIMCl in PBS for 3h. **(B)** Picture of *Staphylococcus aureus* incubated with Cy5, SE-C_{12}MIMCl. **(C–E)** CLSM images of C_{12}MIMCl interacting with *Staphylococcus aureus*. Green: *Staphylococcus aureus* transfected with GFP **(C)**, Red: Cy5, SE-C_{12}MIMCl **(D)**, merged **(E)**. Data in **(A)** represent the mean ± s.d. Statistical significance of **(A)** was calculated *via* two-tailed unpaired Student's *t*-test. Ns means no significant difference, ****$P < 0.0001$.

membrane potential increased. The potential of *S. aureus* is in full correlation with their EC50 values and is concentration dependent. It could be seen that the bacterial color changed after incubation with Cy5, SE-C_{12}MIMCl, indicating that C_{12}MIMCl was adsorbed on the bacterial surface (Figure 5B). Because the *S. aureus* surface was negatively charged, it could attract the IL cation with a positive charge to gather on the bacterial surface by CLSM (Figures 5C–E). It was once again demonstrated that C_{12}MIMCl could interact with bacterial cell membranes.

3.3.3. Observation of the destruction process of S. aureus by ILs

TEM images further confirmed that *S. aureus* was treated with C_{12}MIMCl, which showed membrane detachment, content leakage, and cell disruption. Figure 6 shows the whole process of *S. aureus* being destroyed. The control group and C_3MIMCl group showed intact and smooth cell membranes. Initially, part of the cell membrane was shed from the bacterial surface in the presence of C_{12}MIMCl (Figure 6A). Subsequently, the cytoplasm flowed out from

10.3389/fmicb.2023.1109972

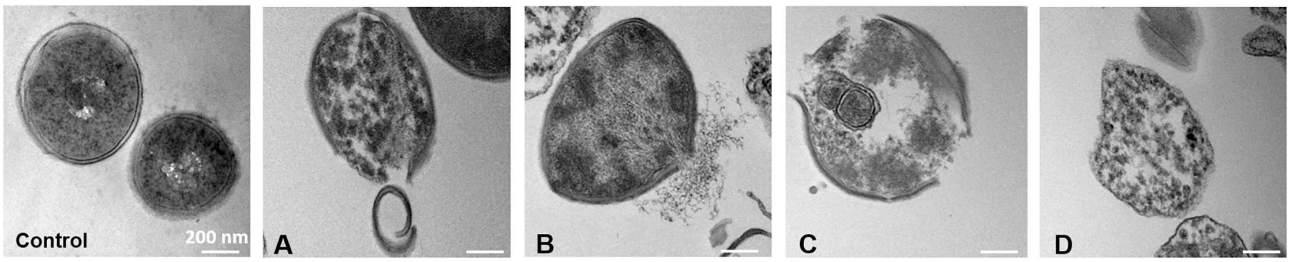

FIGURE 6
TEM images of *Staphylococcus aureus* within 3 h treatment with 0.16 mM of C_{12}MIMCl. **(A-D)**: The destruction process of *Staphylococcus aureus* by C_{12}MIMCl.

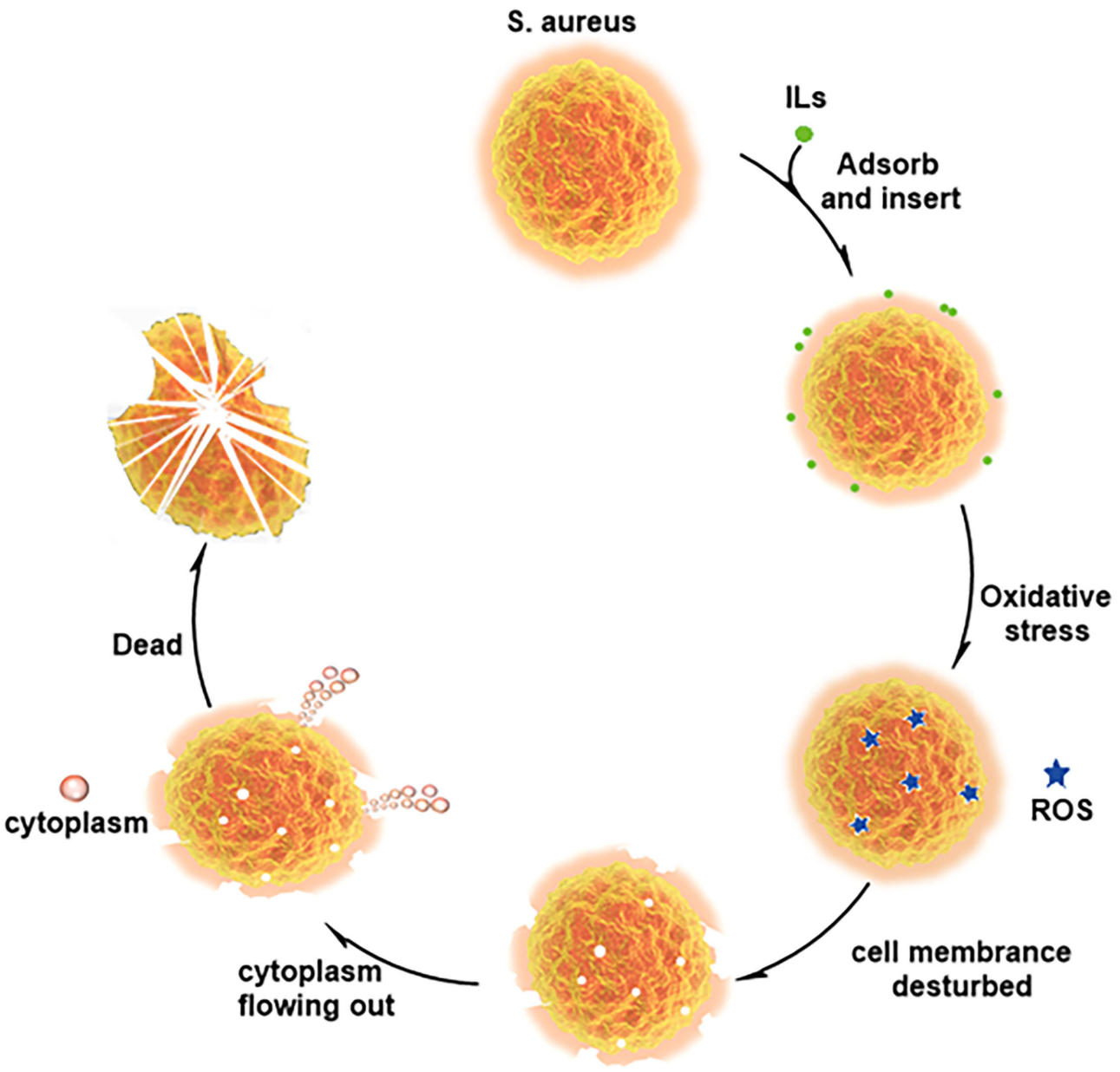

FIGURE 7
Plausible antibacterial mechanism for interaction between C_{12}MIMCl and *Staphylococcus aureus*.

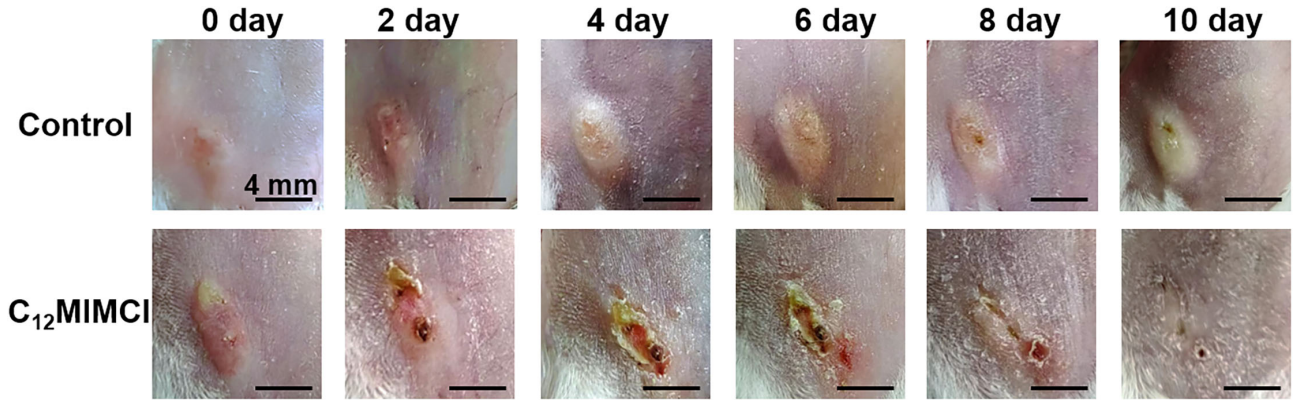

FIGURE 8
Changes of skin abscess in mice after *Staphylococcus aureus* infection and C_{12}MIMCl treatment.

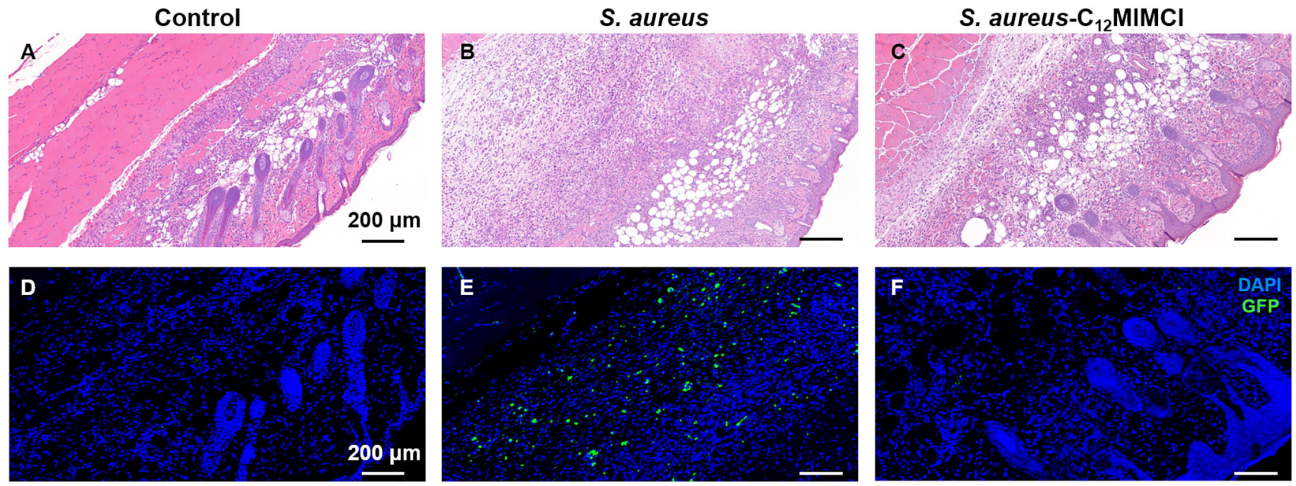

FIGURE 9
Histopathology of skin abscess and fluorescent scan in mice after *Staphylococcus aureus* infection and C_{12}MIMCl treatment. **(A)** Histopathology of the control group (PBS). **(B)** Histopathology of skin abscess after *Staphylococcus aureus* injection. **(C)** Histopathology of C_{12}MIMCl treatment in skin abscess. **(D)** Fluorescent scan of the control group (PBS). **(E)** Fluorescent scan of skin abscess after *Staphylococcus aureus* injection. **(F)** Fluorescent scan of C_{12}MIMCl treatment in skin abscess. DAPI (blue), GFP-*Staphylococcus aureus* (green).

the broken cell membrane (Figure 6B). Then, the cell membrane of *S. aureus* was completely disrupted (Figure 6C). Finally, *S. aureus* was dead (Figure 6D).

3.4. Antibacterial mechanism of ionic liquids against *S. aureus*

The cell membrane mainly consists of phospholipids with a negative charge on the surface and hydrophobicity. ILs are amphiphilic, and long cationic side chains can be inserted into the phospholipid bilayer, causing cell membrane disorder (Kaur et al., 2020; Liu et al., 2021). According to the above experimental contents, C_{12}MIMCl could be adsorbed on the surface of *S. aureus* by electrostatic action. Afterward, C_{12}MIMCl was inserted into cell membranes driven by hydrophobicity. This led to an oxidative stress reaction in bacteria, that is, the rapid production of a large amount of ROS. At the same time, it changed the permeability of the bacterial cell membrane, which could change the bacterial osmotic pressure, destroying the cell membrane and allowing cytoplasm to flow out of the broken cell membrane. Figure 7 depicts a plausible antibacterial mechanism for interacting C_{12}MIMCl with *S. aureus*.

3.5. The therapeutic effect of C_{12}MIMCl on skin abscess *in vivo*

3.5.1. Observation of a skin abscess

The skin of *S. aureus*-infected mice developed visible abscesses, redness, edema, and ulcers within 1–2 days of infection. The abscess was injected with 2 mM C_{12}MIMCl (50 μl) for 3–4 days. On the second day of C_{12}MIMCl administration, the abscess showed a distinct black scab, and the abscess under the skin gradually decreased, while the abscess in the control group gradually grew larger (Figure 8). In the following days, the scabbed area gradually expanded. The subcutaneous abscess did not disappear completely

until 3–4 days after the C_{12}MIMCl injection. After 8 days, the scab gradually fell off. The skin in the treatment group could be healed for 10–12 days. However, the subcutaneous abscess remained in the control group.

3.5.2. Analysis of skin tissue

Skin biopsy samples collected on day 11 were fixed and prepared for histopathological evaluation (Figures 9A–C). Compared with the control group, the wavy curves of the epidermis and dermis at the subcutaneous abscess sites of *S. aureus* infection disappeared, indicating that the epidermis and dermis were severely damaged. In addition, there was a large infiltration of monocytes in the dermis. After the C_{12}MIMCl injection, the morphology of the epidermis and dermis gradually recovered, and the number of inflammatory cells decreased significantly. H&E staining of skin sections from the mice revealed that C_{12}MIMCl had a good therapeutic effect on the subcutaneous abscess. After DAPI staining and GFP spontaneous fluorescence scanning, it could be seen that the number of *S. aureus* in the skin was nearly zero after the C_{12}MIMCl injection. The number of *S. aureus* cells in the skin remained largely unchanged in the untreated group (Figures 9D–F). In conclusion, C_{12}MIMCl could improve the skin abscess infected with *S. aureus* in mice.

4. Conclusion

A variety of imidazole chloride ILs with varying length substituents was investigated for their antibacterial mechanisms against *S. aureus*. Imidazole chloride ILs containing twelve and sixteen carbon lengths had strong antibacterial and anti-biofilm activity against *S. aureus*. The results showed that the antibacterial efficiency of ILs could be improved by changing the alkyl chain length due to the tunable structure of ILs. The above research demonstrated that long cationic side-chain ILs effectively inhibited *S. aureus*. This study provided new ideas for creating new antibacterial drugs. ROS release tests confirmed that long cationic side-chain ILs have a strong impact on the metabolism of *S. aureus*. SEM and membrane potential test experiments revealed that ILs could collapse and damage the surface of *S. aureus*. TEM images clearly showed how C_{12}MIMCl disrupts the cell membrane of *S. aureus,* causing the contents to leak. Ultimately, the antibacterial mechanism of C_{12}MIMCl against *S. aureus* was proven. *In vivo* tests, C_{12}MIMCl had significant antibacterial effects and accelerated the healing of skin abscesses. After the new coronavirus pandemic in 2019, it is urgent to develop new antibacterial and antiviral drugs. ILs have not been found to be appropriate drugs for clinical use. At present, we know that the toxicity of ILs to *S. aureus* depends on the length of cationic alkyl chain substituents. In the future, we will expand the types of organism models (e.g., Gram-negative bacteria, viruses, cells, and animals) and design specific properties for different diseases by regulating different types of ILs substituents.

Data availability statement

The original contributions presented in the study are included in the article/supplementary material, further inquiries can be directed to the corresponding authors.

Ethics statement

The animal study was reviewed and approved by the Institutional Animal Care and Use Committees at the Institute of Process Engineering, Chinese Academy of Sciences.

Author contributions

YH, GW, and YD contributed to the conception and design of the study. YH, PY, and HY performed the experiments. YH, PY, and XM contributed significantly to data analyses. YH and YX organized the pictures of the experiment. YH wrote the manuscript. HY, YX, and YS revised the manuscript. GW and YD oversaw the completion of this study. All authors contributed to the article and approved the submitted version.

Funding

This study was supported by the National Natural Science Foundation of China (21978292 and 21676280), the Innovation Academy for Green Manufacture, the Chinese Academy of Sciences (IAGM2020C20), the Major Program of the National Natural Science Foundation of China (21890762), and the International Partnership Program of the Chinese Academy of Sciences (grant no. 122111KYSB20190060).

Acknowledgments

The authors sincerely appreciate Prof. Suojiang Zhang (IPE, CAS) for his careful academic guidance and great support.

Conflict of interest

The authors declare that the research was conducted in the absence of any commercial or financial relationships that could be construed as a potential conflict of interest.

Publisher's note

References

Albadawi, H., Zhang, Z., Altun, I., Hu, J., Jamal, L., Ibsen, K. N., et al. (2021). Percutaneous liquid ablation agent for tumor treatment and drug delivery. *Sci. Transl. Med. 13*, eabe3889. doi: 10.1126/scitranslmed.abe3889

Brunel, F., Lautard, C., Garzino, F., Giorgio, S., Raimundo, J. M., Bolla, J. M., et al. (2016). Antibacterial activities of fluorescent nano assembled triphenylamine phosphonium ionic liquids. *Bioorg. Med. Chem. Lett.* 26, 3770–3773. doi: 10.1016/j.bmcl.2016.05.055

Brynildsen, M. P., Winkler, J. A., Spina, C. S., MacDonald, I. C., and Collins, J. J. (2013). Potentiating antibacterial activity by predictably enhancing endogenous microbial ROS production. *Nat. Biotechnol.* 31, 160–165. doi: 10.1038/nbt.2458

Chen, S. M., Zhang, S. J., Liu, X. M., Wang, J. Q., Wang, J. J., Dong, K., et al. (2014). Ionic liquid clusters: structure, formation mechanism, and effect on the behavior of ionic liquids. *Phys. Chem. Chem. Phys.* 16, 5893–5906. doi: 10.1039/C3CP53116C

Dinis, T. B. V., Sousa, F., and Freire, M. G. (2020). Insights on the DNA stability in aqueous solutions of ionic liquids. *Front. Bioeng. Biotechnol.* 8, 547857. doi: 10.3389/fbioe.2020.547857

Dupont, J. (2011). From molten salts to ionic liquids a "nano" journey. *Accounts Chem. Res.* 44, 1223–1231. doi: 10.1021/ar2000937

Egorova, K. S., Gordeev, E. G., and Ananikov, V. P. (2017). Biological activity of ionic liquids and their application in pharmaceutics and medicine. *Chem. Rev.* 117, 7132–7189. doi: 10.1021/acs.chemrev.6b00562

Florio, W., Becherini, S., D'Andrea, F., Lupetti, A., Chiappe, C., and Guazzelli, L. (2019). Comparative evaluation of antimicrobial activity of different types of ionic liquids. *Mater. Sci. Eng. C* 104, 109907. doi: 10.1016/j.msec.2019.109907

Fu, D., Sun, Y., Zhang, F., Sun, Z., Li, W., Wang, L., et al. (2022). Enabling polymeric ionic liquid electrolytes with high ambient ionic conductivity by polymer chain regulation. *Chem. Eng. J.* 431, 133278. doi: 10.1016/j.cej.2021.133278

Gao, S. R., Fang, S. F., Song, R. Z., Chen, X. C., and Yu, G. R. (2020). Extractive denitrogenation of shale oil using imidazolium ionic liquids. *Green Energ. Environ.* 5, 173–182. doi: 10.1016/j.gee.2020.04.002

Gao, Y. R., Cao, J. F., Shu, Y., and Wang, J. H. (2021). Research progress of ionic liquids-based gels in energy storage, sensors and antibacterial. *Green Chem. Eng.* 2, 368–383. doi: 10.1016/j.gce.2021.07.012

Hess, D. J., Garni, R. M., Henry-Stanley, M. J., and Wells, C. L. (2005). *Escherichia coli*modulates extraintestinal spread of *Staphylococcus aureus*. *Shock* 24, 376–381. doi: 10.1097/01.shk.0000180615.75822.fe

Kaur, N., Fischer, M., Kumar, S., Gahlay, G. K., Scheidt, H. A., and Mithu, V. S. (2020). Role of cationic head-group in cytotoxicity of ionic liquids: probing changes in bilayer architecture using solid-state NMR spectroscopy. *J. Colloid. Interface Sci.* 581, 954–963. doi: 10.1016/j.jcis.2020.08.115

Li, M., Chen, J., Li, L., Ye, C., Lin, X., and Qiu, T. (2021). Novel multi–SO3H functionalized ionic liquids as highly efficient catalyst for synthesis of biodiesel. *Green Energ. Environ.* 6, 271–282. doi: 10.1016/j.gee.2020.05.004

Liang, L., Yan, J. P., He, Q., Luong, T., Pray, T. R., Simmons, B. A., et al. (2019). Scale-up of biomass conversion using 1-ethyl-3-methylimidazolium acetate as the solvent. *Green Energ. Environ.* 4, 432–438. doi: 10.1016/j.gee.2018.07.002

Liu, J., Wang, Y., Wang, C., Gao, J., Cui, W., Zhao, B., et al. (2021). Thermodynamical origin of nonmonotonic inserting behavior of imidazole ionic liquids into the lipid bilayer. *J. Phys. Chem. Lett.* 12, 9926–9932. doi: 10.1021/acs.jpclett.1c02566

Lu, B. B., Zhou, G. X., Xiao, F., He, Q. J., and Zhang, J. H. (2020). Stimuli-responsive poly(ionic liquid) nanoparticles for controlled drug delivery. *J. Mater. Chem. B* 8, 7994–8001. doi: 10.1039/D0TB01352H

Md Moshikur, R., Chowdhury, M. R., Fujisawa, H., Wakabayashi, R., Moniruzzaman, M., and Goto, M. (2020). Design and characterization of fatty acid-based amino acid ester as a new "green" hydrophobic ionic liquid for drug delivery. *ACS Sustain. Chem. Eng.* 8, 13660–13671. doi: 10.1021/acssuschemeng.0c03419

Moshikur, R. M., Ali, M. K., Moniruzzaman, M., and Goto, M. (2021). Recent advances in surface-active ionic liquid-assisted self-assembly systems for drug delivery. *Curr. Opin. Colloid In.* 56, 101515. doi: 10.1016/j.cocis.2021.101515

Ning, H.-Q., Li, Y.-Q., Tian, Q.-W., Wang, Z.-S., and Mo, H.-Z. (2019). The apoptosis of *Staphylococcus aureus* induced by glycinin basic peptide through ROS oxidative stress response. *LWT-Food Sci. Technol.* 99, 62–68. doi: 10.1016/j.lwt.2018.09.028

Nithya, P., and Sundrarajan, M. (2020). Ionic liquid functionalized biogenic synthesis of Ag-Au bimetal doped CeO_2 nanoparticles from *Justicia Adhatoda* for pharmaceutical applications: antibacterial and anti-cancer activities. *J. Photochem. Photobiol. B* 202, 111706. doi: 10.1016/j.jphotobiol.2019.111706

Sadjadi, S. (2021). Magnetic (poly) ionic liquids: a promising platform for green chemistry. *J. Mol. Liq.* 323, 114994. doi: 10.1016/j.molliq.2020.114994

Schilling, N. A., Berscheid, A., Schumacher, J., Saur, J. S., Konnerth, M. C., Wirtz, S. N., et al. (2019). Synthetic lugdunin analogues reveal essential structural motifs for antimicrobial action and proton translocation capability. *Angew. Chem. Int. Ed. Engl.* 58, 9234–9238. doi: 10.1002/anie.201901589

Schröder, C. (2017). Proteins in ionic liquids: current status of experiments and simulations. *Top. Curr. Chem.* 375, 25. doi: 10.1007/s41061-017-0110-2

Shamshina, J. L., and Berton, P. (2020). Use of ionic liquids in chitin biorefinery: a systematic review. *Front. Bioeng. Biotechnol.* 8, 11. doi: 10.3389/fbioe.2020.00011

Shangguan, J., Li, Y., He, D., He, X., Wang, K., Zou, Z., et al. (2015). A combination of positive dielectrophoresis driven on-line enrichment and aptamer-fluorescent silica nanoparticle label for rapid and sensitive detection of *Staphylococcus aureus*. *Analyst* 140, 4489–4497. doi: 10.1039/C5AN00535C

Tang, W. T., Liu, B., Wang, S. P., Liu, T. L., Fu, C. H., Ren, X. L., et al. (2016). Doxorubicin-loaded ionic liquid-polydopamine nanoparticles for combined chemotherapy and microwave thermal therapy of cancer. *RSC Adv.* 6, 32434–32440. doi: 10.1039/C6RA02434C

Veríssimo, N. V., Saponi, C. F., Ryan, T. M., Greaves, T. L., and Pereira, J. F. B. (2021). Imidazolium-based ionic liquids as additives to preserve the enhanced green fluorescent protein fluorescent activity. *Green Chem. Eng.* 2, 412–422. doi: 10.1016/j.gce.2021.08.001

Wang, Y., Wang, S., and Liu, L. (2022). Recovery of natural active molecules using aqueous two-phase systems comprising of ionic liquids/deep eutectic solvents. *Green Chem. Eng.* 3, 5–14. doi: 10.1016/j.gce.2021.07.007

Xue, Y., Zhang, X. G., Lu, Z. P., Xu, C., Xu, H. J., and Hu, Y. (2022). Enhancing the catalytic performance of candida antarctica lipase b by chemical modification with alkylated betaine ionic liquids. *Front. Bioeng. Biotechnol.* 10, 850890. doi: 10.3389/fbioe.2022.850890

Yuan, X., Liu, J., Wang, Y., Jie, X., Qin, J., and He, H. (2023). Ionic liquids enable highly efficient knoevenagel reaction by dual-responsive emulsion microreactor. *Chem. Eng. J.* 451, 138941. doi: 10.1016/j.cej.2022.138941

Zhang, S. J., Sun, J., Zhang, X. C., Xin, J. Y., Miao, Q. Q., and Wang, J. J. (2014). Ionic liquid-based green processes for energy production. *Chem. Soc. Rev.* 43, 7838–7869. doi: 10.1039/C3CS60409H

Zhang, Y., Cao, Y., Meng, X., Li, C., Wang, H., and Zhang, S. (2020). Enhancement of transdermal delivery of artemisinin using microemulsion vehicle based on ionic liquid and lidocaine ibuprofen. *Colloid. Surfaces B* 189, 110886–110886. doi: 10.1016/j.colsurfb.2020.110886

Zhao, Y., Wei, J., Li, C., Ahmed, A. F., Liu, Z., and Ma, C. (2022). A comprehensive review on mechanism of natural products against *Staphylococcus aureus*. *J. Future Foods* 2, 25–33. doi: 10.1016/j.jfutfo.2022.03.014

Zhu, X. L., Tang, X. X., Lin, H. Y., Shi, S. G., Xiong, H. H., Zhou, Q. J., et al. (2020). A fluorinated ionic liquid-based activatable 19 fMRI platform detects biological targets. *Chem* 6, 1134–1148. doi: 10.1016/j.chempr.2020.01.023

frontiers | Frontiers in Bioengineering and Biotechnology

TYPE Mini Review
PUBLISHED 09 March 2023
DOI 10.3389/fbioe.2023.1159989

OPEN ACCESS

EDITED BY
Zhen Liu,
Beijing University of Chemical Technology, China

REVIEWED BY
Gao Fengxiang,
Changchun Institute of Applied Chemistry (CAS), China
Guodong Yang,
Air Force Medical University, China

*CORRESPONDENCE
Yayun Nan,
nanyy_2009@163.com
Qiong Huang,
qionghuang@csu.edu.cn
Kelong Ai,
aikelong@csu.edu.cn

†These authors have contributed equally to this work

SPECIALTY SECTION
This article was submitted to Nanobiotechnology, a section of the journal Frontiers in Bioengineering and Biotechnology

RECEIVED 06 February 2023
ACCEPTED 23 February 2023
PUBLISHED 09 March 2023

CITATION
Chen Q, Wang X, Yuan C, Nan Y, Huang Q and Ai K (2023), 2D-nanomaterials for AKI treatment.
Front. Bioeng. Biotechnol. 11:1159989.
doi: 10.3389/fbioe.2023.1159989

2D-nanomaterials for AKI treatment

Qiaohui Chen[1,2†], Xiaoyuan Wang[2,3†], Chao Yuan[2,3†], Yayun Nan[4*], Qiong Huang[1,5*] and Kelong Ai[2,3*]

[1]Department of Pharmacy, Xiangya Hospital, Central South University, Changsha, Hunan, China, [2]Xiangya School of Pharmaceutical Sciences, Central South University, Changsha, Hunan, China, [3]Hunan Provincial Key Laboratory of Cardiovascular Research, Xiangya School of Pharmaceutical Sciences, Central South University, Changsha, China, [4]Geriatric Medical Center, People's Hospital of Ningxia Hui Autonomous Region, Yinchuan, Ningxia, China, [5]National Clinical Research Center for Geriatric Disorders, Xiangya Hospital, Central South University, Changsha, Hunan, China

Acute kidney injury has always been considered a sword of Damocles over hospitalized patients and has received increasing attention due to its high morbidity, elevated mortality, and poor prognosis. Hence, AKI has a serious detrimental impact not only on the patients, but also on the whole society and the associated health insurance systems. Redox imbalance caused by bursts of reactive oxygen species at the renal tubules is the key cause of the structural and functional impairment of the kidney during AKI. Unfortunately, the failure of conventional antioxidant drugs complicates the clinical management of AKI, which is limited to mild supportive therapies. Nanotechnology-mediated antioxidant therapies represent a promising strategy for AKI management. In recent years, two-dimensional (2D) nanomaterials, a new subtype of nanomaterials with ultrathin layer structure, have shown significant advantages in AKI therapy owing to their ultrathin structure, large specific surface area, and unique kidney targeting. Herein, we review recent progress in the development of various 2D nanomaterials for AKI therapy, including DNA origami, germanene, and MXene; moreover, we discuss current opportunities and future challenges in the field, aiming to provide new insights and theoretical support for the development of novel 2D nanomaterials for AKI treatment.

KEYWORDS

two-dimension, nanomaterials, targeted therapy, acute kidney injury, antioxidant therapy

Introduction

Acute kidney injury, characterized by a sudden loss of renal function and rapid increases in serum creatinine (Cre) and urea nitrogen levels (BUN), is a common and critical clinical condition involving multiple etiologies (Kellum et al., 2021). AKI has long been a significant factor influencing ICU patient prognosis, with a prevalence of 30%–60% and a high correlation with fatal events (Pickkers et al., 2021). Especially in the context of the COVID-19 pandemic, AKI often complicates the hospitalization of patients diagnosed with the virus and may lead to increased disease severity, prolonged hospitalization, and poor prognosis (Ronco et al., 2020). Unfortunately, current clinical support therapies such as dialysis, rehydration, and renal transplantation do not fundamentally stop the progression of the disease, but merely relieve symptoms and wait for the self-repair of kidneys. (Ostermann et al., 2020). Therefore, focusing on the common pathological mechanisms of AKI and providing targeted drug therapies is an effective strategy to stop the progression of the disease and promote renal repair (Chen et al., 2023). Emerging evidence has revealed that the key

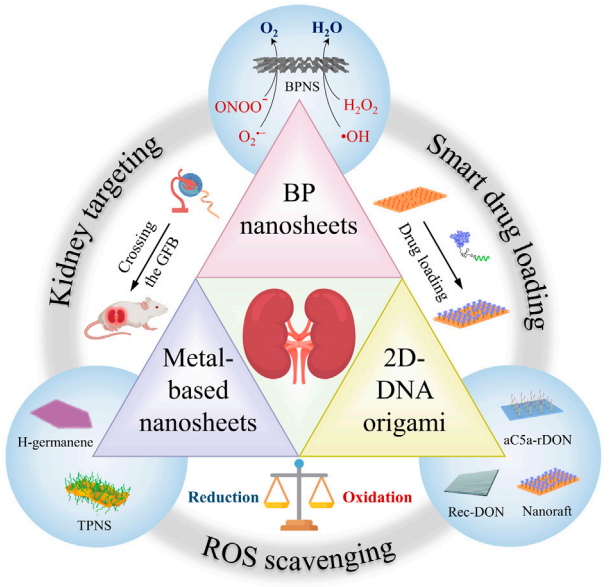

FIGURE 1
Schematic illustration of 2D nanomaterials for AKI treatment. In recent years, several emerging 2D nanomaterials have demonstrated excellent therapeutic effects in AKI due to their excellent kidney targeting, smart drug loading and ROS scavenging capabilities, including 2D-DNA origami, metal-based nanosheets and BP nanosheets.

mechanism of AKI is an uncontrolled burst of toxic reactive oxygen species (ROS) in kidneys, which initiates a chain reaction involving cell apoptosis, necrosis, and excessive inflammation (Wu et al., 2019; Zhao et al., 2021a; Chen et al., 2023). As the second energy-consuming organ of the body, renal tubules with a high density of mitochondria become the main site of ROS production and the target of attack during ischemia or hypoxia (Tian and Liang, 2021; Li et al., 2022). ROS storms induce severe oxidative stress, causing irreversible damage to DNA, proteins, and other biomolecules, and ultimately leading to tubular cell dysfunction, i.e., a sudden decline in kidney function (Weng et al., 2021; Zhao et al., 2022a; Huang et al., 2023a; Wang et al., 2023a; Su et al., 2023). Therefore, kidney-targeted scavenging of excess ROS offers a new potential solution for AKI treatment (Wang et al., 2021a; Wang et al., 2022). However, typical antioxidants such as *N*-acetylcysteine (NAC) have produced highly mixed results in clinical studies due to rapid excretion, poor bioavailability and low ROS scavenging efficacy (Su et al., 2017; Zhang et al., 2021a). Accordingly, biosafe nanomedicines are highly desirable for the treatment of AKI, because of their high kidney-targeting ability and strong antioxidant (Zhou et al., 2020).

Since the beginning of the 21st century, the successful exfoliation of graphene has triggered the explosive growth of two-dimensional (2D) nanomaterials, which have two dimensions outside the nanoscale and only one dimension with one thickness or a few atomic layers (Choi et al., 2022). Most atoms in 2D nanomaterials are directly exposed on their surfaces, endowing these materials with the largest specific surface area and extraordinary surface activity (Ouyang et al., 2022). Notably, 2D nanomaterials can maintain their atomic thickness while retaining their large longitudinal dimensions. Compared to zero-dimensional (0D) or larger-size nanomaterials, 2D nanomaterials have many unique features, such as lamellar structures, excellent optical/ultrasonic/magnetic responses, and high thermal conversion efficiency, which endow them with considerable potential and several advantages in the biomedical field (Hu et al., 2019; Zhao et al., 2022b). Therefore, they can act as antioxidants with maximum exposure for efficient ROS scavenging and possess abundant anchoring sites, which enable them to serve as drug carriers through diverse functional modifications while improving the drug loading rates (Zhang et al., 2020). Most importantly, the ultrathin and flexible structure of 2D nanomaterials endows them with unique preferential renal excretion properties, allowing them to coil and fold longitudinally across the glomerular filtration barrier (Jiang et al., 2020). Therefore, 2D nanomaterials with high surface activity and natural kidney targeting are highly promising candidates for antioxidant therapy of AKI.

Over the past few years, the extensive development of 2D nanomaterials has provided fertile ground for the exploration of high-performance AKI therapeutic nanomedicines. However, to the best of our knowledge, no reviews of 2D nanomaterials for AKI treatment have been published to date. To fill this gap, in this minireview we summarize recent progresses on 2D nanomaterials for AKI antioxidant therapy, including 2D DNA origami, metal-based and black phosphorus (BP) nanosheets (Figure 1; Table 1). We focus on the structural design, biodistribution characteristics, reactivity, and biosafety of these 2D nanomaterials. Finally, we discuss the challenges and prospects of the application of 2D nanomaterials in related fields, with the aim of triggering further innovative researches to advance the development of AKI therapeutics.

2D-DNA origami

Over the past three decades, significant advances have been made in structural DNA nanotechnology, enabling the fabrication of highly programmable DNA origami with unprecedented accuracy and complexity, making them ideal precision nanomaterials (Wang et al., 2023b; Parsons et al., 2023). In addition, DNA is particularly advantageous in biomedical applications, owing to its intrinsic biocompatibility and biodegradability as the transporter of genetic information in living organisms (Li et al., 2021a; Zhang et al., 2021b; Lucas et al., 2022). DNA origami structures have been widely investigated and applied in various biomedical fields, including tissue engineering, immune engineering, drug delivery, diagnosis, and biosensing (Tian et al., 2022; Zhang et al., 2022). Importantly, the nucleophilic of the DNA bases could effectively neutralize toxic ROS, allowing DNA to be employed as an exogenous ROS scavenger for antioxidant therapy of AKI (Chen et al., 2023).

Recently, Jiang et al. reported that rectangular 2D-DNA origami exhibited preferential renal accumulation properties as well as low immunogenicity and minimal cytotoxicity (Jiang et al., 2018). The authors fabricated tightly folded DNA origami with three distinct morphologies (Rec-DON, Tub-DON, and Tri-DON), along with the corresponding partially folded structures through a single-step annealing procedure. After radiolabeling, all three intact DNA origami structures exhibited preferential renal accumulation in

TABLE 1 2D-nanomaterials in AKI treatment.

Category	Nanomaterials	Size	Thickness	Cargo	Therapeutic mechanism	Animal model
2D-DNA origami	Rec-DON Jiang et al. (2018)	90 × 60 nm	—	—	Antioxidation	Rhabdomyolysis induced AKI
	aC5a-rDON Chen et al. (2021)	90 × 60 nm	—	aC5a	Antioxidative and Anti-inflammation	Ischemia reperfusion induced AKI
	Nanoraft Li et al. (2021b)	—	4 nm	IL-33	Antioxidation and Anti-inflammation	Ischemia reperfusion induced AKI
Metal-based nanosheets	H-germanene Chen et al. (2022)	100–400 nm	<1 nm	—	Antioxidation	Rhabdomyolysis induced AKI
	TPNS Zhao et al. (2021c)	~200 nm	—	—	Antioxidation and Anti-inflammation	Rhabdomyolysis induced AKI
Black phosphorus nanosheets	BPNSs Hou et al. (2020)	225.8 ± 4.0 nm	3.8–4.5 nm	—	Antioxidation	Rhabdomyolysis induced AKI

both healthy and AKI mice, while the partially folded structures exhibited increased liver sequestration like M13 ssDNA (long single-stranded DNA). The similar biodistribution patterns of partially folded DNA strictures and M13 ssDNA indicated the rapid recognition and clearance of circulating foreign antigens by the endothelial reticular system. In contrast, the dense structure, high degree of folding, and negative surface charge of the intact DNA origami efficiently avoided foreign DNA-triggered immunosurveillance or enzyme/protein interactions, as well as the subsequent liver sequestration. More significantly, the ultra-thin and soft morphology of the 2D-DNA origami structures enabled them to pass through the glomerulus filtration barrier upon coiling and folding, which ultimately led to their accumulation at the target, i.e., the renal tubules. Moreover, all types of DNA origami effectively neutralized various types of ROS (•OH, $O_2^{\bullet-}$, and H_2O_2) through the oxidation of DNA bases. Rec-DNA, with the highest kidney uptake, effectively restored the redox balance (superoxide dismutase levels), and renal function (Cre, BUN) in AKI mice at an effective dose of only 1/420 of NAC (one of the commonly used clinical antioxidants).

Furthermore, the ultra-high specific surface area and precision of DNA origami technology also enable the application of 2D-DNA origami as smart drug delivery devices with optimized loading rates and targeting efficiency (Jiang et al., 2019). Tailored 2D-DNA nanorobots for kidney-targeted drug delivery were easily obtained by rationally arranging capture strands as anchoring sites on the surface of nanosheets (Thai et al., 2020; Zhao et al., 2021b). For example, Chen et al. reported a rectangular DNA origami (aC5a-rDNAs) loaded with nucleic acid aptamers of complement component (C5a) for the sequential therapy of AKI (Chen et al., 2021). In agreement with previous studies, the rDNAs exhibited preferential renal accumulation *in vivo*, and their persistence time in AKI mice could exceed 12 h post-injection due to their decreased renal function, compared to only 3 h in healthy mice. Such high drug retention provided a longer therapeutic window and was a prerequisite for achieving sequential treatment. During AKI, excessive ROS can also cause excessive inflammatory responses by activating the complement system along with direct oxidative injury. Therefore, the aC5a-rDNAs enabled stage-sensitive sequential therapy based on the direct link between oxidative stress and complement activation. Accordingly, aC5a-rDNAs could scavenge excess ROS during the first stage of AKI (0–4 h) *via* the oxidation of DNA bases, displayed as a significantly reduced malondialdehyde (MDA) level in renal tissue. When the AKI advanced to the second stage (4–8 h), the nucleic acid aptamers on the surface of aC5a-rDNAs specifically bound C5a and competitively inhibited the activation of the complement system, which in turn decreased the expression of myeloperoxidase, tumor necrosis factor-α, interleukin-6, and interleukin-1 expression in renal tissues. As a result, aC5a-rDNAs possessing renal targeting and bifunctionality properties exhibited a superior therapeutic effect compared with bare rDNAs and free aC5a, with significantly recovered and improved renal function indicators (BUN, Cre) and renal tissue morphology.

Cytokine interleukin-33 (IL-33) is a powerful immunomodulator that plays a crucial role in suppressing inflammation and promoting tissue repair (Dagher et al., 2020; Faas et al., 2021). However, its non-specific activation on immune cells outside the focus and short circulating half-life represent major obstacles for its application in AKI therapy. Recently, Li et al. constructed a DNA nanoraft-based cytokine delivery platform by precisely arranging IL-33 arrays on rectangular DNA origami, aiming to achieve preferentially kidney delivery of IL-33 with accurate dosage and sustained drug release (Li et al., 2021b). Compared to free IL-33, nanorafts showed a predominant renal distribution with the fluorescent signal that lasted for more than 48 h in the kidney, indicating that nanorafts can significantly increase the specific renal distribution and retention time of IL-33 in the kidney. During the process, the fluorescence intensity and co-localization of nanorafts with IL-33 in the kidney decreased with time, reflecting the slow and continuous release of IL-33 from the surface of nanorafts. As an important immunomodulator, IL-33 could subsequently induce rapid expansion of type 2 innate lymphoid cells (ILC2s) and regulatory T cells (Tregs) by binding to their specific surface receptors ST2. As a result, the treatment with nanorafts led to a significant increase in the percentage and absolute number of renal ILC2s and Tregs, accompanied by an upregulated expression of IL-4 and IL-13, which play important roles in repolarization of macrophages from the pro-inflammatory M1 subtype to the anti-inflammatory M2 subtype. Furthermore,

the renal function indices (Cre, BUN) and tubular injury score of nanoraft-treated mice (two times injection at 2 and 48 h after surgery) were better than those of the free-IL-33-treated group (five consecutive days of injection after surgery). Taking these results together, the authors offered a structurally well-defined delivery platform for controlled cytokine immunotherapy, achieving a higher therapeutic efficiency with less treatment intensity in AKI treatment.

Metal-based nanosheets

Germanene, group-IV graphene-like 2D buckled nanosheets, has recently received considerable attention as one of the newest members of 2D nanomaterials (Feng et al., 2020; Rohaizad et al., 2021). Germanium is a frequently employed trace element in the human body, with many crucial biological functions, including erythropoiesis as well as antibacterial, anticancer, antiviral, and immunoregulation activities, suggesting its high biocompatibility and potential medical value (Ge et al., 2021). However, the biomedical applications of germanene remain largely unexplored. Recently, Chen et al. reported the design of 2D germanene nanosheets and their antioxidant application for AKI therapy. Hydrogen-terminated germanene (H-germanene) was synthesized through Ca layer deintercalation from the precursor Zintl-phase $CaGe_2$ crystals followed by delamination and ultrasonic treatment (Chen et al., 2022). The hydrogenation strategy tuned the band gap of germanene, allowing H-germanene to be employed as an electron donor and thus serve as an antioxidant. As a result, ultrathin H-germanene (<1 nm) exhibited superior broad-spectrum ROS scavenging ability (H_2O_2, $O_2^{\bullet-}$, •OH) and ultra-high reaction efficiency compared to typical antioxidant nanoparticles such as CeO_2, Au, TiO_2, and MnO_2. After intravenous injection, H-germanene rapidly accumulated in the kidneys of AKI mice and maintained high renal concentrations for the first 3 h. The passive targeting further amplified the ROS scavenging effect of H-germanene, and the corresponding treatment significantly reduced the levels of the DNA oxidation product 8-OhdG and the lipid peroxidation product MDA in kidney tissues of AKI mice. The restoration of renal function indices (Cre, BUN) in AKI mice further demonstrated the excellent efficacy of H-germanene nanosheets. In addition, the injection of high-concentration H-germanene showed no effect on body weight, hematological parameters, or liver and kidney function indices in mice, which demonstrated the biosafety of H-germanene and its potential for further clinical applications.

MXenes are a class of two-dimensional inorganic compounds that consist of atomically thin layers of transition metal carbides, nitrides, or carbonitrides (Mostafavi and Iravani, 2022). As an emerging branch of the 2D material family, MXenes have drawn substantial interest in biomedical applications due to their planar structure and unique physicochemical properties such as surface hydrophilicity, optical/magnetic/thermal properties, and abundant surface functional groups (Lin et al., 2018; Soleymaniha et al., 2019). More importantly, 2D Ti_3C_2 MXenes display strong chemical reactivity toward ROS, which makes them effective antioxidants for the treatment of AKI (Wang et al., 2021b; Hou et al., 2022). Recently, Zhao et al. reported ultrathin Ti_3C_2-PVP nanosheets (TPNs) and explored their therapeutic potential in AKI (Zhao et al., 2021c). The modification of (polyvinylpyrrolidone) PVP on the surface of TPNs improved the colloidal stability and dispersion of the nanosheets under physiological conditions, because of the steric hindrance of the macromolecular chains. Through adsorption and reduction at [Ti_3C] and Ti top sites, TPNs additionally displayed broad-spectrum (H_2O_2, $O_2^{\bullet-}$, •OH) and powerful ROS scavenging ability. In particular, they exhibited intrinsic enzyme/H_2O_2-responsive triggered biodegradability, with significant size reduction and subsequent degradation into Ti^{2+}, Ti^{3+}, and Ti^{4+} oxides (TiO_x species), ensuring their excellent biodegradability and biosafety. Owing to their planar structure, TPNs showed preferential renal accumulation at 5 min post-injection, peaking at 12 h. After treatment with TPNs, the renal function indices (BUN, Cre) and histopathological sections of AKI mice demonstrated their excellent therapeutic effects. Furthermore, transcriptomic and WB analyses showed that the TPNs served as a powerful antioxidant platform to scavenge extra ROS and then attenuate oxidative stress-induced inflammatory responses in AKI by inhibiting the NF-κB signaling pathway, illustrating their high clinical translational potential in AKI and other ROS-related diseases.

Black phosphorus nanosheets

Layered BP, a new member of the 2D nanomaterial family, has received a warm reception from scientists due to its unique physicochemical characteristics, controllable size, and excellent surface activity (Hu et al., 2020; Sui et al., 2021). In the field of optoelectronics, layered BPs undergo severe degradation and gradually lose their original properties when exposed to air or aqueous solutions, hindering their practical applications (Thurakkal and Zhang, 2020). However, such drawbacks can be turned into a great advantage in the biomedical field. The responsive degradation property makes BP a very competitive candidate compared to other 2D nanomaterials, because it minimizes the long-term toxicity and poor excretion issues when exposed to the physiological environment. Recently, Hou et al. used liquid-phase exfoliation to prepare black phosphorus nanosheets (BPNSs) with 7–9 individual BP layers for AKI antioxidant treatment (Hou et al., 2020). Each P atom in the individual BP layers is covalently bonded with three neighboring P atoms by sp^3 hybridization, forming a puckered honeycomb structure, and the adjacent layers are weakly stacked through van der Waals interactions. Due to their stacked layer structure (enabling rapid electron transfer) and elemental state (facilitating a rapid oxidative reaction to generate P–O bonds), the BPNSs exhibit a great capacity for ROS consumption. In AKI mice, BPNSs demonstrated excellent renal targeting ability thanks to their high planar/thickness topology and the suppressed renal clearance; after 12 h of intravenous administration, the renal distribution of BPNSs was up to 80%. The preferential accumulation of BPNS at the focal site maximized their antioxidant effect in AKI mice, and their nephroprotective effect was superior to that of two clinical antioxidant drugs (amifostine and NAC) at the same dose. Additionally, HE staining results and TUNEL fluorescence images demonstrated less tissue damage and apoptosis in BPNS

group. Notably, after fulfilling their protective role, BPNSs can be readily degraded to biocompatible P_xO_y ions after reacting with ROS, guaranteeing their excellent biosafety.

Conclusion and prospects

Despite the rapid advances in clinical care using modern biomedical technologies, dealing with serious and complex diseases such as AKI is still a major challenge. To combat these dangerous diseases, it is essential to develop creative therapeutic strategies. Nanomedicine is an innovative technology for designing and synthesizing various materials with fascinating physicochemical properties at the sub-micron level and exploiting them in the biomedical field (Liu et al., 2022a; Zhu et al., 2022; Huang et al., 2023b; Sun et al., 2023). Multiple medical fields are already benefiting from the advantages offered by nanotechnology, including disease diagnosis and surveillance, cancer therapy, and regenerative medicine, etc (van der Meel et al., 2019; Yang et al., 2019; Xu et al., 2020; Liu et al., 2022b). Encouragingly, outstanding progress in the development of novel antioxidant nanodrugs for AKI has been achieved in the past decades through the concerted efforts of many research groups (Chen et al., 2023). Considering the failure of conventional small-molecule antioxidant drugs, specific renal targeting ability, efficient and broad-spectrum ROS scavenging activity, and excellent biocompatibility have become the core principles of the design of therapeutic nanodrugs for AKI therapy. In these studies, 2D nanomaterials with their flexible and ultra-thin lamellar structure and well-exposed antioxidant active sites have demonstrated their unique appeal in AKI treatment, highlighting the "structure-function" correlation. Despite these encouraging developments, 2D nanomaterials still have a long way to go before further clinical translation.

Firstly, it has been founded that the size, thickness, composition, and surface properties of 2D nanomaterials are closely related to their biological behavior after entering the body (Fan et al., 2022). However, apart from the synthesis of DNA origami following a well-defined and controllable procedure, it is still challenging to achieve the controlled synthesis of 2D nanomaterials with adjustable size, uniform thickness, and stable dispersion. For example, liquid-phase exfoliation is currently the most common synthesis method of 2D material; however, despite its easy application, it is challenging to use this approach for the production of high-quality 2D materials, owing to aggregation, inhomogeneous morphology, random surface distribution, and size restriction issues (Alam et al., 2021). Secondly, although substantial evidence demonstrates the preferential kidney accumulation properties of 2D nanomaterials, their exact pharmacokinetic behavior, including the exact retention time in the focus and the actual clearance mechanism, remains unclear (Zheng et al., 2021). On the one hand, the large surface area of 2D nanomaterials increases their ability of the materials to interact with human tissues, which may complicate their metabolism (Fan et al., 2022). On the other hand, the novelty of some 2D nanomaterials also implies that limited information is available on the physiological characteristics of their interactions with living tissues. As a result, beyond the incomplete understanding gained so far, a more systematic assessment of the *in vivo* fate of 2D nanomaterials is needed. Thirdly, as an intelligent drug-delivery platform for targeting kidney tissues, the controlled drug release of 2D nanomaterials deserves further exploration and improvement. The development of DNA origami structures has enabled precise and quantitative control of drug loading and oxidative decomposition of DNA molecules by ROS to be achieved upon drug release; however, it is difficult to completely avoid premature drug leakage outside the focus and stable drug release at the focus. Future studies may aim to utilize the optical, thermal, magnetic, or microenvironmental response of 2D materials to control the drug concentration at the target site and achieve the optimal therapeutic impact.

Despite the many challenges involved, the special physiochemical and kidney targeting properties of 2D nanomaterials continue to attract interest for their applications in kidney disease treatment. In addition to the excellent work discussed above, 2D nanomaterials require a broader range of material innovations in the field of AKI therapy. We expect that additional 2D nanomaterials with great biocompatibility, such as carbon-based 2D materials, silicate clays, and transition metal disulfides, will be investigated for the treatment of oxidative stress-related illnesses. Furthermore, innovative combinations of 2D nanomaterials with different dimensions provide new development opportunities for these systems. For example, Xu et al. designed a novel 2D DNA origami equipped with a microRNA-responsive one-dimensional nanoantenna, which enables the smart early diagnosis of AKI through PA imaging (Xu et al., 2022). Further 2D smart nanostructures with responsive, multifunctional, and programmable properties are expected to be developed in the future, which will lead to novel concepts and approaches for the treatment of kidney diseases such as AKI.

Author contributions

All authors listed have made a substantial, direct, and intellectual contribution to the work and approved it for publication.

Funding

This work was supported by the National Natural Science Foundation of China (No. 81974508, 21974134), Hunan Provincial Natural Science Foundation of China (No. 2021JJ31066), the Hunan Science Fund for Distinguished Young Scholar of China (No. 2021JJ10067), Innovation-Driven Project of Central South University (No. 202045005), Central South University Research Programme of Advanced Interdisciplinary Studies (2023QYJC017), Key Research Project of Ningxia Hui Autonomous Region in 2021 of China (Major Project) (No. 2021BEG01001), Key Program of Ningxia Hui Autonomous Region Natural Science Foundation of China (No. 2022AAC02058).

Conflict of interest

The authors declare that the research was conducted in the absence of any commercial or financial relationships that could be construed as a potential conflict of interest.

Publisher's note

References

Alam, S., Asaduzzaman Chowdhury, M., Shahid, A., Alam, R., and Rahim, A. (2021). Synthesis of emerging two-dimensional (2D) materials – advances, challenges and prospects. *FlatChem* 30, 100305. doi:10.1016/j.flatc.2021.100305

Chen, Q., Ding, F., Zhang, S., Li, Q., Liu, X., Song, H., et al. (2021). Sequential therapy of acute kidney injury with a DNA nanodevice. *Nano Lett.* 21 (10), 4394–4402. doi:10.1021/acs.nanolett.1c01044

Chen, Q., Nan, Y., Yang, Y., Xiao, Z., Liu, M., Huang, J., et al. (2023). Nanodrugs alleviate acute kidney injury: Manipulate RONS at kidney. *Bioact. Mater.* 22, 141–167. doi:10.1016/j.bioactmat.2022.09.021

Chen, Z., Qi, F., Qiu, W., Wu, C., Zong, M., Ge, M., et al. (2022). Hydrogenated germanene nanosheets as an antioxidative defense agent for acute kidney injury treatment. *Adv. Sci.* 9 (33), 2202933. doi:10.1002/advs.202202933

Choi, S. H., Yun, S. J., Won, Y. S., Oh, C. S., Kim, S. M., Kim, K. K., et al. (2022). Large-scale synthesis of graphene and other 2D materials towards industrialization. *Nat. Commun.* 13 (1), 1484. doi:10.1038/s41467-022-29182-y

Dagher, R., Copenhaver, A. M., Besnard, V., Berlin, A., Hamidi, F., Maret, M., et al. (2020). IL-33-ST2 axis regulates myeloid cell differentiation and activation enabling effective club cell regeneration. *Nat. Commun.* 11 (1), 4786. doi:10.1038/s41467-020-18466-w

Faas, M., Ipseiz, N., Ackermann, J., Culemann, S., Gruneboom, A., Schroder, F., et al. (2021). IL-33-induced metabolic reprogramming controls the differentiation of alternatively activated macrophages and the resolution of inflammation. *IMMUNITY* 54 (11), 2531–2546.e5. doi:10.1016/j.immuni.2021.09.010

Fan, T., Yan, L., He, S., Hong, Q., Ai, F., He, S., et al. (2022). Biodistribution, degradability and clearance of 2D materials for their biomedical applications. *Chem. Soc. Rev.* 51 (18), 7732–7751. doi:10.1039/d1cs01070k

Feng, C., Ouyang, J., Tang, Z., Kong, N., Liu, Y., Fu, L., et al. (2020). Germanene-based theranostic materials for surgical adjuvant treatment: Inhibiting tumor recurrence and wound infection. *MATTER* 3 (1), 127–144. doi:10.1016/j.matt.2020.04.022

Ge, M., Zong, M., Xu, D., Chen, Z., Yang, J., Yao, H., et al. (2021). Freestanding germanene nanosheets for rapid degradation and photothermal conversion. *Mater. TODAY Nano* 15, 100119. doi:10.1016/j.mtnano.2021.100119

Hou, J. J., Wang, H., Ge, Z. L., Zuo, T. T., Chen, Q., Liu, X. G., et al. (2020). Treating acute kidney injury with antioxidative black phosphorus nanosheets. *Nano Lett.* 20 (2), 1447–1454. doi:10.1021/acs.nanolett.9b05218

Hou, L., Gong, F., Liu, B., Yang, X., Chen, L., Lie, G., et al. (2022). Orally administered titanium carbide nanosheets as anti-inflammatory therapy for colitis. *THERANOSTICS* 12 (8), 3834–3846. doi:10.7150/thno.70668

Hu, K., Xie, L., Zhang, Y. D., Hanyu, M., Yang, Z. M., Nagatsu, K., et al. (2020). Marriage of black phosphorus and Cu2+ as effective photothermal agents for PET-guided combination cancer therapy. *Nat. Commun.* 11 (1), 2778. doi:10.1038/s41467-020-16513-0

Hu, T. T., Mei, X., Wang, Y. J., Weng, X. S., Liang, R. Z., and Wei, M. (2019). Two-dimensional nanomaterials: Fascinating materials in biomedical field. *Sci. Bull.* 64 (22), 1707–1727. doi:10.1016/j.scib.2019.09.021

Huang, Q., Yang, Y. Q., Zhao, T. J., Chen, Q. H., Liu, M., Ji, S. T., et al. (2023). Passively-targeted mitochondrial tungsten-based nanodots for efficient acute kidney injury treatment. *Bioact. Mater.* 21, 381–393. doi:10.1016/j.bioactmat.2022.08.022

Huang, Q., Yang, Y., Zhu, Y., Chen, Q., Zhao, T., Xiao, Z., et al. (2023). Oral metal-free melanin nanozymes for natural and durable targeted treatment of inflammatory bowel disease (IBD). *Small* n/a, 2207350. doi:10.1002/smll.202207350

Jiang, D., Rosenkrans, Z. T., Ni, D., Lin, J., Huang, P., and Cai, W. (2020). Nanomedicines for renal management: From imaging to treatment. *ACCOUNTS Chem. Res.* 53 (9), 1869–1880. doi:10.1021/acs.accounts.0c00323

Jiang, D. W., Ge, Z. L., Im, H. J., England, C. G., Ni, D. L., Hou, J. J., et al. (2018). DNA origami nanostructures can exhibit preferential renal uptake and alleviate acute kidney injury. *Nat. Biomed. Eng.* 2 (11), 865–877. doi:10.1038/s41551-018-0317-8

Jiang, Q., Liu, S., Liu, J., Wang, Z.-G., and Ding, B. (2019). Rationally designed DNA-origami nanomaterials for drug delivery *in vivo*. *Adv. Mater.* 31 (45), 1804785. doi:10.1002/adma.201804785

Kellum, J. A., Romagnani, P., Ashuntantang, G., Ronco, C., Zarbock, A., and Anders, H.-J. (2021). Acute kidney injury. *Nat. Rev. Dis. Prim.* 7 (1), 52. doi:10.1038/s41572-021-00284-z

Li, J., Wei, L., Zhang, Y., and Wu, M. (2021). Tetrahedral DNA nanostructures inhibit ferroptosis and apoptosis in cisplatin-induced renal injury. *Acs Appl. Bio Mater.* 4 (6), 5026–5032. doi:10.1021/acsabm.1c00294

Li, W., Wang, C. S., Lv, H., Wang, Z. H., Zhao, M., Liu, S. Y., et al. (2021). A DNA nanoraft-based cytokine delivery platform for alleviation of acute kidney injury. *Acs Nano* 15 (11), 18237–18249. doi:10.1021/acsnano.1c07270

Li, Z., Liu, Z., Luo, M., Li, X., Chen, H., Gong, S., et al. (2022). The pathological role of damaged organelles in renal tubular epithelial cells in the progression of acute kidney injury. *Cell Death Discov.* 8 (1), 239. doi:10.1038/s41420-022-01034-0

Lin, H., Chen, Y., and Shi, J. L. (2018). Insights into 2D MXenes for versatile biomedical applications: Current advances and challenges ahead. *Adv. Sci.* 5 (10), 1800518. doi:10.1002/advs.201800518

Liu, M., Huang, Q., Zhu, Y., Chen, L., Li, Y., Gong, Z., et al. (2022). Harnessing reactive oxygen/nitrogen species and inflammation: Nanodrugs for liver injury. *Mater Today Bio* 13, 100215. doi:10.1016/j.mtbio.2022.100215

Liu, M., Xiang, Y., Yang, Y., Long, X., Xiao, Z., Nan, Y., et al. (2022). State-of-the-art advancements in liver-on-a-chip (LOC): Integrated biosensors for LOC. *Biosens. Bioelectron.* 218, 114758. doi:10.1016/j.bios.2022.114758

Lucas, C. R., Halley, P. D., Chowdury, A. A., Harrington, B. K., Beaver, L., Lapalombella, R., et al. (2022). DNA origami nanostructures elicit dose-dependent immunogenicity and are nontoxic up to high doses *in vivo*. *SMALL* 18 (26), 2108063. doi:10.1002/smll.202108063

Mostafavi, E., and Iravani, S. (2022). MXene-graphene composites: A perspective on biomedical potentials. *NANO-MICRO Lett.* 14 (1), 130. doi:10.1007/s40820-022-00880-y

Ostermann, M., Bellomo, R., Burdmann, E. A., Doi, K., Endre, Z. H., Goldstein, S. L., et al. (2020). Controversies in acute kidney injury: Conclusions from a kidney disease: Improving global outcomes (KDIGO) conference. *KIDNEY Int.* 98 (2), 294–309. doi:10.1016/j.kint.2020.04.020

Ouyang, J., Rao, S., Liu, R., Wang, L., Chen, W., Tao, W., et al. (2022). 2D materials-based nanomedicine: From discovery to applications. *Adv. DRUG Deliv. Rev.* 185, 114268. doi:10.1016/j.addr.2022.114268

Parsons, M. F., Allan, M. F., Li, S., Shepherd, T. R., Ratanalert, S., Zhang, K., et al. (2023). 3D RNA-scaffolded wireframe origami. *Nat. Commun.* 14 (1), 382. doi:10.1038/s41467-023-36156-1

Pickkers, P., Darmon, M., Hoste, E., Joannidis, M., Legrand, M., Ostermann, M., et al. (2021). Acute kidney injury in the critically ill: An updated review on pathophysiology and management. *INTENSIVE CARE Med.* 47 (8), 835–850. doi:10.1007/s00134-021-06454-7

Rohaizad, N., Mayorga-Martinez, C. C., Fojtu, M., Latiff, N. M., and Pumera, M. (2021). Two-dimensional materials in biomedical, biosensing and sensing applications. *Chem. Soc. Rev.* 50 (1), 619–657. doi:10.1039/d0cs00150c

Ronco, C., Reis, T., and Husain-Syed, F. (2020). Management of acute kidney injury in patients with COVID-19. *LANCET Respir. Med.* 8 (7), 738–742. doi:10.1016/S2213-2600(20)30229-0

Soleymaniha, M., Shahbazi, M. A., Rafieerad, A. R., Maleki, A., and Amiri, A. (2019). Promoting role of MXene nanosheets in biomedical Sciences: Therapeutic and biosensing innovations. *Adv. Healthc. Mater.* 8 (1), 1801137. doi:10.1002/adhm.201801137

Su, L., Zhang, J., Gomez, H., Kellum, J. A., and Peng, Z. (2023). Mitochondria ROS and mitophagy in acute kidney injury. *Autophagy* 19 (2), 401–414. doi:10.1080/15548627.2022.2084862

Su, X. L., Xie, X. F., Liu, L. J., Lv, J. C., Song, F. J., Perkovic, V., et al. (2017). Comparative effectiveness of 12 treatment strategies for preventing contrast-induced acute kidney injury: A systematic review and bayesian network meta-analysis. *Am. J. KIDNEY Dis.* 69 (1), 69–77. doi:10.1053/j.ajkd.2016.07.033

Sui, Y. L., Zhou, J., Wang, X. W., Wu, L., Zhong, S. K., and Li, Y. G. (2021). Recent advances in black-phosphorus-based materials for electrochemical energy storage. *Mater. TODAY* 42, 117–136. doi:10.1016/j.mattod.2020.09.005

Sun, Q., Ma, H., Zhang, J., You, B., Gong, X., Zhou, X., et al. (2023). A self-sustaining antioxidant strategy for effective treatment of myocardial infarction. *Adv. Sci.* 10 (5), 2204999. doi:10.1002/advs.202204999

Thai, H. B. D., Kim, K. R., Hong, K. T., Voitsitskyi, T., Lee, J. S., Mao, C. D., et al. (2020). Kidney-targeted cytosolic delivery of siRNA using a small-sized mirror DNA

tetrahedron for enhanced potency. *Acs Central Sci.* 6 (12), 2250–2258. doi:10.1021/acscentsci.0c00763

Thurakkal, S., and Zhang, X. (2020). Recent advances in chemical functionalization of 2D black phosphorous nanosheets. *Adv. Sci.* 7 (2), 1902359. doi:10.1002/advs.201902359

Tian, T., Li, Y., and Lin, Y. (2022). Prospects and challenges of dynamic DNA nanostructures in biomedical applications. *BONE Res.* 10 (1), 40. doi:10.1038/s41413-022-00212-1

Tian, Z., and Liang, M. (2021). Renal metabolism and hypertension. *Nat. Commun.* 12 (1), 963. doi:10.1038/s41467-021-21301-5

van der Meel, R., Sulheim, E., Shi, Y., Kiessling, F., Mulder, W. J. M., and Lammers, T. (2019). Smart cancer nanomedicine. *Nat. Nanotechnol.* 14 (11), 1007–1017. doi:10.1038/s41565-019-0567-y

Wang, K. Y., Zhang, Y., Mao, W. P., Feng, W., Lu, S. T., Wan, J., et al. (2022). Engineering ultrasmall ferroptosis-targeting and reactive oxygen/nitrogen species-scavenging nanozyme for alleviating acute kidney injury. *Adv. Funct. Mater.* 32 (10), 2109221. doi:10.1002/adfm.202109221

Wang, L. F., Zhang, Y. J., Li, Y. Y., Chen, J. H., and Lin, W. Q. (2021). Recent advances in engineered nanomaterials for acute kidney injury theranostics. *Nano Res.* 14 (4), 920–933. doi:10.1007/s12274-020-3067-3

Wang, L., Zhang, N., Li, Y., Kong, W., Gou, J., Zhang, Y., et al. (2021). Mechanism of nitrogen-doped Ti3C2 quantum dots for free-radical scavenging and the ultrasensitive H2O2 detection performance. *ACS Appl. Mater. INTERFACES* 13 (36), 42442–42450. doi:10.1021/acsami.1c11242

Wang, S., Chen, Q., Zhao, T., Ai, K., and Hu, C. (2023). Nanomedicine-based treatment: An emerging therapeutical strategy for pulmonary hypertension. *Nano Res.* doi:10.1007/s12274-022-5310-6

Wang, T., Bai, T., Tan, Z., Ohayon, Y. P., Sha, R., Vecchioni, S., et al. (2023). Mesojunction-based design paradigm of structural DNA nanotechnology. *J. Am. Chem. Soc.* 145, 2455–2460. doi:10.1021/jacs.2c11731

Weng, Q. J., Sun, H., Fang, C. Y., Xia, F., Liao, H. W., Lee, J. Y., et al. (2021). Catalytic activity tunable ceria nanoparticles prevent chemotherapy-induced acute kidney injury without interference with chemotherapeutics. *Nat. Commun.* 12 (1), 1436. doi:10.1038/s41467-021-21714-2

Wu, J., Wang, X., Wang, Q., Lou, Z., Li, S., Zhu, Y., et al. (2019). Nanomaterials with enzyme-like characteristics (nanozymes): Next-generation artificial enzymes (II). *Chem. Soc. Rev.* 48 (4), 1004–1076. doi:10.1039/c8cs00457a

Xu, J., Shi, R., Chen, G., Dong, S., Yang, P., Zhang, Z., et al. (2020). All-in-One theranostic nanomedicine with ultrabright second near-infrared emission for tumor-modulated bioimaging and chemodynamic/photodynamic therapy. *ACS Nano* 14 (8), 9613–9625. doi:10.1021/acsnano.0c00082

Xu, Y., Zhang, Q., Chen, R., Cao, H., Tang, J., Wu, Y., et al. (2022). NIR-II photoacoustic-active DNA origami nanoantenna for early diagnosis and smart therapy of acute kidney injury. *J. Am. Chem. Soc.* 144 (51), 23522–23533. doi:10.1021/jacs.2c10323

Yang, B., Chen, Y., and Shi, J. (2019). Reactive oxygen species (ROS)-Based nanomedicine. *Chem. Rev.* 119 (8), 4881–4985. doi:10.1021/acs.chemrev.8b00626

Zhang, D. Y., Tu, T. H., Younis, M. R., Zhu, K. S., Liu, H. K., Lei, S., et al. (2021). Clinically translatable gold nanozymes with broad spectrum antioxidant and anti-inflammatory activity for alleviating acute kidney injury. *THERANOSTICS* 11 (20), 9904–9917. doi:10.7150/thno.66518

Zhang, H., Fan, T., Chen, W., Li, Y., and Wang, B. (2020). Recent advances of two-dimensional materials in smart drug delivery nano-systems. *Bioact. Mater.* 5 (4), 1071–1086. doi:10.1016/j.bioactmat.2020.06.012

Zhang, Q., Lin, S. Y., Wang, L., Peng, S. L., Tian, T. R., Li, S. H., et al. (2021). Tetrahedral framework nucleic acids act as antioxidants in acute kidney injury treatment. *Chem. Eng. J.* 413, 127426. doi:10.1016/j.cej.2020.127426

Zhang, T., Tian, T., and Lin, Y. (2022). Functionalizing framework nucleic-acid-based nanostructures for biomedical application. *Adv. Mater.* 34 (46), 2107820. doi:10.1002/adma.202107820

Zhao, H., Huang, J., Miao, L., Yang, Y., Xiao, Z., Chen, Q., et al. (2022). Toward Urease-free wearable artificial kidney: Widened interlayer spacing MoS2 nanosheets with highly effective adsorption for uremic toxins. *Chem. Eng. J.* 438, 135583. doi:10.1016/j.cej.2022.135583

Zhao, M., Wang, Y., Li, L., Liu, S., Wang, C., Yuan, Y., et al. (2021). Mitochondrial ROS promote mitochondrial dysfunction and inflammation in ischemic acute kidney injury by disrupting TFAM-mediated mtDNA maintenance. *Theranostics* 11 (4), 1845–1863. doi:10.7150/thno.50905

Zhao, S., Tian, R., Wu, J., Liu, S. L., Wang, Y. N., Wen, M., et al. (2021). A DNA origami-based aptamer nanoarray for potent and reversible anticoagulation in hemodialysis. *Nat. Commun.* 12 (1), 358. doi:10.1038/s41467-020-20638-7

Zhao, T., Wu, W., Sui, L., Huang, Q., Nan, Y., Liu, J., et al. (2022). Reactive oxygen species-based nanomaterials for the treatment of myocardial ischemia reperfusion injuries. *Bioact. Mater.* 7, 47–72. doi:10.1016/j.bioactmat.2021.06.006

Zhao, X., Wang, L.-Y., Li, J.-M., Peng, L.-M., Tang, C.-Y., Zha, X.-J., et al. (2021). Redox-mediated artificial non-enzymatic antioxidant MXene nanoplatforms for acute kidney injury alleviation. *Adv. Sci.* 8, 2101498. doi:10.1002/advs.202101498

Zheng, Y., Hong, X., Wang, J., Feng, L., Fan, T., Guo, R., et al. (2021). 2D nanomaterials for tissue engineering and regenerative nanomedicines: Recent advances and future challenges. *Adv. Healthc. Mater.* 10 (7), 2001743. doi:10.1002/adhm.202001743

Zhou, Z., Ni, K., Deng, H., and Chen, X. (2020). Dancing with reactive oxygen species generation and elimination in nanotheranostics for disease treatment. *Adv. Drug Deliv. Rev.* 158, 73–90. doi:10.1016/j.addr.2020.06.006

Zhu, Y., Zhao, T., Liu, M., Wang, S., Liu, S., Yang, Y., et al. (2022). Rheumatoid arthritis microenvironment insights into treatment effect of nanomaterials. *Nano Today* 42, 101358. doi:10.1016/j.nantod.2021.101358

frontiers | Frontiers in Bioengineering and Biotechnology

TYPE Original Research
PUBLISHED 17 March 2023
DOI 10.3389/fbioe.2023.1176046

OPEN ACCESS

EDITED BY
Hua Yue,
Institute of Process Engineering (CAS), China

REVIEWED BY
Fang Ma,
Beijing Chaoyang Hospital, Capital Medical University, China
Ru-Ping Liang,
Nanchang University, China

*CORRESPONDENCE
Lishi Wang,
wanglsh@scut.edu.cn

SPECIALTY SECTION
This article was submitted to Nanobiotechnology, a section of the journal Frontiers in Bioengineering and Biotechnology

RECEIVED 28 February 2023
ACCEPTED 08 March 2023
PUBLISHED 17 March 2023

CITATION
Yu X, Bai S and Wang L (2023), *In situ* reduction of gold nanoparticles-decorated MXenes-based electrochemical sensing platform for KRAS gene detection.
Front. Bioeng. Biotechnol. 11:1176046.
doi: 10.3389/fbioe.2023.1176046

In situ reduction of gold nanoparticles-decorated MXenes-based electrochemical sensing platform for KRAS gene detection

Xiongtao Yu, Silan Bai and Lishi Wang*

School of Chemistry and Chemical Engineering, South China University of Technology, Guangzhou, China

In this work, gold nanoparticles@Ti_3C_2 MXenes nanocomposites with excellent properties were combined with toehold-mediated DNA strand displacement reaction to construct an electrochemical circulating tumor DNA biosensor. The gold nanoparticles were synthesized *in situ* on the surface of Ti_3C_2 MXenes as a reducing and stabilizing agent. The good electrical conductivity of the gold nanoparticles@Ti_3C_2 MXenes composite and the nucleic acid amplification strategy of enzyme-free toehold-mediated DNA strand displacement reaction can be used to efficiently and specifically detect the non-small cell cancer biomarker circulating tumor DNA KRAS gene. The biosensor has a linear detection range of 10 fM –10 nM and a detection limit of 0.38 fM, and also efficiently distinguishes single base mismatched DNA sequences. The biosensor has been successfully used for the sensitive detection of KRAS gene G12D, which has excellent potential for clinical analysis and provides a new idea for the preparation of novel MXenes-based two-dimensional composites and their application in electrochemical DNA biosensors.

KEYWORDS

MXenes, gold nanoparticle, biomarker, CtDNA, electrochemical, biosensor

Introduction

In recent years, Ti_3C_2 MXenes, a new type of two-dimensional layered nanomaterial has received much attention because of its excellent properties such as good electrical conductivity (up to 2.4×10^5 S/m), large surface area, easy film formation, and good biocompatibility (Yuan et al., 2018; Zhang et al., 2018; Pang et al., 2019). Ti_3C_2 MXenes have a wide range of promising applications in catalysis (Li and Wu, 2019; Su et al., 2019), environmental protection (Lim et al., 2020), biosensors (Wen et al., 2017; Kumar et al., 2018; Wang et al., 2020; Lu et al., 2021), supercapacitors (Wang et al., 2018; Chen et al., 2021), batteries (Li et al., 2021; Lee et al., 2022), etc. Based on these excellent properties, Ti_3C_2 MXenes have great potential for sensor construction.

MXenes compounded with other nanomaterials provide better performance and enhance the detection performance of the sensing platform (Song et al., 2022; Yang et al., 2022). Ti_3C_2 MXenes-based composites could be used in sensing platforms not only as carriers of signal probes but also to facilitate interfacial electron transfer (Chen et al., 2013; Wang et al., 2013). Compounding of Ti_3C_2 MXenes with metal nanoparticles or metal

TABLE 1 A list of the oligonucleotide sequences.

DNA	Sequence (5′-3′)
template DNA	SH-$(CH_2)_6$-GAAATGGTGGAAAGGTCAACTG
	GAGCTGGTGGCGTAG
assisted DNA	CACCAGCTCCAGTTGACCCTATATCCATAA
protected DNA	CCTTTCCACCATTTC
probe DNA	CACCAGCTCCAGTTGACCTTTCCACCATTTC-methylene blue
KARS G12D	CTACGCCACCAGCTCCA
Single-base mismatch (1 M)	CTA*T*GCCACCAGCTCCA
Two-base mismatch (2 M)	CTA*T*GC*A*ACCAGCTCCA
Three-base mismatch (3 M)	CTA*T*GC*A*ACGAGCTCCA
Random DNA	AGCATTGACTACGCCGT

oxides is more favored in the synthesis of Ti_3C_2 MXenes-based composites. Metal nanoparticles, metal oxides, and other nanomaterials are synthesized by adding stabilizers such as surfactants to avoid aggregation. However, surfactants may cover the surface of the nanomaterials, thus obscuring the active sites and blocking electron transfer, which may adversely affect the performance of the sensors. (Steigerwalt et al., 2002; Bing et al., 2010; Dey et al., 2013). Therefore, nanomaterials without surfactants with excellent conductivity may be more suitable for the construction of electrochemical sensors. Ti_3C_2 MXenes have great potential for the preparation of MXenes-metal nanoparticle composites due to their strong reducing ability. For example, the synthesized composites MXenes/magnetic iron oxide and MXenes/Ag have a strong catalytic capacity (Zhang et al., 2016; Zou et al., 2016). Ti_3C_2 MXenes are widely used in the synthesis of surfactant-free nanomaterials due to their unique properties and simple preparation process.

Liquid biopsy is a method of sampling and analyzing body fluids such as blood, urine, and saliva to detect and diagnose cancer or other diseases. Liquid biopsy can detect a range of biomarkers such as circulating tumor DNA (ctDNA), circulating tumor cells, and exosomes (Wu et al., 2020). CtDNA is a biomarker for tumor cells to release their DNA fragments in body fluids. Breakthroughs in ctDNA analysis and detection technologies are driving the development of minimally invasive liquid biopsy for disease (Das et al., 2016). Therefore, ctDNA detection has received a lot of attention in the field of tumor diagnosis and treatment. Colorectal cancer (CRC) is a type of gastrointestinal malignancy with a high mortality rate and an increasing incidence, currently causing at least 890,000 deaths per year (Bray et al., 2018; Siegel et al., 2020; Wang et al., 2022). Mutation and activation of the KRAS gene in the human body are important causes of the development and progression of colorectal cancer (Shaukat et al., 2012). The KRAS gene is often mutated at codons 12 and 13 and is an unfavorable factor in the development, progression, and prognosis of colorectal cancer (Zhu et al., 2007). Therefore, the detection and evaluation of the KRAS gene is an important tool for the early diagnosis and treatment of colorectal cancer. Commonly used analytical methods in clinical settings include polymerase chain reaction (PCR), mass spectrometry, surface-enhanced Raman scattering (SERS), and next-generation sequencing (NGS). Although these methods have some advantages, the development of low-cost, simple, sensitive, and portable nucleic acid detection methods remains a challenge. Electrochemical methods have been widely used in clinical diagnostics, environmental monitoring, food safety, and immunoassays due to their high sensitivity, short time consumption, ease of control, and low cost. (Yang et al., 2016; Zheng et al., 2020; Yu et al., 2022). On the other hand, many analytical techniques including some electrochemical methods require enzyme participation to improve sensitivity. However, the non-specificity of enzyme-catalyzed reaction and the need for harsh reaction conditions bring difficulties to the detection technology (Yang F. et al., 2021; Yang J. et al., 2021; Zhuang et al., 2021). The toehold-mediated DNA strand displacement reaction (TMSD) is widely used in the construction of biosensors due to its ability to amplify signals without the involvement of enzymes and its high reaction efficiency and simple design (Zhang et al., 2020a; Zhang et al., 2020b; Bialy et al., 2021).

In this study, a large number of AuNPs were synthesized *in situ* on the surface of Ti_3C_2 MXenes as a reducing and stabilizing agent, thus successfully preparing two-dimensional nanocomposite AuNPs@Ti_3C_2 MXenes with excellent electrochemical properties. The large surface area of Ti_3C_2 MXenes can be loaded with a lot of AuNPs and then self-assembled with more DNA double-strand probes *via* Au-S bonds thus efficiently facilitating the chain substitution reaction. The KARS G12D electrochemical DNA biosensor was constructed using the excellent electrochemical properties of AuNPs@Ti_3C_2 MXenes combined with nucleic acid amplification strategy of enzyme-free toehold-mediated DNA strand displacement reaction. The designed sensor exhibits excellent sensitivity and can be applied to the analysis of serum samples.

Materials and methods

Materials

Ti_3AlC_2 MAX was acquired from Aladdin (Shanghai, China). Tris (hydroxymethyl)aminomethane (Tris), and 6-Mercapto-1-hexanol (MCH) were acquired from Sigma. Tris (2-carboxyethyl) phosphine hydrochloride (TCEP) and chloroauric acid ($HAuCl_4{\cdot}4H_2O$, ≥99.9%) were ordered from J&K scientific. Hydrofluoric acid was acquired from Sinopharm Chemical Reagent Co., Ltd. (Shanghai, China). 0.1 M pH 7.4 Tris-HCl buffer (100 mM NaCl and 20 mM $MgCl_2$) was used for electrochemical measurement, and 10 mM pH 7.4 Tris-HCl buffer was used as washing buffer. All DNA strands were ordered from Sangon Biotech Co., Ltd. (Shanghai, China), and the DNA sequences were provided in Table 1. 18.2 MΩ cm ultrapure water was used in whole experiments.

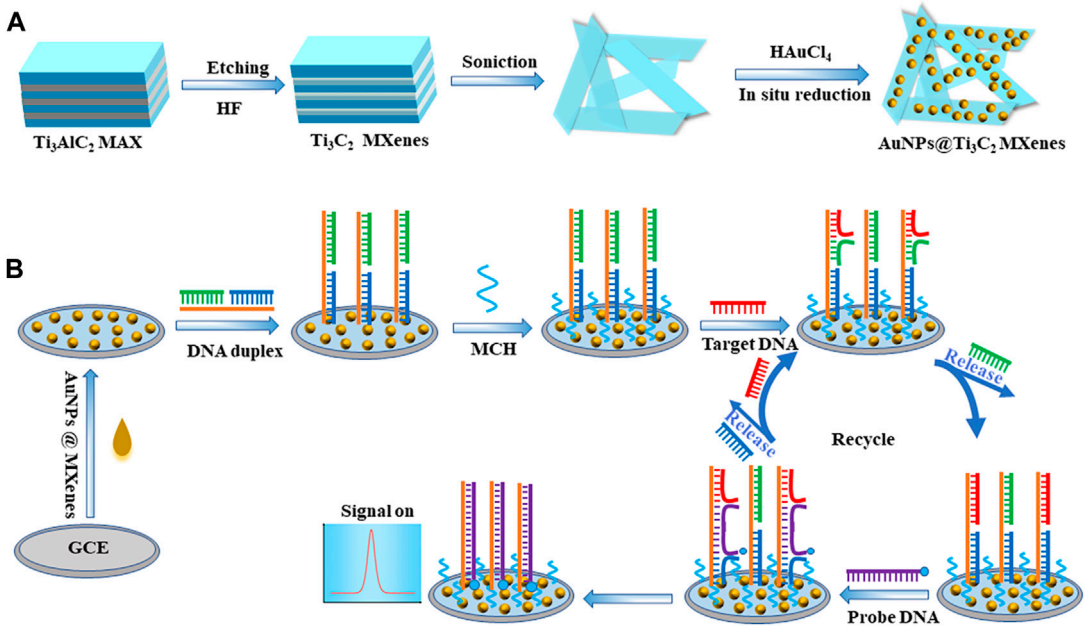

SCHEME 1
Schematic illustrations of **(A)** the synthesis route for AuNPs@Ti3C2 MXenes nanocomposites, and **(B)** electrochemical sensing platform for KRAS gene detection via toehold-mediated strand displacement reaction.

Apparatus

Scanning electron microscopy (SEM) images and elemental mapping were characterized by SU8220 field-emission scanning electron microscope (Hitachi Ltd, Japan, 10.0 kV). X-ray diffraction (XRD) was characterized by X'pert Powder X-ray diffraction (Panalytical. Ltd, Netherlands). Transmission electron microscope (TEM) images were recorded on a JEM-2100F field emission electron microscope (JEOL, Japan) at an accelerating voltage of 200 kV.

Preparation of Ti_3C_2 MXenes

Ti_3C_2 MXenes were prepared by etching the Al element in Ti_3AlC_2 MAX with HF solution referring to the previous literature with minor modifications (Lin et al., 2020) (Scheme 1A). Briefly, 1 g Ti_3AlC_2 was added to 50 mL 45% HF solution, and then etched at room temperature for 24 h. The precipitate was collected by centrifugation at 6,000 rpm for 15 min. Finally, the precipitate was washed several times with deionized water until the pH of the supernatant exceeded 6. The Ti_3C_2 MXenes were obtained.

Synthesis of AuNPs@Ti_3C_2 MXenes nanocomposites

AuNPs@Ti_3C_2 MXenes nanocomposites were synthesized referring to the previous literature with minor modifications (Mi et al., 2021; Song et al., 2022) (Scheme 1A). AuNPs were synthesized by *in situ* reduction on the surface of Ti_3C_2 MXenes and Ti_3C_2 MXenes were used as the reducing agent and support material. Firstly, 15 mg pre-prepared Ti_3C_2 MXenes were well-dispersed in 45 mL deionized water, and the Ti_3C_2 suspension (0.33 mg mL^{-1}) was prepared after sonicating for 4 h. Then, 600 μL of 1 g mL^{-1} $HAuCl_4$ solution was slowly added to the Ti_3C_2 suspension drop by drop with gentle stirring. After the reaction at room temperature for 30 min, the resulting suspension was centrifuged at 8,000 rpm for 10 min and the precipitate was collected. The AuNPs@Ti_3C_2 two-dimensional nanocomposites were successfully prepared by washing with deionized water several times for subsequent studies.

Fabrication of DNA biosensor

The bare glassy carbon electrode (GCE) was polished with 0.05 μm alumina slurry for 5 min before modification and then sonicated in ethanol and deionized water for 2 min, respectively. Finally, the bare GCE was rinsed with deionized water and then dried with nitrogen gas for the following experiment. Subsequently, 1 mg mL^{-1} AuNPs@Ti_3C_2 MXenes nanocomposites were dropped onto the GCE surface to obtain the AuNPs@Ti_3C_2 MXenes/GCE and dried naturally. 5 μM template DNA, 5 μM protected DNA and 5 μM auxiliary DNA were incubated at 90°C for 5 min, and then gradually cooled to room temperature to form stable DNA duplex structures. Then, a final concentration of 10 mM of TCEP was added to the DNA duplex for 1 hour at room temperature to break the disulfide bond. Subsequently, drop 10 μL 1 μM DNA double-strand probes onto the modified electrode AuNPs@Ti_3C_2 MXenes/GCE and incubate at room temperature for 3 h to form self-assembled monolayers. The electrodes were immersed in 1 mM MCH to block the unbound sites, then washed with Tris-HCl buffer and dried with nitrogen subsequently.

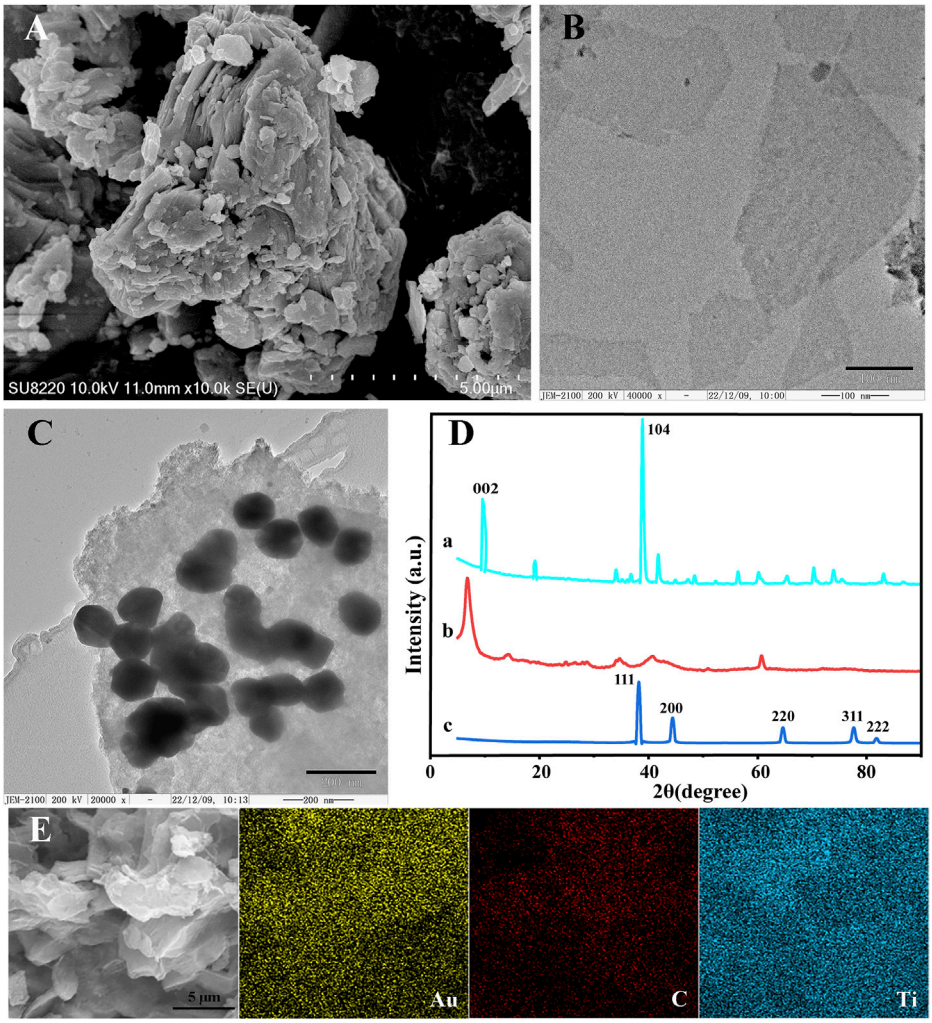

FIGURE 1
SEM images of Ti_3AlC_2 **(A)**. TEM images of Ti_3C_2 **(B)** and AuNPs@Ti_3C_2 MXenes **(C)**. **(D)** XRD of Ti_3AlC_2 **(a)**, Ti_3C_2 **(b)**, AuNPs@Ti_3C_2 **(c)**. **(E)** Elemental mapping images of AuNPs@Ti_3C_2.

Detection of KARS G12D

The electrodes of the modified DNA duplex probes were washed with buffer and then immersed in a solution containing 50 μL^1 μM probe DNA and various concentrations of target DNA KARS G12D. The TMSD recycling process took 2 hours to complete at room temperature. Subsequently, the electrodes were washed with 10 mM Tris-HCl buffer and were used for electrochemical measurement.

Electrochemical measurements

A CHI660E electrochemical workstation (Shanghai Chenhua Instrument Co. Ltd., China) was used for all electrochemical measurements which contained a three-electrode system consisting of a modified 3 mm GCE, a platinum auxiliary electrode, and a saturated Ag/AgCl reference electrode. Square wave voltammetry (SWV) experiments were carried out in 10 mM Tris–HCl buffer (100 mM NaCl and 20 mM $MgCl_2$, pH 7.4) using the following parameters: a potential range of −0.6 to 0 V, an amplitude of 25 mV, a frequency of 25 Hz, and a step potential of 4 mV. To prevent the interference of oxygen reduction during the electrochemical measurement, high-grade nitrogen should be used to purge the detection buffer for 30 min. Electrochemical impedance spectroscopy (EIS) was performed in 5 mM $[Fe(CN)_6]^{3-/4-}$ contained 0.1 M KCl, in frequency range from 0.03 Hz to 10 kHz with the bias potential of 0.192 V and the amplitude of 5 mV, respectively.

Results and discussion

Characterizations of the Ti_3C_2 MXenes and AuNPs@Ti_3C_2 MXenes nanocomposites

The morphologies of Ti_3AlC_2, Ti_3C_2, and AuNPs@Ti_3C_2 MXenes were characterized by SEM and TEM. Ti_3AlC_2 without etching treatment exhibited an irregular morphology (Figure 1A).

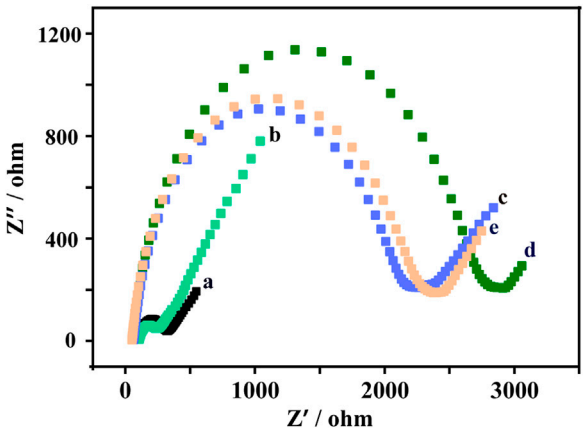

FIGURE 2
Electrochemical impedance spectroscopy (EIS) response of bare GCE **(a)**, gold nanoparticles @ Ti_3C_2 MXenes/GCE **(b)**, DNA double-strand probes/gold nanoparticles @Ti_3C_2 MXenes/GCE **(c)**, MCH/DNA double-strand probes/gold nanoparticles@ Ti_3C_2 MXenes/GCE **(d)**, probe DNA/target DNA/MCH/DNA double-strand probes/gold nanoparticles@Ti_3C_2 MXenes/GCE **(e)** in 5 mM $[Fe(CN)_6]^{3-/4-}$ containing 0.1 M KCl.

The Ti_3C_2 MXenes prepared by etching and ultrasound show a smooth, thin, and flake structure (Figure 1B) due to the disappearance of the Al layer after the HF etching. Figure 1C shows that the size of AuNPs synthesized by *in situ* reduction on the surface of Ti_3C_2 is about 125 nm. Because of the large surface area of Ti_3C_2, a lot of AuNPs were synthesized. By measuring the elemental properties of AuNPs@Ti_3C_2 MXenes, the results showed that the Ti, C, and Au elements of AuNPs@Ti_3C_2 MXenes were uniformly distributed and continuously (Figure 1E).

The XRD characterization further determined the composition and crystal structure of the nanocomposites (Figure 1D). The diffraction peaks of Ti_3AlC_2 at 9.5°, 19.06°, 38.7°, and 41.84° matched well with the diffraction peaks of the standard card (JCPDS card number: 52-0875) (curve a in Figure 1D). The XRD results of the Ti_3C_2 showed the disappearance of the 38.7° diffraction peak in the Al (104) plane and the left shift of the diffraction peak in the (002) plane of Ti_3C_2 from 9.5° to 8.27°, which indicated the successful preparation of Ti_3C_2 (curve b in Figure 1D) (Ran et al., 2017; Alhabeb et al., 2018; Meng et al., 2021). When AuNPs are generated by *in situ* reduction on the surface of Ti_3C_2, curve c in Figure 1D shows that AuNPs@Ti_3C_2 have the characteristic diffraction peaks of both Ti_3C_2 and AuNPs (Yang et al., 2022). The SEM images, TEM images, mapping, and XRD results indicated that the two-dimensional nanocomposite AuNPs@Ti_3C_2 MXenes were successfully synthesized.

The construction of electrochemical biosensor based on TMSD and AuNPs@Ti_3C_2 MXenes nanocomposites

Toehold-mediated strand displacement reaction was used in the development of many biosensors due to its high specificity and without the involvement of enzymes. In the toehold-mediated strand displacement reaction, one oligonucleotide hybridizes with the toehold domain of double-strand DNA resulting in the dissociation of the substrate strand from the double-strand DNA (Irmisch et al., 2020; Li et al., 2023). In this study, we developed two efficient and simple toehold-mediated strand displacement reactions (Scheme 1B). The first toehold-mediated strand displacement reaction was performed when target DNA KARS G12D hybridizes with the double-strand DNA probes. The second toehold-mediated strand displacement reaction was performed when the signal probes were present in the reaction system, and the dissociated target DNA KARS G12D entered the next cycle of reaction. The fabrication of the DNA biosensor based on toehold-mediated strand displacement reaction was illustrated in Scheme 1. First, the pre-prepared AuNPs@Ti_3C_2 MXenes were modified on the GCE. Then double-strand DNA probes were self-assembled onto the

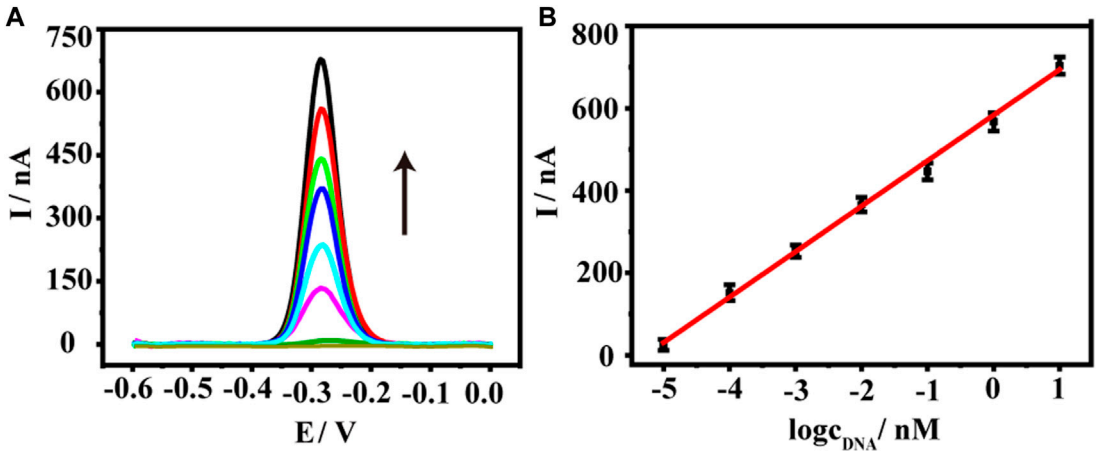

FIGURE 3
(A) Square wave voltammetry (SWV) curves of the DNA biosensor to KARS G12D gene at a series of concentrations, from down to top (black arrow): 0, 10^{-5}, 10^{-4},10^{-3}, 10^{-2}, 10^{-1}, 1, 10 nM. **(B)** The logarithmic plot of the current value of the oxidation peak versus the KARS G12D gene concentrations from 10^{-5} nM–10 nM. Error bars represent the standard deviations of three independent experiments.

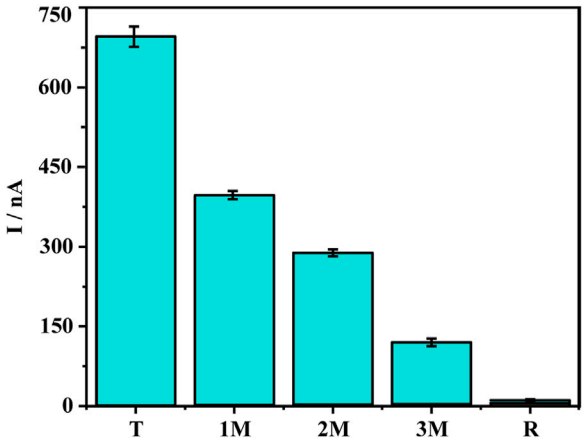

FIGURE 4
Specificity investigation of five different DNA sequences: Target DNA KARS G12D (T), single-base mismatched DNA (1 M), two-base mismatched DNA (2 M), three-base mismatched DNA (3 M), random DNA sequence (R). Error bars represent the standard deviations of three independent experiments.

AuNPs surface *via* Au-S bonding. The toehold of strand displacement reaction was formed. Subsequently, the target DNA KARS G12D and the signal probe were added for strand displacement reactions to achieve circular hybridization of KARS G12D. Meanwhile, the signal probe was linked to the electrode by the second strand displacement reaction to generate an electrochemical signal.

The EIS measurement results were shown in Figure 2. The bare glassy carbon electrode shows a small Ret value (curve a). When the bare glassy carbon electrode was modified with AuNPs@Ti_3C_2 MXenes composites, the Ret value became smaller (curve b), indicating that AuNPs@Ti_3C_2 MXenes composites have excellent electrical conductivity. The Ret value gradually increased when the DNA duplex structure and MCH were gradually modified, which was caused by the low conductivity of the DNA duplex structure and MCH (curves c and d). When the TMSD occurred after adding probe DNA and KARS G12D, the Ret value became smaller, probably due to the reduction of a steric hindrance after the hybridization of probe DNA and template DNA (curve e). The results of EIS and PAGE (Supplementary Figure S1) demonstrate the successful modification of AuNPs@Ti_3C_2 MXenes composites on glassy carbon electrodes and the successful design of TMSD.

Analytical performance of AuNPs@Ti_3C_2 MXenes-based biosensor

We thus used the sensor to detect a range of KARS G12D at concentrations from 10^{-5} nM–10 nM. As shown in Figure 3A, as the concentration of KARS G12D increased, the electrochemical signal values of methylene blue progressively increased, showing a typical concentration-dependent event. Further quantitative analysis exhibited a logarithmic relationship between the electrochemical signal values of methylene blue and the concentration of KARS G12D (Figure 3B). The calibrated regression equation was fitted to y (nA) = 110.6 log C_{tDNA} + 583.4 (R^2 = 0.9946), with a detection limit of 0.38 fM (S/N = 3). Such a low detection limit was equivalent to many enzyme-free sensors or even those sensors using enzymes. The constructed DNA sensor has high sensitivity and a wide linear range (Supplementary Table S1).

TABLE 2 Detection of KARS G12D gene added in serum samples.

Sample	Added (pM)	Found (pM)	Recovery (%)
1	1	1.09	109
2	5	5.03	100.1
3	10	9.33	93.3

Specificity, stability, and reproducibility of DNA sensor

Since the sensor has good detection performance, we further test the specificity of the sensor. Point mutations increase the difficulty of gene detection because they cause changes in the characteristics of genes. Therefore, the ability to identify point mutations is an important parameter for gene detection technology (Chang et al., 2015; Yu et al., 2022). We verified the specificity of the DNA sensor using five types of DNA sequences, including target DNA KARS G12D (T), single-base mismatched DNA (1 M), double-base mismatched DNA (2 M), triple-base mismatched DNA (3 M) and random sequence DNA (R) (Figure 4). A comparison of the oxidation peak current values of methylene blue revealed the current value of the 1 M group was much smaller than the T group, only 57% of the T group, revealing the ability of the sensor to recognize single base mismatches effectively. The oxidation peak current values of 2 M and 3 M were only 41% and 17% of the target DNA, while the peak current values of the random sequence DNA were almost close to the background values. To further ensure the performance of the sensor, the reproducibility and stability were also tested. The relative standard deviation (RSD) of the current signal values for the four parallel electrodes was 3.59%. In addition to this, the current signal value of the treated electrodes after 7 days at 4°C was 96.4% of the original value. The above results indicate that the sensor has good specificity, reproducibility, stability, and has good potential for clinical applications.

Real sample analysis

The sensor has good sensitivity, specificity, and stability. We further evaluated its ability to be used in clinical practice with real samples. Different concentrations of KARS G12D were added to a 10-fold dilution of healthy human serum for recovery testing. The recoveries of different concentrations of KARS G12D were 109%, 100.1%, and 93.3%, respectively (Table 2). The results showed that the sensor has good potential for monitoring ctDNAs in complicated biological samples.

Conclusion

In this work, we constructed an electrochemical DNA biosensor based on two-dimensional nanocomposite AuNPs@Ti_3C_2 MXenes and a non-enzymatic toehold-mediated strand displacement reaction. The good electrical conductivity of AuNPs@Ti_3C_2 MXenes and the signal amplification strategy of toehold-mediated strand displacement reaction can be used to detect KRAS G12D with high efficiency and specificity. The biosensor has excellent detection performance with a detection limit of 0.38 fM, and also effectively distinguishes single-base mismatched DNA sequences. In addition to detecting KRAS G12D, the platform also allows for rapid and easy detection of other disease biomarkers by redesigning disease-related DNA probes. The novel 2D composite material based on MXenes has good potential for application in biosensing platforms.

Data availability statement

The original contributions presented in the study are included in the article/Supplementary Material, further inquiries can be directed to the corresponding authors.

Author contributions

All authors conceptualized the study. XY: Conceptualization, investigation, visualization, and writing. SB: Formal analysis, conceptualization, resources. LW: Conceptualization, funding acquisition, and supervision.

Funding

This work was supported by the Natural Science Foundation of China (Grant No. 21874047).

Conflict of interest

The authors declare that the research was conducted in the absence of any commercial or financial relationships that could be construed as a potential conflict of interest.

Publisher's note

All claims expressed in this article are solely those of the authors and do not necessarily represent those of their affiliated organizations, or those of the publisher, the editors and the reviewers. Any product that may be evaluated in this article, or claim that may be made by its manufacturer, is not guaranteed or endorsed by the publisher.

Supplementary Material

The Supplementary Material for this article can be found online at: https://www.frontiersin.org/articles/10.3389/fbioe.2023.1176046/full#supplementary-material

References

Alhabeb, M., Maleski, K., Mathis, T. S., Sarycheva, A., Hatter, C. B., Uzun, S., et al. (2018). Selective etching of silicon from Ti3SiC2 (MAX) to obtain 2D titanium carbide (MXene). *Angew. Chemie-International Ed.* 57 (19), 5444–5448. doi:10.1002/anie.201802232

Bialy, R. M., Li, Y., and Brennan, J. D. (2021). Target-dependent protection of DNA aptamers against nucleolytic digestion enables signal-on biosensing with toehold-mediated rolling circle amplification. *Chem. – A Eur. J.* 27 (58), 14543–14549. doi:10.1002/chem.202102975

Bing, Y., Liu, H., Zhang, L., Ghosh, D., and Zhang, J. (2010). Nanostructured Pt-alloy electrocatalysts for PEM fuel cell oxygen reduction reaction. *Chem. Soc. Rev.* 39 (6), 2184–2202. doi:10.1039/B912552C

Bray, F., Ferlay, J., Soerjomataram, I., Siegel, R. L., Torre, L. A., and Jemal, A. (2018). Global cancer statistics 2018: GLOBOCAN estimates of incidence and mortality worldwide for 36 cancers in 185 countries. *CA A Cancer J. Clin.* 68 (6), 394–424. doi:10.3322/caac.21492

Chang, K., Deng, S., and Chen, M. (2015). Novel biosensing methodologies for improving the detection of single nucleotide polymorphism. *Biosens. Bioelectron.* 66, 297–307. doi:10.1016/j.bios.2014.11.041

Chen, Z., Liu, Y., Wang, Y., Zhao, X., and Li, J. (2013). Dynamic evaluation of cell surface N-glycan expression via an electrogenerated chemiluminescence biosensor based on concanavalin A-integrating gold-nanoparticle-modified Ru(bpy)32+-Doped silica nanoprobe. *Anal. Chem.* 85 (9), 4431–4438. doi:10.1021/ac303572g

Chen, Z., Xu, X., Ding, Z., Wang, K., Sun, X., Lu, T., et al. (2021). Ti3C2 MXenes-derived NaTi2(PO4)3/MXene nanohybrid for fast and efficient hybrid capacitive deionization performance. *Chem. Eng. J.* 407, 127148. doi:10.1016/j.cej.2020.127148

Das, J., Ivanov, I., Sargent, E. H., and Kelley, S. O. (2016). DNA clutch probes for circulating tumor DNA analysis. *J. Am. Chem. Soc.* 138 (34), 11009–11016. doi:10.1021/jacs.6b05679

Dey, D., Bhattacharya, T., Majumdar, B., Mandani, S., Sharma, B., and Sarma, T. K. (2013). Carbon dot reduced palladium nanoparticles as active catalysts for carbon–carbon bond formation. *Dalton Trans.* 42 (38), 13821–13825. doi:10.1039/C3DT51234G

Irmisch, P., Ouldridge, T. E., and Seidel, R. (2020). Modeling DNA-strand displacement reactions in the presence of base-pair mismatches. *J. Am. Chem. Soc.* 142 (26), 11451–11463. doi:10.1021/jacs.0c03105

Kumar, S., Lei, Y., Alshareef, N. H., Quevedo-Lopez, M. A., and Salama, K. N. (2018). Biofunctionalized two-dimensional Ti3C2 MXenes for ultrasensitive detection of cancer biomarker. *Biosens. Bioelectron.* 121, 243–249. doi:10.1016/j.bios.2018.08.076

Lee, D. K., Ahn, C. W., and Lee, J. W. (2022). TiO2/Carbon nanosheets derived from delaminated Ti3C2-MXenes as an ultralong-lifespan anode material in lithium-ion batteries. *Adv. Mater. Interfaces* 9 (10), 2102375. doi:10.1002/admi.202102375

Li, M., Li, X., Qin, G., Luo, K., Lu, J., Li, Y., et al. (2021). Halogenated Ti3C2 MXenes with electrochemically active terminals for high-performance zinc ion batteries. *ACS Nano* 15 (1), 1077–1085. doi:10.1021/acsnano.0c07972

Li, S. T., Zhu, L. J., Lin, S. H., and Xu, W. T. (2023). Toehold-mediated biosensors: Types, mechanisms and biosensing strategies. *Biosens. Bioelectron.* 220, 114922. ARTN 114922. doi:10.1016/j.bios.2022.114922

Li, Z., and Wu, Y. (2019). 2D early transition metal carbides (MXenes) for catalysis. *Small* 15 (29), 1804736. doi:10.1002/smll.201804736

Lim, S., Park, H., Kim, J. H., Yang, J., Kwak, C., Kim, J., et al. (2020). Polyelectrolyte-grafted Ti3C2-MXenes stable in extreme salinity aquatic conditions for remediation of contaminated subsurface environments. *RSC Adv.* 10 (43), 25966–25978. doi:10.1039/D0RA04348F

Lin, J., Yu, Y., Zhang, Z., Gao, F., Liu, S., Wang, W., et al. (2020). A novel approach for achieving high-efficiency photoelectrochemical water oxidation in InGaN nanorods grown on Si system: MXene nanosheets as multifunctional interfacial modifier. *Adv. Funct. Mater.* 30 (13), 1910479. doi:10.1002/adfm.201910479

Lu, L., Han, X., Lin, J., Zhang, Y., Qiu, M., Chen, Y., et al. (2021). Ultrasensitive fluorometric biosensor based on Ti3C2 MXenes with Hg2+-triggered exonuclease III-assisted recycling amplification. *Analyst* 146 (8), 2664–2669. doi:10.1039/D1AN00178G

Meng, Y., Qin, N., and Hun, X. (2021). ZnSe nanodisks:Ti3C2 MXenes-modified electrode for nucleic acid liquid biopsy with photoelectrochemical strategy. *Mikrochim. Acta* 189 (1), 2. doi:10.1007/s00604-021-05117-0

Mi, X., Li, H., Tan, R., Feng, B., and Tu, Y. (2021). The TDs/aptamer cTnI biosensors based on HCR and Au/Ti3C2-MXene amplification for screening serious patient in COVID-19 pandemic. *Biosens. Bioelectron.* 192, 113482. doi:10.1016/j.bios.2021.113482

Pang, S.-Y., Wong, Y.-T., Yuan, S., Liu, Y., Tsang, M.-K., Yang, Z., et al. (2019). Universal strategy for HF-free facile and rapid synthesis of two-dimensional MXenes as multifunctional energy materials. *J. Am. Chem. Soc.* 141 (24), 9610–9616. doi:10.1021/jacs.9b02578

Ran, J., Gao, G., Li, F.-T., Ma, T.-Y., Du, A., and Qiao, S.-Z. (2017). Ti3C2 MXene co-catalyst on metal sulfide photo-absorbers for enhanced visible-light photocatalytic hydrogen production. *Nat. Commun.* 8, 13907. doi:10.1038/ncomms13907

Shaukat, A., Arain, M., Anway, R., Manaktala, S., Pohlman, L., and Thyagarajan, B. (2012). Is KRAS mutation associated with interval colorectal cancers? *Dig. Dis. Sci.* 57 (4), 913–917. doi:10.1007/s10620-011-1974-6

Siegel, R. L., Miller, K. D., Goding Sauer, A., Fedewa, S. A., Butterly, L. F., Anderson, J. C., et al. (2020). Colorectal cancer statistics, 2020. *CA A Cancer J. Clin.* 70 (3), 145–164. doi:10.3322/caac.21601

Song, X., Gao, H., Yuan, R., and Xiang, Y. (2022). Trimetallic nanoparticle-decorated MXene nanosheets for catalytic electrochemical detection of carcinoembryonic antigen via Exo III-aided dual recycling amplifications. *Sensors Actuators B Chem.* 359, 131617. doi:10.1016/j.snb.2022.131617

Steigerwalt, E. S., Deluga, G. A., and Lukehart, C. M. (2002). Pt–Ru/Carbon fiber nanocomposites: Synthesis, characterization, and performance as anode catalysts of direct methanol fuel cells. A search for exceptional performance. *J. Phys. Chem. B* 106 (4), 760–766. doi:10.1021/jp012707t

Su, T., Hood, Z. D., Naguib, M., Bai, L., Luo, S., Rouleau, C. M., et al. (2019). 2D/2D heterojunction of Ti3C2/g-C3N4 nanosheets for enhanced photocatalytic hydrogen evolution. *Nanoscale* 11 (17), 8138–8149. doi:10.1039/C9NR00168A

Wang, P., Wang, Z., Li, Z., Wang, Y., and Ma, Q. (2022). Electrochemically deposited Ag structure-based ECL sensing platform for KRAS gene detection in the tumor tissues. *Sensors Actuators B Chem.* 368, 132212. doi:10.1016/j.snb.2022.132212

Wang, R., Wang, S., Zhang, Y., Jin, D., Tao, X., and Zhang, L. (2018). Graphene-coupled Ti3C2 MXenes-derived TiO2 mesostructure: Promising sodium-ion capacitor anode with fast ion storage and long-term cycling. *J. Mater. Chem. A* 6 (3), 1017–1027. doi:10.1039/C7TA09153B

Wang, Y., Cai, Y.-J., Liang, R.-P., and Qiu, J.-D. (2020). Electrochemical biosensor for telomerase activity assay based on HCR and dual interaction of the poly-adenine DNA with Au electrode and Ce-Ti dioxide nanorods. *J. Electroanal. Chem.* 877, 114633. doi:10.1016/j.jelechem.2020.114633

Wang, Y., Li, Z., Weber, T. J., Hu, D., Lin, C.-T., Li, J., et al. (2013). *In situ* live cell sensing of multiple nucleotides exploiting DNA/RNA aptamers and graphene oxide nanosheets. *Anal. Chem.* 85 (14), 6775–6782. doi:10.1021/ac400858g

Wen, S., Zhang, C., Liang, R., Chi, B., Yuan, Y., and Qiu, J. (2017). Highly sensitive voltammetric determination of arsenite by exploiting arsenite-induced conformational change of ssDNA and the electrochemical indicator Methylene Blue. *Microchim. Acta* 184 (10), 4047–4054. doi:10.1007/s00604-017-2432-8

Wu, L., Wang, Y., Zhu, L., Liu, Y., Wang, T., Liu, D., et al. (2020). Aptamer-based liquid biopsy. *ACS Appl. Bio Mater.* 3 (5), 2743–2764. doi:10.1021/acsabm.9b01194

Yang, F., He, Y.-W., Chai, Y.-Q., Yuan, R., and Zhuo, Y. (2021a). Engineering a high-efficient DNA amplifier for biosensing application based on perylene decorated Ag microflowers as novel electrochemiluminescence indicators. *Biosens. Bioelectron.* 182, 113178. doi:10.1016/j.bios.2021.113178

Yang, F., Wang, S., Zhang, Y., Tang, L., Jin, D., Ning, Y., et al. (2016). Toehold enabling stem-loop inspired hemiduplex probe with enhanced sensitivity and sequence-specific detection of tumor DNA in serum. *Biosens. Bioelectron.* 82, 32–39. doi:10.1016/j.bios.2016.03.054

Yang, J., Dong, P., Wang, Y., Liu, T., Huang, Y., and Lei, J. (2021b). A stepwise recognition strategy for the detection of telomerase activity via direct electrochemical analysis of metal-organic frameworks. *Analyst* 146, 1859–1864. doi:10.1039/d0an02233k

Yang, X., Zhao, L., Lu, L., Feng, M., Xia, J., Zhang, F., et al. (2022). *In situ* reduction of gold nanoparticle-decorated Ti3C2 MXene for ultrasensitive electrochemical detection of MicroRNA-21 with a cascaded signal amplification strategy. *J. Electrochem. Soc.* 169 (5), 057505. doi:10.1149/1945-7111/ac6a7f

Yu, X., Jiang, B., and Wang, L. (2022). A signal-on electrochemical DNA biosensor based on exonuclease III-assisted recycling amplification. *Anal. Methods* 14 (48), 5041–5046. doi:10.1039/D2AY01592G

Yuan, W., Cheng, L., Wu, H., Zhang, Y., Lv, S., and Guo, X. (2018). One-step synthesis of 2D-layered carbon wrapped transition metal nitrides from transition metal carbides (MXenes) for supercapacitors with ultrahigh cycling stability. *Chem. Commun.* 54 (22), 2755–2758. doi:10.1039/C7CC09017J

Zhang, Q., Teng, J., Zou, G., Peng, Q., Du, Q., Jiao, T., et al. (2016). Efficient phosphate sequestration for water purification by unique sandwich-like MXene/magnetic iron oxide nanocomposites. *Nanoscale* 8 (13), 7085–7093. doi:10.1039/C5NR09303A

Zhang, Q., Wang, F., Zhang, H., Zhang, Y., Liu, M., and Liu, Y. (2018). Universal Ti3C2 MXenes based self-standard ratiometric fluorescence resonance energy transfer platform for highly sensitive detection of exosomes. *Anal. Chem.* 90 (21), 12737–12744. doi:10.1021/acs.analchem.8b03083

Zhang, Y., Wang, W., Lin, Z., Liu, B., and Zhou, X. (2020a). Dual-output toehold-mediated strand displacement amplification for sensitive homogeneous electrochemical detection of specie-specific DNA sequences for species identification. *Biosens. Bioelectron.* 161, 112256. doi:10.1016/j.bios.2020.112256

Zhang, Y., Xu, G., Lian, G., Luo, F., Xie, Q., Lin, Z., et al. (2020b). Electrochemiluminescence biosensor for miRNA-21 based on toehold-mediated strand displacement amplification with Ru(phen)32+ loaded DNA nanoclews as signal tags. *Biosens. Bioelectron.* 147, 111789. doi:10.1016/j.bios.2019.111789

Zheng, X., Li, L., Zhang, L., Xie, L., Song, X., and Yu, J. (2020). Multiple self-cleaning paper-based electrochemical ratiometric biosensor based on the inner reference probe and exonuclease III-assisted signal amplification strategy. *Biosens. Bioelectron.* 147, 111769. doi:10.1016/j.bios.2019.111769

Zhu, Y.-M., Huang, Q., Lin, J., Hu, Y., Chen, J., and Lai, M.-D. (2007). Expression of human DNA methyltransferase 1 in colorectal cancer tissues and their corresponding distant normal tissues. *Int. J. Colorectal Dis.* 22 (6), 661–666. doi:10.1007/s00384-006-0224-4

Zhuang, J., Wan, H., and Zhang, X. (2021). Electrochemical detection of miRNA-100 in the sera of gastric cancer patients based on DSN-assisted amplification. *Talanta* 225, 121981. doi:10.1016/j.talanta.2020.121981

Zou, G., Zhang, Z., Guo, J., Liu, B., Zhang, Q., Fernandez, C., et al. (2016). Synthesis of MXene/Ag composites for extraordinary long cycle lifetime lithium storage at high rates. *ACS Appl. Mater. Interfaces* 8 (34), 22280–22286. doi:10.1021/acsami.6b08089

frontiers | Frontiers in Bioengineering and Biotechnology

TYPE Original Research
PUBLISHED 28 April 2023
DOI 10.3389/fbioe.2023.1187632

OPEN ACCESS

EDITED BY
Hua Yue,
Chinese Academy of Sciences (CAS), China

REVIEWED BY
Shi Gang Liu,
Hunan Agricultural University, China
Hui Ding,
The First Affiliated Hospital of Shenzhen University Health Science Center, China

*CORRESPONDENCE
Naiyun Liu,
liuny@ujs.edu.cn
Xiang Liu,
liuxiang0222@126.com
Haitao Li,
liht@ujs.edu.cn

RECEIVED 16 March 2023
ACCEPTED 20 April 2023
PUBLISHED 28 April 2023

CITATION
Du Y, Li Y, Liu Y, Liu N, Cheng Y, Shi Q, Liu X, Tao Z, Guo Y, Zhang J, Askaria N and Li H (2023), Stalk-derived carbon dots as nanosensors for Fe^{3+} ions detection and biological cell imaging.
Front. Bioeng. Biotechnol. 11:1187632.
doi: 10.3389/fbioe.2023.1187632

Stalk-derived carbon dots as nanosensors for Fe^{3+} ions detection and biological cell imaging

Yongchao Du[1], Yaxi Li[1], Yunliang Liu[1], Naiyun Liu[1]*, Yuanyuan Cheng[1], Qiuzhong Shi[2], Xiang Liu[2]*, Zhimin Tao[3,4], Yumeng Guo[3], Jianguo Zhang[3,5], Najmeh Askaria[1] and Haitao Li[1,6]*

[1]Institute for Energy Research, School of Chemistry and Chemical Engineering, Jiangsu University, Zhenjiang, China, [2]Institute of Medicine and Chemical Engineering, Zhenjiang College, Zhenjiang, China, [3]Jiangsu Province Key Laboratory of Medical Science and Laboratory Medicine, School of Medicine, Jiangsu University, Zhenjiang, China, [4]Zhenjiang Municipal Key Laboratory of High Technology for Basic and Translational Research on Exosomes, Zhenjiang, China, [5]Department of Critical Care Medicine, The Affiliated Hospital of Jiangsu University, Zhenjiang, China, [6]Guangxi Key Laboratory of Electrochemical Energy Materials, Guangxi University, Nanning, China

Introduction: Iron is one of the most important needed elements for the growth and reproduction of living organisms. The detection of iron levels is important and developing fluorescent probes with excellent sensitivity for Fe^{3+} ions is of great significance. Carbon dot (CDs) is a new type of fluorescent nanomaterial based on abundant and low-cost carbon elements. The use of widely distributed renewable agricultural waste straw as a carbon precursor to prepare CDs sensor can not only reduce the pollution caused by burning straw to the atmospheric environment, but also achieve the transformation of resources from waste to treasure.

Methods: In this study, CDs were obtained from corn stalk powder by pyrolysis and microwave process. The sensitivity and linear response range of CDs sensor was studied through analyzing the effect of different Fe^{3+} ions concentrations on the fluorescence quenching. The application of CDs in biological cell imaging was investigated using HGC-27 cells.

Results: The fluorescence quenching showed a good linear relationship with the Fe3+ concentration in the range from 0 to 128 μM, and a low detection limit of 63 nM. In addition, the CDs have high recognition for Fe3+ ions. Meanwhile, the CDs have a low cytotoxicity and desirable biocompatibility, allowing the multicolor living cell imaging.

Conclusion: The prepared CDs can be used as fluorescent sensors for the selective detection of Fe^{3+} ions and biological cell imaging. Our results supported that the conversion of agricultural waste into carbon nanomaterials has great potential to be developed.

KEYWORDS

carbon dots, detection, cell imaging, nanosensors, biomass

1 Introduction

Iron is one of the most important needed elements for the growth and reproduction of living organisms. Iron is widely distributed on the earth, playing an important role in oxygen transport (Dutt et al., 2022), enzymatic reactions (Stoyanovsky et al., 2019), cellular metabolism (Soares and Hamza, 2016), electron transport (Gupta et al., 2021) and DNA synthesis (Li et al., 2021). Although iron plays a key role in these aspects, too much iron will be toxic to our bodies due to the generation of free radicals, which results in the destruction of biological macromolecules (Wang and Babitt, 2019). Moreover, excessive levels of iron can cause imbalances in the intracellular environment as well (Navazesh and Ji, 2022). The dual function of iron highlights the importance of maintaining a strict balance of iron levels in the body (Duck and Connor, 2016). Therefore, the detection of iron levels is greatly important. Currently, UV spectrophotometry (Cheng et al., 2022a), atomic absorption (Zvěřina et al., 2019) and inductively coupled plasma mass spectrometry (ICP-MS) (Wheal et al., 2016) are mainly used for the detection of iron ions. However, these methods have numerous disadvantages, such as tedious, time-consuming operation, low recovery, small detection range of solution pH, easy to be interfered by other metal ions and high testing costs (Wu et al., 2019). Thus, a number of methods based on fluorescence analysis have been developed to detect elemental iron (Lin et al., 2017; Duan et al., 2022). Fluorescence spectrophotometry is widely used for the analysis and detection of substances because of its simplicity of operation, high sensitivity and low cost (Yang et al., 2015; Mehta et al., 2021; Liu et al., 2023).

Carbon dot (CDs) as a new type of fluorescent nanomaterial based on abundant and low-cost carbon elements have achieved great attention (Liu et al., 2016; Chen et al., 2020; Yan et al., 2022). Compared with traditional semiconductor quantum dots and organic fluorescent dye molecules, CDs have the following advantages: high fluorescence intensity, high quantum yield, excellent selectivity, suitable biocompatibility, low toxicity, etc. (Park et al., 2020; Nagaraj et al., 2022; Wang and Lu, 2022) Therefore, CDs are widely used in analytical detection, biosensing and other fields (Keerthana et al., 2022). There are two current methods for CDs synthesis, including top-down and bottom-up processes. The top-down method is to "fracture" carbon material precursors (such as graphite), usually under harsh conditions, and requires a long synthesis time (Li et al., 2015; Perumal et al., 2021). In the bottom-up process, a large number of molecular precursors can be used as carbon sources, and uniform CDs can be obtained through microwave and hydrothermal process, etc. (Yang et al., 2013; Singh et al., 2019; Rani et al., 2020) Among them, the microwave synthesis method has gained increasing attention because of its fast reaction rates, simplicity, green and low energy consumption (Rodríguez-Padrón et al., 2018; Karakoçak et al., 2021). In addition, the molecular precursors of CDs are usually citric acid (Liu et al., 2017), glucose (Ferreyra et al., 2020), and various amino acids (Kang and Kang, 2021). However, the process of the aforementioned synthesis methods is tedious, high cost with long dialysis time.

In recent years, a large number of studies have been carried out using biomass as natural precursors for the synthesis of CDs (Wareing et al., 2021). Crop straw is renewable, in line with the concept of green chemistry and sustainable development, and is a green and friendly carbon material. After crop harvest, straw is usually left idle and wasted or burned on site, which will not only cause air, soil and water pollution, but also waste the significant resources (Zhang et al., 2011). In fact, a large portion of crop nutrients are stored in the straw, being rich in organic matter and nutrients such as nitrogen, phosphorus and potassium. Meanwhile, crop straw is rich in lignin and cellulose, and the rich unsaturated bonds are more conducive to the formation of graphite carbon lattice in CDs (Mittal et al., 2017). Therefore, straw is a valuable biological resource with reuse value.

This research presents a method to prepare CDs nanosensors by microwave using crop straw product (CSP) as the carbon source. The synthesized CDs exhibited a large Stokes shift (about 100 nm) when excited by UV light at 365 nm. The surface of CDs was rich in -COOH and -NH_2, forming stable chelates with Fe ligands and thus causing fluorescence quenching of CDs. This quenching effect is influenced by the Fe^{3+} ions concentration, which provides a basis for studying the detection of Fe^{3+} ions concentration in the environment. This study also investigated the application of CDs in biological cell imaging using HGC-27 cells. Based on the results, the fluorescent CDs have desired biocompatibility and low toxicity, which will lay the foundation for their application in bioanalytical and biomedical science.

2 Experimental section

2.1 Chemicals and materials

CSP was obtained from a local supplier and used as required. Sodium sulfide, methanol, and hydrogen peroxide were purchased from Sinopharm Chemical Regent Co., Ltd. All chemical reagents were used without further processing and purification. The water used in this experiment was ultrapure water.

2.2 Synthesis of CDs and characterization

CDs were produced from CSP by pyrolysis and microwave methods. The synthesis steps are shown in Figure 1A. For the easier generation of CDs, the CSP was simply pretreated, resulting in its internal structure disruption. Then, the pretreated CSP was transferred to a tube furnace and calcined at 450°C for 5 h under a nitrogen atmosphere to obtain black carbon powder (BCP) as the precursor of CDs. Thereafter, 30 mg of BCP was added to 30 mL of 30% H_2O_2 and the mixture was reacted in a microwave reactor for 30 min (500 W). Finally, the dark brown CDs solution was collected from the supernatant and stored at 4°C for further use. The condensed solution was filtered (0.22 μm), dialysis (100Da) and further characterized.

Transmission electron microscopy (TEM) images were obtained on a HITACHI H-8100 electron microscopy (Hitachi, Tokyo, Japan) operated at 200 kV. The X-ray diffraction (XRD) patterns were investigated by a LabX XRD-6100 X-ray diffractometer with Cu Kα radiation (40 kV, 30 mA) of wavelength 0.154 nm (SHIMADZU, Japan). The absorbance data of spectrophotometer were measured by SHIMADZU UV-2,700 ultraviolet-visible (UV-Vis) spectrophotometer. Fourier-transform infrared spectra (FTIR)

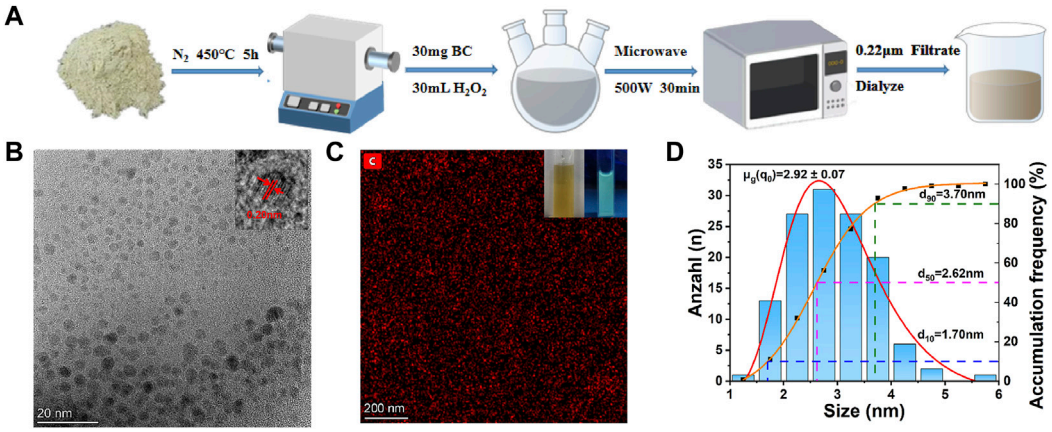

FIGURE 1
(A) The synthetic scheme of CDs from CSP. **(B)** TEM images of CDs. Inset is the high-resolution TEM image. **(C)** EDX mapping images of CDs. Insets are the photographs of the obtained CDs solution illuminated under sunlight and a UV lamp (365 nm), respectively. **(D)** Particle size distribution of CDs.

were measured by Nicolet iS50 FTIR (Thermo Fisher Scientific, United States). Raman spectroscopy was conducted using a confocal Raman system (RTS2, Zolix) with a 532 nm excitation source. The PL spectra were recorded at an excitation wavelength of 365 nm at room temperature using a photoluminescence spectrometer (Perkin Elmer, United States).

2.3 Photoluminescence spectra

The test of Fe^{3+} ions detection was investigated at room temperature by adding the Fe^{3+} ions related salt to the CDs solution (0.05 mg/mL). First, 0.337 g $FeCl_3{\cdot}6H_2O$ was dissolved in 10 mL ultrapure water to obtain a 5.12 mM Fe^{3+} ions solution. Then, the solution was diluted with ultrapure water to obtain a series of Fe^{3+} ions solution with the concentration of 2.56 mM, 1.28 mM, 640 μM, 320 μM, 160 μM, 80 μM, 40 μM, 20 μM, 10 μM, 5 μM, 1 μM and 500 nM, respectively. These Fe^{3+} ions solution was added in sequence with a specific amount to the previous CDs solution to obtain the CDs solution with a series of Fe^{3+} concentrations of 1 μM, 2 μM, 4 μM, 8 μM, 16 μM, 32 μM, 64 μM, 128 μM. For example, for obtaining the 10 μM Fe^{3+} ions in CDs, 200 μL of 100 μM Fe^{3+} ions solution was diluted with 2 mL of previous CDs. Then the solution was investigated in fluorescence spectrometer for the emission spectra from 380 nm to 600 nm, with the excitation wavelength of 365 nm and the slit width of 10 nm.

The parameters of the photoluminescence spectrometer were set as follows: Chopper Speed (Hz) = 10, Excitation Wavelength (nm) = 365, Excitation Slit (nm) = 10, Excitation Filter = Air, Emission Slit (nm) = 10, Emission Filter = Air, PMT Voltage(V) = 550, PMT Gain = x1, Response Width (nm) = 10.

2.4 Quantum yield measurements

The quantum yield (QY) of the CDs was calculated by the following equation:

$$\Psi_x = \Psi_s \frac{I_x}{I_s} \frac{A_s}{A_x} \frac{\eta_x^2}{\eta_s^2}$$

Where, Ψ_x is the fluorescence quantum yield; x and S represent the test substance and reference compound. Quinine sulfate dissolved in 0.05 M H_2SO_4 ($\psi_s = 0.54$) was chosen as the reference. η is the refractive index (1.33 for aqueous solution). A is the absorbance at the excitation wavelength of 365 nm and I is the integrated fluorescence intensity in the fluorescence emission spectrum.

2.5 Cytotoxicity assay

The cytotoxicity of CDs was determined using the CCK8 method. HGC-27 cells were inoculated in 96-well plates with a final volume of 100 μL. Each group is set with 8 cell number gradients, and each gradient is set with three replicate wells, a total of 2 groups (sample group to be assayed and qualified sample group as control). The cell number gradients in each group were: 0, 400, 800, 1,600, 3,200, 6,400, 12,800 and 25,600 cells/well, respectively. 10 μL CCK-8 solution was added to each well at the end of plate laying and incubated at 37°C for 2 h. Then, 0.05 mg/mL of CDs solution was added to each group of samples and incubated for 24 h and 48 h, respectively. The absorbance of the synthesized well contents was monitored at 450 nm using an enzyme marker (Permanent Medical, DNM-9606). Relative cell viability was determined by comparison with the control. These experiments were repeated three times. The results are presented as mean ± standard deviation. The cell viability was calculated by following equation (Fu et al., 2021):

Cell viability (%)
= (the absorbance of the experimental group/the absorbance of the control group) × 100%

2.6 Cell imaging

The combined effect of CDs in HGC-27 cells was investigated. HGC-27 cells were cultured in DMEM culture

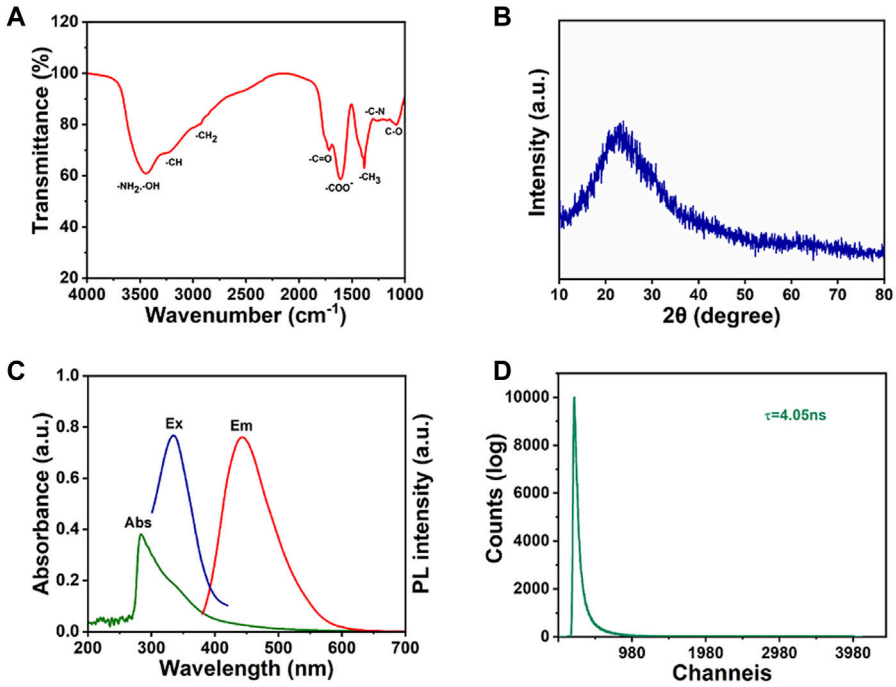

FIGURE 2
(A) FTIR spectrum, **(B)** XRD spectrum, **(C)** UV absorption, excitation and emission spectra and **(D)** fluorescence lifetime spectrum of CDs.

medium with 10% (v/v) fetal bovine serum and 1% penicillin-streptomycin. Approximately 2 × 105 HGC-27 cells were seeded in culture dishes (diameter: 40 mm) and incubated for 24 h at 37°C under an atmosphere of 5% CO_2. The synthetic CDs (0.05 mg/mL) were then mixed with cell cultures and further incubated at 37°C for 1 h. The cells were washed with PBS three times and examined under a confocal microscope (Zeiss, LSM 880 NLO) using the 405 nm laser.

3 Results and discussion

3.1 Characterization of CDs

The CDs was prepared from CSP by pyrolysis and microwave processes (Figure 1A). The TEM images (Figure 1B) were used to study the morphology of the CDs, and the inset shows that the lattice spacing of CDs is about 0.20 nm. As shown in Figure 1C, the uniform distribution of C element in CDs is determined, and the existence of its related elements is proved. As can be seen from the inset of Figure 1C, the CDs solution is transparent and homogeneous yellowish solution under visible light, while it emits blue-green fluorescence under UV light at 365 nm. The CDs have uniform dimensions in the size range of 1.5–6 nm as illustrated in Figure 1D, and the average particle size of CDs is 2.92 nm. 90% of CDs are below 3 nm, 50% of CDs are below 2 nm, and only 10% of CDs are below 1 nm.

The CDs surface functional groups were further determined by FTIR spectrum (Figure 2A). The peak at ~1,072 cm^{-1} is attributed to the C-O stretching vibration and the peak at ~1,265 cm^{-1} is contributed to the torsional vibration of the $-CH_2$ or the stretching vibration of the C-N (Long et al., 2022).[40] The strong peak at ~1,384 cm^{-1} is contributed to the symmetric variable angle of the $-CH_3$. The peak at 1,616 cm^{-1} is due to the antisymmetric stretching of $-COO^-$. The peaks at 1732, 2,927 and 3,220 cm^{-1} are attributed to the stretching vibration of C=O, the antisymmetric stretching of $-CH_2$ and the stretching vibration of -CH, respectively. The strong peak at 3,300 cm^{-1} is attributed to the O-H stretching vibration and the anti-symmetric stretching of $-NH_2$ (Cheng et al., 2022b). This indicates the presence of a large number of carboxyl groups and other oxygen-containing functional groups on the surface of CDs, resulting in beneficial water dispersion of CDs (Naciri et al., 2022). Oxidation causes the introduction of C=O-containing groups, such as -COOH, on the surface of CDs. The Raman spectrum of CDs exhibits two distinct carbon peaks (Supplementary Figure S1) (Li et al., 2019). In addition, XRD analysis reveals a broad diffraction peak at 22.5°, indicating that the CDs structure is disordered amorphous, as shown in Figure 2B (Xu et al., 2021).

The optical properties of as-prepared CDs were then investigated. The UV absorption, excitation and emission spectra of CDs are shown in Figure 2C. The CDs solution typically shows strong absorption in the UV region with the maximum absorption peak at 284 nm, while the tail extends into the visible absorption range. The peak of 284 nm is attributed to $\pi \rightarrow \pi^*$ electron transitions (Ezati and Rhim, 2022). The CDs shows the maximum excitation and the emission wavelengths at 326 nm and 445 nm, respectively.

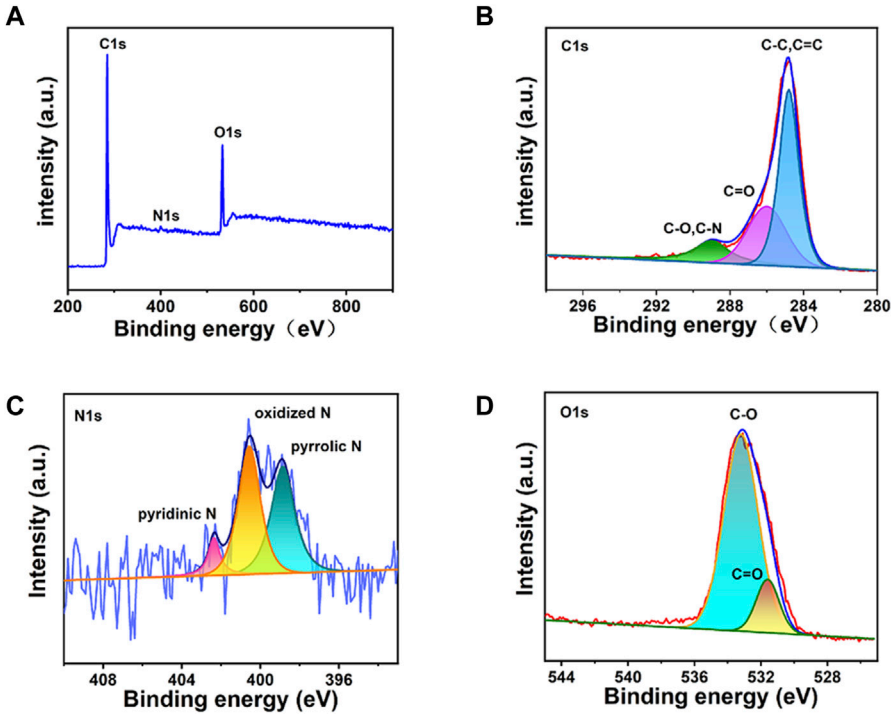

FIGURE 3
The XPS spectra of the CDs: **(A)** the total spectrum, **(B)** C1s enlarged region, **(C)** N1s enlarged region, **(D)** O1s enlarged region.

In addition, the fluorescence lifetime of CDs can reach as long as 4.05 ns (Figure 2D).

XPS characterization was used to further investigate the structure of CDs. In Figure 3A, three obvious peaks are observed regarding to C1s, N1s and O1s at the binding energy of 284.8, 400, and 533 eV, respectively. For the high-resolution XPS pattern of C1s (Figure 3B), three peaks at 284.9, 286.1, and 288.5 eV are attributed to [C-O, C-N], C=O and [C-C, C=C] groups, respectively (Zhao et al., 2020; Liu et al., 2021b). In the N1s XPS spectrum of CDs (Figure 3C), three peaks are observed with binding energies of 399, 400.5, and 402.5 eV, corresponding to pyridine nitrogen, nitrogen oxide and pyrrole nitrogen, respectively (Li et al., 2022a). The presence of the -NH_2 structure was further confirmed. Based on the O1s XPS spectrum (Figure 3D), two main peaks located at 533.1 and 531.5 eV indicate the presence of C-O and C=O groups, which coincided with the C1s spectrum (Li et al., 2022b).

3.2 Fluorescence detection

In this work, we investigated the sensitivity and linear response range of this metal ion sensor by preparing a series of Fe^{3+} ions solutions with different concentrations and mixed with CDs. The fluorescent properties of CDs were studied in detail firstly. With the increase of excitation wavelength, the fluorescence intensity first increased and then decreased. The maximum value was reached at the excitation wavelength of 325 nm (Figure 4A). The position of the fluorescence emission peak gradually increased, which may be due to the non-uniform particle size of carbon particles in the CDs solution. At 365 nm excitation, the characteristic emission maximum at 480 nm appeared with a fluorescence quantum yield of 2.1% using rhodamine B as a reference.

The effects of the pH of the solution on the stability of fluorescence intensity were investigated as well (Figure 4B). Under acidic conditions, the fluorescence intensity decreased gradually with pH decreasing. It may be due to the combination of nitrogen-containing functional groups in the CDs solution with H^+ at lower pH values. The introduction of H^+ leads to the weakening of the fluorescence intensity of CDs. Considering that the pH of the physiological environment is 7–8, the fluorescence intensity in this range is relatively stable and favourable for biofield applications. As shown in Figure 4C, the stability of CDs at different time is obtained. The fluorescence intensity of CDs remained highly stable after being irradiated by 300 W xenon lamp for 3 h. The synthesized CDs shows long-term stability in ultrapure water for more than 2 weeks. As can be seen in Supplementary Figure S2, at room temperature, the fluorescence intensity of the CDs solution remained almost unchanged after 2 weeks, proving that it has good stability, and thus it can be used as a fluorescent probe under optimal conditions.

The effect of different metal ions on the fluorescence intensity of CDs solution was further studied. Different cations such as Na^+, NH_4^+, K^+, Ca^{2+}, Mn^{2+}, Fe^{3+}, Co^{2+}, Ni^{2+}, Zn^{2+} ions were added to the CDs solution, respectively (Supplementary Figures S3–S7). After each cation solution was added to the CDs solution and mixed thoroughly for 10 min, separately, the fluorescence changes were

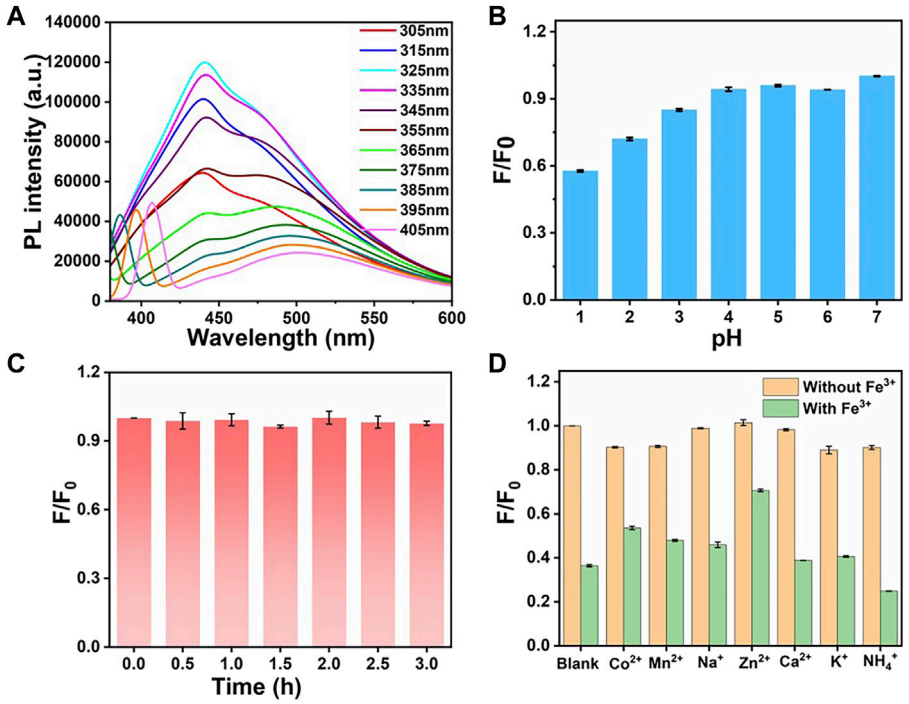

FIGURE 4
(A) Fluorescence emission spectra of CDs at different excitation wavelengths. **(B)** Fluorescence intensity of CDs under different pH conditions. **(C)** Fluorescence intensity changes of CDs after being irradiated by 300 W xenon lamp for different time. **(D)** Fluorescence intensity changes in the presence of different metal ions (yellow) and after the addition of Fe^{3+} ions (green). For panel B–D, F_0 and F are the fluorescence intensities of the CDs before and after treatment, respectively.

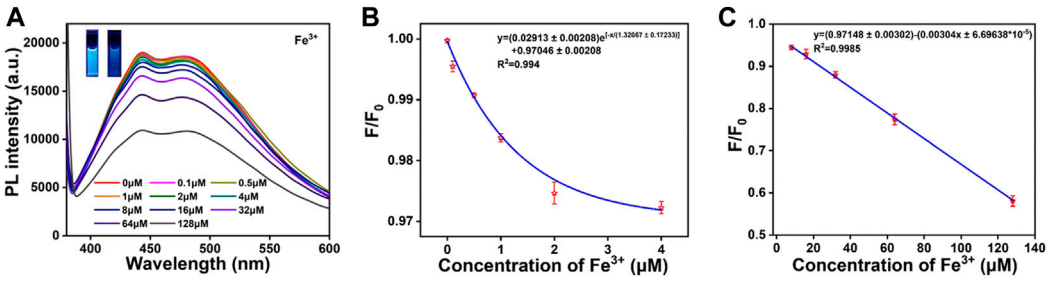

FIGURE 5
(A) Fluorescence emission response of CDs solution (0.05 mg/mL) with different concentrations of Fe^{3+} ions (0–128 μm). The inset shows the photographs of CDs solution (left) and CDs-Fe^{3+} complexes (right) under 365 nm UV irradiation. **(B)** When the Fe^{3+} ions concentration is 0–4 μM, linear correlation between F/F_0 and Fe^{3+} ions concentration. **(C)** When the Fe^{3+} ions concentration is 4–128 μM, the linear correlation between F/F_0 and Fe^{3+} ions concentration. F_0 and F are the fluorescence intensity for CDs solution in the absence and presence of corresponding ions, respectively.

recorded (red bar). As can be seen in Figure 4D, the other monovalent cations and divalent metal ions have little effect on the fluorescence intensity of CDs, while the addition of Fe^{3+} ions caused a significant quenching of the fluorescence (orange bar). It can be demonstrated that the CDs have high recognition for Fe^{3+} ions instead of other cations. The addition of Fe^{3+} ions immediately induced a fluorescence quench, which can be attributed to the paramagnetic nature of Fe^{3+} ions and can be used as a fluorescence quencher (Liu et al., 2021a).

According to the results shown in Figure 5A, the fluorescence intensity of CDs was decreased with the Fe^{3+} ions concentration increasing. From the inset of Figure 5A, it can be seen that there is a significant decrease in the brightness of the CDs solution under the UV lamp irradiation at 365 nm. The fluorescence emission intensity decreases by 43% when the Fe^{3+} ions concentration increases from 0 to 128 μM. As shown in Figure 5B, the fluorescence intensity of CDs is strongly correlated with different concentrations of Fe^{3+} ions. This paves the way for qualitative and quantitative detection of Fe^{3+}

TABLE 1 Results for the determination of Fe^{3+} of tap water.

Sample	Added Fe^{3+} (μM)	Detected Fe^{3+} (μM)	Recovery (%)	RSD (%), n = 3
Tap water	0	0.46	0	0
	8.00	8.09	95.3	1.7
	16.00	16.10	97.8	1.6

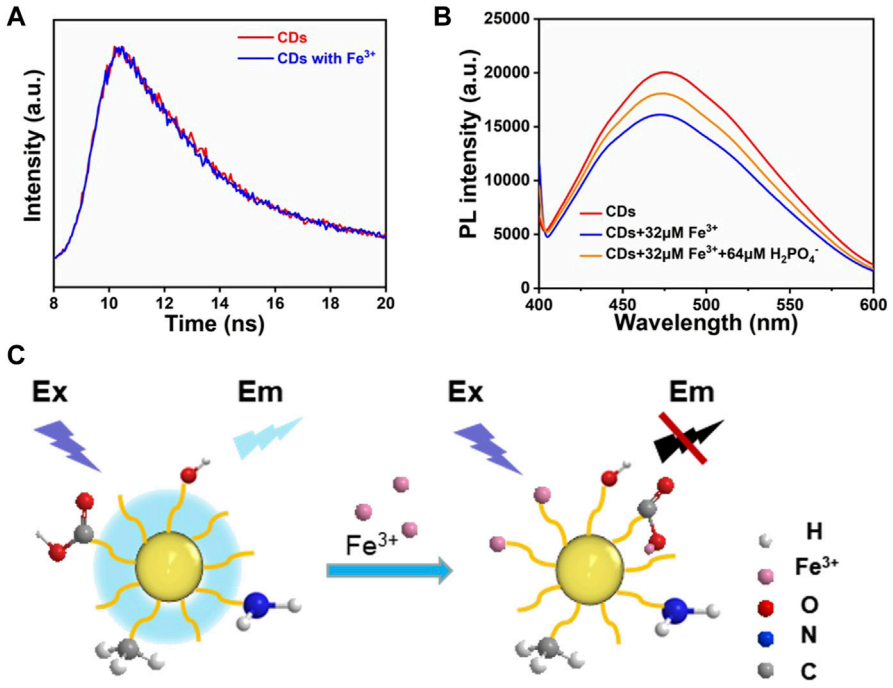

FIGURE 6
(A) The fluorescence decay curves of the CDs and CDs with Fe^{3+}. **(B)** Comparison of fluorescence intensity after the addition of Fe^{3+} ions and $H_2PO_4^-$ ions to CDs solution. **(C)** Fluorescence quenching mechanism of CDs.

ions concentrations in the real environment. According to the Stern–Volmer theoretical equation:

$$F_0/F = 1 + K_{SV}C_q$$

Where Ksv is the bursting constant, C_q is the concentration of the quencher (Fe^{3+}), F_0 is the maximum fluorescence emission intensity of CDs without Fe^{3+} ions addition, and F is the maximum fluorescence emission intensity of CDs with Fe^{3+} ions addition. When the concentration of added Fe^{3+} ions is 0–4 μM, the linear regression equation is as follows (Figure 5B):

$$F/F_0 = (0.02913 \pm 0.00208)e^{[-C_{Fe^{3+}}/(1.32067\pm0.17233)]} + (0.97046 \pm 0.00208), R^2 = 0.994$$

When the concentration of added Fe ions is 4–128 μM, the linear regression equation is as follows (Figure 5C):

$$F/F_0 = (0.97148 \pm 0.00302) - (0.00304C_{Fe^{3+}} \pm 6.69638 \times 10^{-5}), R^2 = 0.9985$$

The regression coefficient of correlation was found to be 0.994 and 0.9985, respectively. Based on LOD = 3σ/S (σ is the standard deviation of 12 blanks, S is the slope of the obtained linear relationship), the limit of detection of Fe^{3+} ions concentration is calculated as 63 nM. The prepared CDs in this work, not only have the maximum absorption peak at 480 nm, but also have a large Stokes shift, better stability, higher selectivity and lower detection limits. These advantages suggest that they can be used as fluorescent probes for the detection of Fe^{3+} ions.

In order to investigate the practical feasibility of CDs, the concentration of Fe^{3+} in the actual water samples of tap water was tested. An absolute concentration of Fe^{3+} ions was added in the tap water, then the fluorescence intensity was measured and the Fe^{3+} ions concentration was calculated through the linear regression equation. The Fe^{3+} concentration in tap water was measured by fluorescence

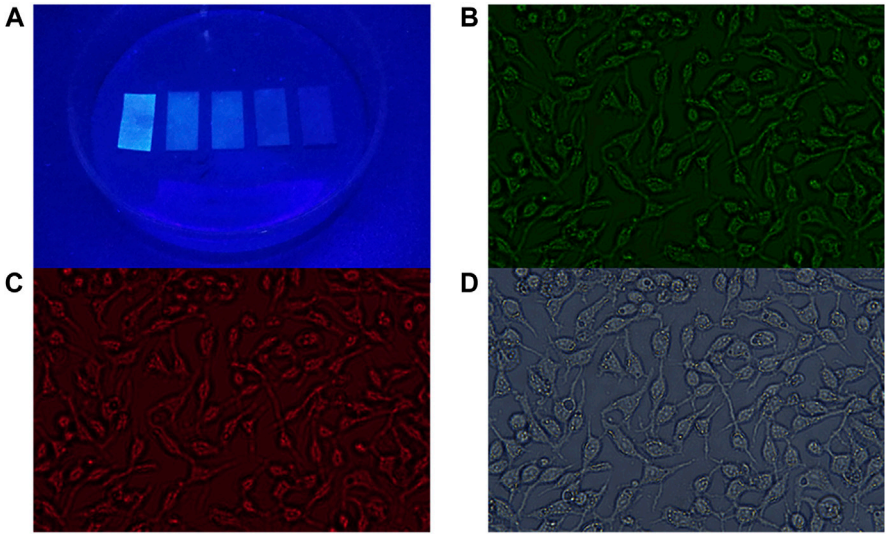

FIGURE 7
(A) Captured PL emission of CDs in series concentrations of Fe^{3+} ions solution (0, 10, 50, 100, and 500 μM from left to right). Confocal laser scanning microscopy images of CDs in cells **(B)** excitation wavelength of 465–495 nm; emission was collected at 512–552 nm; **(C)** excitation wavelength of 540–580 nm; emission was collected at 600–660 nm; **(D)** bright field.

quenching method and inductively coupled plasma-mass spectrometry (ICP-MS) as well (Supplementary Figure S8). In this method, the concentration of added Fe^{3+} ions standard solutions were 8.00 μM and 16.00 μM and the measured values were 8.09 μM and 16.10 μM, respectively. The measured recovery rate of Fe^{3+} ions by this method was between 95%–98%, and the standard deviation was less than 1.7% (Table 1). The above results show that the detection results of this method have adequate accuracy and can be used to detect the content of Fe^{3+} ions in tap water.

3.3 Fluorescence detection mechanism

The fluorescence quenching mechanism was investigated in some detail. To distinguish between the dynamic and static quenching modes clearly, fluorescence lifetime measurements for the CDs were conducted. The average fluorescence lifetime of CDs has no obvious change in the absence of Fe^{3+} (Figure 6A), which seems to indicate that the fluorescence decay is ascribed to the static quenching (Wahba et al., 2015; Zhang et al., 2022). Therefore, the high selectivity of CDs to Fe^{3+} may be attributed to the fact that compared with the other metal ions, the Fe^{3+} has the stronger binding affinity and faster chelating kinetics with carboxylic groups and N-containing function groups on the surfaces of the CDs (Li et al., 2017; Zhang et al., 2021). From the FTIR and XPS analysis, it can be found that the surface of the CDs was covered with a large number of functional groups (-NH_2, -OH, -COOH). As an electron donor, the N atoms have a sufficient negative charge, easily losing its outermost electron, which promotes the complexation reaction between Fe^{3+} ions and the functional groups on the surface of CDs. In addition, the CDs solution was treated with an appropriate amount of $H_2PO_4^-$ ions to further investigate the interaction between CDs and Fe^{3+} ions. The $H_2PO_4^-$ introduced can compete with CDs and form complexes with Fe^{3+} ions. The results show that the fluorescence intensity of the Fe^{3+} ions/CDs solution can be restored to different degrees (Figure 6B). This may be due to the larger coordination constants of Fe^{3+} ions and $H_2PO_4^-$ ions, which leads to the recovery of the fluorescence intensity of the CDs solution (Figure 6C). It is reasonable to assume that the occurrence of fluorescence quenching may be due to the formation of non-fluorescent complexes between the CDs surface functional groups and Fe^{3+} ions.

3.4 Sensor application

The principle of PL emission was implemented in the application as Fe detection paper. First, the CDs solution was dropped on non-fluorescent glass fiber test paper. After natural drying, Fe^{3+} solutions of different concentrations were dropped into the test papers. Subsequently, the test papers were placed under a UV lamp and the corresponding emission light was captured at 480 nm. As shown in Figure 7A, different test papers exhibit different intensities of emitted light, which provides an effective and convenient method for qualitatively testing the content of Fe^{3+} ions in water. This method can be used for water quality testing in remote areas without advanced instruments. From the above results, the sensor demonstrated proper sensitivity to Fe^{3+} ions under fluorescence emission, and the color change was seen in Fe^{3+} ions solutions ranging from 0 μM to 500 μM (Figure 7A).

3.5 Cytotoxicity and living cell imaging

The prepared CDs present desirable optical properties, therefore the prepared CDs are expected to be applied to cell imaging. To determine whether CDs can be used as biological

probes, we examined the cytotoxicity of HGC-27 cells after treatment with CDs. As shown in Supplementary Figure S9, after 24 h of incubation, the viability of HGC-27 cells is maintained above 76%. After 48 h of incubation, the viability of HGC-27 cells is maintained above 72%, indicating that the prepared CDs have good biocompatibility and can be used for biological applications. In addition, we investigated the *in vitro* bioimaging of HGC-27 cells containing CDs using confocal techniques (Figures 7B–D) (Liu et al., 2020) Cells incubated with CDs exhibit intense green and red fluorescence under 465–495 nm and 512–552 nm excitation, respectively. Therefore, the prepared CDs with beneficial biocompatibility can be applied in the field of biological cell imaging (Huang et al., 2021).

4 Conclusion

In summary, we developed a facile method for synthesizing CDs from agricultural waste. The synthesized CDs possessed the advantages of good stability, low cost, green, and they exhibited a large Stokes shift with an emission wavelength of 480 nm under 365 nm excitation. The CDs can be used as fluorescent nanosensors for the detection of Fe^{3+} ions. The detection limit (63 nM) for Fe^{3+} in water is much lower than WHO recommended value. In addition, we also demonstrated that the CDs have low cytotoxicity and excellent biocompatibility, and the CDs can be applied for living cell imaging. We believe that the synthesis of CDs using agricultural waste conforms to the concept of green chemistry and is a green and environmentally friendly synthesis method, and will pave a new way for a rational use of agricultural waste resources.

Data availability statement

The raw data supporting the conclusion of this article will be made available by the authors, without undue reservation.

Author contributions

YD: methodology, validation, and writing-original draft. YAL: investigation, and writing-original draft. YUL: data curation, writing-original draft. NL: methodology, writing-review and editing. YC: investigation. QS: validation. XL: writing-review and editing. ZT: writing-review and editing. YG: data curation and investigation. JZ: writing-review. NA: investigation. HL: conceptualization, supervision, writing-review and editing, and funding acquisition.

Funding

This work was supported by the National Natural Science Foundation of China (Grants 52072152, 51802126), the Jiangsu University Jinshan Professor Fund, the Jiangsu Specially-Appointed Professor Fund, Open Fund from Guangxi Key Laboratory of Electrochemical Energy Materials, Zhenjiang "Jinshan Talents" Project 2021, China PostDoctoral Science Foundation (2022M721372) and "Doctor of Entrepreneurship and Innovation" in Jiangsu Province (JSSCBS20221197).

Conflict of interest

The authors declare that the research was conducted in the absence of any commercial or financial relationships that could be construed as a potential conflict of interest.

Publisher's note

Supplementary material

The Supplementary Material for this article can be found online at: https://www.frontiersin.org/articles/10.3389/fbioe.2023.1187632/full#supplementary-material

References

Chen, Y., Cao, Y., Ma, C., and Zhu, J. J. (2020). Carbon-based dots for electrochemiluminescence sensing. *Mater. Chem. Front.* 4 (2), 369–385. doi:10.1039/C9QM00572B

Cheng, F., Zhang, T., Yang, C., Zhu, H., Li, Y., Sun, T., et al. (2022a). A direct and rapid method for determination of total iron in environmental samples and hydrometallurgy using UV–Vis spectrophotometry. *Microchem. J.* 179, 107478. doi:10.1016/j.microc.2022.107478

Cheng, Y., Liu, Y., Liu, Y., Li, Y., Wu, R., Du, Y., et al. (2022b). A core-satellite structured type II heterojunction photocatalyst with enhanced CO2 reduction under visible light. *Nano Res.* 15 (10), 8880–8889. doi:10.1007/s12274-022-4714-7

Duan, N., Feng, J., Deng, B., Yang, S., Tian, H., and Sun, B. (2022). A colourimetric fluorescent probe for the sensitive detection of total iron in wine. *Food Chem.* 383, 132594. doi:10.1016/j.foodchem.2022.132594

Duck, K. A., and Connor, J. R. (2016). Iron uptake and transport across physiological barriers. *BioMetals* 29 (4), 573–591. doi:10.1007/s10534-016-9952-2

Dutt, S., Hamza, I., and Bartnikas, T. B. (2022). Molecular mechanisms of iron and heme metabolism. *Annu. Rev. Nutr.* 42 (1), 311–335. doi:10.1146/annurev-nutr-062320-112625

Ezati, P., and Rhim, J. W. (2022). Pectin/carbon quantum dots fluorescent film with ultraviolet blocking property through light conversion. *Colloids Surfaces B Biointerfaces* 219, 112804. doi:10.1016/j.colsurfb.2022.112804

Ferreyra, D. D., Rodríguez Sartori, D., Ezquerra Riega, S. D., Rodríguez, H. B., and Gonzalez, M. C. (2020). Tuning the nitrogen content of carbon dots in carbon nitride nanoflakes. *Carbon* 167, 230–243. doi:10.1016/j.carbon.2020.05.062

Fu, P., Zhang, J., Li, H., Mak, M., Xu, W., and Tao, Z. (2021). Extracellular vesicles as delivery systems at nano-/micro-scale. *Adv. Drug Deliv. Rev.* 179, 113910. doi:10.1016/j.addr.2021.113910

Gupta, D., Guzman, M. S., Rengasamy, K., Stoica, A., Singh, R., Ranaivoarisoa, T. O., et al. (2021). Photoferrotrophy and phototrophic extracellular electron uptake is common in the marine anoxygenic phototroph Rhodovulum sulfidophilum. *ISME J.* 15 (11), 3384–3398. doi:10.1038/s41396-021-01015-8

Huang, S., Song, Y., He, Z., Zhang, J. R., and Zhu, J. J. (2021). Self-assembled nanomaterials for biosensing and therapeutics: Recent advances and challenges. *Analyst* 146 (9), 2807–2817. doi:10.1039/D1AN00077B

Kang, J. W., and Kang, D. H. (2021). Effect of amino acid-derived nitrogen and/or sulfur doping on the visible-light-driven antimicrobial activity of carbon quantum dots: A comparative study. *Chem. Eng. J.* 420, 129990. doi:10.1016/j.cej.2021.129990

Karakoçak, B. B., Laradji, A., Primeau, T., Berezin, M. Y., Li, S., and Ravi, N. (2021). Hyaluronan-conjugated carbon quantum dots for bioimaging use. *ACS Appl. Mater. Interfaces* 13 (1), 277–286. doi:10.1021/acsami.0c20088

Keerthana, P., Cherian, A. R., Sirimahachai, U., Thadathil, D. A., Varghese, A., and Hegde, G. (2022). Detection of picric acid in industrial effluents using multifunctional green fluorescent B/N-carbon quantum dots. *J. Environ. Chem. Eng.* 10 (2), 107209. doi:10.1016/j.jece.2022.107209

Li, C., Liu, W., Ren, Y., Sun, X., Pan, W., and Wang, J. (2017). The selectivity of the carboxylate groups terminated carbon dots switched by buffer solutions for the detection of multi-metal ions. *Sensors Actuators B Chem.* 240, 941–948. doi:10.1016/j.snb.2016.09.068

Li, C., Zhang, Y., Liu, J., Kang, R., Klionsky, D. J., and Tang, D. (2021). Mitochondrial DNA stress triggers autophagy-dependent ferroptotic death. *Autophagy* 17 (4), 948–960. doi:10.1080/15548627.2020.1739447

Li, H., Deng, Y., Liu, Y., Zeng, X., Wiley, D., and Huang, J. (2019). Carbon quantum dots and carbon layer double protected cuprous oxide for efficient visible light CO2 reduction. *Chem. Commun.* 55 (30), 4419–4422. doi:10.1039/C9CC00830F

Li, H., Zhang, X., and MacFarlane, D. R. (2015). Carbon quantum dots/Cu2O heterostructures for solar-light-driven conversion of CO2 to methanol. *Adv. Energy Mater.* 5 (5), 1401077. doi:10.1002/aenm.201401077

Li, L., Zhang, F., Tu, R., Yu, H., Wang, H., Sun, Y., et al. (2022a). N,N-Dimethylformamide solvent assisted hydrothermal pretreatment of Chlorella for coproduction of sugar, nitrogenous compounds and carbon dots. *Bioresour. Technol.* 344, 126143. doi:10.1016/j.biortech.2021.126143

Li, Y., Liu, Y., Liu, X., Liu, Y., Cheng, Y., Zhang, P., et al. (2022b). Fe-doped SnO2 nanosheet for ambient electrocatalytic nitrogen reduction reaction. *Nano Res.* 15 (7), 6026–6035. doi:10.1007/s12274-022-4298-2

Lin, S. M., Geng, S., Li, N., Liu, S. G., Li, N. B., and Luo, H. Q. (2017). l-Histidine-protected copper nanoparticles as a fluorescent probe for sensing ferric ions. *Sensors Actuators B Chem.* 252, 912–918. doi:10.1016/j.snb.2017.06.079

Liu, C., Bao, L., Tang, B., Zhao, J. Y., Zhang, Z. L., Xiong, L. H., et al. (2016). Fluorescence-converging carbon nanodots-hybridized silica nanosphere. *Small* 12 (34), 4702–4706. doi:10.1002/smll.201503958

Liu, N., Liu, Y., Liu, Y., Li, Y., Cheng, Y., and Li, H. (2023). Modulation of photogenerated holes for enhanced photoelectrocatalytic performance. *Microstructures* 3 (1), 2022022. doi:10.20517/microstructures.2022.23

Liu, Q., Niu, X., Xie, K., Yan, Y., Ren, B., Liu, R., et al. (2021a). Fluorescent carbon dots as nanosensors for monitoring and imaging Fe^{3+} and $[HPO4]^{2-}$ ions. *ACS Appl. Nano Mater.* 4 (1), 190–197. doi:10.1021/acsanm.0c02515

Liu, S. L., Wang, Z. G., Xie, H. Y., Liu, A. A., Lamb, D. C., and Pang, D. W. (2020). Single-virus tracking: From imaging methodologies to virological applications. *Chem. Rev.* 120 (3), 1936–1979. doi:10.1021/acs.chemrev.9b00692

Liu, X., Li, H. B., Shi, L., Meng, X., Wang, Y., Chen, X., et al. (2017). Structure and photoluminescence evolution of nanodots during pyrolysis of citric acid: From molecular nanoclusters to carbogenic nanoparticles. *J. Mater. Chem. C* 5 (39), 10302–10312. doi:10.1039/C7TC03429F

Liu, Y., Deng, P., Wu, R., Zhang, X., Sun, C., and Li, H. (2021b). Oxygen vacancies for promoting the electrochemical nitrogen reduction reaction. *J. Mater. Chem. A* 9 (11), 6694–6709. doi:10.1039/D0TA11522C

Long, W. J., Li, X. Q., Yu, Y., and He, C. (2022). Green synthesis of biomass-derived carbon dots as an efficient corrosion inhibitor. *J. Mol. Liq.* 360, 119522. doi:10.1016/j.molliq.2022.119522

Mehta, P. K., Neupane, L. N., Park, S. H., and Lee, K. H. (2021). Ratiometric fluorescent detection of silver nanoparticles in aqueous samples using peptide-based fluorogenic probes with aggregation-induced emission characteristics. *J. Hazard. Mater.* 411, 125041. doi:10.1016/j.jhazmat.2021.125041

Mittal, A., Katahira, R., Donohoe, B. S., Pattathil, S., Kandemkavil, S., Reed, M. L., et al. (2017). Ammonia pretreatment of corn stover enables facile lignin extraction. *ACS Sustain. Chem. Eng.* 5 (3), 2544–2561. doi:10.1021/acssuschemeng.6b02892

Naciri, Y., Hsini, A., Ahdour, A., Akhsassi, B., Fritah, k., Ajmal, Z., et al. (2022). Recent advances of bismuth titanate based photocatalysts engineering for enhanced organic contaminates oxidation in water: A review. *Chemosphere* 300, 134622. doi:10.1016/j.chemosphere.2022.134622

Nagaraj, M., Ramalingam, S., Murugan, C., Aldawood, S., Jin, J. O., Choi, I., et al. (2022). Detection of Fe3+ ions in aqueous environment using fluorescent carbon quantum dots synthesized from endosperm of Borassus flabellifer. *Environ. Res.* 212, 113273. doi:10.1016/j.envres.2022.113273

Navazesh, S., and Ji, P. (2022). Cellular iron imbalance alters metabolite profile in gut epithelial cells. *FASEB J.* 36 (S1). doi:10.1096/fasebj.2022.36.S1.R3972

Park, S. H., Kwon, N., Lee, J. H., Yoon, J., and Shin, I. (2020). Synthetic ratiometric fluorescent probes for detection of ions. *Chem. Soc. Rev.* 49 (1), 143–179. doi:10.1039/C9CS00243J

Perumal, S., Atchudan, R., Edison, T. N. J. I., and Lee, Y. R. (2021). Sustainable synthesis of multifunctional carbon dots using biomass and their applications: A mini-review. *J. Environ. Chem. Eng.* 9 (4), 105802. doi:10.1016/j.jece.2021.105802

Rani, U. A., Ng, L. Y., Ng, C. Y., and Mahmoudi, E. (2020). A review of carbon quantum dots and their applications in wastewater treatment. *Adv. Colloid Interface Sci.* 278, 102124. doi:10.1016/j.cis.2020.102124

Rodríguez-Padrón, D., Algarra, M., Tarelho, L. A. C., Frade, J., Franco, A., de Miguel, G., et al. (2018). Catalyzed microwave-assisted preparation of carbon quantum dots from lignocellulosic residues. *ACS Sustain. Chem. Eng.* 6 (6), 7200–7205. doi:10.1021/acssuschemeng.7b03848

Singh, R. K., Kumar, R., Singh, D. P., Savu, R., and Moshkalev, S. A. (2019). Progress in microwave-assisted synthesis of quantum dots (graphene/carbon/semiconducting) for bioapplications: A review. *Mater. Today Chem.* 12, 282–314. doi:10.1016/j.mtchem.2019.03.001

Soares, M. P., and Hamza, I. (2016). Macrophages and iron metabolism. *Immunity* 44 (3), 492–504. doi:10.1016/j.immuni.2016.02.016

Stoyanovsky, D. A., Tyurina, Y. Y., Shrivastava, I., Bahar, I., Tyurin, V. A., Protchenko, O., et al. (2019). Iron catalysis of lipid peroxidation in ferroptosis: Regulated enzymatic or random free radical reaction? *Free Radic. Biol. Med.* 133, 153–161. doi:10.1016/j.freeradbiomed.2018.09.008

Wahba, M., El-Enany, N., and Belal, F. (2015). Application of the Stern–Volmer equation for studying the spectrofluorimetric quenching reaction of eosin with clindamycin hydrochloride in its pure form and pharmaceutical preparations. *Anal. Methods* 7, 10445–10451. doi:10.1039/C3AY42093K

Wang, B., and Lu, S. (2022). The light of carbon dots: From mechanism to applications. *Matter* 5 (1), 110–149. doi:10.1016/j.matt.2021.10.016

Wang, C. Y., and Babitt, J. L. (2019). Liver iron sensing and body iron homeostasis. *Blood* 133 (1), 18–29. doi:10.1182/blood-2018-06-815894

Wareing, T. C., Gentile, P., and Phan, A. N. (2021). Biomass-based carbon dots: Current development and future perspectives. *ACS Nano* 15 (10), 15471–15501. doi:10.1021/acsnano.1c03886

Wheal, M. S., DeCourcy-Ireland, E., Bogard, J. R., Thilsted, S. H., and Stangoulis, J. C. R. (2016). Measurement of haem and total iron in fish, shrimp and prawn using ICP-MS: Implications for dietary iron intake calculations. *Food Chem.* 201, 222–229. doi:10.1016/j.foodchem.2016.01.080

Wu, Y., Liu, Y., Yin, J., Li, H., and Huang, J. (2019). Facile ultrasonic synthesized NH_2-carbon quantum dots for ultrasensitive Co^{2+} ion detection and cell imaging. *Talanta* 205, 120121. doi:10.1016/j.talanta.2019.120121

Xu, Y. L., Mo, R. X., Qi, C. Y., Ren, Z., Jia, X. Z., Kan, Z. G., et al. (2021). Dual-property blue and red emission carbon dots for Fe(III) ions detection and cellular imaging. *Rare Met.* 40 (7), 1957–1965. doi:10.1007/s12598-020-01506-1

Yan, N., Zheng, Z., Liu, Y., Jiang, X., Wu, J., Feng, M., et al. (2022). Photo-responsive shape memory polymer composites enabled by doping with biomass-derived carbon nanomaterials. *Nano Res.* 15 (2), 1383–1392. doi:10.1007/s12274-021-3674-7

Yang, G., Zhu, C., Du, D., Zhu, J., and Lin, Y. (2015). Graphene-like two-dimensional layered nanomaterials: Applications in biosensors and nanomedicine. *Nanoscale* 7 (34), 14217–14231. doi:10.1039/C5NR03398E

Yang, Z., Li, Z., Xu, M., Ma, Y., Zhang, J., Su, Y., et al. (2013). Controllable synthesis of fluorescent carbon dots and their detection application as nanoprobes. *Nano-Micro Lett.* 5 (4), 247–259. doi:10.1007/BF03353756

Zhang, Q., He, S., Zheng, K., Zhang, L., Lin, L., Chen, F., et al. (2022). Green synthesis of mustard seeds carbon dots and study on fluorescence quenching mechanism of Fe^{3+} ions. *Inorg. Chem. Commun.* 146, 110034. doi:10.1016/j.inoche.2022.110034

Zhang, T., Huang, J., Deng, S., and Yu, G. (2011). Influence of pesticides contamination on the emission of PCDD/PCDF to the land from open burning of corn straws. *Environ. Pollut.* 159 (6), 1744–1748. doi:10.1016/j.envpol.2011.01.042

Zhang, Y., Qin, H., Huang, Y., Zhang, F., Liu, H., Liu, H., et al. (2021). Highly fluorescent nitrogen and boron doped carbon quantum dots for selective and sensitive detection of Fe^{3+}. *J. Mater. Chem. B* 9, 4654–4662. doi:10.1039/D1TB00371B

Zhao, Y., Jing, S., Peng, X., Chen, Z., Hu, Y., Zhuo, H., et al. (2020). Synthesizing green carbon dots with exceptionally high yield from biomass hydrothermal carbon. *Cellulose* 27 (1), 415–428. doi:10.1007/s10570-019-02807-0

Zvěřina, O., Kuta, J., Coufalík, P., Kosečková, P., and Komárek, J. (2019). Simultaneous determination of cadmium and iron in different kinds of cereal flakes using high-resolution continuum source atomic absorption spectrometry. *Food Chem.* 298, 125084. doi:10.1016/j.foodchem.2019.125084

Frontiers in
Bioengineering and Biotechnology

Accelerates the development of therapies, devices, and technologies to improve our lives

A multidisciplinary journal that accelerates the development of biological therapies, devices, processes and technologies to improve our lives by bridging the gap between discoveries and their application.

Discover the latest Research Topics

See more →

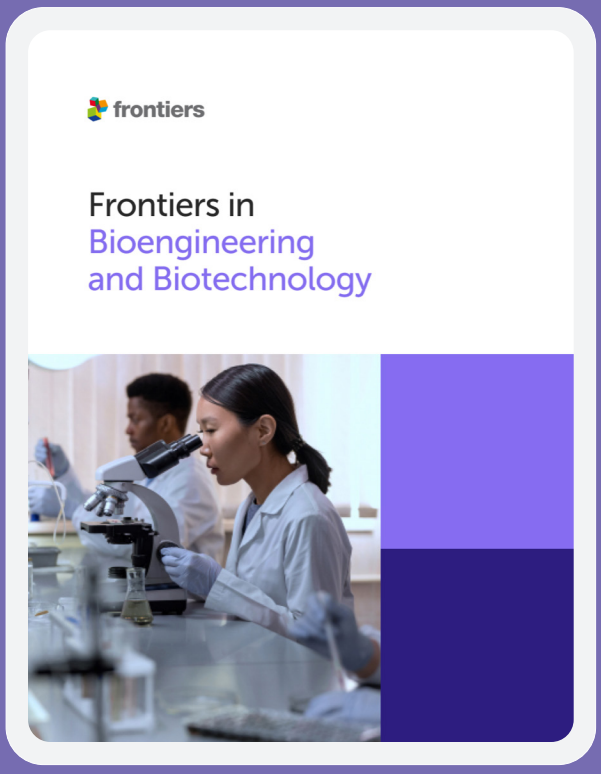

Frontiers

Avenue du Tribunal-Fédéral 34
1005 Lausanne, Switzerland
frontiersin.org

Contact us

+41 (0)21 510 17 00
frontiersin.org/about/contact